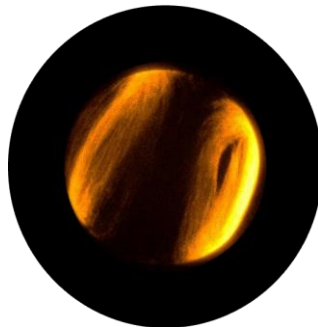
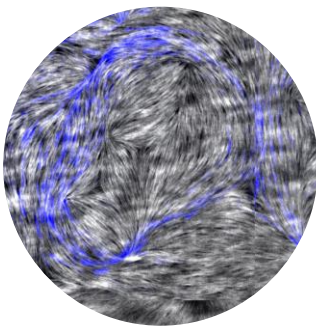


Active Cytoskeletal Systems on Lipid Membranes

Dissertation von:
Alfredo Sciortino





Fakultät für Physik

Active Cytoskeletal Systems on Lipid Membranes

Alfredo Sciortino

Vollständiger Abdruck der von der Fakultät für Physik der Technischen Universität München zur Erlangung des akademischen Grades eines Doktors der Naturwissenschaften genehmigten Dissertation.

Vorsitzende/-r: Prof. Dr. Martin Zacharias

Prüfende/-r der Dissertation:

1. Prof. Dr. Andreas Bausch
2. Prof. Dr. Erwin Frey

Die Dissertation wurde am 04.10.2021 bei der Technischen Universität München eingereicht und durch die Fakultät für Physik am 24.11.2021 angenommen.

Acknowledgements

First of all, I want to warmly thank my Doktorvater Prof. Andreas Bausch for allowing me to perform research in this group. Discussing with him always provided deep, interesting and often beyond-scientific insight. His powerful laughter has been the sweet, sweet background of these years of research.

I had the opportunity to spend this time in a relaxed, friendly and stimulating working environment and for this I also thank all of my colleagues at the E22/E27 chair, with a special mention to my present and former office mates: Katherina Dürre, who introduced me to cDICE, Philip Walter Bleicher, my favorite co-author, Timon Nast-Kolb, master of wordplay, and Chiao-Peng Hsu, the Taiwanese with a very Italian name. I also had the opportunity of supervising several talented students. Especially to the last ones, Alice Yu De La Trobe and Lukas Neumann, I owe particular gratitude and deserve credit to some of the results here included. Finally, I want to explicitly mention and thank our TAs, Monica, Gabi and especially Karin, that have been providing me with liters of fresh actin and myosin.

Several other people have been collaborating to the results of this thesis. I want to thank: Remi Boros, John Berezney (from Zvonimir Dogic's group) for introducing me to their amazing microtubules system; Ivan Maryshev and Timo Krüger (from Erwin Frey's group) for a long and insightful series of quick chats; Hammad Faizi (from Petia Vlahovska's group), Matt Petterson and Sarvesh Uplap (from Aparna Baskaran's and Mike Hagan's group) for joining the effort of analyzing and simulating active GUVs, a feat I would have not been able to complete without their help.

These long, often frustrating, years I have always been accompanied by two important friends: Ben Buchmann (*aka* Dr. Kirschblut) and Henry Dehne (*aka* Dr. H-Dizzy). They started as colleagues and ended up being more: the only people I can forgive for messing with my German coming up with (invented?) words such as *Panzerfrosch*¹ and *Gullideckel*². And for putting pineapple on pizza. I don't say this lightly. They say that finding a German friend is hard, but they will stay forever. Well, I even got two. I love you *Freunde*.

Finally, thanks to my family, my parents and my sister, for the support, love, the shipments of first-necessity goods from Italy and for teaching me how to think in words and numbers interchangeably.

Thanks to Francesca, for always being close, even when at a distance. *Longtemps je me suis couché de bonne heure*, mais à tes côtés. I hope you can be proud of me as I am of you.

All of these people share part of the merit for this work. The bad parts are entirely on me.

¹Much better than *Schildkröte*!

²Definitely an invented word!

Abstract

Cells rely on their cytoskeleton for a vast number of reasons, ranging from mechanical stability to plasticity, motion, division and differentiation. Cytoskeletal filaments and their associated proteins indeed not only provide a scaffold for the cell, allowing it to maintain its shape and transport material throughout its inside, but can also produce active forces, which are at the base of cellular dynamics. In order to do so, however, the cytoskeleton is highly regulated: filaments assemble where needed, motors activate when necessary and so on. Hence, as a whole, the cytoskeleton is an organized active structure, that continuously self-organizes out of equilibrium. Additionally, cells are also surrounded by a lipid cellular membrane, which separates them from the outside. Actively deforming the cell means actively deforming the membrane. Indeed, the cross-talk between the cytoskeleton and the membrane is tight: cytoskeleton-related proteins are often membrane-bound and allow local regulation, localizing the necessary tools when needed, and thus tuning any deformation of the cell shape. Much is however yet unknown on how the interplay between the cytoskeleton and the membrane affects both sides: clearly, the membrane can be deformed by the cytoskeleton but at the same time the self-organization of the filaments is affected by the presence of a fluid lipid membrane and by the elastic confinement induced due to the membrane.

The aim of this thesis is to develop *in vitro* reconstituted model systems that allow to further explain the interaction between these two components. We use two model systems for cytoskeletal dynamics, i.e. the gliding assay and a microtubule-based active fluid, and two model systems of membranes, i.e. supported bilayers and giant vesicles, combining them appropriately to learn more about how, on the one hand, active motion of cytoskeletal filaments can be affected by the presence of a membrane and, on the other hand, how the membrane reacts to active forces. By merging membrane and cytoskeletal model systems and using fluorescence microscopy (in different forms) we gain access to a range of simplified and tunable set-ups that allow us to observe and analyze the final results.

The first combinations (gliding assays on a supported membranes) will shed light on the effect of fluidity and complex environments on the motion of filaments. The main result is that the fluidity of the membrane enforces steric interaction between filaments that has, as main consequence, the formation of polar structures of filaments gliding in the same direction and to the self-assembly of structures (topological defects) that we find can further tune the behavior of the system. This is further explored by performing gliding assays inside giant vesicles which will not only confirm the previous results, but also hint at the importance of confinement for the self-organization of ordered structures. The second combination (microtubule fluids inside lipid vesicles) will instead focus on the effect of membrane deformation on cytoskeletal organization and *vice versa*. By encapsulating an active microtubule-based fluid inside a giant vesicle we not only observe large membrane deformation but also that the behavior of the active fluid is affected by them. A feedback between the two components ensues, that we try to decouple and study in detail.

These results suggest general organizational principles that have relevance in biological systems. Moreover, reconstituting specific systems and dissecting their dynamics is also a step further in the ambitious program of building a functional cell from scratch.

Contents

Preface	1
General outline	4
1 Theoretical background	5
1.1 General physics at the micron scale	6
1.1.1 Motion at the micron scale	6
1.1.2 Depletion interaction	8
1.1.3 Active matter in very general	9
1.2 The cell cytoskeleton: filaments, motors, crosslinkers	11
1.2.1 The cytoskeleton in general	11
1.2.2 Cytoskeleton-membrane interactions	20
1.2.3 Main <i>in vitro</i> reconstituted cytoskeletal systems	22
1.3 Nematic materials	23
1.3.1 Order parameters	23
1.3.2 Microscopic model of nematics: hard rods	24
1.3.3 Continuous model of nematics: the elastic energy	29
1.3.4 Defects and topological constraints	31
1.4 Membranes and their mechanics	35
1.4.1 Lipid membranes in general	35
1.4.2 Membrane models: vesicles (GUVs) and supported bilayers (SLBs)	37
1.4.3 Mechanics of membranes	38
2 Gliding on a membrane:	
Polar pattern formation of driven filaments on lipid membranes	45
2.1 Introduction	45
2.1.1 Chapter outline	46
2.2 General background: self-propelled rod theory	47
2.3 The gliding assay as a model system for collective pattern formation	48
2.3.1 Actin gliding assay	49
2.3.2 Microtubule gliding assay	52
2.3.3 Gliding assays with surface modifications	53
2.3.4 Filaments gliding on a membrane	54
2.4 Actin gliding on a supported lipid bilayer	57

2.4.1	Actin filaments on a SLB align nematicly	58
2.4.2	Collective behavior at intermediate densities	59
2.4.3	Collective behavior at higher densities	63
2.4.4	Polarity of observed structures	66
2.4.5	Discussion	67
2.5	Gliding inside a giant unilamellar vesicle	70
2.5.1	Encapsulation of actin and motors in a GUV	71
2.5.2	Filaments gliding on a GUV form polar patterns	72
2.5.3	Mechanisms of pattern formation	75
2.5.4	Discussion	80
2.6	Gliding in a nematic	82
2.6.1	Experimental system	82
2.6.2	Microtubules align in the nematic material and follow its distortions	84
2.6.3	Defects and nematic distortions break the global symmetry	87
2.6.4	Microtubules gliding in a nematic form polar lanes	91
2.6.5	Effect of filaments' length, concentration and sedimentation	93
2.6.6	Theoretical and computational models describe the experiments well	95
2.6.7	Discussion	102
2.7	Conclusions of Chapter 2	104

3 Pushing on a membrane

	Active microtubule fluids and their confinement inside lipid vesicles	105
3.1	Introduction	105
3.1.1	Chapter outline	106
3.2	Active microtubule fluids (AMFs)	107
3.2.1	Basic mechanism	107
3.2.2	Active nematics	108
3.2.3	Bundled active networks	108
3.2.4	Hydrodynamic theories: an overview	109
3.2.5	The microscopic origin of extensile activity	109
3.3	The interplay of activity and connectivity in AMFs	113
3.3.1	Experimental system	113
3.3.2	Experimental results	113
3.3.3	Cytosim simulations	117
3.3.4	Discussion	126
3.4	AMFs under confinement and active GUVs	128
3.4.1	The role of confinement for AMFs	128
3.4.2	Active GUVs	129
3.5	An active microtubule fluid deforms lipid vesicles	133
3.5.1	Experimental system	133
3.5.2	GUVs deform due to pushing of microtubules bundles	133
3.5.3	Spectral behavior of the GUV membrane	137
3.5.4	Analysis of the active forcing	140

3.5.5	Effect of confinement on the AMF	143
3.5.6	Simulations of an AMF inside a GUV	145
3.5.7	Discussion	148
3.6	Conclusions of Chapter 3	150
Conclusions		151
4	Materials and Methods	153
4.1	Materials: buffer, proteins and reagents	153
4.2	Experimental model systems of lipid membranes: SLBs and cDICE GUVs .	157
4.3	Microscopy	160
4.4	Gliding assays	161
4.5	Data analysis for gliding filaments	162
4.6	Active microtubule fluids	167
4.7	Data analysis for active microtubule fluids	167
4.8	Cytosim simulations	169
List of publications		177
References		179
List of Figures		193
A	The Monge representation and the Helfrich-Canham energy in Fourier form	I
A.1	The Monge representation	I
A.2	The Helfrich-Canham energy in Fourier space	II
B	Motion of filaments propelled by SLB-bound motors	III

Preface

There is a common (at least, in some fields) joke that, for a Physicist a cell is, in the best case, just a 'bag of proteins' and in the worst case, simply a 'flaccid sphere'. This is not only clearly wrong, but also misses one fundamental point of cell biology, which is the importance of understanding how different components inside the cell *interact* to obtain the needed result. In order to move, grow, divide and so on, cells have to continuously regulate each individual component and react to an enormous set of external conditions. Proteins, and material in general, need to be present where and when needed, need to be activated on a glimpse, need to do what they do and then somehow disappear. Attempting to understand how all of this works is one of the main goal of Biological sciences.

However, a full description of a cell and its behavior is far from being in our reach. We hence choose, in this thesis, to focus on only one of the main components of a cell, i.e. the cytoskeleton, and in particular on the reconstitution and study of cytoskeletal processes that act on or against a lipid membrane. A cell is indeed not really *flaccid* at all, it actually has a skeleton of sort, named the cytoskeleton, a global name that gathers together a huge number of proteins which provide some mechanical stability to the cell. Amongst these proteins, two classes play a major role, i.e. cytoskeletal filaments (especially actin and microtubules, which will be the main protagonists of this thesis) and molecular motors (especially myosin and kinesin). Filaments are elongated polymers, each monomer being a protein, and act as a scaffold for the cells, in other words, they give the cell a given shape. At the same time, because the cell has to adapt to different conditions and perform a number of task which require changing shape, the cytoskeleton is also able to remodel itself and exert forces on the cell membrane in order to deform it. To do that, motors and other filament-associated proteins act in unison to assemble and disassemble the filaments, push them to provide force or strengthen them when resistance is required. In order to do that, the cytoskeleton has to self-organize into complex, higher-ordered structures that perform the necessary task. Examples include the formation of the cytokinetic ring, when actin filaments form a membrane-bound, ring-like structure that contracts and severs the cell in two daughter cells; the formation of filopodia and lamellipodia, two kind of actin-propelled protrusions of the cellular membrane that allow the cell to feel and navigate its environment; the formation of the mitotic spindle, in which microtubule filaments extend in order to separate the chromosomes during cell division and many more.

How do these ordered structure, that all have in common their being composed of filaments and motors, arise? This point is particularly interesting from a Physicist's point of view since understanding how, given a set of interactions, elements in a system evolve into ordered structure is one of the main points of Physics and one that has recently advanced much in the field of

active matter [Giardina 2008; Vicsek and Zafeiris 2012; Poon 2013], i.e. the study of objects and living beings able to self-propel and how they interact and assemble together. What are the relevant interaction between cytoskeletal filaments and how does the presence of motors pushing them affect their assembly?

Moreover, the cytoskeleton also has to act against the membrane, pushing it to and deforming it to change the cell's overall shape. The lipid membrane, as an elastic material, can indeed be remodelled, but this requires the right amount of energy so that it will just change shape but not break. Additionally, most cytoskeleton-related proteins are bound to the membrane and, this latter being fluid, they diffuse on it. How does this fluidity affect the dynamics of the cytoskeleton is also an open question. And, in addition, how are cytoskeletal filaments, that can reach a size from hundreds of nanometers up to the millimeter scale, and their dynamics affected by the fact that they are confined inside a cellular membrane (with a size of $\approx 1 - 100 \mu\text{m}$)? And how does the fact that the cytoskeleton actively deforms the membrane affects, in return, the cytoskeleton itself?

To (partially) answer these questions, we use simple and tunable model systems which recapitulate some of these behaviors but in a controlled setting. There is indeed at least a point of view from which a simplified approach to the cell can be useful, and that is that a holistic, full understanding of the behavior of a cell is incredibly challenging. Thus one can hope that some partial, but general, understanding of how a cell works might come from identifying a small set of biological components that when mixed together perform a single task resembling that of a cell. This approach, generally known as *in vitro* cell reconstitution, consists in purifying proteins in the laboratory and find a way to assemble them such that they do what they would do inside a real cell. The hope, in the spirit of Richard Feynmann's quote *What I cannot create I don't understand*, is that by reconstituting something we can also learn how it works, why it works and, more importantly, why it sometimes does not work. Recently, *in vitro* reconstituted systems have recently started to shed more light on this issue in the context of the cytoskeleton [Weber et al. 2015; Huber et al. 2018], underlining the importance of the microscopic interaction as a fundamental element shaping the macroscopic behavior. Tuning the former indeed tunes the resulting structures. Much is however still not known on how, given a specific microscopic interaction, we can actually predict the macroscopic outcome. And in particular, how are these interactions modified when cytoskeletal filaments move bound to a lipid membrane has been studied only recently [Roux et al. 2002; Grover et al. 2016]. Understanding it better would mean being able to predict how and why do cellular structure form and how does that affect the cell's shape. Moreover, the ability to study cytoskeletal motors and filaments bound to membrane allows a better understanding of their kinetics and behavior when on a fluid substrate [Lee et al. 2010; Pyrpassopoulos et al. 2012; Jiang et al. 2019; García-Soriano et al. 2020].

Additionally, in the very recent years, a great body of works has focused on the reconstitution of cytoskeletal systems in cell-like confinement using giant vesicles as a model system. Giant vesicles indeed provide a perfect-sized, relatively simple model for a full cell that can be filled by a minimal system of proteins (an improved version of the 'bag of protein' approach). This has allowed to study membrane plasticity and regulation in the presence of an active actin network [Loiseau et al. 2016; Maan, Loiseau, and Bausch 2018; Dürre et al. 2018; Simon et al. 2019; Paraschiv et al. 2021], the behavior of confinement in the self-assembly of active cytoskeletal

fluids [Keber et al. 2014] and the shape-remodelling ability of cytoskeletal filaments [Sato et al. 2017; Rodríguez-García et al. 2020].

Here we exploit two model systems for membranes (supported bilayers and giant vesicles) to study complementary regimes of cytoskeletal activity. The first system (supported lipid bilayers or SLBs) will allow us to study how the fluidity of the membrane affects the filament-filament interaction on an individual, microscopic level if molecular motors are bound to a membrane, but also to what kind of patterns does this change leads on a collective scale. By binding molecular motors *on* a SLB we indeed force filaments to align upon collision due to fluidity-induced steric interactions, which leads to the formation of polar structures. We identify the main mechanism by which polarity emerges and we focus especially on the effect the transient formation of wedge-like structures has on the pattern formation process. We additionally further tune the system to also study how the motion of membrane-bound filaments is affected when moving in complex environments (an elastic, nematic material, to be precise) and how confinement in a spherical topology (a giant vesicle) can affect the pattern formation process. This first part is meant to extract general but realistic organizational principles and constraints that the cell cytoskeleton must cope with, in particular the fluidity of the cellular membrane or of organelles and the presence of a crowded, complex and confined environment. In summary, SLBs allow to study the effect of local interactions in two dimensional systems on the formation of collective ordered patterns.

The second system (giant unilamellar vesicles or GUVs), coupled with an active fluid composed of short microtubules and molecular motors, will instead address how the cytoskeleton can deform a membrane and how the presence of the membrane affects the organization of the fluid itself. By encapsulating the active fluid *inside* the GUV we can study how the resulting cytoskeletal bundles react under elastic confinement and also how the membrane reacts to this active pushing force. We observe large GUV shape deformations due to activity that we can study in time and space to understand the coupling of the membrane's passive mechanical properties and the out-of-equilibrium active forcing. In short, GUVs allow to study the effect of a fluid-like, hydrodynamic forcing on the membrane and of the membrane on the cytoskeletal self-organization in three dimensions.

These findings, together, shed further light on the membrane-cytoskeleton interaction on different scales and in different geometries and suggest new systems and strategies along the road of building a cell from scratch. While we do not identify any precise cellular counterparts, we expect the processes we observe to play a role ubiquitously and suggest strategies to further study them and / or manipulate them.

General outline

This thesis is divided in three Chapters, a theoretical introduction one (Chapter 1) and two results Chapters (2 and 3). A Methods section (4) is present at the end. We also include, at the beginning of each chapter, a small table of contents. At the end of the work also a full list of Figures can be found, together with the Bibliography and a small Appendix.

The first Chapter provides a general theoretical background. In an attempt to keep this work self-consistent most of the relevant Physics we are going to use or hint at is discussed more or less in details. In particular, the general Physics at the micron scale (i.e., that of cells) is discussed (Section 1.1), with two more in depth Sections about nematic materials, as filaments are elongated and therefore nematic order is relevant (Section 1.3), and on lipid membranes, which are a main topic of this thesis (Section 1.4). Chapter 1 also gives an overview of the cytoskeleton in general (Section 1.2). Since this work will not focus on any particular biological process, but rather on general underlying principles, we only hint at relevant details and literature, while still giving all of the necessary information. Further and more specific reviews and theoretical details are also included in their relevant Chapter.

The remaining Chapters are two complementary ones exploring the interplay between cytoskeleton and membranes.

The second Chapter deals with filaments gliding on lipid membranes. First, an introduction on the gliding assay as a technique to study cytoskeletal organization is given (Section 2.3). Afterward, the three main experimental projects of the Chapter, i.e., actin gliding on a supported membrane (Section 2.4), on a giant vesicle (Section 2.5) and in a nematic material (2.6) are presented with their results. This chapter focuses on the role of steric interactions due to the fluidity of the membrane, of confinement in different topologies and on the effect of the environment on pattern formation by cytoskeletal systems. In short, this Chapter deals with locally interacting, gliding filaments that move *on* a membrane.

The third Chapter explores instead active fluids made of cytoskeletal components (in particular, microtubules), their description (Section 3.2), the role of crosslinking and nematic order on shaping their activity (Section 3.3) and finally, their encapsulation inside vesicles (Section 3.5). In this case, filaments will move as a fluid, with long-range interaction and it will push *against* a membrane, thus deforming it. The effect of the microtubules on the membrane and of the membrane on the microtubules is discussed here. This chapter also includes a quick review of vesicle-based systems to study the cytoskeleton and active systems in general (Section 3.4).

In the end, we draw some conclusion and, of course, give an in-depth overview of the Methods used throughout this work (Methods, Chapter 4).

Chapter 1

Theoretical background

Contents

1.1	General physics at the micron scale	6
1.2	The cell cytoskeleton: filaments, motors, crosslinkers	11
1.3	Nematic materials	23
1.4	Membranes and their mechanics	35

Chapter outline

This chapter introduces the general background and theoretical framework for this thesis. As this work focuses mainly on the active motion of cytoskeletal filaments in connection to membranes, we describe how things move at the microscopic scale, what the cytoskeleton actually is, how its components behave and organize and, finally, what is so interesting about membranes. The Physics of this chapter is limited mainly to equilibrium results. In the next chapters we will expand them by describing systems in which activity is present (in the form of molecular motors) in order to study the resulting organization of filaments and membranes. Here, however, they are mostly described in their equilibrium behavior as a benchmark.

This chapter is meant to be read in independent blocks and is structured as follows:

Section 1.1 deals with the general physics. It gives a quick but overview of motion at the microscopic scale and introduces the depletion interaction used often in this work. A quick section about active matter is also present.

Section 1.2 focuses on the cytoskeleton, and in particular on the main protagonists of this work, i.e. filaments and motors.

Section 1.3 deals with the isotropic-nematic transition in systems of elongated objects which is one of the main framework of the next chapter, together with an account of how to write a general free energy for nematic materials and is the theoretical introduction relevant for Chapter 2.

Finally, section 1.4 deals with the second protagonists of this work, i.e. lipid membranes and their fluctuations, these latter being fundamental in Chapter 3.

1.1 General physics at the micron scale

The microscopic scale is the intermediate one: it ranges from the size of a molecule ($\sim 10^{-9} m$) to the size of a cell ($10^{-5} m$). In this Section we discuss general physics at the micron scale. While of course the laws of physics do not change at any scale, the relative importance of different contribution do. In particular, the microscopic scale is in a sweet spot where quantum mechanics barely plays any significant role but the scale is still small enough for other features being present which makes it profoundly different from the macroscopic scale we are used to.

1.1.1 Motion at the micron scale

1.1.1.1 The role of thermal fluctuations

Because of the small size and speed, objects at the microscopic scale are affected by an energy which is comparable with that of their environment. The relevant scale is that of thermal fluctuations: molecules continuously and randomly interact with each other and collisions occurs. The typical energy exchange during such interactions is of the order of $k_B T$ where k_B is Boltzmann's constant and T is the temperature¹.

At room temperature ($T = 300K$) the typical energy scale is $k_B T = 4.1 \cdot 10^{-21} J$. While it does not make sense for us to consider such small quantities at our every-day macroscopic scale, they can be relevant for micron-sized objects. Indeed, to accelerate a non-moving, spherical particle (with density comparable to that of water and linear size of $\approx 10 \mu m$) up to a speed of one body length per second one needs a total energy which is comparable to $k_B T$ at room temperature².

This shows that almost nothing is completely still at the micron scale, as thermal fluctuations always have enough energy to displace particles. Notice that this scale is also the relevant scale for biology: cells, enzymes, nutrients, bacteria etc. are small enough to be subject to a continuous bombardment from the fluid solvent and to suffer the system's fluctuations. Then one must account for it when studying them.

We need to address the problem from two different point of views: how do microscopic object move when subject to a force and how they move when displaced by fluctuations.

1.1.1.2 Low-Reynolds hydrodynamics

Motion at the microscopic scale is set by the adimensional number $Re = LU\rho/\eta$ in which the scaling behavior of the system condensed as we change its linear scale L and the typical speed U . It is called Reynolds number and estimates the relative importance of inertia over viscosity at the considered scale. If we are at the microscopic scale, we can assume objects have a typical size $L = 1 \mu m$ and move at a speed of one body-length per second, i.e. $U = L s^{-1} = 1 \mu m/s$.

¹Roughly, $k_B T/2$ is the average kinetic energy of a particle's motion along a given axis. This result goes under the name of equipartition theorem. It still is a good estimate of the typical energy scale of a microscopic system.

²Indeed the kinetic energy required is $E = \frac{1}{2} \frac{4}{3} \pi r^3 \rho \left(\frac{r}{1s}\right)^2 = \frac{2}{3} \pi \rho r^5 s^{-2}$ with $\rho = 1000 Kg/m^3$ and $r = 10 \cdot 10^{-6} \mu m$ is $E \approx 10^{-21} J \approx k_B T$

By putting in these number, we find $Re \sim 10^{-4}$ so we see that we can *completely neglect* any inertial term as it is ≈ 10000 times smaller than the corresponding drag term [Purcell 1977]. This simple scaling argument shows that forces applied to particles of microscopic size do not alter their acceleration, as inertia is negligible, but rather their velocity. In other words, objects *immediately* reach terminal velocity due to the fluid's drag force. Thus given an external force \mathbf{F} we assume the particle immediately moves with velocity:

$$\mathbf{v} = \frac{F}{\gamma} = \mu \mathbf{F} \quad (1.1)$$

where $\mu = \frac{1}{\gamma}$, i.e. the inverse of the drag coefficient γ , is the mobility coefficient of the particle, it has a mainly geometrical origin and can be computed using Stokes' law.

Equivalently, given all the forces, including drag, acting on a particle, we can write

$$\Sigma_i \mathbf{F}_i = 0 \quad (1.2)$$

In the case of no external driving force, however, the main mechanism of movement the micron-scale is *diffusion*, which is due to thermal fluctuations and hence statistical in nature. We hint at it in next section.

1.1.1.3 Diffusion

Small objects ($\approx 1 \mu m$) immersed in a fluid exhibit an erratic motion known initially as Brownian motion, in honor of Robert Brown [Brown 1828] who first observed and described it. It is now considered more in general as diffusion.

Such a motion does not depend on any external flow or force acting on the particles but arises from the interaction of it with the solvent molecules. Thanks to seminal work by physicists such as Einstein [Einstein 1905; Einstein 1908], Smoluchowski [Smoluchowski 1906], Perrin [Perrin 1912] and Langevin [Langevin 1908] we now have a clear, quantitative way of dealing with this motion and to characterize it, albeit in probabilistic terms.

The main result is that while objects moving randomly in this way do not move on average, having a mean position $\langle \mathbf{r} \rangle = 0$. However, over time, particles will spread more and more, as given by the mean-squared displacement (MSD) equation

$$\langle |\mathbf{r}(t + \tau) - \mathbf{r}(t)|^2 \rangle = 2nD\tau \quad (1.3)$$

where D , called the diffusion coefficients, is a constant. This shows that particles indeed *do* move at the microscopic scale just because of the presence of noise, as they disperse over time. However, they move less efficiently, as the MSD scales slowly, i.e., linearly with the time and not quadratically ($\sim \tau^2$) as instead would a particle moving persistently (ballistic motion) rather than randomly.

Einstein was also able to connect the diffusion coefficient D to measurable physical quantities. Indeed, he proved that

$$D = \mu k_B T \quad (1.4)$$

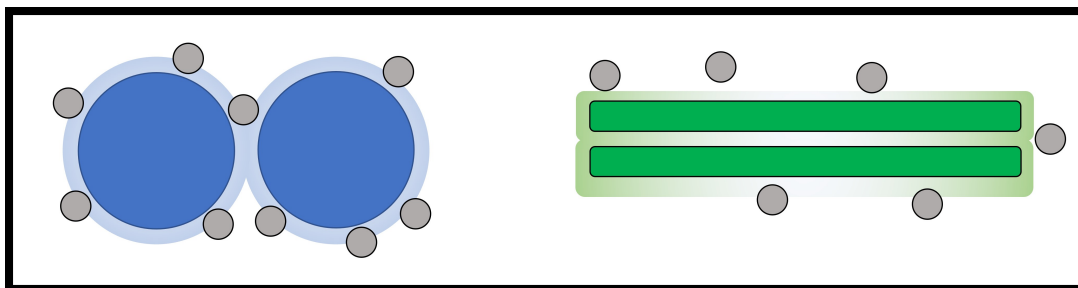


Figure 1.1: **Depletion force** Big objects immersed in a bath of smaller objects feel an attractive force. This is because by aggregating together bigger objects can decrease the volume that was previously inaccessible to the smaller ones, thus increasing their entropy. The same phenomenon is present in the case of elongated objects (e.g., filaments) in a bath of smaller polymers (e.g., PEG or methylcellulose).

where k_B is Boltzmann's constant, T is the temperature and μ is the mobility we already encountered in the force-velocity relationship 1.1.1.2. The result is known as the Einstein-Smoluchowski relation. We can use this equation to compute the value of D for an object of a given size. As already mentioned, μ can be computed by geometrical principles and connected with the solvent's properties using the formula for Stokes' coefficients.

Diffusion also affects objects' rotation and, in the case of elongated particles such as filaments, their shape fluctuations.

1.1.2 Depletion interaction

Microscopic particles can interact with each other in a number of ways that, as we will see further on, can change dramatically their ability to self assemble. The depletion interaction is one of these ways and we will use it extensively in this work.

Depletion is an entropic force³ arising at the microscopic scale when small objects are in solution together with bigger ones and the objects are hard, i.e. they can not penetrate each other. The presence of bigger objects impedes smaller ones to occupy some of the volume around them (for example, in the case of a small spheres of radius r and a big sphere of radius R , a spherical shell of inner radius R and outer radius $R + r$ is unavailable to the center of mass of the smaller sphere as otherwise they would have to penetrate the bigger one). However, if the bigger objects aggregate, they free some of this previously excluded volume. As having more volumes available for the smaller objects increases the total entropy, this latter condition is favored [Asakura and Oosawa 1954; Lekkerkerker and Tuinier 2011].

Figure 1.1 show an example of particles of different shape interacting through depletion.

The net effect is that small objects in solution exert a pressure on bigger ones. In the case of elongated objects, such as filaments (see Section 1.2.1.1) this can lead to the formation of filaments' bundles. Additionally, filaments (and bigger objects in general) are effectively pushed against the container walls. This interaction can be used experimentally (we will, in Chapter 2) to change the interaction between filaments or to sediment them on a surface without having to

³That is, roughly, a force that works towards the increase of the total entropy of the system, requiring no change in its potential energy.

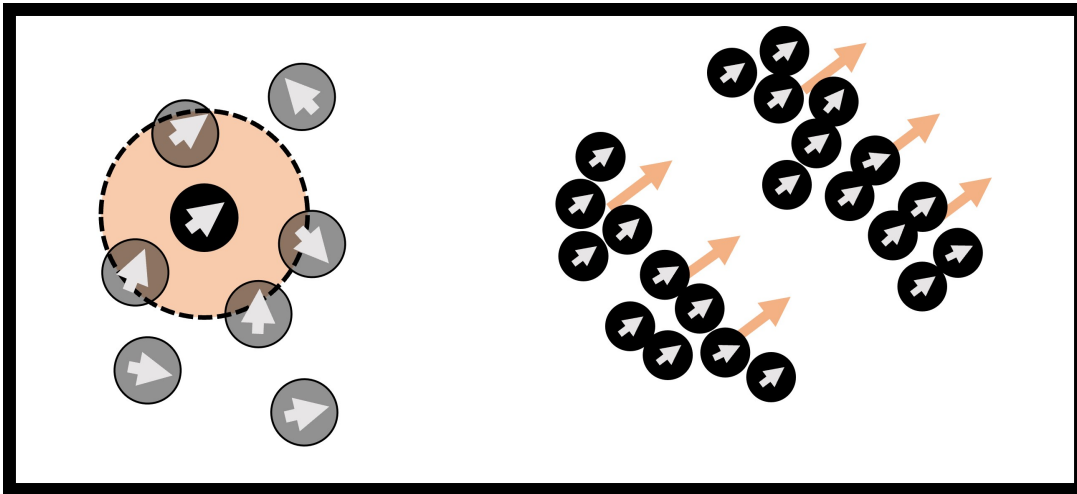


Figure 1.2: **Scheme of the Vicsek model as an example of agent-based model** A) Scheme of the Vicsek model [Vicsek et al. 1995]. Particles with a given self-propulsion speed interact locally with their neighbors and change their speed accordingly. B) Pattern forming in the Vicsek model: at high activity collective bands form, at low activity the phase is isotropic.

immobilize them. This is usually done via the addition of a *depletant*, i.e. a small polymer such as PEG, methylcellulose or dextrane, which however might also have the effect of increasing the medium's viscosity.

Depletion interaction are also tightly connected to the isotropic-nematic transition discussed in Section 1.3.2. As the cell is a crowded environment made of particles of different size, additionally, depletion interactions are of particular importance when studying cell-related processes.

1.1.3 Active matter in very general

Most of the physics discussed so far is based on the behavior of objects at thermal equilibrium. However, due to their capacity of self-propelling by consuming chemical energy, cells and any living organism actually live in an out-of-equilibrium environment, where statistical physics, in principle, does not apply. Molecular motors (see Section 1.2.1.2) for example move by consuming ATP and thus can break those equilibrium rules that would make it impossible for them to move directionally.

The fact that objects move directionally and additionally *interact* with each other (either by explicit communication or by chemical or steric interaction between them) can give rise to a (huge) plethora of collective behavior. These behaviors are observed at different length-scales (from bacteria moving collectively to flocks of birds and fish) and timescales and are usually studied and grouped under the general term of *active matter* [Giardina 2008; Vicsek and Zafeiris 2012; Poon 2013]. Active systems can also be studied by synthesizing self-propelled particles that move converting a chemical fuel into motion. What most active systems have in common is the fact that a local interaction between agents propagates giving rise to macroscopic, ordered behavior that can not be accounted for by equilibrium Physics and are purely due to the possibility agents have, on the one hand, of moving persistently, on the other hand, of interacting

with each other. The search for out-of-equilibrium (or almost-out-of-equilibrium) principles governing these patterns is one of the most active and interesting fields of biological Physics and Biology at the moment. Understanding active pattern formation is for example fundamental in the understanding of how cells are able to regulate transport, to move collectively, to react to external stimuli as efficiently as they do. In particular, the cell's cytoskeleton is able to self organize to shape the cell by assembling a huge amount of components into ordered structures, such rings, spindles, cortexes, vortices, etc. (see Section 1.2).

We are going to use concepts from this field to model the self-organization of cytoskeletal filaments actively moving. Given the huge size of the field, however, we here only add a short paragraph to define and classify active-matter models in general and then deal specifically with the ones this work focuses on in the next Chapters.

1.1.3.1 Agent-based models

Agent based (or discrete) models are based on a collection of discrete agents characterized by a self-propulsion term and an interaction term. One of the most famous although very simple models of this kind, the Vicsek model, composed of agent moving at constant speed but changing orientation depending on the direction of their first neighbors, first showed that given such an interaction an activity-based transition from an isotropic state to a state in which all agents moved coherently was possible because of the agent-agent interaction. See Figure 1.2 [Vicsek et al. 1995]. Agent based models thus mimic each agent individually and monitor their evolution in time. When long range interactions are absent and agents interact only locally, it is often the best approach to active systems.

1.1.3.2 Hydrodynamic models

Contrary to agent based models, hydrodynamic (or continuous) ones attempt to describe an active material starting from general symmetries. This approach allows to understand the role of material-like properties (and indeed active systems are often dubbed as *active materials*) such as the total flow or the total order, and are more prone to a fully theoretical treatment. Of course, one can start by writing microscopic equations for the individual components and then coarse-grain them to obtain continuous ones. This approach is perfectly valid as long as the right microscopic description is taken into account.

Chapter 2 and 3 will focus mostly on agent-based models of filaments. In Chapter 3, the relationship between an agent based model and a hydrodynamic one in the case of an active fluid will be discussed. Active microtubules fluids indeed (see Section 3.2) are particularly prone to hydrodynamic descriptions but one must not forget that their microscopic components have behavior sometimes far more complex than what a coarse-grain would allow to grasp. Additionally, in Chapter 3 the interaction between an fluid described as a set of agents and a membrane described as a continuous material will be explored, thus somewhat bridging the gap between discrete and continuous models from a different point of view.

1.2 The cell cytoskeleton: filaments, motors, crosslinkers

Among the many proteins inside a cell, we can identify a subset of them that deals with providing structural integrity to cell, i.e., allowing it both to maintain a desired shape and, if needed, to change it. In analogy with an animal's skeleton, this set is called the cellular skeleton or *cytoskeleton*. The analogy is not far-fetched, as the cytoskeleton is indeed composed of a set of somewhat rigid structures that maintain the cell shape. At the same time, however, cytoskeletal proteins are very dynamic, allowing for fast rearrangement of the cell structure.

In short, the cytoskeleton provides a scaffold for the cell, accounting for both its mechanics and morphology. A particular feature of the cytoskeleton is that the individual building blocks are proteins with a size of $\approx 10 \text{ nm}$ but are able to assemble into structures up to 1 mm in size. This assembly ability, together with the possibility to modulate it locally, is at the base of the cell's flexibility.

Of the several thousands proteins that have been ever associated with the cytoskeleton in general, we will discuss some, separated into three major classes: filaments, motors and additional binding proteins. Very roughly, filaments provide mechanical stability, motors provide force generation via ATP-hydrolysis and other proteins allow for regulation of each of these step. However, all the components are intertwined with each other: filaments have been found to produce forces⁴, motors can also change the filaments mechanical properties locally and other proteins can increase or decrease the filaments' or motors properties locally. We here give an overview of the main components of the cytoskeleton, focusing on two filaments/motors couples, i.e. actin/myosin and microtubules/kinesins.

This chapter is heavily based on Howard 2001 and Phillips et al. 2019.

1.2.1 The cytoskeleton in general

1.2.1.1 Filaments

The cell contains three major classes of filaments⁵: actin, microtubules and a rather big set of the so-called intermediate filaments. They all provide the cell with mechanical properties and play a role in each of the cell's fundamental functions: as general examples, actin is involved in the formation of protrusions which allow the cell to move and is involved in the formation of the cytokinetic ring during cell division whereas microtubules play their most fundamental role in separating the chromosomes during cell's division. All filaments share the fact that they are microscopically composed of protein monomers able however to assemble into more complex structure. While they all share a similar monomer size ($\approx 50 \text{ kDa}$ in mass or $\approx 5 - 25 \text{ nm}$ in size), the structures they assemble into are completely different in terms of size and mechanical properties, due to the fact that different monomers form filaments with different lattice structures. One can indeed identify, along the filaments, monomers arranged into some repeated structures (proto-filaments) which assemble together to form the final filament.

⁴This will not be discussed: however, the way it works, is that filaments can push an object by polymerizing an extra monomer between them and the object and thus displace it by approximately one monomer size

⁵Although another class, septins, is now usually considered as a fourth one.

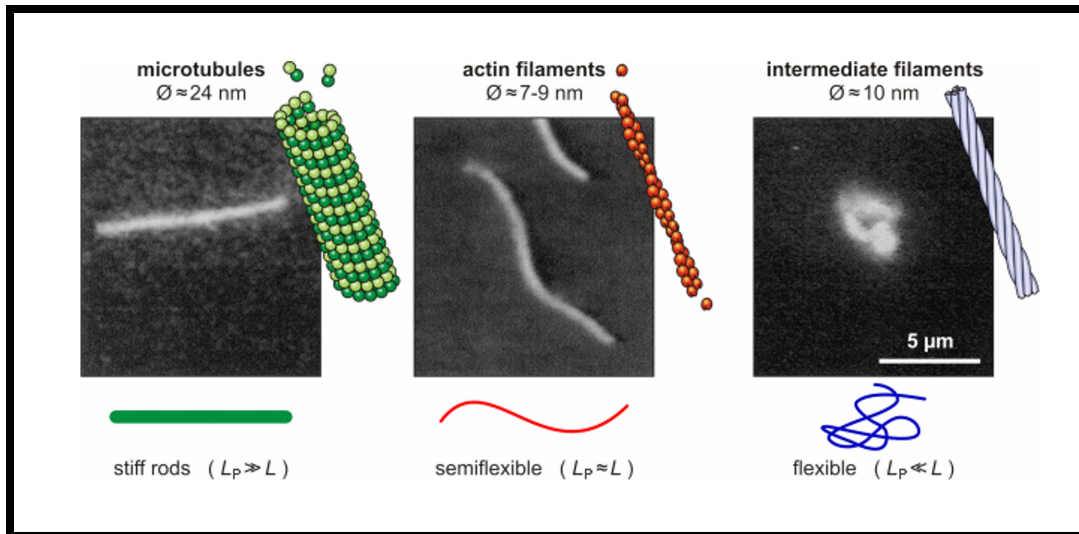


Figure 1.3: **Cytoskeletal filaments** Cell contains different kinds of cytoskeletal filaments. Microtubules (left) are rigid and mainly used for cargo transport. Actin (center) is a semiflexible and mainly use for plasticity and dynamics of the cytoskeleton. Intermediate filaments (right) are flexible and perform a variety of different roles we do not discuss here. Image from [Käs et al. 1996]

Another fundamental features of actin and microtubules filaments⁶ is that they are *polar* i.e. the structure of the monomers is not symmetric and, additionally, they have a binding pocket for nucleotides (ATP for actin or GTP for microtubules) so that monomers can also spatially vary their characteristics by nucleotide hydrolysis. One can thus define two different ends, usually called plus- and minus-end and assign the filaments with an orientation. A consequence is that ATP hydrolysis also allows for non-equilibrium kinetics, i.e., the affinity of monomers to the filament can depend on the state of the bound nucleotide. In particular, the assembly rate can differ at the two different ends allowing for dynamical control of polymerization.

Figure 1.3 gives an overview of cytoskeletal filaments, described in detail just below here.

Actin Actin is a 42 kDA monomer able to assemble into a left-handed helix with a period of 72 nm. As one full period contains 26 subunits, each subunit occupies only ≈ 2.8 nm along the filaments, despite the monomer size being ≈ 8 nm. This is because, due to the helical structure, monomers are staggered rather than placed on a straight lines. Its structures can be thought of as two parallel helical strands staggered and wrapped around each other. Actin is usually thought of as the dynamic, (semi)flexible (with a persistence length, defined below, of $L_p \approx 15$ μ m, comparable to the filaments' mean length) filament inside the cell, providing structure when needed but able to quickly assemble and disassemble, also thanks to a myriad of actin-binding proteins which can affect its properties. Additionally, actin is rarely found as individual filaments but rather arranged in a crosslinked network or bundle form.

Actin, in tandem with myosin (see 1.2.1.2), is the main constituent of muscles, where it forms aligned fibers that the myosin can then contract to generate force.

⁶Intermediate filaments are apolar, in general.

Microtubules Microtubules (MTs) are somewhat the opposite of actin. They have a much more complex lattice structure, based on two different monomers, α -tubulin and β -tubulin which first assemble in an heterodimer ($\alpha\beta$). The $\alpha\beta$ -dimer forms protofilaments which assemble laterally forming an hollow cylinder, i.e. the MT. Again, due to an offset in the way protofilaments align laterally, the structure also features an helical pattern composed of three helices of monomers stacked together.

MTs have 13 protofilaments, a diameter of $\approx 25 \text{ nm}$ and contain ≈ 1600 monomers per micrometer.

Contrary to actin, microtubules are rigid (with a persistence length, define below, of $L_p \approx 6 \text{ mm}$, much longer than the filaments' mean length) but still very dynamic.

Intermediate filaments Intermediate filaments are only recently been an object of attention. We do not discuss them in this work, so we just give a brief overview. They are short, have a persistence length of $\approx 150 \text{ nm}$ and are therefore very flexible compared to their micron-long length. They assemble in a particular way, forming individual protofilaments that further assemble in fibrils.

Filaments' mechanics Because one of the most important properties of filaments that will concern this work is their flexibility, we here give a quick account of filaments' mechanics.

Suppose we have a long beam of length L whose equilibrium state is being straight. If we deform it, we pay an energy penalty which we assume to be elastic i.e. proportional to the square of the deformation. By calling s the position along the beam, if locally the beam is deformed up to the point where it reached a curvature $c(s)$, we assume the corresponding energy to be $\propto c^2(s)$ and thus, by integrating along the beam, the total elastic energy of the deformation is given by

$$E_b = \frac{1}{2}K \int_0^L ds c^2(s) \quad (1.5)$$

where K is an elastic constant and can be proved to be the product of the Young modulus Y of the material and the geometric moment I (see Phillips et al. 2019), so $K = YI$.

We can also define a tangent vector $\mathbf{t}(s)$ which describes the tangent to the beam at position s . This allows for a geometric definition of the filament as a curve. We can then not only rewrite the previous equation using the fact that $c(s) = d\mathbf{t}/ds$ (we will see a similar treatment in Section 1.4 about lipid membranes) but also define a correlation function for the tangent along the beam, telling us how far along the filament, following its tangent, can we walk before we loose memory of the initial direction $\mathbf{t}(0)$. We call this quantity the persistence length L_p and can assume for the correlation function the form

$$\langle \mathbf{t}(s)\mathbf{t}(0) \rangle \approx e^{-s/L_p} \quad (1.6)$$

The persistence length is a measure of a filaments' flexibility: if for the filament $L \gg L_p$ the filament is flexible (its orientation decorrelates multiple times along its length), if $L \ll L_p$ the filament is rigid (does not decorrelate at all) and if $L \approx L_p$ the filament is semi-flexible i.e.

it can bend easily but does not decorrelate much. As mentioned, actin is an example of semi-flexible filaments, as its mean length is comparable to the persistence length, and microtubules are a case of rigid filaments. The persistence length can also be defined as the length after which the bending energy of the filament is of order of the thermal fluctuations $k_B T$. Using the equation for the elastic energy 1.5 for a filament of mean curvature $k = 1/L$ and of length⁷ L , and setting $L \approx L_p$ when that energy reaches $k_B T$, i.e. the bending energy is comparable to thermal fluctuations, then one gets

$$k_B T \approx \frac{1}{2} Y I L \frac{1}{L^2} \Big|_{L=L_p} \quad (1.7)$$

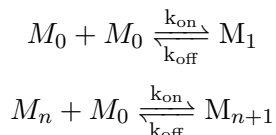
which is a mechanical definition of the persistence length in terms of material properties (neglecting factors):

$$L_p \approx \frac{Y I}{k_B T} \quad (1.8)$$

From this discussion we also see that while the Young modulus is a material property of the filament, its flexibility also depends on the ratio between the length of the filament and its persistence length (e.g., a filament with $L \ll L_p$ is rigid regardless of its Young modulus). Thus the cytoskeleton mechanical properties can be tuned locally by shortening or elongating filaments.

Filaments' polymerization One of the main features of filaments is their ability to (dis)assemble when needed starting from a pool of monomers that aggregate. We here give a quick overview of filaments' polymerization to account for the cytoskeleton's flexibility and also some of the methods used in this work.

Assume we have a pool of monomers with concentration $[M_0]$. Monomers can bind together forming filaments according to the reactions



i.e. monomers can form a couple (M_1) and then additional monomers can join the chain to form a filament (M_n). Joining the chain lowers the energy G of the monomers by an amount ΔG which is connected to the rates k_{on} and k_{off} of the process. The rates thus can also be modulated by changing the monomer's affinity to each other, e.g. by addition of salts or ions.

Such a simple process would indeed lead to the formation of chains of monomers with different length but the quantitative results this model leads to would be wrong when compared when actual filaments. And this for the following reasons:

Monomers also interact laterally: cytoskeletal filaments are multi-stranded chains. Because of this, while the formation of a dimer follows the dynamics above, additional monomers joining

⁷Equivalent to assuming that the filament is a circumference segment of length equal to the radius, so that the it has bent of approximately $1 \text{ rad} \approx 60^\circ$ so that the orientation has decorrelated of $\approx 50\%$ of the initial value.

the chain gain a better energy advantage as they can form not a single bond but multiple ones, since they also interact with the side chains. This stabilizes the filaments once a given threshold of monomers is reached. The final length distribution is found to be exponential.

Another consequence of this is that filaments grow and shrink only at their ends. Indeed, while for a single chain breaking a bond anywhere entails the same energy cost regardless of the position, for a multi-stranded filament depolymerization happens only in those places where the minimum number of bonds has to be broken, i.e. at the filament's ends. Thus the only rates which effectively count are those at the ends. This also leads to the fact that there is a critical concentration of monomers below which filaments stop growing and disassemble. Indeed, if what counts are only the rates of addition and removal of a monomer at the ends, which we call k_+ and k_- , then we can write a differential equation for the number of monomers n in a filament as

$$\dot{n} = k_+[M_0] - k_- \quad (1.9)$$

with the k_- rate now *independent of the filaments length* as removal only takes place at the ends no matter how long the filament is. Thus if $k_+[M_0] - k_- > 0$ the filament grows, otherwise it shrinks. The critical concentration $[M_c]$ is thus given by $k_+[M_c] - k_- = 0 \rightarrow [M_c] = k_-/k_+$.

Filaments can tune their rates at different ends: using the fact that filaments are polar and that they can hydrolyze ATP to change their chemical affinity, filaments can tune separately the rates at the two ends, k_{on}^\pm and k_{off}^\pm where \pm refers to the plus and minus ends and on/off to the addition and removal of monomers. In the case of actin, one can identify a fast growing end (barbed end) and a shrinking one (pointed end). However the cell can tune the assembly rate of filaments so that for example they grow faster on one end or even to tune the rates in a way that for every monomer leaving one side, one enters on the other side (*treadmilling*).

Stabilized filaments We can use phalloidin (for actin) or GMP-CPP (for microtubules) to stabilize filaments. These drugs inhibit monomer dissociation so that the filaments do not de-polymerize even if below their equilibrium concentration. However, these treatments can change properties of the filaments, such as their rigidity. Phalloidin, which binds preferentially to filamentous actin, can be fluorescently tagged to enhance contrast and differentiate between filaments and monomers.

1.2.1.2 Motors

Molecular motors are a (vast) class of proteins which interact with filaments and can walk on them⁸. Each motor interacts with one kind of filament⁹ (for example, the motor kinesin only interacts with microtubules). Motors are able to walk consistently in one direction, guided by the filaments' polarity. This allows to distinguish plus-end directed motors and minus-end directed ones depending on the direction the motors choose. Persistent motion would of course

⁸Under the name of motors, one actually finds other kind of proteins that can rotate cellular elements, such as flagella in bacteria, that move other elements, etc. We ignore them

⁹Although some cross-talk between motor complexes comprising different kind of motors or *in vitro* engineered motors interacting with different kinds of filaments do exist

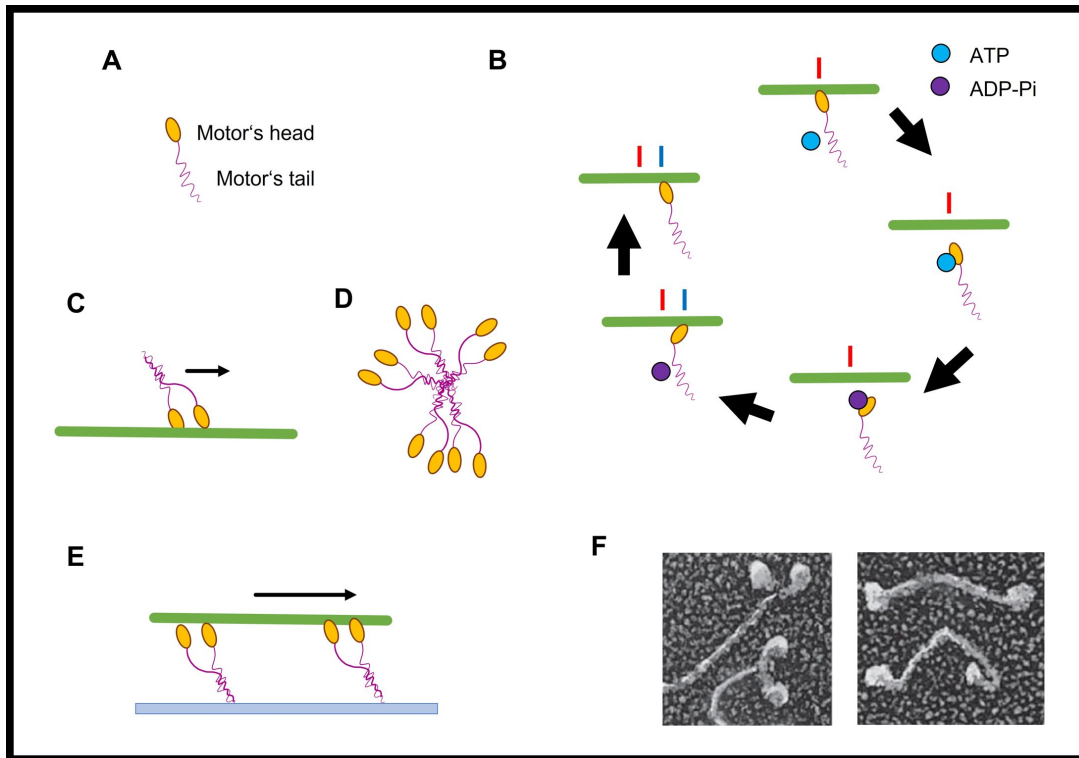


Figure 1.4: **Cytoskeletal motors** A) Motors are composed by a head (binding filaments) and a tail (binding cargo or other motors) B) Motors can coordinate to walk on filaments and they always move in a specific direction given by the filaments' polarity. C) Motors can assemble into multi-motors minifilaments. D) Motors stuck on a solid substrate propel filaments instead of walking on them. This technique (gliding assay) can be used to study motors' properties. D) Example of the ATP-based cycle of myosin: without ATP, the motor is bound to the filament in a given position (red bar). Upon ATP binding, the motors detaches and then hydrolyzes the ATP into ADP-Pi. This leads to a conformational change. Upon dissociation of the ATP the motor binds again, now in a new position (blue bar) and eventually recovers its initial configuration so the cycle can start over. F) Micrograph of a myosin (left) and a kinesin (right) dimers, from [Schliwa and Woehlke 2003]

not be possible at equilibrium, where each forward step would be equally probable than a backward step, and therefore motors need to consume energy, in the form of ATP, to walk. Motors walk on filaments to perform a variety of operations, for example to accumulate in some point or to move cargoes inside the cell, but they are also the main force-generating units inside the cell.

Motors can indeed also exert a force on the filament they walk on. In some conditions, for example if the motor is held fixed, instead of walking, it will *push* (or pull) the filament, thus displacing it. As motors walk in discrete steps of $\approx 10 \text{ nm}$ (see next section), each of them fueled by the hydrolysis of one ATP molecule, the work they exert is approximately in the ATP-hydrolysis energy of $\approx 20k_B T$ which, in the case of a $\approx 10 \text{ nm}$ step is equivalent to a force of $\approx 10 \text{ pN}$. It can be shown that given the average filaments' size a similar force is more than enough to displace a filament!

How do molecular motors work? Motors are, in general, composed of a head domain (or multiple head domains), which interacts with the filament, and a tail domain, which allows them to interact with each-other or with the external cargo they need to transport. The tail allows for the formation of motors' aggregates (for example, myosins assemble into mini-filaments and kinesins assemble into dimers).

The head is the propelling element. Motors indeed move by attaching their head to a filament, then detaching from it, undergoing an ATP-based conformational change which displaces the head and then reattaching, but now in a different position. After that, they can revert to their original conformation, unbind from the ADP molecule and restart the cycle with a fresh ATP one. It has been shown that each step of the motor consumes exactly one ATP molecule. Figure 1.4.B shows a scheme of the myosin cycle.

In general, each motor has a slightly different cycle: some motors consist of multiple heads, a number of which stays attached to the filament at all time. Some motors have a single head which attaches and detaches continuously. Some motors have two heads, so that while one moves the other acts as a placeholder and vice-versa, when the other moves the other is fixed. This latter kind of motors can be said to actually *walk* on the filament, as at least one head is always attached, but all motors share the ability to displace themselves on the filament. See section 1.2.1.2 for an overview of different motors. Figure 1.4.A, C and D show a scheme of both an individual motor a dimer and of an assembled mini-filament.

Motors bind only on discrete sites on the filaments, displacing themselves of one step per cycle. Thus the distance d between consecutive sites is roughly equivalent to the motors' step size δ along the filaments, although motors can in principle skip a number of binding sites so that $\delta \approx nd$ with n integer. Hence the speed at which motors move is roughly given by $v_m \approx \delta/\tau_c$ where τ_c is the time necessary to hydrolyze one ATP molecule and release it, hence completing the cycle. Because this latter time also depends on the availability of ATP, the speed is also tuned by the ATP concentration ($[ATP]$) as

$$v_m = v_0 \frac{[ATP]}{K_M + [ATP]} \quad (1.10)$$

where v_0 is a limit speed and K_M a constant depending on the cycle's rates. If $[ATP] \gg K_M$ then the motors are in saturating ATP conditions and therefore move at $v_M \approx v_0$.

How to measure motors' speed The easiest way to measure motors' speed in the laboratory is to attach motors to a solid substrate (e.g. a glass slide) and let some fluorescently labeled filaments sediment on top before adding ATP. In this conditions motors, rather than walking, as they are fixed, will actually push the filaments on top and, due to the bigger size, filaments can be easily recorded. The gliding assay is described in more detail in Section 2.3. This also allows to study motors' collective activity. More recent methods include labeling of individual motors and observing directly how they move. Figure 1.4.E shows a scheme of a gliding assay.

Stall force Something else worth mentioning is that motors usually work under load, i.e. they drag something. If there is a drag force F_d opposing motion, for example because they are

transporting a cargo, for each step δ the motor does the drag force causes a work $W = -F_d\delta$. This causes a slow down of the motors as the rate at which the motors walk is decreased.

In general, the final result is that motors can be described as having a force-velocity relationship of the kind

$$v(F_d) = v_0\left(1 - \frac{F_d}{f_s}\right) \quad (1.11)$$

where v_0 is the *unloaded* motor's speed and f_s is the so-called *stall-force* i.e., the drag force at which a motor is unable to walk.

Processivity Another parameter that must be taken into account when describing a motor is their *processivity* i.e. the fraction τ_{on} of the ATP-cycle that the motors spends attached to the filament. Some motors (like kinesin) are very processive and actually walk on the filament whereas other (like individual myosin heads) spend a very small fraction attached to the filament and thus, if continuous motion is desired, multiple different heads must be present at the same time. Indeed, non-processive motors tend to form minifilaments of several heads together. Also in this case, as both the total time of the cycle and the time spent attached are ATP-dependent, processivity can be tuned by the concentration of ATP. A subtle result to which processivity is related is that individual processive motors can push a microtubule in a (roughly) density-independent way, whereas non-processive motors do push filaments in a density-dependent speed, as at low density the limiting step is the attachment of the motor on the filament to push it, whereas at high density this lag time is reduced as an head might always be available. Briefly, the minimum number of motors that need to be available is $N_{min} \approx \frac{\tau_{tot}}{\tau_{on}} := 1/r$ where τ_{on} is the time spent attached, τ_{total} is the total length of the cycle and their ratio is the so called *duty ratio* $r = \tau_{on}/\tau_{total}$. Having $\approx N_{min}$ motors guarantees that at least one head is attached at all times. If not enough heads are present so that the number of heads bound to a filament is lower then N_{min} , the filament will not be propelled continuously as after a single step motors will detach and diffuse away before another head can bind.

The duty ratio is also connected to the motor's speed when motors do not act as individual heads but as multi-mers with several heads acting in a coordinated way. For example, a kinesin head has a duty ratio of $r \approx 0.5$ with $\delta \approx 8nm$ and consumes 1 ATP molecule in 0.02s ($k_{ATP} = 50$). This leads to a speed per head of $v_0 \approx \delta k_{ATP} = 400 nm/s$ but, as a dimer, to a speed $v_0/r \approx 800 nm/s$ obtained by dividing the individual speed by the duty ratio. On the other hand, an individual myosin has a much lower duty ratio in the $r \approx 0.02$ range. This means that an individual myosin, which consumes 1 ATP molecule in $\tau_{on} \approx 0.05$ s and moves by $\delta \approx 5nm$ would have a speed of $v_0 = \delta/\tau = 5nm/0.05s = 100 nm/s$ but a myosin-minifilament with 100 heads, having a $r_a \approx 1$ can move up to $v_0/r \approx 5 \mu m/s \gg v_0$.

Notice that this also implies that individual processive motors' heads must consume ATP much faster than non processive ones to move at noticeable speed, as they can not rely on collective effects.

Run-length In the case when the motors can take multiple steps on a filament ($r \approx 1$) as they (a myosin minifilament or a kinesin dimer, for example) always have an head attached to the filament, we can also introduce a new rate, k_{det} indicating the rate at which the aggregate

detaches from the filament it is walking on. From this, the so called *run-length* λ can be computed, i.e. the average length the motors walks on the filament, given by

$$\lambda = v_0/k_{det}.$$

A long run length means that the motors is very good at transporting things on the filament track, whereas a short run length rather suggests that the motors is rather meant to locally rearrange the network as it will not travel far.

Overview of cytoskeletal motors The main classes of motors are myosins, which bind to actin, and kinesins or dyneins, that bind to microtubules. Chapter 2 of this work is extensively based on myosins and kinesins, whereas Chapter 3 is based on a modified version of kinesin only. Dyneins, another important class of microtubule associated motors, are not treated in this work.

Myosin Myosins are a large family, each with very different characteristics. From now on, we refer to Myosin but actually mean Myosin II. Myosin (II) are very non-processive motors, and therefore assemble in filaments with ≈ 200 heads to be able to push progressively on the actin. They are at the base of muscle activity in that myosin-filaments contract the actin based fibers that constitute muscles. Myosins can be also found as individual heads, especially when the concentration of the salt KCl is high, and can be modified in the laboratory to eliminate the filament-forming tail, in order to obtain individual heads which do not bind (called Heavy-meromyosin or HMM). The speed of Myosin is in the $1 - 5 \mu m/s$ range with an ATP-hydrolysis rate of $\approx 6 s^{-1}$ and the direction of motion is towards the plus end. Because of their low processivity, around ≈ 1000 molecules/ μm^2 are needed to push a $1 \mu m$ actin filament. Another member of the myosin family, Myosin-V, is on the other hand a very processive motor, as it is related to cargo transport in the cell. Figure 1.4.F shows a micrograph of a Myosin-V dimer. Several other members of the myosin family exist, each with different roles, not always related to filaments' motion, including for instance pruning and depolymerization of filaments.

Kinesin Kinesins (we will deal mostly with Kinesin-401), conversely, are very processive motors, have a speed in the $500nm/s$ range. They move on microtubules towards the plus-end of the filament. Kinesin assembles into dimers, with two heads, having a run length of $\approx 1 \mu m$ during which at least one head is always attached. Each head has a hydrolysis rate of $\approx 50s^{-1}$. They serve as transport vectors. Because of its processivity and its very high stall force, a single kinesin is able to push a microtubule. Each kinesin head is found to have a duty ratio of $r \approx 0.5$, consistent with the fact that one of the two heads is always attached to the filament. Figure 1.4.F shows a micrograph of a kinesin dimer.

Dynein Dyneins are also a large family of MT-based motors. They play a big role in the motion of flagella and cilia. Differently from kinesins, dyneins move towards the minus-end of the filament.

1.2.1.3 Crosslinkers and other filament-binding proteins

The cytoskeleton features incredible flexibility. To achieve that, cells employ a number of proteins able to regulate filaments and motors' dynamics. We review some of them generally, based on [Pollard 2016; De La Cruz and Gardel 2015; Zhang and Maddox 2010]

Crosslinkers Crosslinkers are a set of proteins able to held together two or more filaments. This can lead to the formation of disordered networks of filaments, which the motor can then contract or expand, to more ordered structures, such as the spindle, or to bundles of filaments, like actin stress-fibers. By binding together different filaments, the mechanical properties of the bundle or the network can differ greatly from those expected for individual filaments.

In general, crosslinkers can be characterized by their on and off rates (i.e. their affinity to filaments), by their resistance to stress (at which load are they forced to release the bond¹⁰) and by the way they crosslink. Some crosslinkers are also able to slide on the filament they are bound to. We mention here briefly that also motors and other filament-binding proteins, while not directly described as crosslinkers, can also bind to more filaments at once thus effectively crosslinking them.

Parallel and anti-parallel crosslinkers Crosslinkers can bind filaments in a random fashion, simply attaching on the sides of two filaments and joining them. Some crosslinkers are however able to only bind filaments when these latter are parallel (their plus-ends are oriented in the same way) or anti-parallel (in opposite way).

Actin crosslinkers Actin features a big number of crosslinkers. Some of the most well-known are *fascin* (parallel crosslinker), *α -actinin* (anti-parallel crosslinker), *anillin* and many more. Anillin will be central in Chapter 3, although not as an actin crosslinker.

Microtubule crosslinkers Microtubules' crosslinkers are not as diffused and well-known as actin's. One of best known is PRC-1, which play a fundamental role in spindle-formation, which bundles MTs in an anti-parallel fashion.

Other relevant filament binding proteins The cytoskeleton also contains a number of other proteins which can sever filaments (*gelsolin*, for actin, will be used in Chapter 2, or *cofilin*), nucleate their growth, i.e., speed-up their polymerization in localized positions (e.g, the actin binding proteins *formin*, *VASP*, and the *Arp2/3* complex) or inhibit filament's polymerization at one end (e.g. *capping protein* for actin).

1.2.2 Cytoskeleton-membrane interactions

As a core part of this thesis is about the interaction between the cytoskeleton and membranes, we here give a short review of the most important biological processes involving both. Membranes are introduced more in detail in Section 1.4.

¹⁰A class of crosslinkers actually feature the so-called *catch-bond*, i.e. a bond whose lifetime actually increases when a given intermediate amount of tensile forces are present.

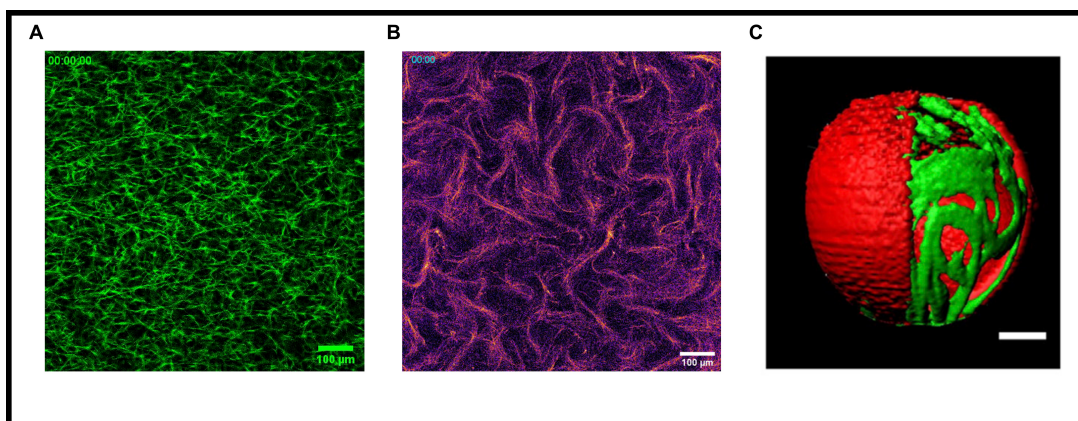


Figure 1.5: **Reconstitution of cytoskeletal networks** Both actin (A) and microtubules (B) networks can be reconstituted *in vitro* using a mixture of filaments, motors and crosslinkers. In A, an actin network will contract due to the presence of motors. In B, microtubules assemble in an active fluid composed of extensile bundles (see Section 3.2). Scale bars are 100 μm . C) Example of a reconstituted GUV containing an actin cortex, from Maan, Loiseau, and Bausch 2018.

First of all, cells membrane are tightly connected by the actin cortex, a thin layer of actin filaments. It is the active deformation and regulation of this actin shell that provides cells with stability. Important roles of the actin cortex are cell's motility (with the formation of the cell's leading edge during crawling), rounding of the cell during cell division and polarization of the cell (i.e., identification of a forward to backward polarity necessary for motion) [Pollard and Cooper 2009; Abu Shah and Keren 2014]. While it is mostly actin that takes care of re-shaping the cell, the actin cortex is also connected to the microtubules cytoskeleton and there is interplay between the two components [Bezanilla et al. 2015]. The connection with the membrane is mediated by a big number of filaments-binding proteins including nucleator (Ena-VASP, formins, Arp2/3), length and assembly regulators (gelsolin, profilin), mediators of specific pathways (e.g. rho, connected to actin contraction). The connection of proteins to the membrane is instead mediated by specific lipids (see Section 1.4), mainly PIP_2 ¹¹.

More specific processes involving the cytoskeleton and the membrane and its deformation also include the formation of an actin ring during cell division, the intake of small vesicles containing material from the outside (endocytosis) and for some bacteria actin-polymerization based propulsion is essential (e.g. *Listeria monocytogenes*). Actin polymerization in thin structures (*filopodia*) and in short, wide ones *lamellipodia* that deform the membrane is essential for locomotion and response to external stimuli [Blanchoin et al. 2014]. In all cases, cortex deformation are mostly led by myosin motors.

Motors can also be bound to the membrane and have been connected to processes such as branching, depolymerization and asymmetric motility of actin networks (Myosin1b and 1c) [Pyrpassopoulos et al. 2012; Pernier et al. 2019; Pernier et al. 2020] and cilia-based motion (dynein) [Stephens 2012].

Microtubules are less directly involved in cellular membrane deformations, but microtubules-

¹¹ *Phosphatidylinositol 4,5-bisphosphate*

based motor are often connected to cargoes contained in lipid vesicles, for which coupling to a fluid membrane is relevant for transport [Grover et al. 2016; Roux et al. 2002]. Microtubules are often also involved in membrane-based organelles transport (e.g. the Golgi apparatus) and are also nucleated from membranes to move the cargo [Stephens 2012]. As microtubules are also essential for separation of the chromosomes during cell division, which is also mediated by the actin cytokinetic ring at the membrane, there exist pathways connecting the two filaments which in turn are linked to membrane deformation [Rizzelli et al. 2020]

1.2.3 Main *in vitro* reconstituted cytoskeletal systems

Several systems exist to study assemblies of motors and filaments *in vitro*. We briefly discuss some that will be relevant for this work, i.e. that mostly have to do with lipid membranes. Actin has been found to polymerize into a 3D-network. The addition of myosin-II filaments to it can lead to global or local contraction of it but only if the network is crosslinked. If motors are processive enough (e.g., when the ATP concentration is low) they can transiently act as crosslinks and lead to crosslinker-less contraction [Bendix et al. 2008; Köhler, Schaller, and Bausch 2011; Köhler et al. 2012; Köhler and Bausch 2012]. A similar system, in 2D, also explained the role of filaments' flexibility in the network contraction [Lenz 2014; Murrell and Gardel 2012]. Actin polymerization can be coupled to a lipid membrane [Loiseau et al. 2016; Maan, Loiseau, and Bausch 2018; Dürre et al. 2018; Simon et al. 2019; Paraschiv et al. 2021] or to a solid surface to mimic the cell's actin-cortex [Bleicher, Sciortino, and Bausch 2020]. This can be done using purified nucleators and severing or capping-proteins that regulate the network morphology. Recent results about GUV-based reconstituted systems are reviewed in Bashirzadeh and Liu 2019 and Litschel and Schwille 2021. Actin has also been bound to supported bilayer (described in Section 1.4) to mimic the formation of filopodia like structures [Lee et al. 2010]. Bilayer have also been used to study the contraction of actin, its assembly in ordered structures and the role of crosslinkers in mediating extensile vs contractile activity [Murrell and Gardel 2012; Soares E Silva et al. 2011; Köster et al. 2016; Zhang et al. 2018; Bleicher et al. 2021].

On the other hand, regarding microtubules, recent attention has been given to the formation of active fluids (see Section 3.2 for a more detailed explanation) powered by the extensile stress of kinesin tetramers [Sanchez et al. 2012; Henkin et al. 2014]. Contractile microtubule networks, often based on dynein, have also been reconstituted [Foster et al. 2015]. Microtubules have also been encapsulated inside GUVs to study their effect in altering the GUV's shape [Sato et al. 2017; Rodríguez-García et al. 2020].

Figure 1.5 shows general examples of reconstituted systems out of cytoskeletal filaments, crosslinkers and motors. A more precise description of some of these systems and on what exactly the role of motors and crosslinkers is in the providing activity to filaments' networks will be discussed in Chapter 2 and 3.

1.3 Nematic materials

Nematic materials are materials composed of microscopic, elongated objects (rods) for which an orientation \mathbf{n} along the main axis can be defined. Rods can interact with each other via steric effects or with a given potential. One striking characteristics of these materials is that they can exhibit, under given conditions, a phase transition from an disordered phase (isotropic phase), in which the filaments have a random, uncorrelated orientation, to an ordered phase (nematic phase), in which filaments locally all have the same orientation \mathbf{n}_0 .

Because, as discussed in Section 1.2, the cytoskeleton comprises a number of filaments-forming proteins, we need to understand the general behavior of such materials formed by elongated objects. Indeed, the alignment of filaments plays a significant role in several cell-based processes such as development ([Cetera et al. 2014; Middelkoop et al. 2021]), in muscles [Maroudas-Sacks et al. 2021] and in tissue regeneration [Doostmohammadi et al. 2018].

In this section we discuss the simplest models that deal with nematic materials, i.e. in first approximation we neglect the flexibility of the filaments and we consider them as (very) elongated rigid rods.

We start with Lars Onsager’s theory of hard rods, the first work showing that the presence of a simple anisotropic volume-exclusion interaction (as for elongated objects) could lead to a phase transition from the isotropic to the nematic phase.

We then take a more material-like approach, attempting to show how such materials can be described in terms of an elastic energy. The content of this section constitutes one of the fundamental theoretical backgrounds of these work as of course cytoskeletal filaments are (very) elongated objects and they can (and indeed, do!) form nematic-like material. Different kinds of them will be discussed in both next chapters.

In addition to that, these materials can be made *active* by supplying energy at the microscopic scale (e.g. with the addition of molecular motors). We refer to Section 3.2 for extended discussion on active nematic materials.

1.3.1 Order parameters

First of all, we need to define how to measure order for aligned objects. We assign each object i an orientation, given by a unit vector \mathbf{n}_i . We also define a unit vector \mathbf{n}_0 , which defines the main axis along which objects align (*director*). Of course, \mathbf{n}_0 is only well defined in the ordered phase (otherwise, any orientation is equivalent). A trivial choice would be to quantify order as the average alignment with the director $\langle \mathbf{n}_i \cdot \mathbf{n}_0 \rangle$ over all rods, which is clearly 0 for the isotropic case. However, because of the symmetry of the problem, for each rod¹² the orientations \mathbf{n} and $-\mathbf{n}$ are equivalent and hence the order parameter defined this way would vanish even in the ordered phase. The solution is to define a tensor \mathbf{T} containing the values

$$\mathbf{T} = \begin{pmatrix} \langle n_x^2 \rangle & \langle n_x n_y \rangle & \langle n_x n_z \rangle \\ \langle n_y n_x \rangle & \langle n_y^2 \rangle & \langle n_y n_z \rangle \\ \langle n_z n_x \rangle & \langle n_z n_y \rangle & \langle n_z^2 \rangle \end{pmatrix} \quad (1.12)$$

¹²We henceforth neglect the subscript i , assuming that unless specified \mathbf{n} is the alignment of a rod and averages are taken over all rods.

where n_x and n_y are the components of \mathbf{n} , averaged over all rods.

The tensor \mathbf{T} has some clear properties. Because the vector \mathbf{n} is unitary $\langle n_x^2 + n_y^2 + n_z^2 \rangle = 1$, \mathbf{T} has a unitary trace. Additionally, in the isotropic state all components are the same by definition of isotropy, so $\langle n_x^2 \rangle = \langle n_y^2 \rangle = \langle n_z^2 \rangle = 1/3$ while mixed components vanish when averaging. We can then subtract from the tensor \mathbf{T} its value in the isotropic state $1/3\mathbf{I}$, where \mathbf{I} is the unit matrix, to obtain the so called \mathbf{Q} -tensor:

$$\mathbf{Q} = \frac{3}{2} \left(\mathbf{T} - \frac{1}{3} \mathbf{I} \right) \quad (1.13)$$

where $3/2$ is a normalization factor¹³.

It can be proven that the biggest eigenvalue of this tensor, called S is given, in 3D, by

$$S = \frac{3}{2} \left(\langle (\mathbf{n} \cdot \mathbf{n}_0)^2 \rangle - \frac{1}{3} \right) = \frac{3}{2} \left(\langle \cos(\theta)^2 \rangle - \frac{1}{3} \right) \quad (1.14)$$

where θ is the angle between the director and the vectors \mathbf{n} . Thus we can use S an order parameter, as $S = 0$ in the isotropic state and $S = 1$ in the ordered phase. Also, it can be proven, that the eigenvector corresponding to S is \mathbf{n}_0 i.e. the main nematic axis of the material.

We will often use both this tensor formalism and the corresponding order parameter or variation of it. We note that, in 2D, which will be more relevant for us, the equation for the tensor and its order parameter 1.14 become

$$\mathbf{Q}_{2D} = 2 \begin{pmatrix} \langle n_x^2 \rangle & \langle n_x n_y \rangle \\ \langle n_y n_x \rangle & \langle n_y^2 \rangle \end{pmatrix} - \mathbf{I} = \begin{pmatrix} 2\langle n_x^2 \rangle - 1 & 2\langle n_x n_y \rangle \\ 2\langle n_y n_x \rangle & 2\langle n_y^2 \rangle - 1 \end{pmatrix} = \begin{pmatrix} \langle n_x^2 - n_y^2 \rangle & 2\langle n_x n_y \rangle \\ 2\langle n_y n_x \rangle & 1 - \langle n_x^2 - n_y^2 \rangle \end{pmatrix} \quad (1.15)$$

(where we used the fact that \mathbf{Q}_{2D} must have a trace of 1, as $n_x^2 + n_y^2 = 1$). This corresponds to a 2D order parameter given by:

$$S_{2D} = 2\langle (\mathbf{n} \cdot \mathbf{n}_0)^2 \rangle - 1 = 2\langle \cos(\theta)^2 \rangle - 1 \quad (1.16)$$

which again is $S_{2D} = 0$ in the isotropic case as $\frac{1}{2\pi} \int d\theta \cos(\theta)^2 = 1/2$, and $S_{2D} = 1$ in the ordered phase. If rods are perpendicular to the main axis, then $S_{2D} = -1$.

1.3.2 Microscopic model of nematics: hard rods

We now describe the eaisistes model showing a transition from a disordered (isotropic) phase to an ordered one. The Onsager model is an example of a relatively simple, microscopic approach that will help us clarify why is there a transition from a disorder to an ordered phase in the case of elongated objects starting from a microscopic description of the interaction between them. This section is based on Onsager's original paper [Onsager 1949] and on [Van Der Schoot 2018]

¹³So that S , defined below, is between -1 and 1 .

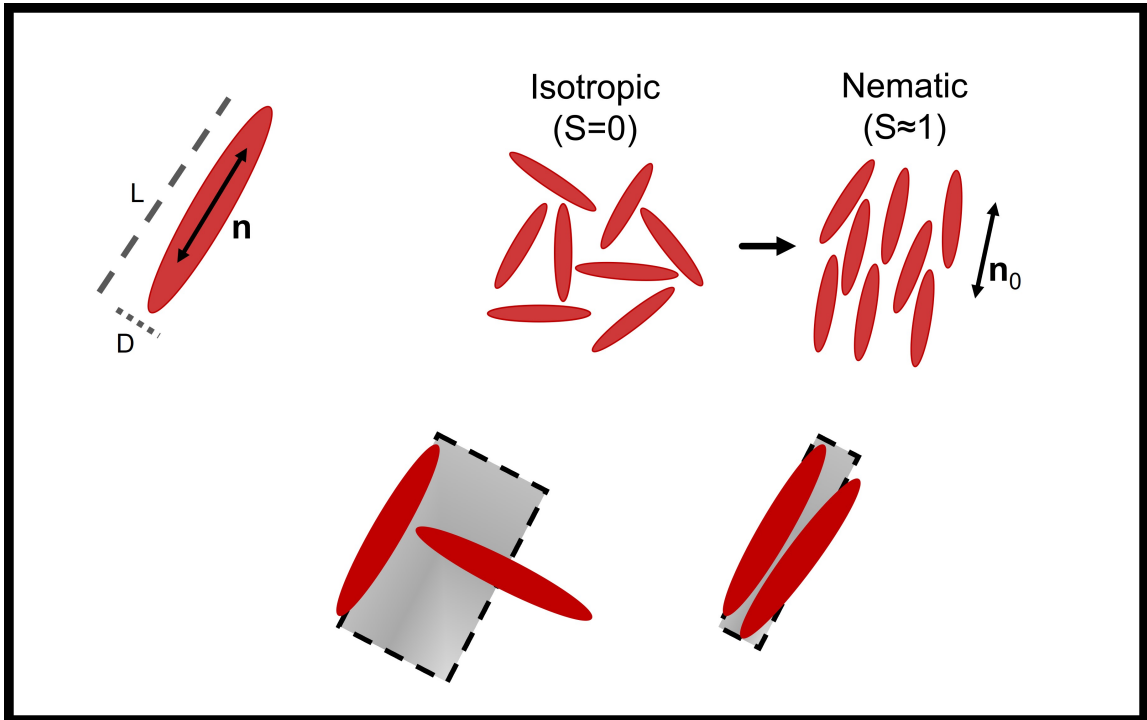


Figure 1.6: **Scheme of the hard-rod model and the isotropic-nematic transition** (top) The hard-rod model features elongated object with a main orientation $\pm \mathbf{n}$ and an aspect ratio D/L . Rods can not occupy the same volume as each other. At high enough density, rods self assemble into an ordered, nematic state with mean alignment $\pm \mathbf{n}_0$. (bottom) If rods are not aligned (high orientational entropy), a big portion of space (shaded area) is unavailable for other rods (resulting in lower translational entropy). Conversely, if they align, the excluded volume is much smaller. This explains the clash between orientational and translational entropy leading to order.

1.3.2.1 The hard rod model in general

We now attempt to write an energy function (free energy) for a simple model of rods that we will show undergoes a transition from isotropic to nematic. We consider a collection of N rods with length L , diameter D (with $L \gg D$), orientation \mathbf{n} and position \mathbf{r} . We further assume that they are dilute and hard i.e. they can not occupy the same volume.

We will show that, by introducing this latter simple interaction between particles that prevents them to occupy the same point in the volume, we also introduce a competition between two kinds of entropy: a translational one, which would push the system towards occupying a volume as sparse as possible, and an orientational one, which would push the system towards random orientations of the rods. In some conditions, counter-intuitively, a reduction in orientational entropy (i.e., alignment of the rods) leads to a increase of the translational one which not only compensates the loss due to orientation, but actually exceeds it, thus making the ordered phase the favored one. The main result is then that even a simple interaction, i.e. volume exclusion, can lead to the formation of an ordered phase and that we can explain this in terms of the relative importance of the system's entropy, which one would think favors a disordered phase, and its energy. This is thus another example of an entropic force, as the depletion effect

discussed in Section 1.1.2. Figure 1.6 (top) shows an example of the transition from a disordered to an ordered state.

To prove that, we will write a free energy describing this system, separating the terms describing the translational entropy, the orientational entropy and the interaction between particles and then analyze each term separately. Eventually, by combining all terms, we will see how in given condition the interplay between all terms leads to a transition to order.

The free energy The free energy will thus be composed of several parts: a constant F_0 , a part related to their center-of-mass position F_{gas} (translational entropy) which will be equivalent to that of a ideal gas of particles, a part related to their orientation F_{ori} (orientational entropy) and finally an interaction term F_{ex} having to do with the interaction potential, in this case volume exclusion. Thus the most general equation for the energy per particle we can write is

$$F(\{\mathbf{r}\}, \{\mathbf{n}\}) = F_0 + F_{gas}(\{\mathbf{r}\}) + F_{ori}(\{\mathbf{n}\}) + F_{ex}(\{\mathbf{r}\}, \{\mathbf{n}\}) \quad (1.17)$$

where $\{\}$ indicate the set of all the positions and/or orientations.

F_{gas} and F_{ori} represent entropic terms, taking into account the fact that our mixture of particles will try to maximize its entropy by having their orientation and position as randomly distributed as possible. On the other hand, F_{ex} is a term, summarizing the fact that particles will try to minimize the total free energy interacting as much as possible. Thus the total free energy is a balance of these two tendencies.

Entropic terms We will now analyze separately each term and write an expression for them starting from F_{gas} . Because our particles are dilute, we will assume they behave like a ideal gas and thus F_{ori} will simply be the free-energy (per particle) of a ideal gas at concentration $\rho = N/V$ i.e.

$$F_{gas} = k_B T \ln(\rho) \quad (1.18)$$

where k_B is Boltzmann's constant and T the temperature of the system¹⁴.

As far as F_{ori} is concerned, we will make a mean-field assumption, i.e. we will assume that all the particles choose their orientation independently from each other and according to a probability distribution $P(\mathbf{n})$. Knowing this distribution, we can write an entropic term (per particle) in the form of a Shannon-like entropy as the mean value of $k_B T \ln P(\mathbf{n})$ averaged over all possible orientations i.e.

$$F_{gas} = \langle k_B T \ln P(\mathbf{n}) \rangle_n = k_B T \int d\mathbf{n} P(\mathbf{n}) \ln P(\mathbf{n}) \quad (1.19)$$

¹⁴Technically speaking, there is a dimensional constant missing inside the logarithm, having to do with the DeBroglie wavelength and connected to the microscopic scale of a particle. Because this term will not play any role later on, we neglect it here, or rather, we have adsorbed it in F_0 .

Excluded volume term We now need to compute the term related to the interaction energy. First, we need to define the interaction between rods given by a potential energy $U(\mathbf{n}_i, \mathbf{n}_j, \mathbf{r}_i, \mathbf{r}_j)$ between rods i and j . As mentioned, we choose an excluded volume interaction, i.e.

$$U_{ij} = \begin{cases} \infty & \text{if the two rods } i, j \text{ overlap} \\ 0 & \text{if the two rods do not overlap} \end{cases} \quad (1.20)$$

so that occupying the same volume is strongly penalized whereas there is no interaction otherwise.

To write the term F_{ex} we use a so-called virial expansion in which we assume that the total energy only depends on the relative position and orientation of *two* rods and then sum the contribution coming from all pairs. Then we also invoke the mean-field approximation we used in the previous section that the particles choose their orientation individually according to a distribution $P(\mathbf{n})$. This gives us an energy which depends on the concentration ρ (as we are summing contributions) but also contains an average of the potential U over orientations and relative positions.

The result is that we can write:

$$\frac{F_{ex}}{k_B T} = \rho \int d\mathbf{n} \int d\mathbf{n}' P(\mathbf{n})P(\mathbf{n}')B(\mathbf{n}, \mathbf{n}') \quad (1.21)$$

where $B(\mathbf{n}, \mathbf{n}')$ is a factor depending on the relative orientations of two rods taking into account the amount of free volume made available by a given conformation. Figure 1.6 (bottom) shows a scheme of the role of volume exclusion in the rod-rod interaction.

Hence the term B describes the entropic gain due to alignment of rods. While one would expect an entropy-driven tendency to a completely disordered phase with random orientations, having inserted an interaction within rods can instead, in given conditions, shift the preferred phase towards the ordered one. This is because the entropy gained by aligning and allowing the rods a bigger free volume compensates and exceeds the orientational entropy lost by aligning. This will lead to an equation for an orientational distribution $P_{eq}(\mathbf{n})$ which is *not* the isotropic one but still minimizes the total free energy.

1.3.2.2 The final free energy and its minimization

By putting all the individual terms, i.e. equations 1.18, 1.19 and 1.21, together (and neglecting the from now on meaningless constant F_0) we end up with the final free energy per particle, normalized by $k_B T$

$$\frac{F}{k_B T} = \ln \rho + \int d\mathbf{n} P(\mathbf{n}) \ln P(\mathbf{n}) + \rho \int d\mathbf{n} \int d\mathbf{n}' P(\mathbf{n})P(\mathbf{n}')B(\mathbf{n}, \mathbf{n}') \quad (1.22)$$

which is a functional of the probability distribution of the orientations $P(\mathbf{n})$. Thus, finding the distribution which minimizes the free energy 1.22 is tantamount to finding the equilibrium probability distribution of the orientation $P_{eq}(\mathbf{n})$.

1.3.2.3 Onsager's approach: the isotropic-nematic transition

Is there a condition for which the free energy in the nematic case can be smaller (therefore favored) than the isotropic counterpart? By minimizing the free energy Onsager was able to find an equation for P_{eq} which is however hard to solve in general and does not allow to solve the problem completely. He then proposed to use as P_{eq} a test function, which he assumed to be peaked at $\mathbf{n} \approx \mathbf{n}_0$, which approximates the free energy for the nematic case. By finally comparing these results, he was able to find the conditions at which the nematic free energy is lower than the isotropic one.

By an analysis¹⁵ of the two contributions at different values of the aspect ratio D/L we can find the volume fraction¹⁶ $\phi := N\pi D^2 L/4V = \rho\pi D^2 L/4$ at which we *do* observe a transition from one phase to the other and the result is that there is a limiting packing fraction

$$\phi_{IN} \approx 4.5 \frac{D}{L} \quad (1.23)$$

above which the system self-orders into an aligned state. Notice that the higher the rods' aspect ratio L/D , the lower the critical concentration.

We here also note that in this model, the critical volume fraction *does not* depend on the temperature as there is no energy-scale (which is either 0 or ∞ , so that energy/ $k_B T$ does not count as a scale) involved. More elaborate theories exist to account for specific interaction between rods (e.g. Maier-Saupe theory). Nematic materials which are *not* temperature dependent are called *lyotropic*. Actin filaments (see Section 1.2 and Chapter 2) can form a lyotropic nematic (see Figure 1.8). Others factors that should be taken into account in general are the rods' flexibility, their microscopic interaction and their precise geometrical characteristics.

The O parameter In two dimensions for rectangles of area $a = DL$ we can rewrite easily ϕ_{IN} in terms of the number density $\sigma = \#rods / \mu m^2$, which is usually a more easily accessible parameter. Indeed, starting from the Onsager critical density $\phi_{IN} = \alpha D/L$, if we have N rods in an area S , the Onsager transition can be rewritten as

$$\alpha \frac{D}{L} = \phi_{IN} = \frac{Na}{S} = \frac{NDL}{S} \quad (1.24)$$

and thus, rearranging

$$\frac{N}{S} L^2 = \sigma L^2 := O = \alpha \quad (1.25)$$

where the value of α in 2D is found to be $\alpha \approx 4.7$ [Kayser and Raveché 1978]. So the O -parameter allows comparison with the equilibrium case, as the isotropic-nematic transition happens, regardless of the specific particles' aspect ratio and density, for $O_{iso} \approx 4.7$. We are going to use this parameter $O := \sigma L^2$ extensively in section 2.4.

¹⁵Common tangent construction, to be precise.

¹⁶Often a better measure than the number concentration ρ ...

1.3.3 Continuous model of nematics: the elastic energy

The Onsager model, and its developments, showed the microscopic reasons for ordering. Here, we will assume ordering has already taken place and analyze the resulting system as a material possessing an elastic energy. This will allow us to study the properties of the ordered phase from a material point of view. We will particularly focus on a 2D nematic material and on the formation of defects in the orientation, which will be important when describing of the results of Chapter 2. This chapter is based on [DeGennes and Prost 1993].

1.3.3.1 Distortions in the nematics and their energy

Assume we have a material described by the local orientation $\mathbf{n}(\mathbf{r})$ i.e. by a unit vector¹⁷ giving the local orientation at position \mathbf{r} . If there is a distortion in the orientation, we expect it to be connected to the derivatives of \mathbf{n} in space i.e. by¹⁸ $\nabla\mathbf{n}$. If we make the assumption that the interaction between different points of the nematic are short-ranged and that $\nabla\mathbf{n} \ll 1$ (small distortions) we can write an energy per unit volume f_e that characterizes such distortions *and* we expect this energy to be an expansion in terms of the derivatives of \mathbf{n} and their combinations.

The following must be true for f_e in terms of the general symmetries:

1) Because \mathbf{n} and $-\mathbf{n}$ are equivalent (nematic symmetry), the expansion can only contain *even* terms with respect to \mathbf{n} .

2) The system is rotation-invariant. Thus, linear terms in $\nabla\mathbf{n}$ are excluded because they are either ruled out by requirement (1) (e.g the divergence $\nabla \cdot \mathbf{n}$ is rotationally invariant but odd in \mathbf{n}) or not invariant with respect to rotations (e.g. $\mathbf{n} \cdot \nabla \times \mathbf{n}$ is even in \mathbf{n} but not rotationally invariant).

The only permitted terms up to order $\nabla\mathbf{n}^2$ are

$$(\nabla \cdot \mathbf{n})^2 \quad (\mathbf{n} \cdot \nabla \times \mathbf{n})^2 \quad (\mathbf{n} \times \nabla \times \mathbf{n})^2 \quad (1.26)$$

This terms represent the fundamental distortions of a nematic field i.e. respectively *splay* (the nematic field is splayed on a plane), *twist* (the nematic field is twisted in the volume) and *bend* (the nematic field is bent on a plane). Figure 1.7 shows a sketch of each of these distortions.

We can then write an energy which is proportional to each of this terms

$$f_e = \frac{1}{2}K_1(\nabla \cdot \mathbf{n})^2 + \frac{1}{2}K_2(\mathbf{n} \cdot \nabla \times \mathbf{n})^2 + \frac{1}{2}K_3(\mathbf{n} \times \nabla \times \mathbf{n})^2 \quad (1.27)$$

which is the most general expansion we can write for the energy. This expression is often called the Landau-DeGennes energy for nematic materials.

The $1/2$ factors are added so that the energy resembles an elastic energy of the form $\sim 1/2K(\text{distortion})^2$. The three constants represent the elastic energy paid in deforming the material in either of the three different ways.

¹⁷We are going to neglect the $\hat{\cdot}$ symbol in the next sections for simplicity.

¹⁸Specifically, $\nabla\mathbf{n}$ is a matrix containing the derivatives of all components of \mathbf{n} with respect to all directions in space.

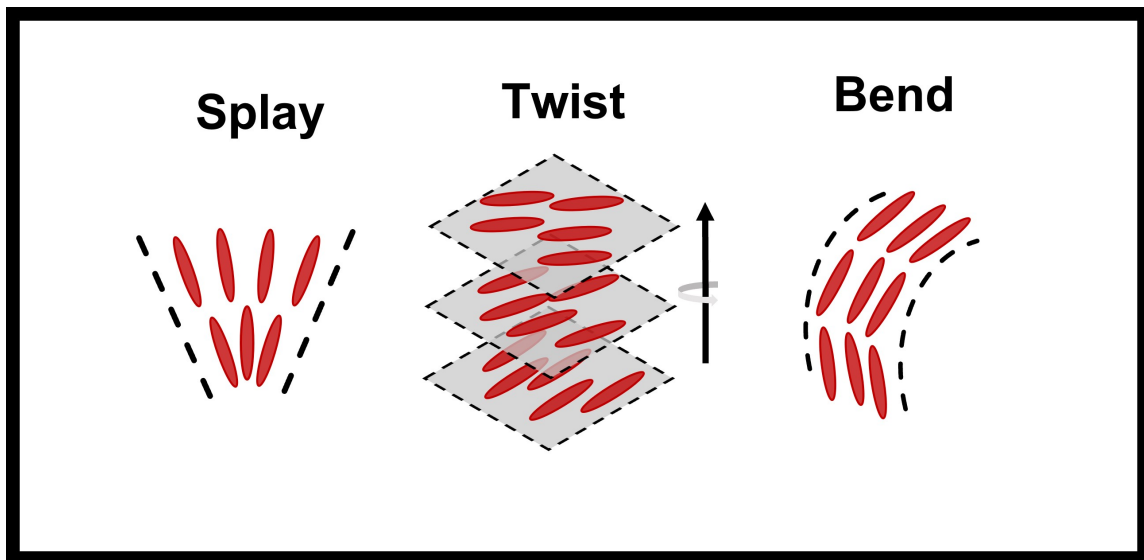


Figure 1.7: **Splay, twist and bend deformations** Scheme of the three main deformations allowed for a nematic material.

However, since we are going to mostly deal with 2-dimensional nematic materials, we can immediately simplify this expression because the twist term is always zero if $\mathbf{n} = (n_x, n_y, 0)$ is bidimensional¹⁹.

Thus, in two dimensions, the elastic energy density is then given by

$$f_e = \frac{1}{2}K_1(\nabla \cdot \mathbf{n})^2 + \frac{1}{2}K_3(\mathbf{n} \times \nabla \times \mathbf{n})^2 \quad (1.28)$$

1.3.3.2 The one-constant approximation

We now consider the most simple assumption, although often used and applicable, in which we consider all the elastic constants to be the same $K_1 = K_3 := K$. The real values of the three constants are actually *not* in general comparable. However the one-constant approximation is very useful in understanding general concepts about nematic materials.

Elastic energy density in the one constant approximation The free energy density 1.27 thus simplifies to

$$f_e(\theta) = \frac{1}{2}K \left((\nabla \cdot \mathbf{n})^2 + (\nabla \times \mathbf{n})^2 \right) \quad (1.29)$$

We can further simplify it considering again its form in two dimensions. By using the definition of divergence and curl and the fact that, in two dimensions, $\mathbf{n} = (n_x, n_y, 0) =$

¹⁹In facts, using the definition of $\nabla \times$, since the derivatives in z of the field \mathbf{n} vanish and $n_z = 0$, the term $\nabla \times \mathbf{n} = (\partial_z n_x, \partial_z n_y, \partial_x n_y - \partial_y n_x) = (0, 0, \partial_x n_y - \partial_y n_x)$ would lie perpendicular to \mathbf{n} i.e. in the z direction and then its scalar product with the vector \mathbf{n} lying on the xy -plane would be 0

$(\cos(\theta(\mathbf{r})), \sin(\theta(\mathbf{r})), 0)$ we get, indicating the derivatives only with a ∂ sign:

$$f_e(\theta) = \frac{1}{2} \left((\partial_x \theta)^2 + (\partial_y \theta)^2 \right) \quad (1.30)$$

so that, recognizing the gradient squared, the final 2D elastic energy density in the one-constant approximation yields

$$f_e(\theta) = \frac{1}{2} K (\nabla \theta)^2 \quad (1.31)$$

Minimum energy condition We now want to find the condition that the field $\theta(\mathbf{r})$ has to satisfy in order to minimize the elastic energy in the one constant approximation. To do that, again we need to resort to a functional derivative which yields a minimum energy condition for θ given by

$$\Delta \theta = 0 \quad (1.32)$$

This computation also yields an equation for the time evolution of the system if the field is distorted from its equilibrium value. A torque $\tau = -\delta F / \delta \theta$ will act on the nematic material, modifying it according to a torque-angular velocity relationship equivalent to the force-velocity one discussed in Section 1.1.1.2, i.e.

$$\gamma_\theta \dot{\theta} = -\delta F / \delta \theta = K \Delta \theta \quad (1.33)$$

This equation can be for example used to predict the temporal evolution of a nematic field given an initial (distorted) condition.

1.3.4 Defects and topological constraints

We now consider defects in the alignment in a 2D nematic. When quenched (i.e., abruptly formed without the time for the system to equilibrate) there is the possibility that the nematic director is locally uniform but presents discontinuities. Where this happens, the director is not well-defined and such positions are called defects. Defects can be points or even lines, along which no nematic director is defined. Defects have a big importance in a huge number of different contexts, every time elongated particles are present, from fingerprints to cytoskeletal structures and cell layers [Penrose 1965; Fardin and Ladoux 2021]

Point defects We start with a definition of point defects. Because in two dimensions $\mathbf{n} = (\cos(\theta), \sin(\theta))$ we can define the nematics just in terms of a scalar $\theta(\mathbf{r})$ or θ in short given by the angle between \mathbf{n} and the x -axis. We also define $\phi(\mathbf{r})$ or ϕ as the angle between \mathbf{r} and the x -axis (i. e. $\phi = \arctan(y/x)$ is the polar angle of the plane).

We look for solutions compatible with the minimization of the free energy 1.32 ($\Delta \theta = 0$) with the additional condition that they have a discontinuity in the origin. The results are of the form

$$\theta(\mathbf{r}) = m\phi(\mathbf{r}) + c \quad (1.34)$$

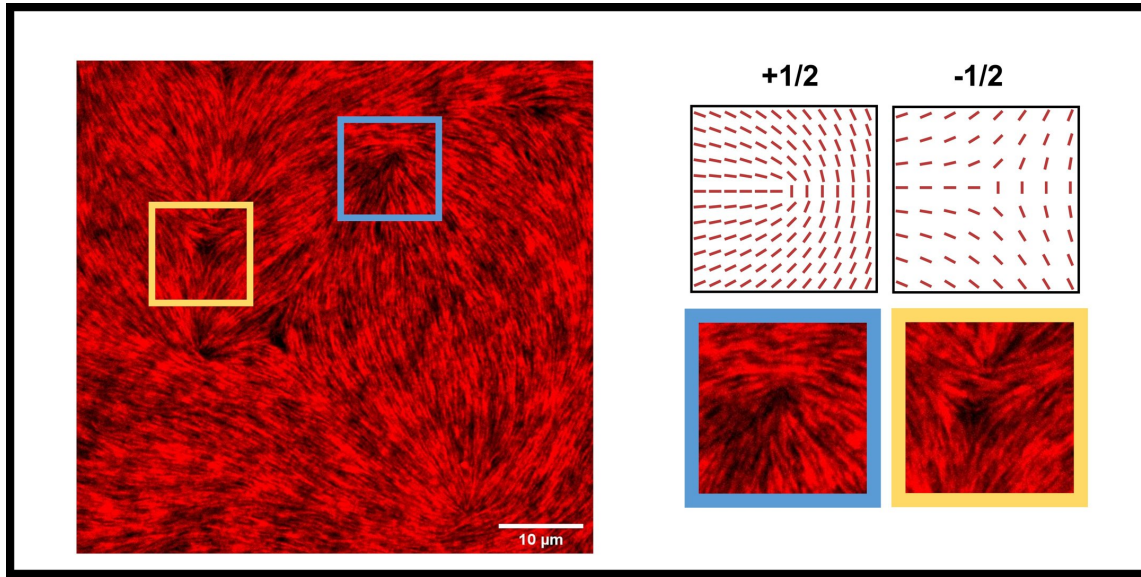


Figure 1.8: **An actin nematic with topological defects** Actin filaments form a lyotropic nematic. When self-assembled, the system can be quenched using depletants so that topological defects of charge $\pm 1/2$ appear.

where c and m are constants²⁰.

The value m is connected to the so called strength or charge of the defect, defined in the following way: if there is a point in the nematics where the θ is not defined, we call it a defect of strength (or charge) q if the line integral of $\theta(\mathbf{r})$ along a curve enclosing the defect is $2\pi q$ i.e. the charge q is defined by the integral

$$\oint_L d\theta(\mathbf{r}) = 2\pi q \quad (1.35)$$

where L is a line enclosing the defect. Clearly for the solution given by 1.34

$$\oint_L d\theta(\mathbf{r}) = \int_0^{2\pi} \frac{d\theta}{d\phi} d\phi = m \int_0^{2\pi} d\phi = 2\pi m \quad (1.36)$$

so m is exactly the charge of the defect ($q = m$). Additionally, because after a full circle the value of θ can either be a multiple of θ or of $\theta + \pi$ (as \mathbf{n} and $-\mathbf{n}$ are the only, equivalent possibilities) m must be either an integer or a half-integer. Figure 1.8 shows sketches of the defects given by $m = +1/2$ and $m = -1/2$ plotted according to equation 1.34, together with a real-life example of an actin nematic.

Elastic energy of a defect Because defects are distortions of the nematic they store an elastic energy. To compute it, we start from the solution 1.34 and integrate the elastic energy density given by the one-constant approximation 1.31

²⁰It can be verified that $\Delta(m\phi(\mathbf{r}) + c) = 0$. Indeed, in polar coordinates (r, ϕ) , then $\nabla(0, m\phi) = (0, m/r)$ and then $\nabla \cdot (0, m/|r|) = 0$, where we used in polar coordinates $\nabla = (\partial_r, 1/r\partial_\phi)$.

$$F = \frac{1}{2}K \int d\mathbf{r} (\nabla\theta)^2 = \frac{1}{2}K \int d\mathbf{r} (\nabla(m\phi(\mathbf{r}) + c))^2 = \frac{1}{2}K \int d\mathbf{r} \left(\frac{m}{|\mathbf{r}|}\right)^2 \quad (1.37)$$

where we used the fact that $|\nabla\phi(\mathbf{r})| = \frac{1}{|\mathbf{r}|}$. As integration limits, we choose as the smallest scale, a value a to avoid the divergence of $1/r$ near the origin²¹ and as the bigger scale we choose R_{max} which is usually the size of the system or the inter-defect distance. The result is, setting $|\mathbf{r}| = r$

$$F = \frac{1}{2}K \int_a^{R_{max}} 2\pi r dr \left(\frac{m}{r}\right)^2 = \pi m^2 K \ln(R_{max}/a) \quad (1.38)$$

so that the choice of R_{max} , it being inside the logarithm, does not matter much. The total energy is thus of order $\approx 10\pi m^2 K$ assuming even a several order-of-magnitude difference between R_{max} and a .

The main defects observed in 2D are $m = \pm 1/2$. Both, and particularly $+1/2$ defects (wedge defects or comet defects), will be particularly important in Chapter 2.

Interaction between defects Defects also interact with each other. In particular, $+1/2$ and $-1/2$ defects are found to attract each other. The conformation with two defects on the same line at a distance d and opposite charge is found to be

$$F(d) = 2\pi K m^2 \ln(d/a) \quad (1.39)$$

where again a is the size of the core of the defect. As lowering d lowers the free energy, there is a force acting on the two defects to move against one another. Defects with opposite charge that meet annihilate. Defects annihilation leads to a lower free energy state in which the material is locally aligned (with total charge 0) so that, over time, at equilibrium, defects eventually annihilate by diffusing and merging until the material becomes completely aligned (provided there are no other constraints on the total charge, see below).

Topological constraints The fact that defects are named after charges is not a coincidence. Indeed, topological (or nematic) defects show similarities with the behavior of charges, albeit having peculiarities of their own. The main properties of defects are:

The attract/repel each other depending on their charge: see, as an example, the above computation.

The total charge is conserved: as defects can only be created or annihilated in pairs, in a nematic material, the total charge is conserved. There are exceptions to this rule only when boundary conditions or external forcing is relevant.

The total charge is dictated by the topology: some rules can be derived from differential geometry constraining the behavior of defects on different topological structures (i.e., structures that can not be morphed into each other continuously without recurring to cuts, holes or

²¹The precise calculation is hard, but the energy of the core of the defect is found to be of order K

handles). More in general, the total topological charge Q of a surface is dictated by topology to be equal to the shape's Euler characteristic number χ given by

$$Q = \chi = V - E + F \quad (1.40)$$

where V , E and F are the number of vertices, edges and faces of the surface. This result is known as Poincaré-Brouwer theorem. The main example is that the total charge on a sphere²² (or a topologically equivalent structure as an ellipsoid) must always be $Q = +2$. This is grounded in the fact that there can not be defect-less alignment on a sphere, which is also the reason for Earth's meridians meeting at the poles and forming two +1 defects (total charge: +2). As another example, the total charge of a nematic material in squared confinement (or topologically equivalent such as circles, triangles, etc) is expected to be $Q = \chi = 4 - 4 + 1 = 1$ [Kamien 2002; Opathalage et al. 2019; Muševič 2019].

²²For a sphere, Euler characteristic can be proven to be $\chi = +2$ for any triangulation of the sphere, despite it not having any vertices, edges etc. This sets $\chi = +2$ for a sphere too.

1.4 Membranes and their mechanics

One of the first challenges an organism faces is to separate itself from the external environment. For this, cells employ membranes, which not only separate themselves from the outside, but also from compartments inside the cell itself to separate each functional units (e.g., the nucleus, mitochondria...). Cellular membranes need not only to physically separate the inside and the outside, but also to allow the exchange of materials and information between the compartment and the rest of the world, to allow the compartment to be plastic and resist deformation. To do that, membranes work in tandem with the cytoskeleton and a huge set of proteins dedicated to deform, wrap, pierce etc the membrane itself.

The better understanding of how membranes interact with the cell's active processes is one of the themes of this thesis, so in this section we review what cellular membranes are composed of (=lipids!), how they behave mechanically and what model systems do we have available to study them.

1.4.1 Lipid membranes in general

1.4.1.1 Lipids

The cell membrane²³ is mainly composed of lipids, i.e. elongated molecules composed of two main parts: a head, which is hydrophilic, and a tail, which is hydrophobic. Such molecules, composed of both a hydrophilic and a hydrophobic parts are called *amphiphiles*. Lipids differ from each other for a variety of reasons including the length and composition of their tail domain, their ability to assemble into solid or liquid phase (depending on the temperature), etc. but they all have in common the head-tail shape that allows them to assemble in a variety of structures.

1.4.1.2 Micelles, monolayers, bilayers, vesicles

Lipids indeed can assemble in different structures depending on their environment in the attempt to maximize hydrophilic interactions of their heads or hydrophobic interactions of their tail. Figure 1.9.A-C show different examples of lipids aggregating.

In the presence of a water/oil interface, lipids will assemble with their heads in contact to the water phase and the tails in contact with the oil phase. For these reasons, lipids can be used to stabilize water-in-oil droplets (or oil-in-water ones) by assembling at the interface and minimizing direct water-to-oil contact. The aggregation of lipids at an interface is usually called a *lipid monolayer*.

When lipid molecules are immersed in a water-based solvent, however, as they have no interface to aggregate against, lipids need to minimize contact between water and the hydrophobic part. In order to do that, lipids assemble in a variety of structures. The simplest one is the *micelle*, a spherical conformation for which several lipids aggregate with their heads towards the water phase and their tails towards the center of the sphere, from which water is expelled. In this way, the water-tail interaction is minimized. This aggregation happens spontaneously

²³With some exceptions, such as plants, exotic bacteria...

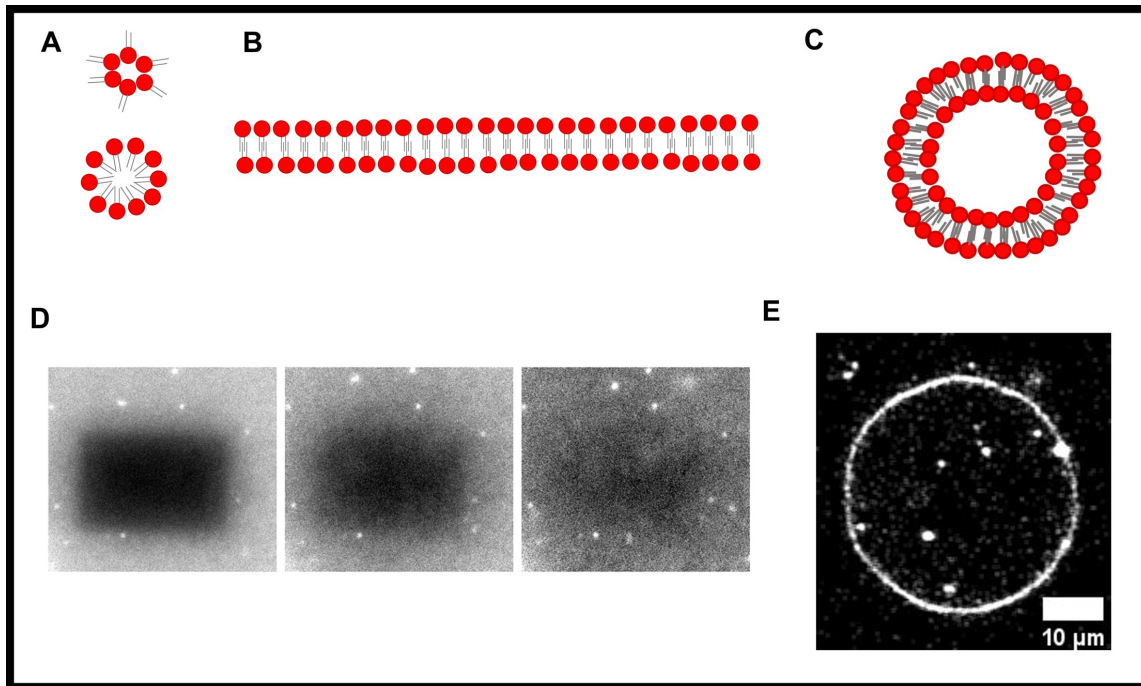


Figure 1.9: **Lipid assembly:** A-C) Different assemblies of lipids including a micelle, an inverted micelle (A), a bilayer (B) and a vesicle (C). Lipids' hydrophilic heads are in red and hydrophobic tails are in grey. D) Examples of a FRAP experiment on a supported bilayer showing the bilayer is fluid. D) Confocal snapshot of an empty vesicle.

as the lipids concentration in water exceeds a given (lipid- and ion-dependent) threshold called *critical micelle concentration*. As in the case of nematic materials, this process is based on the balance between an entropic term (lipids would like to be as dispersed as possible to maximize their translational entropy) and an energetic term (lipids want to lower their energy by pairing heads to water while keeping tails far from it). In this case, micelles are again made of a monolayer, but they do not separate two liquid phases (e.g. water and oil) but rather segregate their tails from the water phase which is the only one present (inverse micelles can also form, in which heads segregate from a oil phase). Figure 1.9.A show exaples of micelles.

This is not however the only way lipids can minimize unwanted interaction with the water solvent. Another option is to form a *lipid bilayer*, that is a conformation in which lipids form a thin sandwich-like sheet in which the heads face the water phase and again the tails segregate inside the sheet. Contrary to micelles, lipid bilayers can grow bigger, extending laterally and can even close on themselves, forming *vesicles* i.e., a closed surface comprising an water-based inside and a water-based outside separated by the bilayer membrane. Both vesicles and bilayers play a central role in this work. This is because the bilayer solution is the one chosen by cells. Figure 1.9.B-C show a schematics of a lipid bilayer in planar and vesicle form.

The reason for this resides in the fact that vesicles, contrary to micelles which are empty, permit the formation of an inside (the cell) and an outside (the environment) which are both water based (separated by a hard-to-cross hydrophobic layer i.e., the tail-based part of the bi-

layer), the fact that the two compartments can be put in contact by proteins that cut through the membrane, the mechanical flexibility of the bilayer itself (see Section 1.4.3) and their thermodynamical stability.

A fundamental feature of bilayers is that, as there is no relevant side interaction between lipids, they are *fluid* i.e. individual lipids can move (or rather, diffuse) on the membrane. We will exploit this feature vastly in Chapter 2.

1.4.2 Membrane models: vesicles (GUVs) and supported bilayers (SLBs)

To study lipid membranes and their interaction with the cytoskeleton *in vitro* we need model systems of a lipid membrane. Several possibilities are possible but we will discuss only two of them, mainly used in this work.

1.4.2.1 Supported lipid bilayers (SLBs)

Supported lipid bilayers are planar, flat²⁴, bidimensional membranes that are formed on a flat, solid hydrophilic substrate (usually, glass made hydrophilic or a polymer brush). They are assembled by incubating small vesicles in a water solution on the substrate, which being hydrophilic favors the formation of a thin water layer on top of the surface, on which the vesicles rupture, depositing their bilayer. This leads, after fusion of all the individual bilayers due to vesicle rupture, to the formation of a homogeneous bilayer sitting on the thin water layer. We refer to Methods 4.2.0.1 for a precise protocol.

The formed membrane is fluid, its lipid composition can be finely tuned and it can mimic the inside or outside of the cell membrane whereas the water phase above can mimic the inside or outside of the cell. Additionally, by adding in solution membrane-binding proteins, the lipid bilayer can be further functionalized and is a perfect model system to study the behavior of proteins when bound to a fluid membrane.

Additional advantages of this method is that the observation of the membrane is relatively easy as it is flat and thus, for example, total internal reflection fluorescence (TIRF) microscopy can be used. A similar system is the supported lipid monolayer, where lipids are deposited on a hydrophobic surface so that only a single layer of lipids forms. While still fluid, the diffusion coefficient of lipids on a monolayer is, due to friction with the substrate, much lower than that of a bilayer, which in turn, again due to friction, is lower than that of a free-floating bilayer.

Figure 1.9.D shows an example of a SLB and a FRAP experiment (see Methods 4.5) showing its fluidity.

1.4.2.2 Giant unilamellar vesicles (GUVs)

Giant unilamellar vesicles are spherical vesicles with a radius in the 10 μm range. They can be formed with a range of different techniques (e.g. electrosweeling, microfluidics, inverted emulsion technique) and we refer to to Methods 4.2.0.2 for a precise description of the one we used, i.e. the continuous droplet interface crossing encapsulation (cDICE) method.

²⁴To be precise, SLBs can also be formed on curved structures, see [Rinaldin et al. 2020; Eto et al. 2021], but we will not discuss this case.

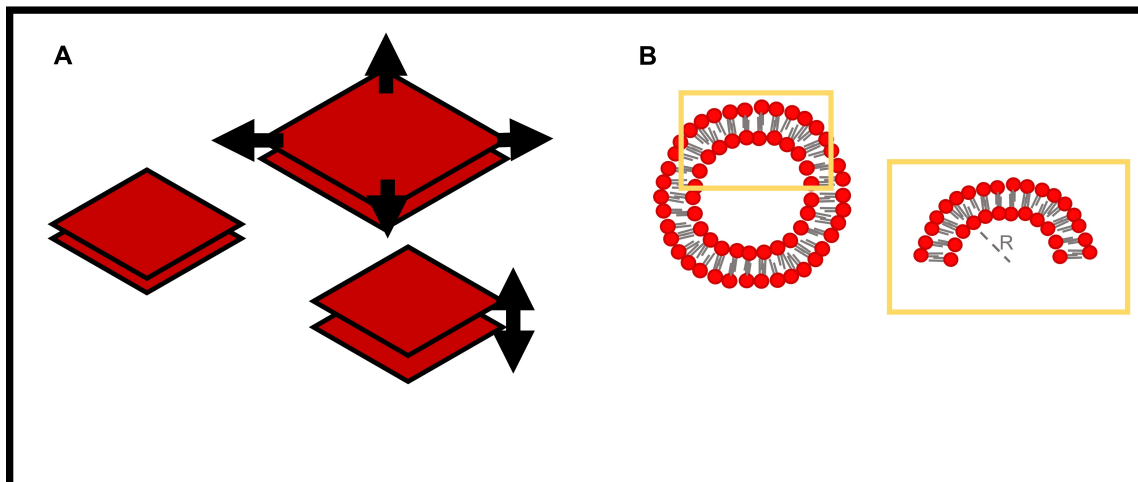


Figure 1.10: **Deformations of membranes:** Membranes can be deformed in different ways. They can be for instance stretched (change in area or in thickness) (A) or bent, for example to form GUVs, giving rise to a curvature $1/R$ to which corresponds an energy penalty (B).

Same as SLBs, GUVs can be functionalized with membrane-binding proteins to mimic the cell membrane, but their biggest advantage is that the inside phase is physically separated from the outside one so, if proteins are added inside the vesicle, the effect of cell-like confinement (indeed, GUVs can be made in the cell-radius range) can be studied, together with the behavior of membranes having a different topology than flat (i.e., spherical). Additionally, GUVs' floppiness can be tuned by osmotic differences between the inside and the outside, and the role of membrane flexibility can also be studied, something not possible on a SLB. In general, GUVs are considered a somewhat accurate cell-like model system.

Figure 1.9.E shows an example of an (empty) GUV produced with the cDICE technique. To be precise, vesicles need not to be spherical: not only can their shape fluctuate (see Section 1.4.3.2) but they can also take a variety of shapes depending on their lipid composition and on differences of osmotic pressures between the inside and outside solution [Dimova and Marques 2019].

1.4.3 Mechanics of membranes

As bilayers are basically sheets composed of lipids they can, as we saw in the case of GUVs, bend and deform. However, as expected, they must pay an energetic penalty to do that, whose microscopic origin mainly depends on the facts that when the bilayer is deformed lipids are forced to occupy a space different than their favorite one. For example, bending a bilayer membrane results in one side of the lipid getting more stretched the other side. Secondly, by deforming, e.g. when stretched, lipids may allow water molecules in the tail-based area, which is an unfavored interaction. Let us also not forget that lipids are microscopic but still solid objects and thus they have a given shape, dependent on the lipid's kind, and also for this reason do not like to deform.

Figure 1.10 shows examples of deformations for membranes. We want then to write an energy describing the energy cost of such deformations. We start with the assumption that the equilibrium state of the membrane is the planar one and then, as we did in 1.3.3, we will separate all the possible distortions with respect to the equilibrium shape and assign an (elastic) cost to it.

This part is mainly based on [Phillips et al. 2019; Nelson et al. 2014].

1.4.3.1 Deformations of a lipid membrane

Stretching As lipids have a favorite area a_0 they want to occupy, any deviation from it will result in an energy penalty proportional to the local variation of the area $\Delta a(\mathbf{r}) = a(\mathbf{r}) - a_0$, where $a(\mathbf{r})$ is the actual area of the membrane at position \mathbf{r} . We write this term using an appropriate elastic constant K_s and integrating over the full area of the bilayer

$$F_{stretch} = \int da \frac{K_s}{2} \left(\frac{\Delta a}{a_0} \right)^2 \quad (1.41)$$

Bending Bending of the bilayer also results in an energy penalty. We assume it to be proportional to the local curvature squared, as the flat membrane has 0 curvature. However, as we are dealing with a surface, there are two curvatures we need to take into account, one along each of the two perpendicular directions of the surface. Briefly, if locally the membrane has, along one direction, a bending deformation with a local radius R , we define the curvature as $c = 1/R$. Curvature is in general a function of the position on the membrane, but we do not write it explicitly. We can then formulate our bending energy as an integral of the curvatures over the whole surface, i.e. as

$$F_{bend} = \int da \frac{K_b}{2} (c_1(\mathbf{r}) + c_2(\mathbf{r}) - c_0)^2 = \int da \frac{K_b}{2} (2c_m - c_0)^2 \quad (1.42)$$

where $c_1(\mathbf{r})$ and $c_2(\mathbf{r})$ are the two main curvatures in a given position²⁵ \mathbf{r} , and thus $c_m = (c_1 + c_2)/2$ is the local mean curvature. We also introduced an equilibrium curvature c_0 , which can be often set to $c_0 = 0$ but is sometimes needed, as lipids *might* have a preferred curvature due to their shape.

As an example, the bending energy required to form a sphere of radius R , hence with mean curvature $c_m = 1/R$, would be

$$F_{sphere} = \int da \frac{K_b}{2} (2/R)^2 = 4\pi R^2 \frac{2K_b}{R^2} = 8\pi K_b \quad (1.43)$$

which is independent of the radius.

Another possibility of combining the two curvatures is the so called *Gaussian curvature* given by the product $c_G = c_1 c_2$. We can associate to it an additional energy cost per unit area

$$F_G = \int da \frac{K_G}{2} c_G^2(\mathbf{r}) \quad (1.44)$$

²⁵Curvatures are in general a function of the position as they can locally change. We state it here but do not explicitly write it in the following equations, unless necessary.

However, because the integral of c_G is the same for any surface with a given topology (e.g. that can be deformed into each other without introducing holes) the energy corresponding to the Gaussian curvature is only relevant when going to one topology to the other, e.g. from a spherical one to a donut-shaped one or from a planar to a spherical one. In the following, Gaussian curvature will not play any role but it is instead important if one is concerned with membranes changing topology.

Thickness change and shearing Other possible deformations include a change in thickness Δw with respect to the equilibrium one w_0 and a relative shift between the two layers of the bilayer (shearing). We neglect these two terms as they will not be relevant to us, but both would have the same form of deformations squared times an elastic constant if we wanted to include them.

1.4.3.2 Membrane fluctuations

The elastic bending constant we have introduced has a value of $K_b \approx 15k_B T$ at room temperature. Thus the energy required to build a cell from scratch is²⁶ in the order of $8\pi K_b \approx 380k_B T$ (and to this, one must add that the cytoskeleton provides additional stability!). Thus large scale spontaneous deformation of the membrane due to thermal fluctuations are unlikely: in other words, a cell will not split in two due to thermal fluctuations, as that would require several hundred times the typical energy $k_B T$. At the same time, this value is equivalent to the hydrolysis of ≈ 20 ATP molecules, so the cell can easily expend some energy to deform it if necessary at its own terms.

However, thermal fluctuations *are* still present and do slightly deform the membrane. In this Section we describe thermal membrane undulations. Here we will focus in particular on bending deformations of the membrane. The trick will be to write an energy for bending, starting from the form we already discussed, and then convert it, using a Fourier transform, in a form which we can handle easily. In Chapter 3 we will deal with active deformation of GUVs, so this part will serve as an important benchmark.

We can write an expression for the energy of bending deformations of a planar membrane, based on the bending energy given in Equation 1.42, to which we add a Lagrange multiplier enforcing the constraint that the area is constant. We, again, neglect Gaussian curvature ($c_G = 0$), since we do not have changes in topology, and we assume the lipids have no preferred curvatures ($c_0 = 0$)

$$E_b = \int da \frac{K_b}{2} (2c_m)^2 + \lambda \int da \quad (1.45)$$

This version of the bending energy is named after Canham and Helfrich who first presented it [Canham 1970; Helfrich 1973]. In this version, λ is a *tension* representing the price paid to form new area (and so it summarizes somehow the stretching term already discussed).

In this form, Equation 1.45 is particularly difficult to handle. One trick is to define a function $h(\mathbf{r})$ describing the height of the membrane at a given position with respect to the equilibrium

²⁶Assuming it is a sphere

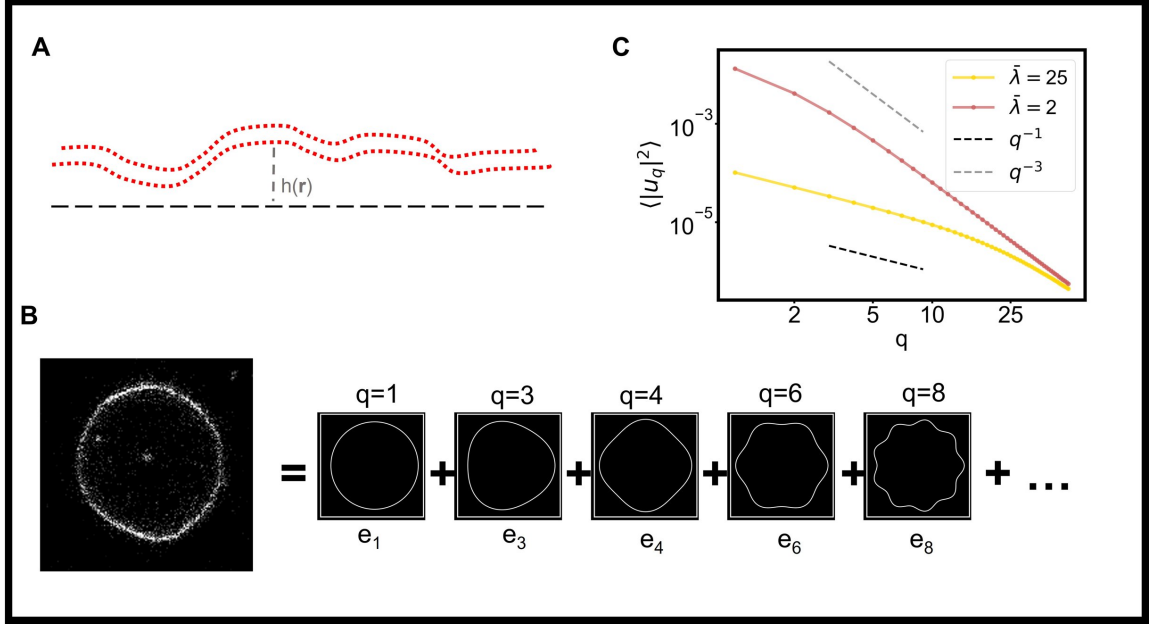


Figure 1.11: **Fluctuations of membranes:** A) Membranes fluctuate due to thermal motion. This gives rise to undulations bringing the membrane at a given height h with respect to the equilibrium $h = 0$. B) We can decompose undulations of a GUV in Fourier series to obtain a fluctuation spectrum. To each mode q indeed a different energy e_q corresponds. C) The final spectrum plotted for two vesicles having same tension and bending rigidity but different radius, leading to changes in the crossover mode $\bar{\lambda}$. The $1/q$ and $1/q^3$ scaling are shown for reference.

state $h = 0$ and rewrite the energy given by Equation 1.45 as a function of $h(\mathbf{r})$ (Fig. 1.11.A). One can then look at this energy in Fourier space i.e., look at it at different scales, given by a wave vector \mathbf{q} corresponding to a wavelength $\ell_q \approx 2\pi/|\mathbf{q}|$. At each scale indeed, the local height of the membrane, and hence its curvature and its area, will be given by a (complex) function $h(\mathbf{q})$. Hence, the contribution to the total energy will in general be dependent on the wave-vector \mathbf{q} . We then have to first rewrite the curvature c_m and the area element da in terms of $h(\mathbf{q})$ and then sum the contribution of each scale to the total energy starting from Equation 1.45 (the full derivation is given in Appendix A.1). By doing this, the energy corresponding to each length-scale is found to be independent and can be easily treated analytically.

The final result for the energy in Fourier form is, defining $q = |\mathbf{q}|$

$$E_b \approx \frac{A}{8\pi^2} \int d\mathbf{q} (\lambda q^2 + K_b q^4) h(\mathbf{q}) \bar{h}(\mathbf{q}) \quad (1.46)$$

with \bar{h} being the complex conjugate of $h(\mathbf{q})$.

This expression can be interpreted as the sum (integral) of harmonic oscillators²⁷, each with an energy $e_b(\mathbf{q}) \propto (\lambda q^2 + K_b q^4) h(\mathbf{q}) \bar{h}(\mathbf{q})$. Because such an energy is quadratic in the height $h(\mathbf{q})$, by the equipartition theorem, each of the quadratic mode must have an average energy,

²⁷By harmonic oscillator we mean something with an energy proportional to the square of the deformation, in this case h , with respect to the equilibrium value $h = 0$

due to thermal fluctuation, of $\langle e_b(q) \rangle = k_B T/2$. Hence, by taking the average value of the integrand in Equation 1.46 and separating each mode (taking into account that each mode occupies a volume in the inverse space of $(dq_x/2\pi)(dq_y/2\pi) = d\mathbf{q}/4\pi^2$, that also needs to be also extracted) one gets,

$$\langle e_b(\mathbf{q}) \rangle = \frac{A}{2} (\lambda q^2 + K_b q^4) \langle h(\mathbf{q}) \bar{h}(\mathbf{q}) \rangle = \frac{k_B T}{2} \quad (1.47)$$

from which we get that, for a given wave vector \mathbf{q} , the fluctuations of the height with respect to the equilibrium state $h = 0$ are given by

$$\langle h(\mathbf{q}) \bar{h}(\mathbf{q}) \rangle = \langle |h(\mathbf{q})|^2 \rangle = \frac{k_B T}{A} \frac{1}{\lambda q^2 + K_b q^4} \quad (1.48)$$

This expression shows that at high wave-vectors ($q \gg 2\pi/\sqrt{A}$, i.e. high local curvature of the fluctuations) the fluctuations of the height (in Fourier space), i.e., $\langle |h(\mathbf{q})|^2 \rangle$, are dominated by the bending rigidity and scale as q^{-4} , whereas at low modes ($q \approx 0$, smooth undulations of the membrane) the fluctuations are mostly due to the tension λ as the membrane tries to keep the area constant (scaling as q^{-2}).

Fluctuations for a vesicle The expression we derived above is well suited to study deformations of a planar membrane. For a spherical GUV we need to take into account the fact that the representation we used in terms of the height $h(\mathbf{r})$ is not one-valued anymore as the vesicle is a closed surface. A general solution is to re-write the expression for the energy in terms of spherical harmonics (equivalent to the Fourier transform for a quasi-spherical object) and then obtain the results for a given plane of the vesicle (usually, the equatorial plane). The fluctuations of the equatorial plane can then be measured by imaging a fluctuating vesicle with phase-contrast or fluorescence microscopy at the equatorial plane and then decompose its contour in Fourier modes to obtain the desired power spectrum [Pécrcéaux et al. 2004; Faris et al. 2009; Faizi et al. 2020]. The obtained spectrum is a function of the bending rigidity K_b and the tension λ , and these two parameters can be fitted to the experimentally measured spectrum (although several other techniques exist to measure K_b and λ) [Manneville et al. 2001; Monzel and Sengupta 2016]. This technique is usually called fluctuation or flicker spectroscopy.

Briefly, the position of the membrane in a spherical vesicle at a time t can be rewritten as a function of polar angles θ and ϕ as the Fourier series, in terms of spherical harmonics of the form $Y_{lm}(\theta, \phi)$, as

$$R(\theta, \phi, t) = R_0 \left(1 + \sum_{l=0}^{l_{max}} \sum_{m=-l}^l f_{lm}(t) Y_{lm}(\theta, \phi) \right) \quad (1.49)$$

where R_0 is the mean radius of the vesicle, l_{max} is the maximum available mode and f_{lm} are Fourier coefficients.

At the same time, we can decompose the contour observed at the equatorial plane in polar coordinates as a Fourier series in terms of the polar angle ϕ and the distance from the center r as

$$r(\phi, t) = R_0 \left(1 + \sum_{q=-q_M}^{q_M} u_q(t) e^{iq\phi} \right) \quad (1.50)$$

where q_M is the maximum experimentally available mode and u_q are the now 2D Fourier coefficients (Fig. 1.11.B).

We can then use expression for the whole vesicle 1.49 and repeat the steps in the previous section, with the spherical harmonics playing the same role as the Fourier transform in the Monge representation. Once obtained the final result for the fluctuation spectrum, as we are only interested in the equatorial plane, we can eventually set $\theta = \pi/2$ and get an expression for the spectrum (analogous to that in Equation 1.48) for the equatorial plane in terms of the 2D Fourier coefficients (u_q), which are connected to the 3D ones (f_{lm}).

The final result reads [Milner and Safran 1987; Faizi et al. 2020]:

$$\langle |u_q|^2 \rangle = \frac{k_B T}{K_b} \sum_{l=q}^{l_{max}} \frac{(2l+1)(l-q)}{4\pi(l+q)!} \frac{P_{lq}^2(0)}{[(l-1)(l+2)(l(l+1)+\bar{\lambda})]} \quad (1.51)$$

where $P_{lq}(0)$ is the associated Legendre polynomial and $\bar{\lambda} = \lambda R_0^2 / K_b$ is a normalized tension related to the crossover mode at which the spectrum shifts from tension to rigidity dominated.

This expression can also be rewritten, to mimic more closely the planar version of the spectrum in Equation 1.48 as

$$\langle |u_q|^2 \rangle \approx \frac{k_B T}{\lambda R_0^2 q + K_b q^3} \quad (1.52)$$

which is now describing the fluctuations of the equatorial plane of a quasi-spherical membrane rather than those of a flat one.

By simple rearrangements one can also get

$$\langle |u_q|^2 \rangle \approx \frac{k_B T}{K_b(q^3 + \frac{\lambda R_0^2}{K_b} q)} = \frac{k_B T}{K_b(q^3 + \bar{\lambda} q)} \quad (1.53)$$

where again we used $\bar{\lambda} = \lambda R_0^2 / K_b$. It is here clear that the crossover happens when the denominator is of the order of a unit, so $q^3 \approx \bar{\lambda} q$ i.e. $q \approx \sqrt{\bar{\lambda}}$, so that one gets a crossover from tension to bending dominated at $q_c \approx \sqrt{\bar{\lambda}}$. This also means that whether a vesicle is tension or bending dominated depends not only on the ratio λ / K_b but also on its radius.

Figure 1.11 shows two examples of the theoretical spectrum of u_q for a passive vesicle with two different values of $\bar{\lambda}$ obtained by changing the GUV radius, showing a change in scaling depending on it.

Equation 1.51 can be used to obtain, by fitting, the values of K_b and λ for a GUV, for example showing the effect of different lipid compositions [Faizi et al. 2020]. Additional techniques have been developed and applied successfully in order to measure vesicle spectra in different conditions. A review of recent experiments is presented in Section 3.4.

Another possibility for a GUV is to use the spectrum obtained for a planar membrane and integrate it over one of the two directions, say q_y , of the wave vector $\mathbf{q} = (q_x, q_y)$, as

the equatorial plane of a vesicle corresponds to a (any) line of a planar membrane of area $A \approx (2\pi R_0)^2$. The results is found to be

$$\langle |h(q_x)|^2 \rangle = \frac{1}{2\pi} \int dq_y \langle |h(q_x, q_y)|^2 \rangle = \frac{k_B T}{2\lambda} \left(\frac{1}{q_x} - \frac{1}{\sqrt{\frac{\lambda}{K_b} + q_x^2}} \right) \quad (1.54)$$

This neglects however the effects of curvature and of the closed topology of the vesicles, which were found to only affect modes at low q ($q < 5$) [Pécrcéaux et al. 2004; Faris et al. 2009].

Chapter 2

Gliding on a membrane:

Polar pattern formation of driven filaments on lipid membranes

Contents

2.1	Introduction	45
2.2	General background: self-propelled rod theory	47
2.3	The gliding assay as a model system for collective pattern formation	48
2.4	Actin gliding on a supported lipid bilayer	57
2.5	Gliding inside a giant unilamellar vesicle	70
2.6	Gliding in a nematic	82
2.7	Conclusions of Chapter 2	104

2.1 Introduction

Active agents moving together are known to form collective patterns much bigger than the individual agents' size. This kind of behavior is observed across length- and timescale, from the collective motion of bacteria to the flocking of birds [Becco et al. 2006; Giardina 2008; Elgeti, Winkler, and Gompper 2015]. What these behavior all have in common, is the presence of an interaction between agents that leads to a change in their velocity [Vicsek and Zafeiris 2012; Bär et al. 2020; Chaté 2020]. Such an interaction can be in the form of chemical signaling, steric interaction, visual or mechanical cues, etc. and is usually modeled as an effective potential between agents at a certain distance. Depending on the shape and behavior of the agents and on the details on the interaction, a different macroscopic pattern will arise.

Despite now long standing interest, it still remains particularly challenging, starting from the knowledge of the precise microscopic interaction, to predict the macroscopic outcome. One limitation is the absence of model systems exhibiting the requested behavior at the given scale. Recently, the gliding assay, composed of cytoskeletal filaments gliding on a surface propelled by

motors, has allowed a better insight in how the microscopic interaction tunes the emergence of patterns (see Section 2.3) at the micron-scale.

Not only is the gliding assay a simple and versatile system, but it is also directly related to the dynamics of the cytoskeleton in cells, which continuously has to self-organize into different, complex functional structures (focal adhesions, cytokinetic ring, mitotic spindle, etc.) and manages to do so with a limited set of ingredients, namely filaments, motors and process-specific regulators. Understanding the behavior of filaments moving in a complex environment is thus key not only to understand general rules for the behavior *elongated* active particles, but also in the more specific field of cell-biology. Studying pattern formation will provide organizational principle that cells must take advantage of but also constraints that the cell has to deal with.

In this chapter, we develop a general model system of filaments gliding on a membrane and tune it in specific ways, obtaining three different behaviors that all have a different relevance in the self-organization of the cytoskeleton. First, we study how gliding on a membrane introduces steric interactions and how they lead to polar patterns. Next, we study the effect of confinement and how polar patterns organize in a spherical geometry. Finally, we see how steric interactions between an active and a passive material lead again to polar structures. The main point of this chapter is to elucidate how we can, using membranes and nematic materials, tune both the microscopic interaction between filaments or the effect of the environment on the filaments' orientation to tune the emerging collective structures.

All these results, taken together, suggest organizational principles for the cytoskeleton (and self organizing active matter systems composed of rod-like agents in general). In particular, we will underline the role of often neglected details such as filaments' flexibility, steric interactions and the influence of confinement, topology and of complex environments on the formation of patterns. In addition, it also suggest strategies on how such patterns can be shaped, controlled and directed by exploiting those same principles.

2.1.1 Chapter outline

This chapter deals with cytoskeletal filaments, both microtubules and actin, gliding bound to a fluid substrate, i.e., on a lipid membrane. This setup is a variation of the standard gliding assay on solid surfaces and will allow us to study the collective behavior of filaments in the presence of strong steric interaction.

First, the standard gliding assay on a solid substrate is described and the difference between an actin gliding assay and a microtubule gliding assay are discussed in section 2.3, together with the main results in the literature regarding high-density gliding assay. Then we will discuss the first main results of this thesis concerning high-density actin gliding assay on a supported lipid bilayer in section 2.4. This setup, whose main results are published in [Sciortino and Bausch 2021], is then extended to actin gliding on the inside leaflet of a giant unilamellar vesicle (Section 2.5 and to microtubules gliding in a passive actin nematic (Section 2.6).

2.2 General background: self-propelled rod theory

Because the formation of patterns based on active-matter systems, i.e. systems that can consume energy to reach out-of-equilibrium conditions, is widely studied, several models have developed to take different conditions into account (see also Section 1.1.3).

As we are going to deal with filaments, it is worth recapitulating the main results in the case of *elongated* self-propelled objects or, more commonly, self-propelled rods (SPRs) [Bär et al. 2020]. SPR models describe indeed a wide variety of systems, including cytoskeletal filaments (our focus in this case), swimming bacteria and granular matter. Briefly, one can think of SPRs as rod-shaped objects with a given length L and diameter D and thus with aspect-ratio $a = L/D$. Because of their shape, the corresponding passive model would be that of a nematic material (see Section 1.3.2), where the aspect ratio determines the isotropic-nematic transition. However, SPRs are also characterized by a definite orientation $\hat{\mathbf{p}}$ (absent in the passive nematic case, in which an orientation \mathbf{p} would be equivalent to $-\mathbf{p}$) and a self-propulsion speed $\mathbf{v}(t) = v\hat{\mathbf{p}}$ that allows them to move along their orientation's axis (Fig 2.1.A). This term models the ability of active particles to consume energy and turn it into self-propulsion. The velocity term \mathbf{v} and the orientation of the rod \mathbf{p} can of course be modelled in different ways, e.g. as constants or as stochastic processes. Additionally, SPR models usually contain an interaction term between rods. Depending on their activity, the chosen rod-rod interaction and the system's packing fraction rods can assemble in a variety of patterns, including lanes, vortices, flocks and bands.

The presence of an oriented shape makes it usually convenient for SPRs to align with each other to resolve collisions, so that in general motility-induced phase separation (MIPS) [Cates and Tailleur 2015], i.e. the formation of immobile clusters as particles push against each other, often observed for spherical active particles, is usually not observed in SPRs systems, which instead rather form clusters of rods moving together with local alignment. While rods are characterized by directed motion along a main axis \mathbf{p} , the global symmetry of the patterns emerging is usually expected to be nematic (i.e., with rods oriented both in the \mathbf{p} and the $-\mathbf{p}$ direction). Still, arguments exist for the possibility of SPRs forming polar phases and some experimental system have indeed observed them. We are going to discuss some of these arguments and show results in this sense in the rest of this chapter.

SPRs models can be briefly separated into two main categories, depending on whether rod-rod interactions are local (steric) or long-range (hydrodynamic), which are the SPR-analogues of the different general views described in Section 1.1.3.

Wet SPRs When interactions are hydrodynamic, i.e. long range, SPRs are usually described, rather than as individual agents, as a fluid with a velocity field $\mathbf{v}(\mathbf{r})$ and an orientation field $\mathbf{p}(\mathbf{r})$, and hydrodynamic equations, based on the chosen symmetries, can be written for such fields. We are going to deal with similar models only briefly in the next chapter, where fluid-like system based on cytoskeletal filaments are introduced (Section 3.2): In this case, the challenge is to identify the relevant symmetries and, more importantly, to implement the (often non trivial, in the presence of activity) interaction between different parts of the fluid.

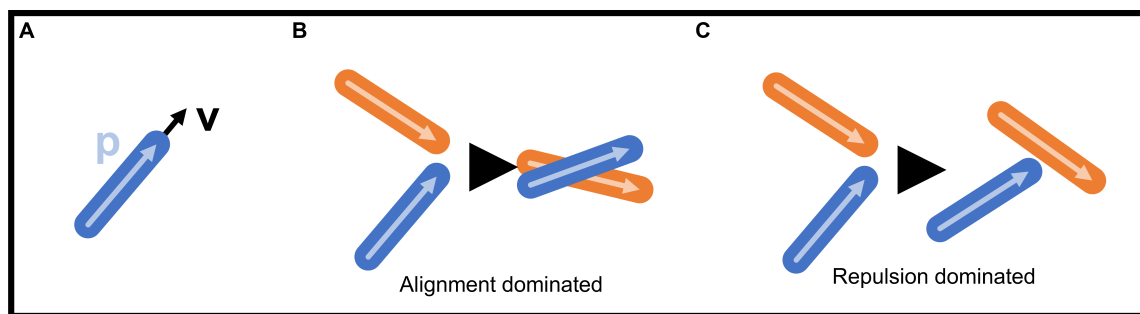


Figure 2.1: **Self-propelled rods**: A) An example of SPR, a particle with an orientation \mathbf{p} and a self propulsion speed \mathbf{v} . B, C) Alignment and repulsion dominated interactions: on the left (alignment-dominated) particles can cross each other but align due to some interaction; on the right (repulsion dominated) particles must stop upon collision.

Dry SPRs Dry SPRs interact via direct collision, which changes their relative orientation. No long-range interaction due to hydrodynamics is present in this case. Because of this, in general, rod-rod collision do not conserve momentum, as the final orientations differ from the initial ones. This can happen if the environment acts as a momentum sink. Depending on the strength of the rod-rod interaction, the collision can be alignment-dominated, in which particles can penetrate each other easily and only align because of the presence of some external aligning potential (Fig 2.1.B), or repulsion-dominated, if rods are unable to occupy each other's volume and thus align because of strong steric interactions (Fig 2.1.C). In this case, steric interaction tend to resolve collisions by alignment rather than jamming particles in place. As we will see, gliding cytoskeletal filaments, especially actin, fall in the alignment-dominated regime, whereas when gliding on a SLB filaments can be forced towards a repulsion-dominated one. This transition is the main topic of Section 2.4.

Clearly, a middle ground must exist between the two descriptions. While dry SPRs provide a better microscopic description of the system and wet SPRs a bigger global description, the connection between the two parts (i.e., between rods interacting with each other and their resulting large-scale motion) is often cumbersome.

2.3 The gliding assay as a model system for collective pattern formation

The gliding assay is a standard experimental technique that allows to measure general properties of a batch of molecular motors such as their speed, the quality of the batch, their processivity, etc. (see Section 1.2.1.2 and [Toyoshima et al. 1987; Hynes et al. 1987; Howard 2001]). A protocol for performing a gliding assay is given in Methods 4.5.

The experimental setup consists of molecular motors' heads bound on a substrate (usually a collodion or nitrocellulose coated coverslip) on top of which filaments are sedimented. Filaments thus bind to the motors and, upon ATP addition, motors will attempt to move on the filaments. As however motors are bound to a solid substrate, it will actually be the filaments gliding, propelled by the motors' power stroke. By then measuring the speed of the gliding filaments

and estimating the surface concentration of motors one can estimate the speed at which motors would walk on the filament, how the filaments' speed depends on the number of bound motors and therefore their processivity, the amount of inactive motors (leading to immobilized filaments or to fragmentation of the filaments due to the resulting stress of a mixture of active and inactive motors) and, more in general, how all of these properties depend on the environmental conditions such as buffer, pH, ATP concentration etc.

Depending on the motors' properties, the speed of the filaments might indeed depend on the motors' concentration and/or on the filaments' length. In general, a higher surface density of motors is required in the case of non-processive motors, since at every instant only a fraction of the motor's heads are bound to the filament. A too low concentration will result in the filaments unbinding upon ATP addition.

From a different point of view, gliding assays also represent a model system to study the collective behavior of active filaments in a two-dimensional setting and at the micron-scale. It serves indeed as an experimental model for the self-organization of a large number of elongated active particles and thus falls in the category of *dry self-propelled rods*, of which it is one of the main members, but it also serves as a reference for studying self-organization of the cytoskeleton in general. The fact that a gliding assay is composed by a minimal number of ingredients but that there also is a huge collection of proteins which interact with both motor and filaments, changing their properties, makes the gliding assay a simple yet versatile model system.

The following sections contain a review of the most important results stemming from gliding assay experiments, divided into two main classes: gliding assays with actin and gliding assays with microtubules.

2.3.1 Actin gliding assay

The actin gliding assay is composed of actin filaments and myosin motors. Most of the results in this and following sections are based on a truncated version of the motor Myosin-II commonly known as heavy-meromyosin (HMM). HMM is a non-processive motor which does not form mini-filaments. Of course, gliding assay with processive motors such as Myosin-V are also possible (refer to the Section 1.2.1.2 for a description of motors).

Because actin is a semi-flexible polymer, gliding actin filaments are easily bent by motors' activity [Weber et al. 2015] and indeed exhibit out-of-equilibrium curvature fluctuations when propelled by a motor. At low filaments' surface density ρ , specifically when $\rho < 5 \mu\text{m}^{-2}$, gliding actin filaments move at a mean speed of $1-5 \mu\text{m}/\text{s}$ and show no sign of collective behavior. It is only when $\rho > 5 \mu\text{m}^{-2}$ that the initially isotropic filaments' distribution in space evolves, upon activity, into collective patterns, more specifically in the forms of clusters of filaments moving together which then, if $\rho > 20 \mu\text{m}^{-2}$, evolve into polar density waves [Schaller et al. 2010] (see Fig. 2.2.A). The emergence of clusters and waves is due to the formation at small time scales of small clusters of aligned filaments, which then act as seeds for further aggregation, giving rise to the emergence of a low and a high density phase [Suzuki and Bausch 2017].

A simple system such as the actin gliding assay has been recently important in clarifying one of the biggest open questions in the field of active matter, i.e., how, starting from microscopic interactions between active agents, can we predict or at least better understand the formation of macroscopic structures. While long-range hydrodynamic interaction might be necessary to

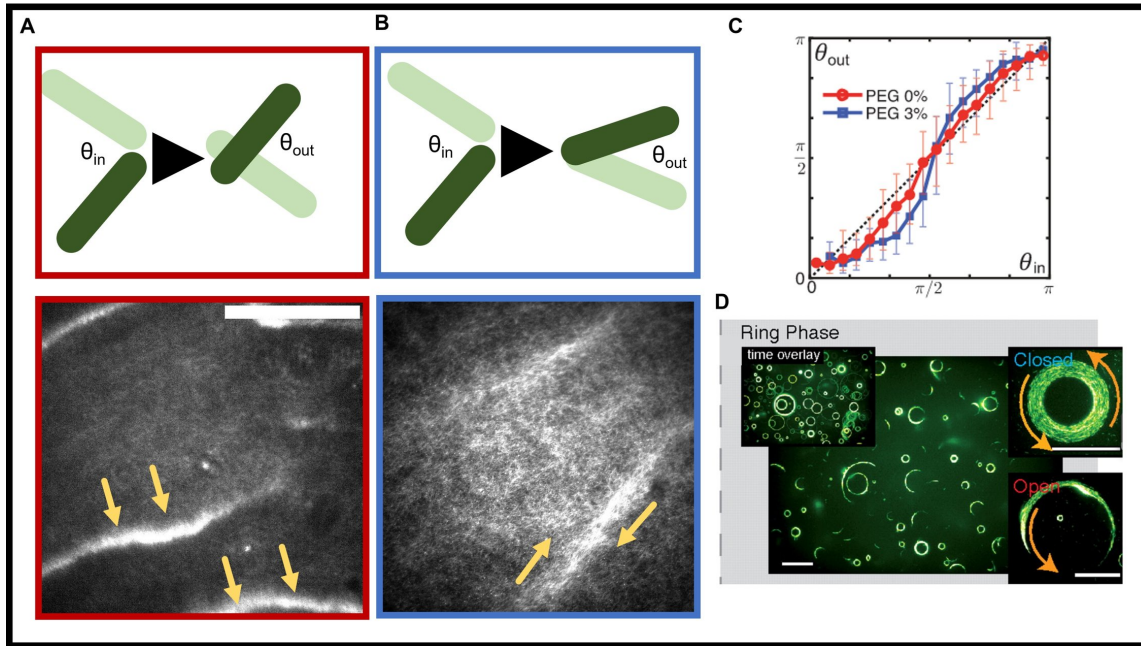


Figure 2.2: **Actin gliding assays:** A, B) Schematics of two different kind of alignments, a very weak one and a slightly stronger one. A) In the case of weak alignment between filaments, the resulting order is polar, featuring density waves moving in the same direction (scale bar: $50 \mu\text{m}$). B) If alignment is slightly strengthened, the resulting order is nematic and lanes form (scale bar: $50 \mu\text{m}$). C) Filament-filament collision statistics for an actin gliding assay with (red) and without (blue) PEG, from [Suzuki and Bausch 2017]. Polar waves and nematic lanes in A and B are labelled with the same color to indicate to which alignment statistic they correspond. D) Rings formed by gliding actin in the presence of fascin, from [Weber et al. 2015].

explain the behavior of big clusters, as the big mass of filaments moving collectively is able to displace the fluid consistently [Schaller et al. 2011], it is more instructive to think about the pattern formation process in terms of collisions between individual filaments. If one looks at binary collisions between two HMM-propelled actin filaments it becomes immediately clear that filaments interact very weakly with each other, i.e., their direction of motion barely changes upon collision [Suzuki et al. 2015]. In this case, the experimental collision statistics has been measured by analyzing individual collisions between filaments and results in a function $\theta_{out}(\theta_{in})$ describing the relative angle θ_{out} that two filaments have after having collided with incoming angle θ_{in} .

The result, depicted in Fig. 2.2.C (in red), shows that while there is a slight skew towards polar alignment in the case of collisions happening at small angles $< 90^\circ$ and, conversely, towards anti-polar alignment at large ($> 90^\circ$) angles, the distribution is almost completely symmetric (there is only a very slight preference towards polar order) and very close to the diagonal line which would indicate no relative alignment at all. The fact that filaments interact weakly indicates that we are rather far from the repulsion-dominated case, as steric interaction matter little. The question then is, whether such a collision statistics, with its weak polar preference, is enough to account for the emergence of polar order in the collective state.

This can be quantified by writing a Boltzmann-like equation for the evolution of the filaments probability distribution $f(\mathbf{r}, \theta, t)$ describing the probability of finding one filament at position \mathbf{r} with orientation on the plane θ at a given time t . Its variation in time is of course due to rotational diffusion (changing the filaments' orientation, with a diffusion coefficient D_θ), to the filaments motion (assumed with speed $v_0 \hat{\mathbf{v}}(\theta)$ directed in direction θ) and to collisions with other filaments. The final equation reads [Suzuki et al. 2015]:

$$\partial_t f = -v_0 \hat{\mathbf{v}}(\theta) \cdot \nabla f + D_\theta \partial_\theta^2 f + C[f^{(2)}]$$

where the binary interaction between filaments is summarized in an integral over the two-particles distribution function $f^{(2)}(\mathbf{r}, \theta_1, \theta_2, t)$ describing the probability that two particles collide in \mathbf{r} with respective orientations θ_1 and θ_2 . Briefly, the collision integral considers all possible relative orientation during a collision and their outcome depending on the distribution $\theta_{out}(\theta_{in})$. By plugging the experimental collision distribution in the collision integral, the result is that *binary* collision can *not* account for the emergence of polar order.

It follows that in this weak collision limit it is required that the density is high enough that multi-particle collisions can play a role and amplify the weak alignment enough for polar order to emerge macroscopically. The emergent order is polar is due to the small polar bias in the collision distribution and on the intrinsic polar bias due to the fact that two filaments colliding polarly keep moving together whereas filaments colliding anti-polarly do not. It follows also that for polar states to emerge at lower densities, the distribution must be significantly more skewed towards polar alignment than in this case.

Another question is then what happens if the interaction between filaments is continuously increased. This point was addressed recently [Huber et al. 2018]. By adding an increasing amount of polyethylene glycol (PEG), which acts as a depletant (see Section 1.1.2) and thus exert an effective force between aligned filaments, the system can be biased towards more and more skewed collisions distributions (see Fig. 2.2.C (in blue)). This pushes the system more and more towards a globally nematic symmetry, and the result is not simply that the polar state observed in the absence of PEG emerges at lower filaments' density but rather a completely new state with nematic symmetry, composed of lanes of filaments moving in both directions (see Fig. 2.2.B). The two phases (polar and nematic) are separated by a coexistence phase at intermediate PEG densities in which polar waves and nematic lanes coexist and mix. This indicates the presence of a phase transition between an order which is polar (at low interaction) and one which is nematic (at higher interaction). That the results as the distribution becomes more skewed is nematic is not surprising, as the binary collisions statistics is indeed pushed more and more towards nematic alignment as PEG is added. However, that such a small change in the microscopic interaction can make the system switch from one symmetry to the other remains remarkable.

Another way to change the microscopic interaction, demonstrating the flexibility of the actin gliding assay, is to add actin-binding proteins to the gliding assay. For example, the addition of a parallel crosslinker such as fascin leads to the formation of frozen states composed of filaments moving in rings. This is because by binding together polarly moving filaments, fascin leads to the formation of active bundles of different rigidity than individual filaments. Such bundles are not completely straight as they are composed of filaments previously gliding in different

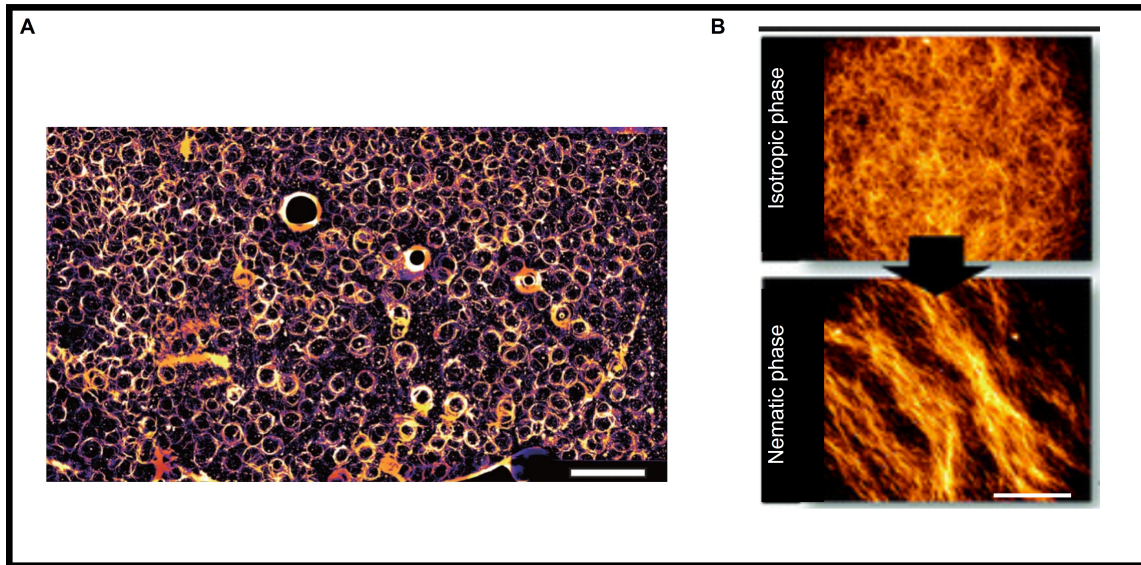


Figure 2.3: **Microtubules gliding assays**: A) Microtubules forming an array of vortices, from [Sumino et al. 2012]. Scale bar is 2 mm. B) Microtubules assembling in nematic lanes, from [Inoue et al. 2015]. Scale bar is 50 μm

directions that, once bound, have a hard time reorienting due to the rigidity of the bundle. One result is that the orientation's fluctuations of such bundles are enhanced, leading to the formation of rings. Fascin can also stabilize such rings by binding the filaments inside them together. On the other hand, adding crosslinkers such as α -actinin, which bundle actin in an anti-parallel fashion, rather leads to stresses forming in the system (as bound filaments would like to glide in opposite directions) and thus to clusters which continuously break as motors disassemble anti-parallel bundles by pushing the filaments in opposite directions [Weber et al. 2015].

Summing up, the actin gliding assay has been a simple system able to show puzzling results. First of all, it is able to assemble into collective structures despite a very weak microscopic interaction, if enough filaments are present. Second of all, we can tune the microscopic interaction making it only *slightly* stronger and this is already enough to push the system to completely different emergent states, i.e., from polar to nematic or even to frozen steady states in the presence of crosslinkers.

2.3.2 Microtubule gliding assay

Microtubules are rigid filaments and therefore are a model system for rigid rod-like filaments gliding, rather than semiflexible as is the case for actin.

Indeed the pattern formation exhibited by microtubules differs in general with that of actin.

One of the first results with collective microtubule gliding consists in a high-density gliding assay of 15 μm long microtubules propelled by dynein, a motor which also rotates the microtubules around their long axis. They were found to spontaneously assemble in an array of vortices with a 400 μm diameter [Sumino et al. 2012] (Fig. 2.3.A). Motion inside the vortices was both clockwise and counterclockwise, indicating a microscopic nematic symmetry in the interaction. Indeed, the microtubules were found to move smoothly in one direction (minus small fluctuations due to thermal noise) but also to bend sharply upon collision. Once more, one can turn to analysis of the individual binary collisions between microtubules and the result is that, unlike actin, microtubules show a stronger tendency towards nematic alignment (although events in which the filaments barely change direction are still observed). A simple computational model consisting of filaments moving along their orientation, which fluctuates as a Ornstein-Uhlenbeck process, and interact nematically upon collision can recapitulate the formation of large scale vortices. The results were also connected to the specific use of the motor dynein, whereas kinesin, in the same conditions, did not lead to vortex formation as microtubules did not interact upon collision. This indicates that the choice of different molecular motors can also affect the microscopic interaction and hence the emerging patterns.

Also in the microtubules case, however, one can again tune the filament-filament interaction by introducing a depletant (in this case, methylcellulose) to increase the side interaction between colliding filaments. If this is done, collective patterns also arise using kinesins [Inoue et al. 2015] (Fig. 2.3.B). Adding a depletant to kinesin-driven microtubules leads to nematic streams of filaments. The details of this nematic phase was further investigated [Saito et al. 2017] and the fact that the emerging phase has a dependency on the depletant's concentration clarified. Interestingly, without depletant, no emerging nematic patterns were observed even at relatively high microtubule concentrations (up to 15 μM) whereas even for low depletant concentration (0.05 - 0.1 wt%) nematic patterns could be observed for any microtubule concentration above 3 μM . Finally, together with the choice of the motor, also the filament-filament steric interlocking and their chirality at the molecular level can be important, as they can tune the filament-filament collision rule or insert biases in the system towards nematic or polar order [Sumino et al. 2012; Afroze et al. 2021]. Summing up, once again the macroscopic behavior can be linked to three main parameters: the binary interaction strength, the surface concentration of filaments and, lastly, their physical properties (rigidity, for example, but also size and the microscopic interaction with the molecular motors).

2.3.3 Gliding assays with surface modifications

There is another way to tune the behavior of gliding assays and that is, controlling the substrate to which they are bound. In this way it is not really the binary interaction which is affected but the interaction with the substrate which, in turn, leads to an effective alignment between microtubules.

One option is to functionalize the surface with discretely-spaced gold nanopillars to which motors are bound. Because the pillars are arranged on a lattice, the microtubule, at each lattice point, can only go in a limited number of directions depending on on which pillar it binds next [Kaneko et al. 2019; Kaneko et al. 2020]. Another option is coating the surface with functionalized benzyl-guanine (BG) in a way that the surface density of motors depends on the surface

density of BG. This allows to form both clusters of microtubules moving together (polarly) at high microtubule and high BG density and a long-range ordered phase, with microtubules aligned along a main direction, at intermediate BG density. This is due to a change in the density of motors which in turns affects the binary interaction between microtubules so that at high BG (high motors) concentration, microtubules align rather than crossing over each other [Tanida et al. 2020]. Another possibility is to bind the gliding filaments to an elastic substrate and see the results of applied stretching. Stretching is found to select some gliding directions rather than other ones and thus can lead to the formation of different patterns, including giant vortices and lanes [Inoue et al. 2019].

This approach has so far been mostly applied to the gliding microtubules system and not to the actin one.

2.3.4 Filaments gliding on a membrane

Most of the discussed gliding assay-like systems are carried out on a solid substrate. However, *in vivo*, motors often are bound to the lipid membrane, i.e., to a fluid substrate. One option to extend the gliding assay system to a fluid substrate is the use of supported lipid bilayers (SLBs), described in Section 1.4.2). This allows a more realistic description of the motion of some motors (which are membrane-bound *in vivo*) and also allows to study the effect fluidity has on filaments' dynamics. One can for example form a SLB containing a fraction of biotin-functionalized lipids to which motors can bind via streptavidin-biotin tags. This approach has been utilized in [Grover et al. 2016] to bind kinesins to a SLB and perform gliding assays on a fluid substrate. This has also allowed to better understand the kinetics of filaments-motors system on fluid substrates and thus with more relevance to biological situations [Lopes et al. 2019; Jiang et al. 2019].

The most striking result when binding filaments on a SLB is that filaments propelled by membrane-bound motors can still move, but do so at a slower speed than they would move on glass.

2.3.4.1 A model of filaments on a SLB

To understand this behavior, a simple model can be developed, in the case of gliding microtubules, taking into account the motors' diffusion on the membrane. The model, adapted from Grover et al. 2016, is fully solved in Appendix B.

Consider the situation in which N motors are bound to a microtubule of length L , each of them moving at a speed \mathbf{v}_{step} on it and hence exerting (and receiving as a reaction) a force \mathbf{F}_M . On a solid substrate, the force of the microtubules on the motors would be balanced by the substrate. This would correspond to the full motors' power stroke being delivered to the filament which would then move at a speed of $\mathbf{v}_{MT} = -\mathbf{v}_{step}$.

On a SLB instead, the motors are also slipping with a speed \mathbf{v}_{slip} on the membrane, pushed by the reaction force of the filament, and thus only a fraction of their stepping speed is adsorbed by the bilayer rather than by the microtubule. The situation is depicted in Figure 2.4. This results in an equation for the speed of the microtubules as a function of both the slipping and the stepping speed of the motors as

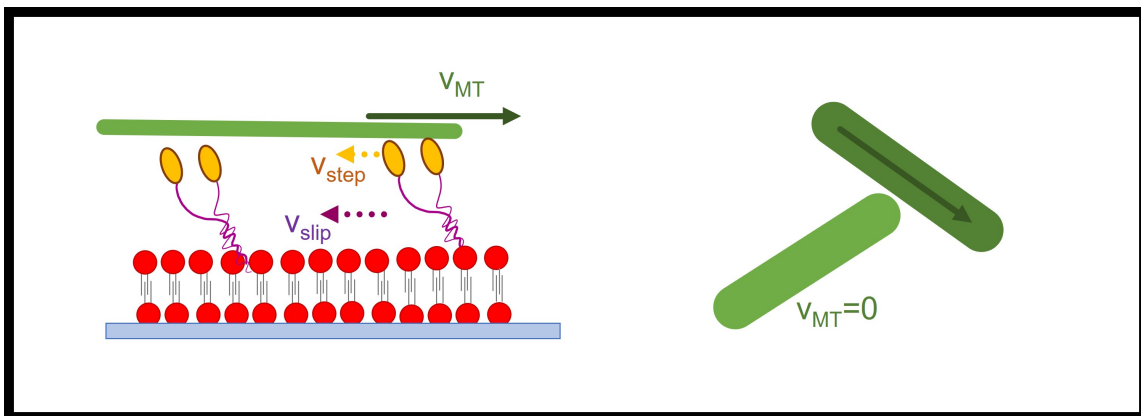


Figure 2.4: **Microtubule gliding on a membrane:** A microtubule gliding on a membrane moves but its speed is decreased as motors slip on the membrane. This also means that colliding microtubules stop as motors are unable to provide enough force to make filaments crawl over each other.

$$|\mathbf{v}_{MT}| = |\mathbf{v}_{step}| - |\mathbf{v}_M| \quad (2.1)$$

If one then uses the equation of motion at the micron scale (see Section 1.1.1.2) and the Einstein-Smoluchowski relation (Equation 1.4) to connect each of these speeds to the drag coefficient each of the components feels (motors on the membrane and filament immersed in the fluid), one ends up with an equation for the efficiency of the motors' in moving the microtubules given by

$$|\mathbf{v}_{MT}| = - \left(\frac{1}{1 + c \frac{D_{SLB}}{\lambda}} \right) |\mathbf{v}_{step}| \quad (2.2)$$

where we have defined $c = \frac{\alpha\pi\eta}{k_B T \ln(2h/r)}$ as a parameter-dependent constant (see Appendix B for details), coming from the drag coefficients, and $\lambda = N/L$ is the motors' linear density along the microtubule, presumably proportional to the surface density of motors. Importantly, this expression is directly related to the fluidity of the membrane by the diffusion coefficient of the SLB D_{SLB} . Equation 2.2 connects directly the stepping speed of the motors to the final speed of the microtubule.

Thus one can easily see that the more the substrate is fluid (i.e., the bigger D_{SLB}) the smaller fraction of the motors' stepping velocity¹ is adsorbed by the microtubule (because the slippage is bigger). Clearly on solid substrates ($D_{SLB} = 0 \mu m^2/s$) the microtubule moves at the motor's stepping velocity, as expected, independently on λ . Indeed another observation is that the microtubule speed depends on the motor density λ whereas this would not be the case on a solid substrate as can also be seen by setting $\mathbf{v}_M = 0$ in Equation 2.1, and obtaining $v_{MT} = v_{step}$. This is in contrast with the fact that for motors with a high duty-ratio density does not count. In this case however, having multiple motors on the filament, decreases the

¹This all is valid if $|\mathbf{F}_{MT}|$ is smaller than the motors' stall force. This is indeed the case in this setup as the maximum drag force of a microtubule is orders of magnitude smaller than the stall force of a kinesin motor.

drag that each motor feels. Indeed on fluid substrates, contrary to glass, the drag force of the microtubule *on* the motors is relevant as it can increase slipping, which does not happen on solid substrates. As seen in Equation B.1 the drag force decreases as N increases and therefore motors are more efficient when they bind in high numbers.

This model has been tested in [Grover et al. 2016] by varying the diffusivity of the SLB with increasing amount of cholesterol, which modifies the SLB’s diffusivity, and by varying the surface concentration of membrane-bound kinesins.

Another striking result of this system is that microtubules *stop* upon collision with an obstacle, for example when a microtubule hits another one and its direction of motion is hindered. This is due to slippage of motors under the load represented by the obstacle, meaning that motors rather slip on the membrane instead than propelling the microtubule forwards and, as seen in Equation B.6, if momentarily γ_{MT} increases and/or $|\mathbf{v}_M|$ increases, then the speed of the microtubule decreases.

Thus, having a filament propelled by a membrane-bound motor affects both its speed and its interaction with other filaments upon collision. We will exploit this behavior in Section 2.4.

2.3.4.2 Other examples of SLB-based systems

Other systems featuring membrane-attached motors have been developed recently. The main ones feature Myosin-Ib and Myosin-Ic, members of the Myosin family which are found bound to the cellular membrane *in vivo*. In these cases, binding on the membrane activated particular properties of these motors, such as a depolymerase activity or the ability to propel actin filaments in a chiral way [Pyrpassopoulos et al. 2012; Pernier et al. 2019; Pernier et al. 2020] or remodel the membrane [Rogez et al. 2019]. However, while the SLB was relevant in these cases to modify motors’ properties, indicating that SLB systems are a powerful tool, no collective behavior was studied in these works. Another system featuring cytoskeletal filaments on a SLB is the one composed by the bacterial cytoskeletal filament FtsZ which, rather than being propelled by a motor, treadmills on the surface by (de)polymerizing continuously. FtsZ filaments on a SLB were found to aggregate in collective structures characterized by vorticity due to the filaments’ own curvature [García-Soriano et al. 2020; Caldas et al. 2019].

All these results confirm SLBs as a valid membrane model system. The substrate’s fluidity can indeed influence the behavior of motors and filaments and their respective interaction. Such features, i.e. substrate’s fluidity and its effects, are often neglected in the microscopic modeling of the cytoskeleton’s self organization, mostly because much is not known about them. Additionally, SLB-filaments system often lack a model system able to tackle them effectively.

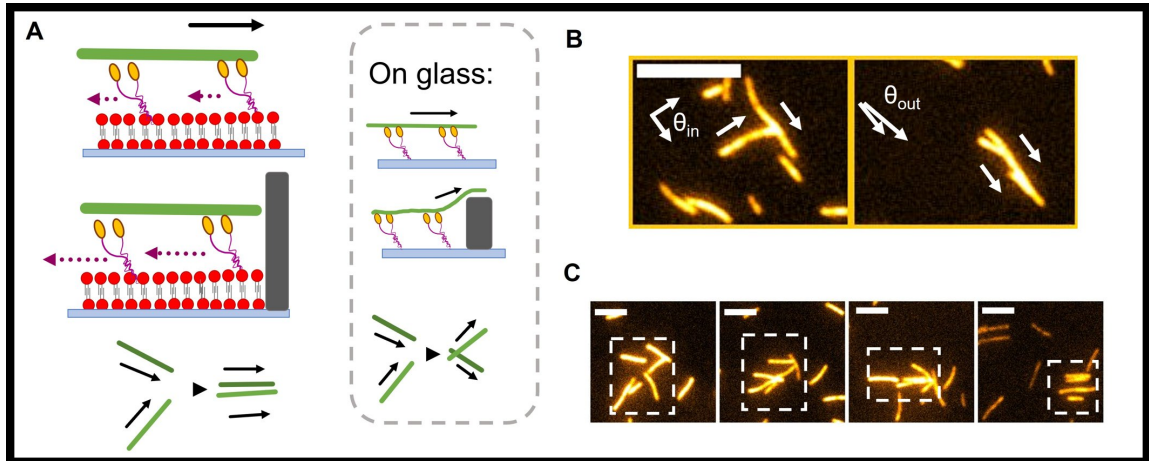


Figure 2.5: **Schematics of the system and microscopic behavior** A) Motors are bound to a SLB and push short actin filaments. Because of slippage of the motors on the membrane, filaments stop upon collision and align. On glass instead, filaments interact weakly. B) Filaments colliding align due to the modification of the substrate. Upon collision, filaments stop, align and then keep moving (Scale bar: $5 \mu m$). C) Multiple filaments can stop and aggregate against obstacles (Scale bar: $2 \mu m$).

2.4 Actin gliding on a supported lipid bilayer

In this section we will discuss the (collective) dynamics of actin filaments gliding propelled by motors (specifically, HMM) bound to a supported lipid bilayer (SLB). In section 2.3 we have seen how, particularly in the case of gliding actin, the emerging patterns can depend on the filament-filament interaction. If the interaction is weak, i.e., filaments barely align upon collision, the resulting patterns are polar cluster or polar density waves for actin and no pattern at all for microtubules. However, if the interaction is pushed towards a stronger nematic interaction then globally nematic patterns appear, including lanes in the case of actin [Huber et al. 2018], bands and vortices in the case of microtubules [Sumino et al. 2012; Inoue et al. 2015].

In this cases the interaction has been modulated either using depletants or surface modifications.

In most of the experimental cases, even when biased towards nematic alignment, the strength of the interaction was relatively weak, with small deflections upon collisions. A recent system of microtubules forced to align in a stronger fashion instead leads to the formation of polar clusters [Tanida et al. 2020]. This raises the question, what would happen if we keep pushing towards nematic alignment in the case of actin. The prediction would seem to be the formation of nematic lanes.

To investigate the matter, we performed actin gliding assays with HMM bound on a SLB, taking advantage of the observation that filaments on a membrane stop and align upon collision. This section recapitulates and expands the results of [Sciortino and Bausch 2021].

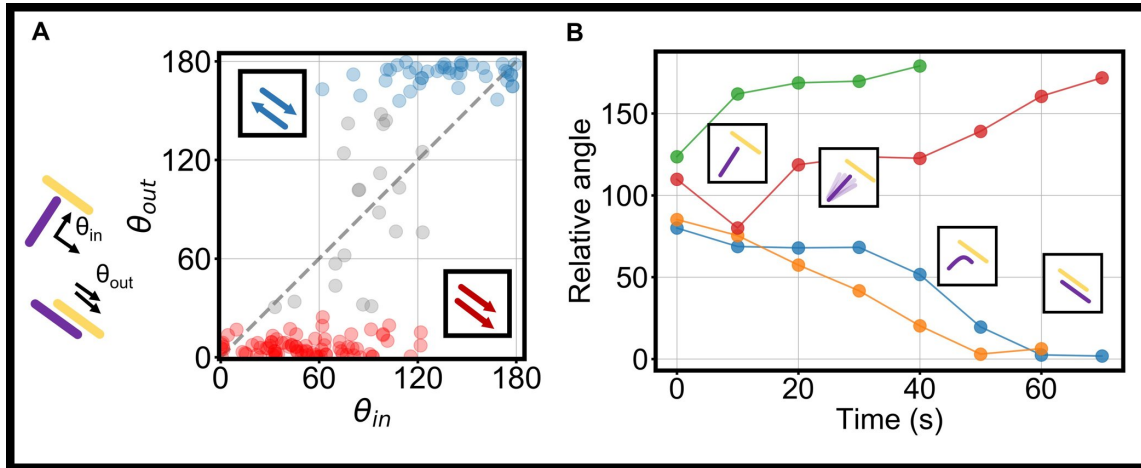


Figure 2.6: **Collision statistics for gliding filaments on a SLB** A) By measuring multiple collisions, we show that the interaction is strongly nematic, with filaments aligning at $\theta_{out} \approx 0^\circ$ or 180° whatever the incoming angle θ_{in} . B) Time evolution of example collisions. Filaments collide, stop, fluctuate and eventually align.

2.4.1 Actin filaments on a SLB align nematically

Briefly, biotinylated-HMM is bound via streptavidin to a biotin-functionalized SLB. The SLB is fluid and has a diffusion coefficient of $D \approx 3.4 \mu\text{m}^2/\text{s}$ as extracted from FRAP measurements (see Methods 4.5). Then, stabilized actin filaments with a mean length of $L = 2 \mu\text{m}$ are allowed to sediment for some time, depending on the desired surface density, and then washed. Filaments' length is regulated with the protein gelsolin (see Methods 4.1). Finally ATP, together with 0.2 wt% methylcellulose (MC) is added to the system to activate it. Fig. 2.5.A shows a scheme of the system. The precise composition and setup is given in Methods 4.4.

We can summarize the main results in terms of the filaments' surface density σ and in terms of the collision parameters $O = \sigma L^2$ indicating the average numbers of interactions per filaments (roughly, the average number of filaments in a box with side equal to the filaments' length) which allows a more direct comparison with theoretical results (see Equation 1.25 for a definition of O). In particular, σ can be controlled by varying the bulk concentration of actin incubated before washing, on which σ is approximately linearly dependent [Schaller et al. 2010].

2.4.1.1 Binary collisions statistics

By performing low density gliding assays on a SLB ($\sigma = 0.08 \text{ filaments}/\mu\text{m}^2$ ($O = 0.32$)) we confirm that, as expected on a SLB, actin filaments do move with a speed of $v_0 = 100\text{--}200\text{nm}/\text{s}$ (thus, one order of magnitude slower than on glass) and that they do align upon collision. Figs. 2.5.B and C show examples of collision between two or more filaments and indicate that that filaments exit collisions in an aligned state.

By measuring the collision statistics $\theta_{out}(\theta_{in})$ we can quantify the binary interaction statistics (Figs. 2.6.A). We found that filaments align in a perfect nematic fashion, i.e., filaments colliding at small angles ($\theta_{out} < 90^\circ$) exit the collision with polar alignment ($\theta_{out} \approx 0^\circ$) and filaments colliding at large angles ($\theta_{out} > 90^\circ$) exit the collision with perfect anti-polar alignment ($\theta_{out} \approx$

180°). Filaments colliding perpendicularly (T-bone collision) exit the collision randomly with either polar or anti-polar alignment. Only a small fraction ($\approx 10\%$) of the T-bone collisions do not result in perfect alignment as the filaments glide away before having time to align.

Overall then, the collisions statistics appears to be strongly nematic and much more skewed than previous systems using depletants. This would in principle lead to a strongly nematic global order. However, because in this system filaments align due to steric hindrance, which has a secondary effect on the microscopic interaction between them, i.e. that filaments must stop when hitting another filament, that will have strong consequences on the symmetry of the emerging patterns.

2.4.1.2 Filaments stop upon collision

We further measured the behavior of filaments upon collision and confirmed that filaments, if they hit an obstacle, *stop* and stay in position. Only eventually, due to fluctuations of their tips resolving the collision, do they eventually align. Figs. 2.6.B shows a time series of $\theta(t)$, where θ is the relative angle between two filaments during a collision. The collisions last 30-60 seconds and end up in a final relative angle of either 0° or 180°. A lag time during which filaments are still in contact but no alignment is yet present is also visible. This behavior stems from motors slipping on the SLB and therefore not being able to push filaments over each other. Thus the nature of the alignment is due to the contribution of a strong steric effect (which does not allow the filaments to crawl over each other) and of thermal fluctuations aligning the tip of the filament with the obstacle. The change in substrate from solid to fluid results thus in an effective nematic interaction with the additional ingredient of stopping upon collision.

This stopping upon collision behavior is a kind of interaction which is usually missing in standard gliding assays on solid substrates. Even when present, motors, during a collision, are usually still actively pushing the filaments thus, if unable to displace it, generating stress in the system. In the case of gliding on a SLB, the motors instead slip on the membrane, which absorbs the stress and filaments stuck in position are not the source of the same amount of frustration in the system. Hence configurations in which one or more filaments are stuck are expected to be more stable on a fluid substrates. Additionally, this stopping behavior is often not included in models of gliding filaments, which usually assume that filaments move at constant speed and change their direction of motion only depending on the strength of their interaction. We will instead see that introducing steric interactions in the system leading to filaments stopping has consequences on the formation of macroscopic patterns.

Indeed, as we have seen from the alignment statistics that the microscopic interaction between filaments is completely nematic already at the binary collision level, we now ask the question: what are then the emerging patterns?

2.4.2 Collective behavior at intermediate densities

We thus raised the surface density to higher values, specifically from $\sigma = 0.18$ filaments/ μm^2 ($O = 0.72$) to $\sigma = 0.83$ filaments/ μm^2 ($O = 3.32$). At these densities, filaments are observed to separate into a low density phase (almost completely devoid of filaments) and a high density one inside collective structures but still glide at a moderate speed of 50 – 100nm/s inside structures

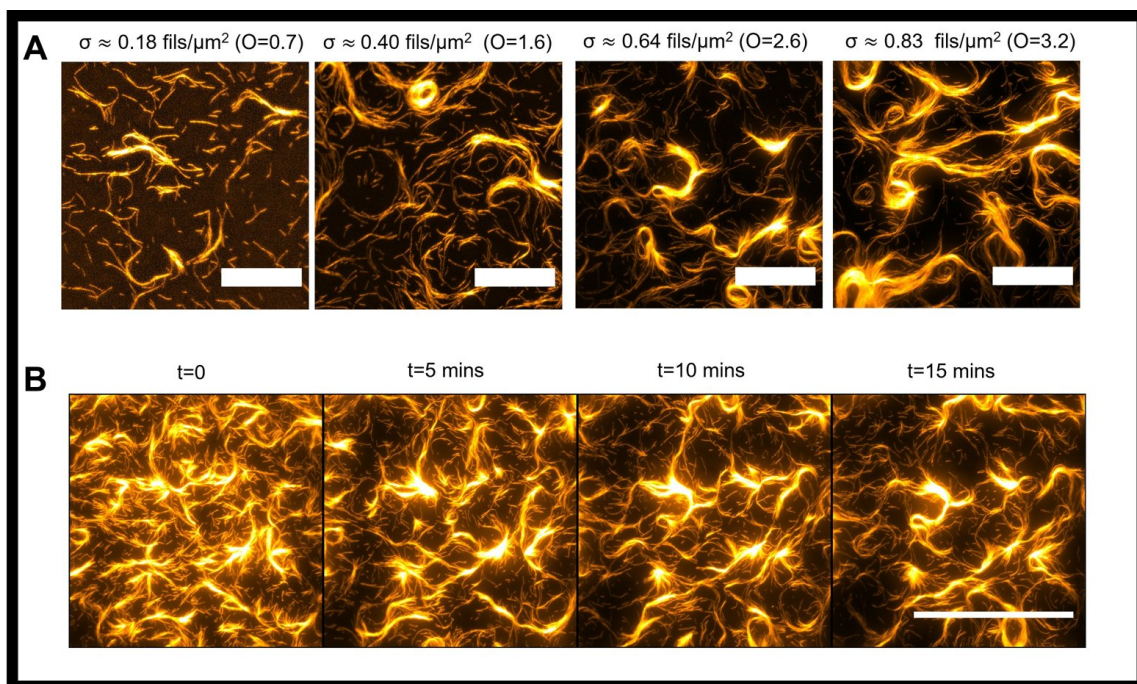


Figure 2.7: **High density pattern formation of gliding actin on a SLB** As the surface density of filaments is increased, collective structures appear, featuring streams and vortices of filaments. A) as the density is increased, patterns start forming (Scale bars: $20 \mu m$) B) time series of the formation of structures at $O = 2.6$, showing aggregation into lanes and vortices (Scale bar: $50 \mu m$).

if the local alignment is high. Figure 2.7 shows examples of the structures forming at different surface densities and a time series showing how they aggregate over time, while Figure 2.8 shows close ups of the formation of such structures and how they separate in space.

In the lower density limit ($\sigma = 0.08$ filaments/ μm^2), filaments start colliding and form small polar clusters (seeds). Depending on the density, seeds can either disassemble or merge together giving rise to elongated structures (streams) or vortices (Fig. 2.7, Fig. 2.8). Figure 2.8.B shows the formation of a stream. Streams are several microns long and are constituted by dozens of filaments laterally aligned. Their thickness, length and persistence in time depends on the surface density σ (See for example Fig. 2.9.A for the thickness of streams). They also are dynamic, can move and change shape over time. On the other hand, vortices are found to be particularly stable as filaments are trapped inside the loop. Differently from the rings observed in [Weber et al. 2015] they are not due to an explicit side cross-linking between filaments but rather to the steric effect due to motors slipping on the SLB (Fig. 2.8.C)

However, when structures collide, steric interactions still play a role at the collective level, and the filaments still stop and accumulate against obstacles. Thus aggregating into collective structures does not enhance the filament's ability to cross over each other. By looking closer at the formation of structures (Fig. 2.8.B-F), we can identify the main mechanisms for collective patterns to arise: seeds can merge into a stream or a vortex (Fig. 2.8.D, E, F), streams can bend into a vortex (Fig. 2.8.C) and individual filaments can join or leave already formed

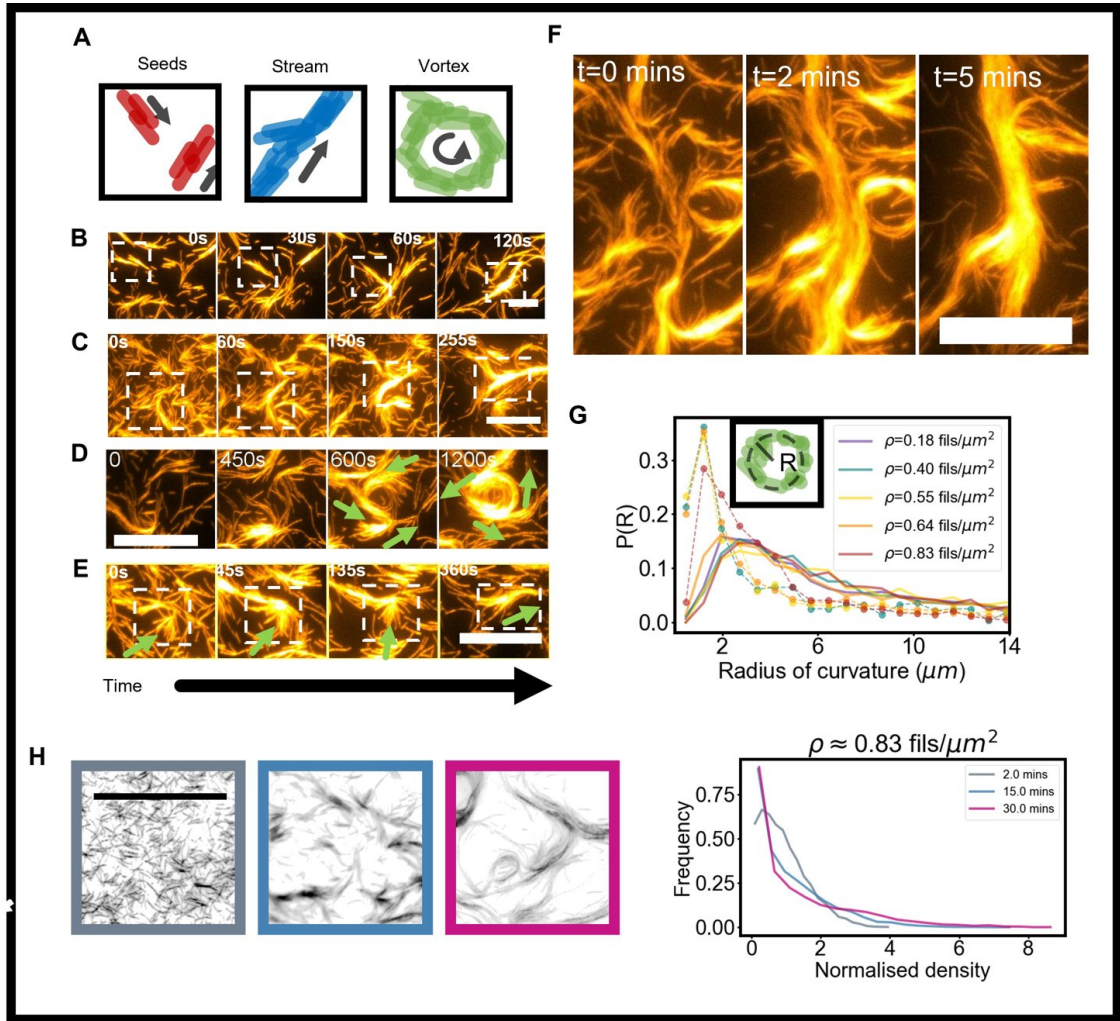


Figure 2.8: **Formation and structure of streams and vortices** A) Schematics of seeds, streams and vortices. B-C) Close up of a stream and a vortex forming. Filaments accumulate in streams at $\sigma = 0.83 \text{ filaments}/\mu\text{m}^2$. Seeds join and leave the stream. Vortices can appear and disappear and sometimes join a close-by stream. (B) A vortex can form by a stream looping on itself due to collisions with other streams (B). Scale bars are $10 \mu\text{m}$. D-G) Details: small seeds of filaments can collide and form streams (D, E, G) or vortices (F). (Scale bars: $10 \mu\text{m}$) Scale bar is $10 \mu\text{m}$.

structures upon collision, but filaments exchange is only permitted on the side of the structures as filaments inside are trapped. Streams can also merge or disaggregate over time. Vortices have a mean circumference ($\approx 10 - 50 \mu\text{m}$) which exceed the individual filaments' length ($\approx 2 \mu\text{m}$), indicating that they are not stabilized by longer filaments but rather by the lateral steric interaction which prevents filaments inside the structure to leave it (Fig. 2.9.B).

In all cases, filaments eventually are almost completely accumulated inside the emerging structures. The separation in space can be quantified by a histogram of the local intensity in space $I(x, y)$, where I is the fluorescence intensity of the images that we assume proportional

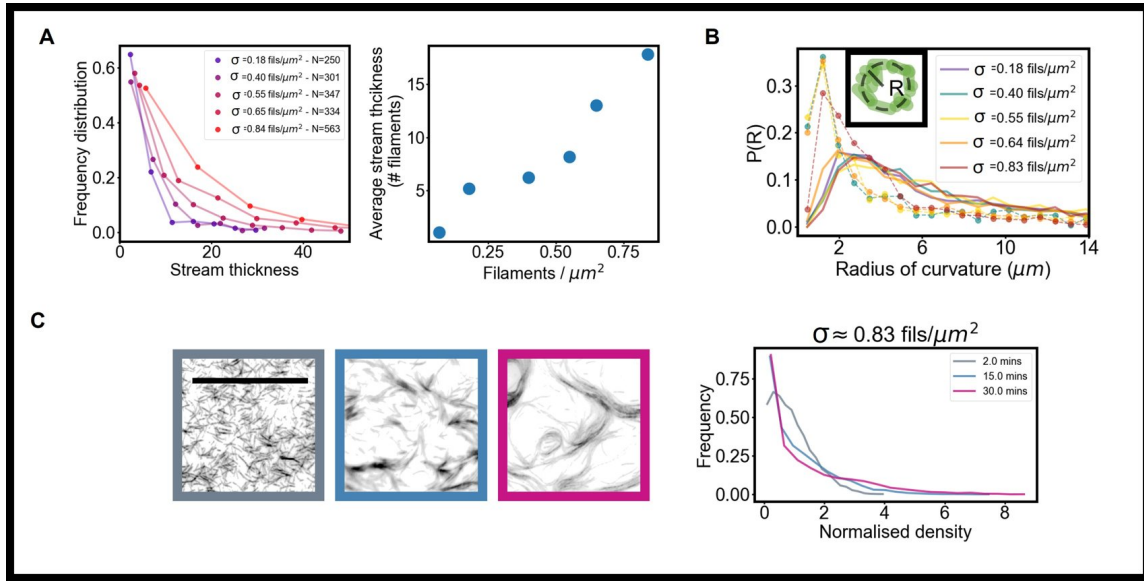


Figure 2.9: **Quantification of structure formation on SLBs** A) Thickness distribution and mean thickness in terms of filaments' number as a function of the concentration of filaments. Streams become longer and thicker. B) Vortices (dashed) and streams (thick) radii of curvatures. This indicates that vortices have diameters much bigger than the individual filaments' size. C) The formation of structures leads to a separation of the filaments density in space over time, from uniform in space to either high or zero. This is visualized by snapshots at different times (left) and by a histogram of the fluorescence intensity at the same times (right) for $\sigma = 0.83$ filaments/ μm^2 . See Methods 4.5 for details.

to the density, as shown in Figure 2.9.C)

In all cases such surface densities are at least one order of magnitude smaller than the ordering threshold found for polar clusters in the case of acting gliding on solid substrate (see section 2.3) and lower than the Onsager ordering threshold for passive rods ($O_{iso} \approx 4.7$). Thus, we confirm that because of activity and of the presence of strong steric interactions, as already predicted in several studies [Peruani, Deutsch, and Bär 2006; Yang, Marceau, and Gompper 2010; Wensink and Löwen 2012; Abkenar et al. 2013] collective pattern formation in this system happens at densities much lower than the Onsager spontaneous ordering threshold and also of the corresponding threshold for actin filaments gliding on a solid substrate [Weber et al. 2015]. This means that increasing the nematic interaction strength significantly lowers the aggregation threshold for the formation of ordered structures.

2.4.2.1 Effect of density and filaments' length

To study the formation of structures as the density and the filaments length are varied, we run the same experiments with different concentrations of actin at different lengths. The results are summarized in Figure 2.10 which shows that, as expected, patterns becomes thicker as the concentration is increased, but also that more vortices appear as the filaments get longer and hence effectively more flexible. Thus one sees that the morphology and stability of emerging structures depends on both the surface concentration and the filaments length. While the O -

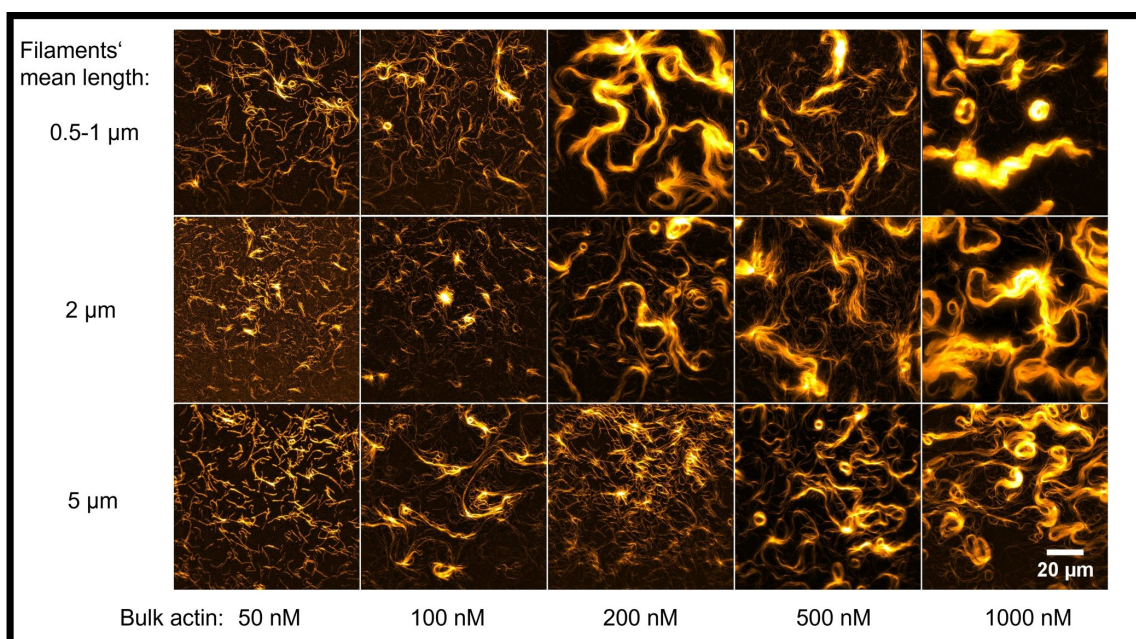


Figure 2.10: **Phase diagram of structures on SLB:** As the filaments' length and concentration is changed, the formation of structures is affected. Higher concentrations lead to longer, more stable, thicker patterns. Longer filaments lead to more vorticity.

parameter aggregates these two values to give a reference with respect to the passive aggregation threshold, the two parameters alone influence the final shape of the patterns. Less dense systems are in general more unstable than denser ones, with streams forming and disaggregating over time and less vorticity present.

2.4.3 Collective behavior at higher densities

We can further increase the surface concentration.

To do that, we vary slightly the incubation protocol so that actin filaments are incubated together with ATP and MC at the final step. This means that filaments sediment and move over time rather than being bound on the surface from the beginning. The main differences are that higher concentrations can be reached, as filaments by moving free additional space on the surface, and that filaments can start aligning progressively (Fig. 2.11.A).

The outcome is that we reach surface densities higher than $\sigma = 5$ filaments/ μm^2 ($O = 20$) (i.e., higher than O_{iso}). The filaments initially start forming thick streams but they again very quickly separate into an empty and a dense phase. Because of the high concentration, filaments in the dense phase locally align but mismatches in the orientation can be present. By looking closely at the initial stages of sedimentation it can indeed be noticed how filaments first aggregate in aligned streams but that afterward streams with different orientations can collide. Because of the higher density with respect to the previous assay, streams are often unable to merge and rather give rise to alignment mismatches. Where this happens and streams with different

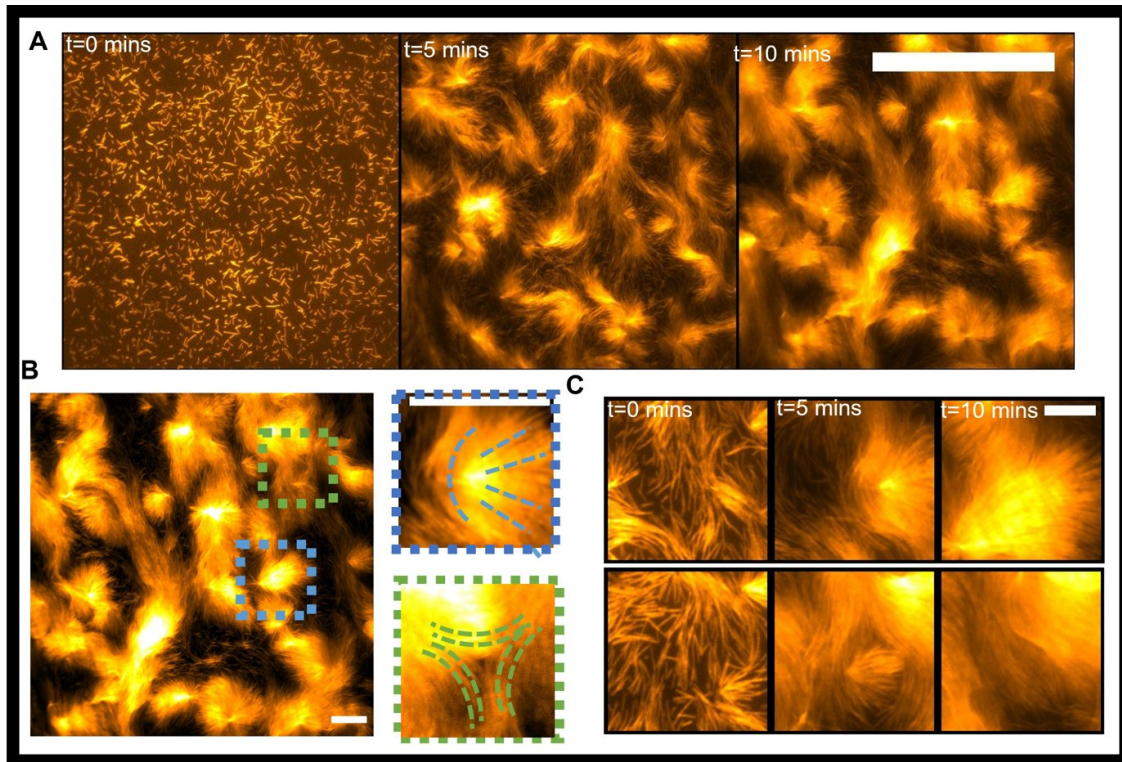


Figure 2.11: **High density sedimentation leads to nematic-like structures comprising $\pm 1/2$ defects**
 A) Sedimenting $1 \mu M$ of actin over time leads to the appearance of a very dense, nematic-like phase and a low density, almost empty phase (Scale bar: $50 \mu m$). B) In the high density phase, where alignment mismatches are present in the dense phase, nematic defects of charge $\pm 1/2$ are present. (Scale bar: $10 \mu m$) C) Time series of defects formation and dissolution (Scale bar: $5 \mu m$). Nematic defects in this case can appear (middle frame) and dissolve over time as they are not constrained by conservation of the total charge since they are isolated in space. Negative defects disappear, positive defects turn into polar comets.

orientations meet, there is indeed a discontinuity in the local alignment, i.e., a topological (or nematic) defect. Both $+1/2$ and $-1/2$ defects (see Section 1.3.4) are clearly recognizable. More in detail, streams which are already particularly bent are very effective in trapping other streams in the bend and there form nematic defects (Fig. 2.11.B).

In common passive and active nematic materials defects are known to form and dissolve in pairs as they have to maintain the total charge and the interaction between defects is dictated by the elastic energy of the nematic material. In this case, however, because the material is only locally nematic and rather composed of different unconnected patches, separated by empty space, there is *no* long range order and defects, being formed by gliding filaments, can transiently form and dissolve over time even independently, without conserving any charge (Fig. 2.11.C). The formation of such transient defects can however still influence the formation of patterns.

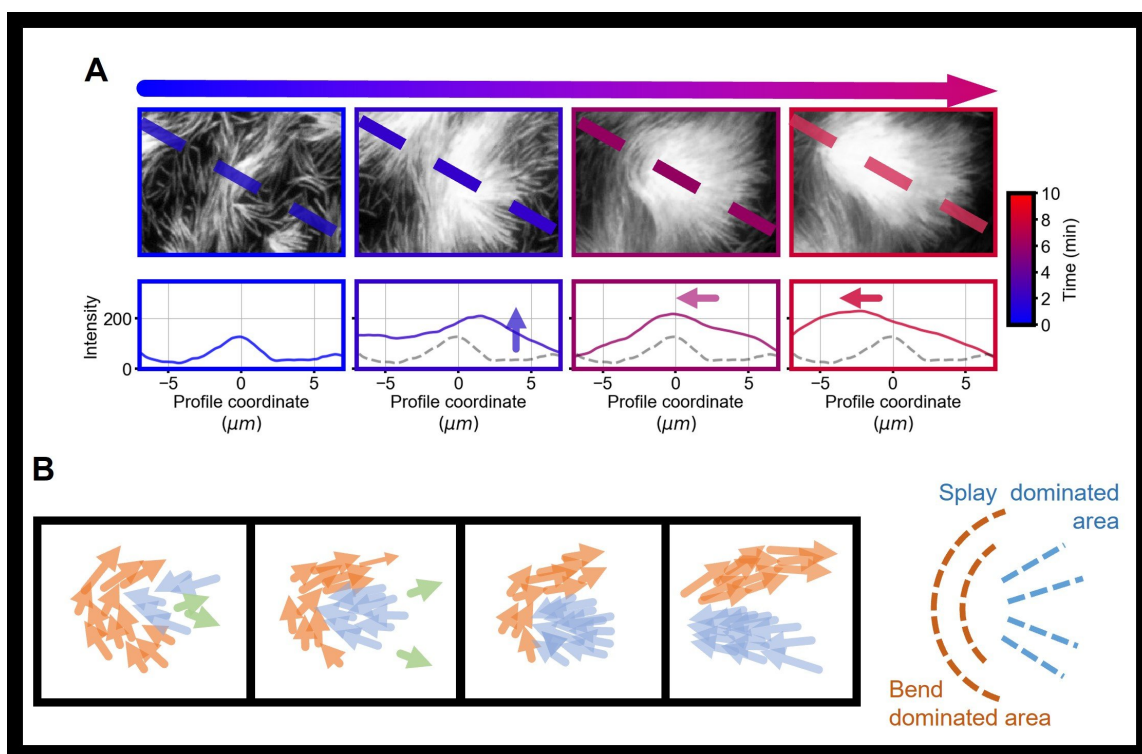


Figure 2.12: **Nematic wedges accumulate and polar sort filaments** A) Formation of a $+1/2$ nematic defect and successive accumulation and ejection of polar filaments. The intensity along the dashed line is plotted, with the intensity at time 0 as a reference, showing accumulation and then motion of filaments. B) schematics of accumulation of filaments in a nematic wedge and successive ejection of a polar comet. On the right, the $+1/2$ defect conformation is shown highlighting the splay- and bend-dominated areas.

2.4.3.1 Nematic wedges lead to polarity sorting

We found that $-1/2$ nematic defects simply form and dissolve as the streams that compose them simply glide away. Conversely, $+1/2$ defects, because they have a wedge-shaped conformation which is known to trap active particles [Di Leonardo et al. 2010; Kaiser, Wensink, and Löwen 2012], are more stable and lead to an accumulation of filaments in the core of the defect. This can be easily understood if one thinks of the microscopic steric interaction: the shape of the $+1/2$ defect and its surrounding can be thought of as if composed of two parts, one which is splay-dominated, i.e. funnel-shaped composed of filaments pointing towards the core, and one which is bend-dominated, surrounding the defect's core on the opposite side (See Fig. 2.12.B, right). These two parts are aligned perpendicularly to each other and are separated by the defect core. Filaments in the bend-dominated side can flow around the defect as they are locally aligned. Instead, filaments in the splay dominated part end up getting stuck if gliding towards the defect's core as they are hindered by a perpendicular lane of filaments. Thus $+1/2$ defects constitute a filament trapping mechanism, which we term *nematic wedge* which, differently from the previous particles-trapping systems, is self-organized by filaments themselves which both trap and get trapped depending on the local alignment. The wedge- or funnel-like shape

of the defect accumulates filaments towards the core, but the defect's global conformation, with a perpendicular stream hindering incoming filaments, stops them, preventing their escape. Additionally, only filaments oriented *towards* the core and entering the funnel are captured and accumulated.

Eventually, however, the defect can dissolve as the bend-dominated side flows away and the filaments previously trapped can start moving again. This gives rise to *comet*-like stream which move together but keep the comet-like shape of a positive defect. As they have been trapped the concentration of filaments emerging from the defect is higher than it was previous to trapping and, more interestingly, they are all aligned in the same direction as filaments previously moving in opposite directions could escape the nematic wedge. Streams emerging from $+1/2$ defects also are indeed completely polar over a big length-scale (several microns). Thus transient $+1/2$ defects act as an efficient polar-sorting mechanism leading to strongly polar structures. The mechanism is sketched in Figure 2.12.

2.4.4 Polarity of observed structures

The observation of polar patterns emerging from nematic defects is striking. Indeed, given what discussed in section 2.3 we would expect the microscopic nematic symmetry to lead to the formation of nematic structures. Even the tiny polar bias present, forcing filaments to travel together for longer times when colliding polarly, was shown to not be enough for the emergence of polar structures if the interaction between filaments is strong enough [Huber et al. 2018]. By then looking back at the structures arising for lower surface density, it is clear instead that even in that case streams and vortices are composed of filaments moving in the same direction, i.e., they are all polar.

To gain deeper understanding, we performed fluorescence recovery after photobleaching (FRAP) experiments at all densities. A rectangular region of interest (RoI) along the collective structures was bleached with a high intensity laser and its recovery was observed. RoIs were chosen to be along the main direction of streams and vortices. By observing the recovery of the fluorescence on both sides of the RoI one can compute a polarity parameter

$$p = \frac{|I_{left} - I_{right}|}{|I_{left} + I_{right}|} \quad (2.3)$$

where I_{left} and I_{right} are the fluorescence intensities on the two sides of the RoI. Of course if recovery is symmetric as filaments move in both direction we expect $I_{left} = I_{right}$ and thus $p = 0$. On the other hand, if filaments move in only one direction (say, from left to right) then $I_{right} = 0$ and $p = 1$. Figure 2.13 shows the results for different structures. It is striking that at all densities we measure values of $p \approx 1$. Streams are polar, although they could be formed by two parallel streams moving in opposite direction. Vortices show a particularly high value of p . Comet-streams are also strongly polar, as already mentioned.

How can then a nematic microscopic symmetry give rise to polar structures? We then looked at polar biases present in the system. A trivial one, is that filaments colliding polarly will keep moving in the same direction for some time whereas anti-polar collision lead to the immediate separation of the couple (Fig. 2.14.A). This bias is always present in active matter system aligning. However, we attribute the strong polar sorting to the presence of the steric

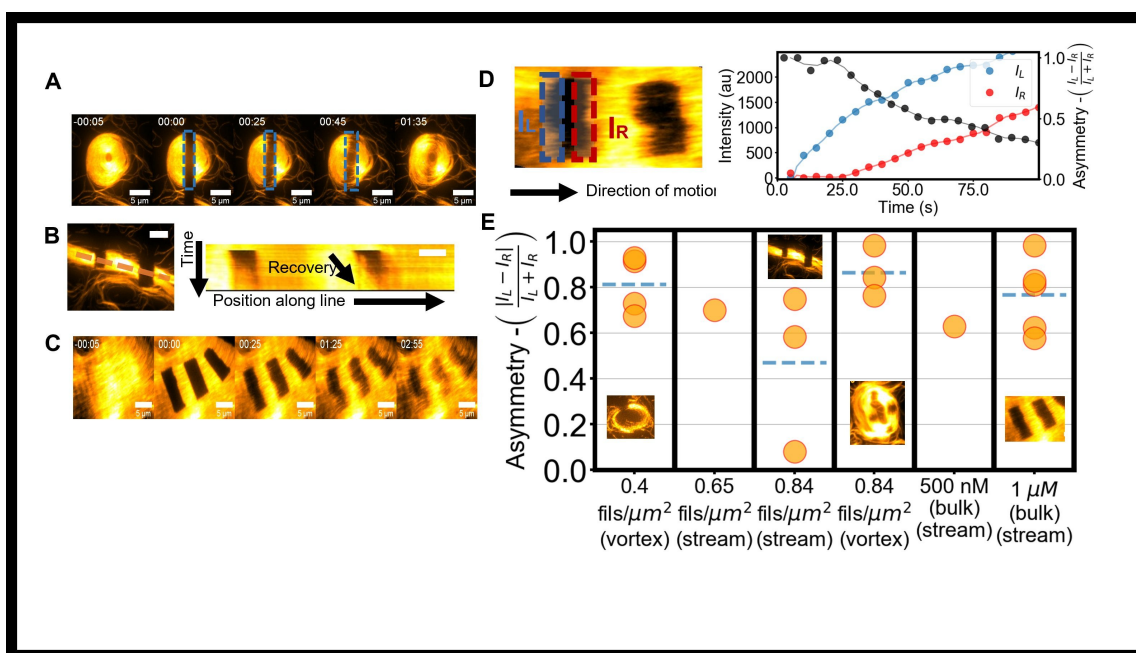


Figure 2.13: **Asymmetric fluorescence recovery indicates polarity** By performing FRAP experiments we can measure the polarity of observed structures. A-C) FRAP experiments indicating asymmetric recovery for a vortex (A), a stream, including its kymograph (B) and a comet lane (C). D) schematics of the measurement: the recovery of the bleached region is measured at two opposite positions I_L and I_R and the parameter p is computed. Both p (black), I_L (blue) and I_R (red) are shown in the plot. E) results of the computation of p , indicating that all structures at all densities have asymmetric recovery and are hence polar. Scale bars: $10 \mu m$.

interaction in the system forcing filaments to stop against an obstacle. As only filaments moving against the obstacles are trapped, whereas those moving in opposite direction can glide away, obstacles give rise to the accumulation of filaments oriented in the same way which, once free, move coherently (Fig. 2.14.B). This behavior can be observed with as little as 4 filaments (Fig. 2.5.C) but it gets more dramatic as more filaments are present.

Streams emerging from $+1/2$ defects (comet streams) are particularly thick and polarly oriented. We also note that even at lower density, locally, defect-like structures form and act as nematic-wedges, explaining the polar-sorting of filaments even at filaments densities where the appearance of defects would not be expected in the passive case (Fig. 2.14.C). Thus this polar sorting mechanism based on steric interactions is effective at all densities and can take advantage of transient, wedge-shaped structures forming when filaments collide to give rise to strongly polar structures. For this reason, $+1/2$ nematic defects are a particularly good polarity-sorting conformation (whereas $-1/2$ defects play no role in this sense).

2.4.5 Discussion

The main results of this Section are that actin filaments on a SLB exhibit polar patterns despite the low activity and despite a *nematic* microscopic symmetry. It is the presence of a strong steric interaction that biases pattern formation towards the formation of polar structures as

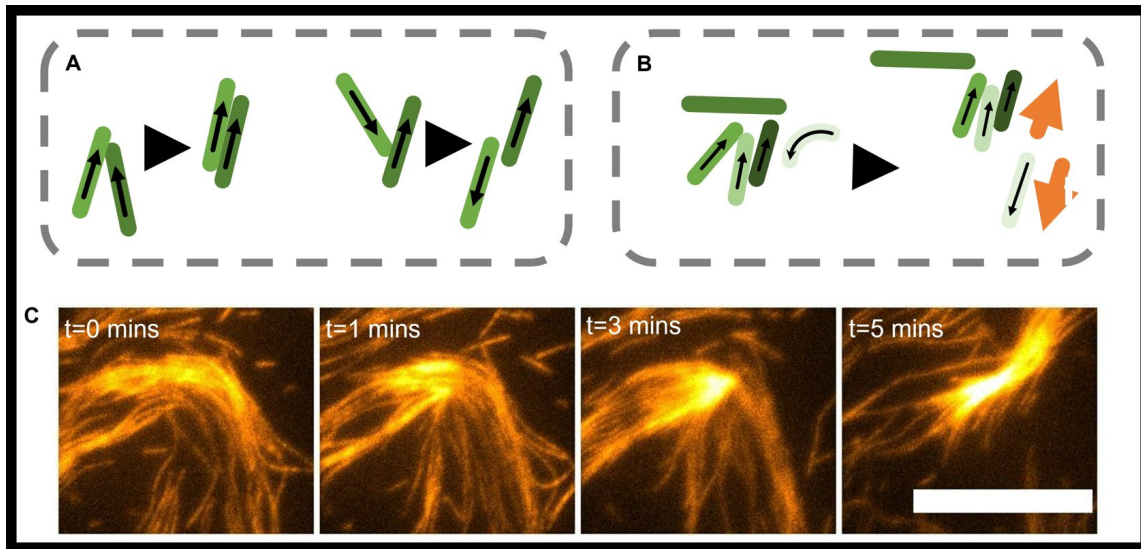


Figure 2.14: **Mechanism of polarity sorting due to steric interaction** A) Already at the single filament collision, there is a bias towards polar order due to filaments colliding polarly moving afterwards in the same direction for a longer time. B) Steric interactions lead to accumulation of filaments against obstacles. All accumulated filaments have the same polarity and when the obstacle vanishes move in the same direction. C) Even at low density, defect-like trapping conformations can be observed (Scale bar is $10 \mu m$).

filaments accumulate against obstacles depending on their orientation. This polarity-sorting mechanism is thus arising from a self-organization of active filaments.

Patterns similar to that observed in the intermediate density phase had been observed in different systems, such as the treadmilling bacterial filament FtsZ [Caldas et al. 2019], with microtubules on a patterned surface [Tanida et al. 2020; Tsitkov et al. 2020] and in simulations of semi-flexible active filaments in the presence of steric interactions [Jung et al. 2020; Moore et al. 2020]. These results confirm that steric interactions are an important factor that needs to be taken into account when developing a theory of collective pattern formation. In particular, the very realistic simulations in [Jung et al. 2020] confirm that the shape of the structures we observe is tightly connected with actin's properties such as its flexibility and that they emerge if strong steric interactions are present². That a nematic microscopic symmetry could lead to polar structures, particularly in the form of flocks of particles, had been reported but polar order on a global scale had been found to be unstable because of the stress accumulated in alignment defects [Weitz, Deutsch, and Peruani 2015; Bär et al. 2020]. In this case however, as the membrane can act as a buffer for the accumulation of stress, polar patterns are supposedly more stable. Thus the substrate, which is usually modelled as a rigid one allowing for the non-conservation of momentum during collisions, must play a role in the emergence of collective patterns.

This system also features the formation of topological defects, abundantly studied in the case of active microtubule fluids [Sanchez et al. 2012; Keber et al. 2014; Shankar et al. 2018; Shankar

²This is currently being explored in a project in preparation with Taeyoon Kim's group at Purdue University.

and Marchetti 2019] (and we refer to Section 3.2) but in this case the defects are isolated and thus free to form and dissolve individually rather than being forced to act in pairs. The total topological charge of the system is not conserved because of the absence of boundary conditions. This is also striking as nematic defects are not predicted to emerge for polar systems. They indeed are only transient and are due to the locally-nematic nature of the system, together with the fact that because of the membrane such conformations are not under stress, as it would be if the motors would try to keep pushing, thus destabilizing the defect. The formation of nematic wedges is thus a previously unobserved pattern formation mechanism. Bacteria swimming in a passive nematic have been found to accumulate in $+1/2$ defects [Genkin et al. 2017] but the formation of resulting polar patterns was not reported. We then consider nematic wedges a previously unobserved polarity sorting mechanism. In particular, nematic wedges have a connection with the trapping transition observed for shaken granular rods [Kumar et al. 2018] and is analogous to the concept of motility-induced phase separation (MIPS)[Cates and Tailleur 2015; Großmann, Aranson, and Peruani 2020; Shi and Chaté 2018]. This latter consists in the accumulation of particles in low mobility regions and, in the case of purely steric interaction it has been usually considered specific to spherical particles as elongated ones can reorient and keep moving, solving the local traffic jam via a transition to a nematic aligned state. In this case however, a MIPS-like transition is observed but rather than to the local density it is related to the local nematic alignment: filaments in aligned dense regions can still move, but filaments in the presence of orientation defects are trapped and thus accumulate. Interestingly, half-integer defects are not expected in polar system and indeed they only form transiently and eventually dissolve. Still, they act as gates that turn a nematic symmetry (which predicts $\pm 1/2$ defects) into a polar one (and this will be discussed even further in the next Sections).

Summing up, what we have shown in this Section is how delicate (and surprising) the transition from a microscopic interaction to a macroscopic order can be if one does not pay attention on hidden biases. In this case, indeed, a significant role is played by the formation of local defect-like conformation, whose shape, particularly effective in polar-sorting filaments, is dictated by both the material properties of the filaments (their flexibility, size, etc), by the topological constraint imposing a precise shape to nematic defects and finally by the steric interaction between them, enforcing alignment. Neglecting one of these effects and only focusing on the observed microscopic nematic symmetry, as tempting as it is, would fail to predict all of the observed behavior. The actin gliding assay on a SLB can thus be considered a model system to study these behaviors in a controlled setting and to improve our understanding of the transition from micro- to macroscopic.

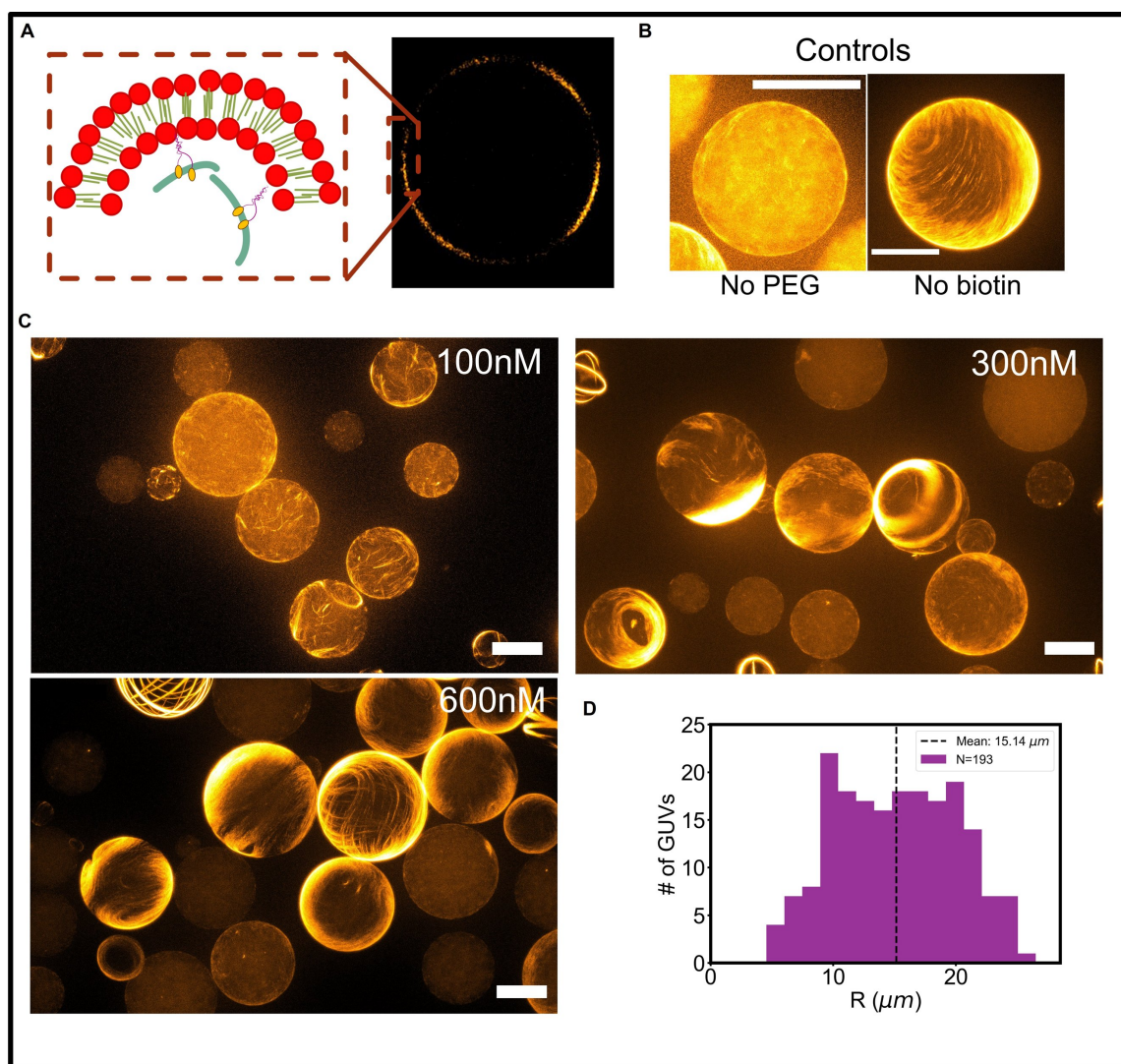


Figure 2.15: **Schematics of the GUV-filaments system and examples** A) We bind HMM inside spherical GUVs using biotin-streptavidin. Upon ATP addition, the filaments assemble into patterns visible as clear bands on the equatorial plane of the GUV. B) Control experiments show instead no organization of the actin, but only accumulation on the membrane in the presence of PEG. C) Microscopy images of GUVs at 100, 300 and 600 nM, indicating the formation of patterns. At low density, only small streams are visible. At higher density, vesicles with vortices and more complex patterns are visible. D) Radius distribution of GUVs ($N=193$), showing a mean radius of $\langle R \rangle = 15 \mu m$. Scale bars are $20 \mu m$.

2.5 Gliding inside a giant unilamellar vesicle

Gliding actin filaments on supported lipid bilayers have been shown to exhibit polar behavior. One limitation of the assay is the fact that one can only look at one (or multiple individual) region(s) of the sample and thus lacks a global description of the system. Additionally, the

planar dimensionality of the system, while making observation and theoretical description easier, lacks biological relevance as cells are three-dimensional and the cytoskeleton is in a confined environment (the cell membrane). Additionally, theoretical and *in silico* works have presented the possibility that polar particles under spherical confinement would result in the formation of stable polar bands [Sknepnek and Henkes 2015; Shankar, Bowick, and Marchetti 2017]. Some of these behaviors do not have a clear planar counterpart.

To address these limitations and thus study polar semiflexible filaments with steric interaction under confinement and in a different topology, we perform gliding actin experiments on the inside surface of giant unilamellar vesicles³. The aim of this chapter is to underline how, as filaments glide on curved geometries, steric and topological constraints start affecting the formation of patterns by imposing rules, that would not be present on a SLB, on the alignment of filaments.

2.5.1 Encapsulation of actin and motors in a GUV

Vesicles are produced with the cDICE technique [Abkarian, Loiseau, and Massiera 2011], described in more detail in Methods 4.2.0.2. GUVs are composed of 5% biotinylated lipids and contain motors (150 nM HMM), actin filaments at an actin concentration of c_0 (with variable mean length L , with $L = 0.75 \mu m$ unless specified) and 0.6 % PEG(36K) as a depletant⁴. Motors can bind to the to inner leaflet of the GUVs and filaments, pushed on the membrane by PEG, can bind and glide propelled by HMM. A schematic of the system is shown in Figure 2.15.A.

The produced vesicles have an average radius of $\langle R \rangle \approx 15 \mu m$ (as measured on $N = 193$ GUVs, see Fig. 2.15.D). Each experimental condition is repeated 1 to 3 times, each repetition leading to 5-10 confocal stacks and several epifluorescence images. The precise composition and setup is given in 4.4.

First, we tested the passive behavior of the system by encapsulating motors (150 nM) and filaments (600 nM) without PEG (so that motors still bind to the membrane) or without biotin lipids (so that motors do not bind) and imaging GUVs after 45 minutes to allow for equilibration. Without PEG, actin filaments either remained in bulk while only a small fraction is captured by motors. With PEG and without biotin, they accumulated on the membrane due to depletion (Fig. 2.15.B). In all cases, without activity, no patterns were observed. Only, over time, accumulation in a nematic layer is observed in the presence of PEG and slight depletion-induced bundling.

³Most of these experiments have been carried out by Alice Yu De La Trobe, under my supervision. She deserves a good deal of the credit! Dr. Chiao-Peng Hsu also took care of this experimental system and helped framing the results.

⁴A fraction of experiments are also done using 0.2 % MC and that is explicitly mentioned in the text. Results are comparable.

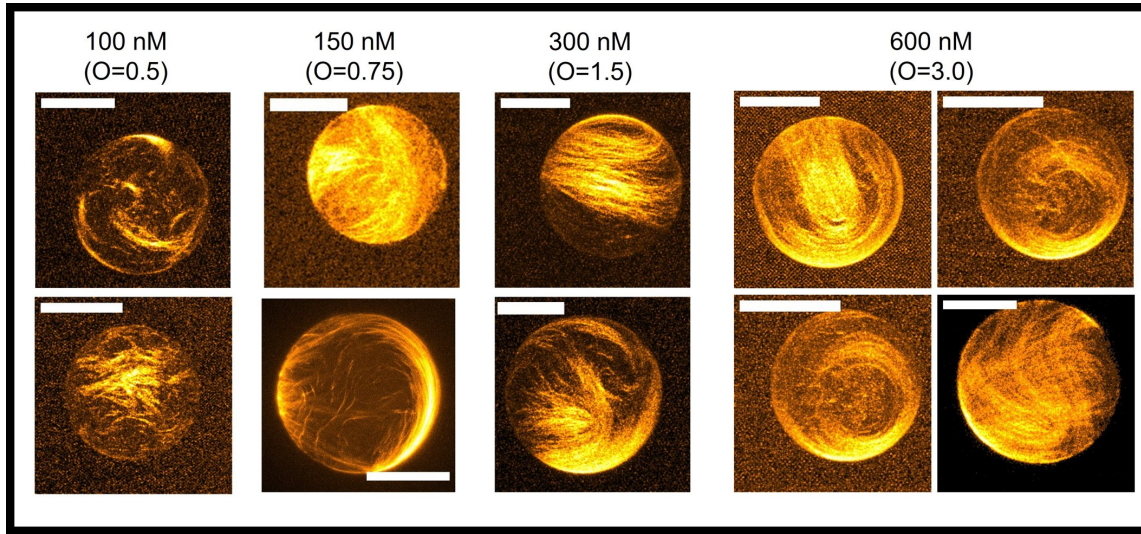


Figure 2.16: **Phase diagram of GUVs containing gliding filaments** GUVs containing respectively an actin concentration of 100, 150, 300 and 600 nM exhibit different patterns. At low density, streams form. As the density increases, comet-streams start emerging and often converge into a vortex. At 600 nM a fraction of the GUVs is jammed, with GUVs exhibiting a well known $4 \times \frac{1}{2}$ defects conformation. Scale bars are 20 μm .

2.5.2 Filaments gliding on a GUV form polar patterns

2.5.2.1 Phase diagram of patterns

Upon ATP addition, motors started propelling the filaments. At the observed densities ($c_0 = 100, 150, 300$ and 600 nM) vesicles immediately start showing the formation of patterns (Fig. 2.15.C).

We observed that the filaments move at speeds in the $v \approx 50$ nm/s range (notice that a speed lower than that observed on SLBs is expected due to the GUVs' higher fluidity). This means that in order to complete a full circle at the equator of the GUV filaments need a time $\tau \approx \frac{2\pi\langle R \rangle}{v} \approx 30$ minutes (for a $15 \mu m$ GUV). We then settled for a observation frame-rate of 30-60 seconds, depending on the number of observed GUVs, and imaged the vesicles for 60-90 minutes.

As a general order parameter we can use again the scaled surface density $O := \sigma L^2$ defined in section 1.3.2.3. Because in this case, due to the encapsulation procedure, we can only control the bulk density c_0 of actin, we can rewrite our expression for O assuming all of the actin is polymerized into filaments and from the volume it accumulates on the GUV's surface. Thus, for a vesicle of radius R filled with a concentration (in micro-molar) $c_0[\mu M]$ of actin with (equal) length L

$$O = \sigma L^2 = \frac{c_0[\mu M] N_A \frac{4}{3} \pi R^3}{4\pi R^2 M_f} L^2 \approx 0.6 c_0[\mu M] R[\mu m] L[\mu m] \quad (2.4)$$

where N_A is Avogadro's number and M_f is number of monomers per filament⁵. The prefactor in the final expression takes care of dimensional conversions. The final result allows to compare

⁵The O parameter is calculated assuming each monomer occupies ≈ 2.8 nm along the filament, so that

GUVs of different size and in different conditions⁶. Fig. 2.16 recapitulates the behavior of the system at different values of the O -parameter when varying only the filaments density. Since $L = 0.75 \mu m$ then, for vesicles with $R \approx 15 \mu m$, $O \approx 5c_0[\mu M]$ so that, at the used concentrations, $O \approx 0.5 - 3$, again lower than the passive threshold $O_{iso} \approx 4.7$ and comparable to results in the previous Section about gliding on a SLB.

Again, we perform a density series (Figures 2.15.C and 2.16). In the low density limit ($c_0 = 100 nM$ actin, $O \approx 0.5$) the filaments are initially homogeneously dispersed but slowly condense into higher-density regions that move on the surface of the GUV. The resulting patterns are analogous to seed/small streams as described in the previous Section. We then observed the behavior and shape of these patterns in different conditions by varying the concentration.

As the density increases, more complex structures emerge, including longer streams, comet-like streams, transient nematic defects and vortices. The structures resemble those observed in the previous Section despite the different topology, with the main difference that, under confinement, structures have an additional tendency towards accumulating rather than dispersing. This seems to slightly lower the aggregation threshold as patterns first emerged on a SLB at $O \approx 0.7$ against $O \approx 0.5$ here.

At $O > 0.7$ ($c_0 = 150 nM$) stable streams are visible and the morphology of patterns starts becoming more variable, while vortices start appearing. At $c_0 = 300 nM$ ($O \approx 1.5$) vortices are the most likely structure whereas at $c_0 = 600 nM$ ($O \approx 3$) the observed morphologies include vortices, bands and vesicles taking the standard $4 \times \frac{1}{2}$ defects configuration expected for a nematic material on a spherical topology (see Section 1.3.4). This latter observation is due to the high packing fraction, approaching O_{iso} , causing the filaments to almost fully covering the surface and getting jammed with each other.

2.5.2.2 Analysis of pattern formation in GUVs

The formation of patterns in GUVs indicate that the microscopic alignment rules studied on a planar geometry in the previous Section also apply in a different topology: filaments stop upon collision and align. This leads over time to a striking phase separation of the density in space, with the filaments concentrating in patterns and the rest of the GUV's surface remaining empty. Figure 2.17 shows times series of the pattern forming at different densities and how each different pattern (streams, vortices, etc.) appears at different densities after having equilibrated (ca. 60 minutes after encapsulation).

The progressive alignment of filaments causes the formation of seeds and small streams observed at $c_0 = 100 nM$. While no clear motion is visible at the beginning, filaments quickly merge into clear streams. Streams again can move and glide on the surface of the GUV. Because of their small size they do not manage to loop on themselves and rather glide around the GUV (Fig. 2.17.A). Similar behavior is observed at $c_0 = 150 nM$ with longer streams appearing and sometimes merging with each other. Vortices are present but rare. At $c_0 = 300 nM$ vesicles start exhibiting consistently the presence of vortices arising from streams merging. As the total

$M_f = L/2.8nm$

⁶We note that, as we are encapsulating filaments and not monomers, the relative error on the number of filaments inside each GUV is bigger than expected in the case of monomers, as each filament aggregates a big number of monomers. So the above computed parameter is only an estimate.

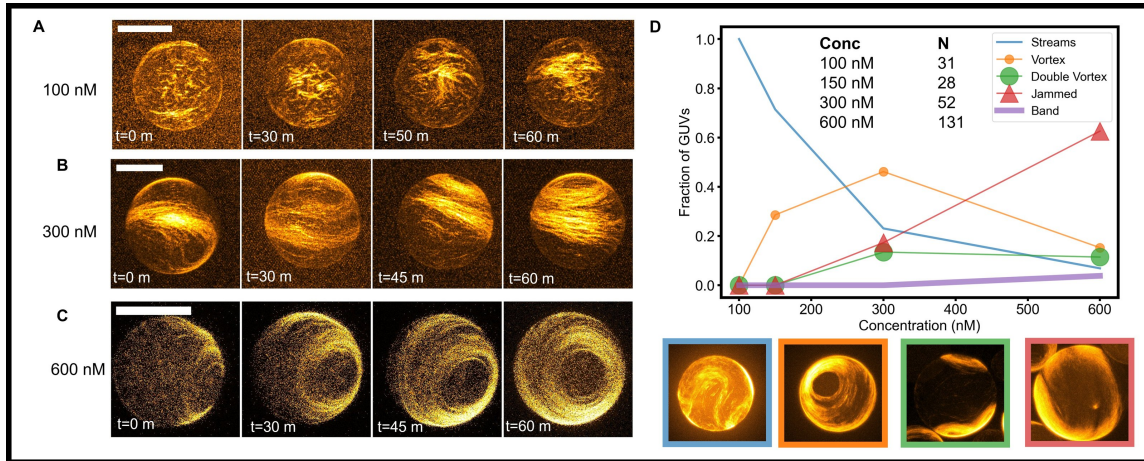


Figure 2.17: **Time series of pattern forming in a GUV** A-C) Over time, patterns appear. At low density, streams are present (A). At higher densities, streams form and merge into vortices also form (B, C). D) Fraction of GUVs observed in a given state as the density changes, showing how streams are soon dominated by vortices which however soon turn into a jammed state. Bands are rarely observed. Close ups on the bottom indicate the different structures. A band-forming GUV is shown in Fig. 2.19. The number of analysed GUVs appears in the inset. Scale bars are $20 \mu m$.

length of the stream is smaller than $\approx 2\pi R$ vortices loop closer to one of the poles and not on the equator. Additional streams can merge with the vortex, if they are gliding in the same direction, or rotate in opposite direction forming a vortex/anti-vortex couple (Fig. 2.17.B). Two different, independent vortices, one at each pole is also a possible configuration (see for example the inset in Fig. Fig. 2.17.D). A similar behavior is observed for $c_0 = 600 \text{ nM}$ with bigger vortices forming (Fig. 2.17.C). However, at this density, often the filaments rather end up jammed in a nematic-like configuration, with filaments all locally aligned with each other but with the presence of nematic defects (because of topological constraints fixing the total charge to $+2$). While the configuration does slightly evolve over time, filaments mostly remain stuck. This is due to the strong steric interaction present in the system, as previously discussed, acting in combination with topological constraints on the filaments' alignment forcing them in an jammed configuration (see below for a more detailed comment).

It clearly appears from the probability of observing each structure at a given density (Fig. 2.17.D) that streams dominate at low density, but very quickly evolve into vortices. Vortices are often predicted to be a stable pattern for polar particles in a spherical topology, however in this case, as the density increases, the system first starts separating in multiple vortices (vortices and double vortices are discussed in the following section) and then jams (jamming is discussed further on), with a polar band spanning the whole vesicle being the most stable pattern and yet the least observed one. This is due to steric interactions preventing the system of filaments to reach the final vortexing state. To understand how that happens, we look more closely at the formation of patterns in GUVs.

2.5.3 Mechanisms of pattern formation

Patterns appear to form with mechanisms analogous to what observed on SLBs. In particular, the presence of $\pm 1/2$ transient defects is again observed and their role (*nematic-wedge* mechanism) seems to be conserved. Already at $c_0 = 150 \text{ nM}$ the formation of transient $+1/2$ defects can be observed. However, because of the above mentioned effect of both confinement and topology on the formation of structures, some differences must be noted.

2.5.3.1 Nematic wedges and polar sorting in GUVs

As expected, also in this case structures emerging are polar, with filaments clearly travelling in the same direction. The formation of patterns in GUVs indicate that the microscopic alignment rules studied on a planar geometry in the previous Section also apply in a different topology: filaments stop upon collision and align.

Streams can be obstructed by perpendicular-gliding filaments and accumulate in place until the obstacle is removed and a comet-stream emerges. The mechanism of nematic wedges (already discussed, see Figures 2.12 and 2.14) is shown in action in a GUV in Figure 2.18.A at $c_0 = 150 \text{ nM}$. Again, the nematic-wedge mechanism can act at densities much lower than the isotropic-nematic transition threshold, as it is based on the formation of local transient defect-like looking conformations which accumulate filaments. However, it is still in action at higher densities. Figure 2.18.B shows defects forming at higher densities ($c_0 = 300 \text{ nM}$). It also shows that (transient) $-1/2$ defects are present. Their observation is however unexpected in a spherical topology as they are not energetically favored, the total charge (in a nematic material) having to equal $+2$. As shown in Figure 2.18.B, $+1/2$ defects again lead to the formation of truly comet-looking streams at higher densities, whereas $-1/2$ defects are only transient. The emerging structures then further evolve. As an example, Figure 2.18.C shows the same vortex formation of Figure 2.17 on a side view taken from a confocal 3D reconstruction. This other point of view shows how, under the vortex, a comet streams form and then travels on the side until it joins the main vortex. Because of confinement, thus, streams have a stronger tendency to coalesce into vortices.

2.5.3.2 Vortex formation

To investigate better the polarity of the observed structures, we perform equirectangular projections so that for each point (R, ϕ, θ) on the surface of a GUV with radius R , where ϕ and θ are the the polar angles in spherical coordinates, the intensity of such point is projected on a plane with coordinate $(R\phi, R\theta)$.

The projection is carried out using the software Map32D [Sendra et al. 2015]. The equirectangular projection causes a distortion for points close to the poles but allows to visualize in a single 2D plane the full behavior of the spherical GUV. These projections allow to better understand the vortex and the pattern formation process in general. Figure 2.19.A shows the formation of a vortex in two different GUVs ($c_0 = 600 \text{ nM}$) with an equirectangular projection at different times. The formation of comet-like streams is evident in the beginning. Those streams then travel on the GUV until they either loop on each other, forming a vortex, or

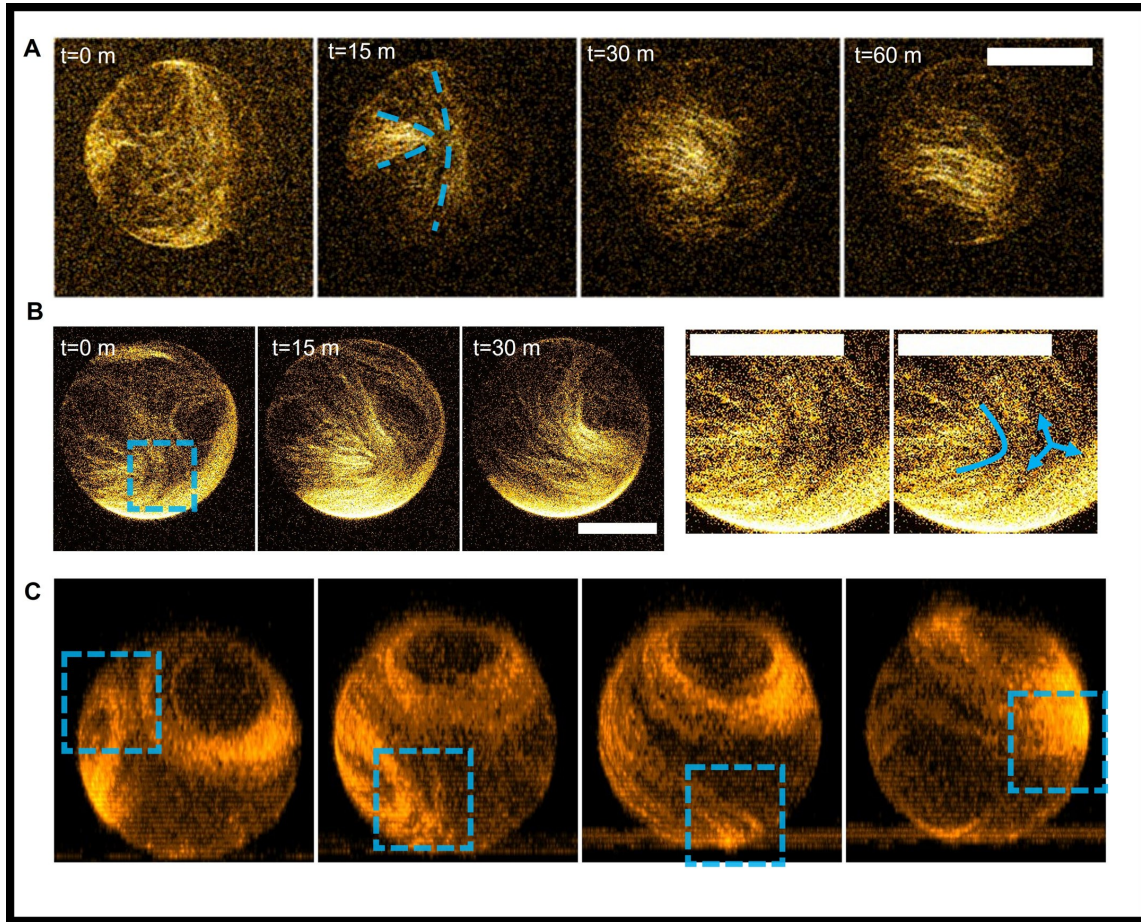


Figure 2.18: **Nematic defects and nematic wedges in GUVs** Nematic wedge-based polarity sorting is present also in the GUV system. A) Time series of a GUV at $c_0 = 150$ with a nematic wedge forming and turning into a polar stream. B) Nematic wedge forming at $c_0 = 600 \text{ nM}$. Close up shows both a $+1/2$ and a $-1/2$ nematic defect are present. C) The same GUV as Fig. 2.16.C at $c_0 = 600 \text{ nM}$ for a vortex. A nematic defect, on the side, turns into a comet-stream and joins the vortex. Scale bars are $20 \mu\text{m}$.

they join an already existing one. The GUV on the right show the formation of two concentric vortices with different rotation direction. Fig. 2.19.B, D and E show other examples ($c_0 = 300$ and $c_0 = 600 \text{ nM}$) of vortices, including the formation of double vortices at two different (not always opposite) poles (B and E(top)) and a GUV-spanning band (E).

The formation of vortices can be further visualized by averaging the intensity $I(r, \phi)$ of the actin fluorescence signal within the vesicle in polar coordinates at different angles, averaging over the radial direction. This leads to an intensity function $I(\phi) = \langle I(\phi, r) \rangle_{r < R}$ indicating the spatial evolution of the structures. A uniform intensity in the initial quasi-isotropic state quickly evolves into peaks (the streams) that merge into a single one over time (vortex) (Fig. 2.20.A). On an equirectangular projection, the motion of individual comet-streams is also easy to track (Fig. 2.20.B, tracked manually using high-intensity regions as references) and clearly shows

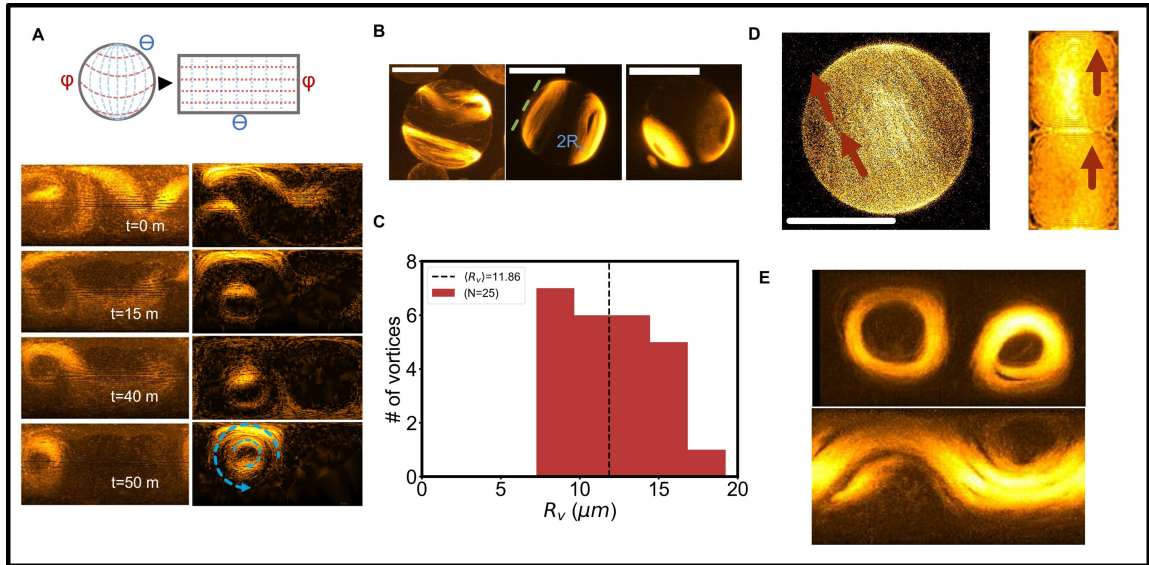


Figure 2.19: **Formation of vortices in GUVs** A) Equirectangular projections of GUVs at 600 nM over time, showing vortex formation. The equirectangular projection allows to see the full formation on a single plane. Merging of streams is evident. B) Snapshot of a vortex and a stream at 300 nM and of two different double vortices at 600 nM . C) A histogram of vortex radii shows a mean radius $R_v \approx 11\ \mu\text{m}$, much bigger than vortices observed on SLBs. D) At high concentration, GUV-wide vortices (bands) can be observed (experiment carried out with $c_0 = 1\ \mu\text{M}$ and 0.25% MC). Scale bars are $20\ \mu\text{m}$. E) Equirectangular projections of a double vortex (top) and a band (bottom) at 600 nM .

how streams move, collide with each other changing direction, end up looping on themselves and finally form a vortex. The same process is visualized in a kymograph done by averaging the equirectangular projection over the vertical spherical angle θ in order to visualize $I(\phi)$ over time (Fig. 2.20.C) showing how different high-intensity bands (comet-streams) over time move and over time aggregate in a single one (vortex). All these results taken together further clarify the mechanism of vortex formation as a consecutive series of events in which streams merge. Depending on the relative direction streams merge with and on whether they manage to merge before looping on themselves, the process can lead to single vortices, vortices and anti-vortices rotating around the same core or a couple of vortices at different poles of the GUV. Couples of vortices need not be at opposite poles but can rotate independently as long as they do not touch each other (see again Fig. 2.19.B).

Clearly, in most cases, the vortices end up accumulating all of the filaments inside the GUV and act as attractors of the trajectories (see for example the projections in Fig. 2.19.E). Together with theoretical predictions and with the observation that at $c_0 \approx 300\text{ nM}$ vortices become the predominant structure at around $c_0 \approx 300\text{ nM}$, we postulate that they would be the most stable state in this system if it were not for the occurrence of jamming (see below) that prevents streams to merge into a vortex.

Additionally, the fact that vortices are formed by longer streams that loop because of confinement makes it so that they have a radius R_v much bigger than what observed on SLBs (see Fig. 2.19.C). The mean radius is indeed found to be $\langle R_v \rangle \approx 11\ \mu\text{m}$, as computed from

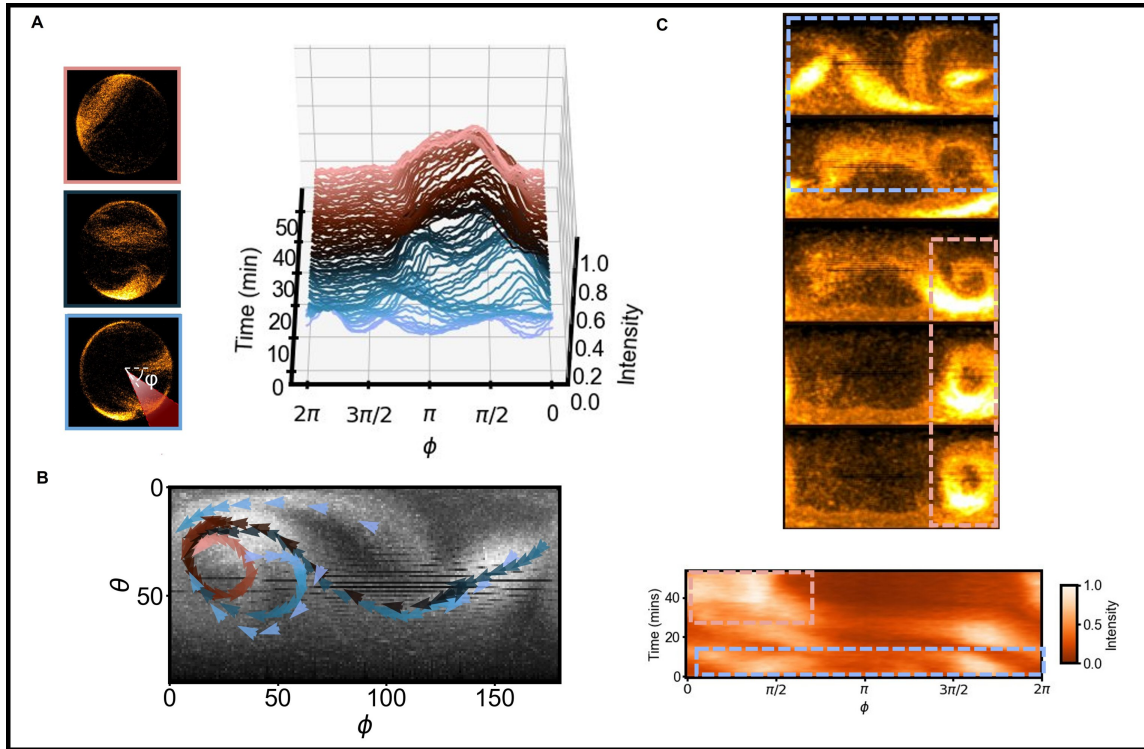


Figure 2.20: **Quantification of formation of vortices in GUVs** A) Taking the intensity of actin fluorescence as a function of the polar angle ϕ we can monitor the stream formation and merging into a vortex. A low intensity (uniform) configuration evolves forming two peaks (streams) that merge into a single one (vortex). B) By observing motion of the structure on an equirectangular projection, it appears clear how vortices form by streams moving, colliding, bending and merging. C) The same vortex formation as Fig. 2.19 in the equirectangular projection can be used to compute a kymograph of streams merging in the vortex. The color-coded time scale is consistent within the figure.

fluorescence images. This has to be compared with $R_v \approx 1 - 3 \mu m$ on SLBs (see again Fig. 2.9.B). On SLBs, vortices were forming by short seeds and streams merging and only occasionally by longer streams looping on themselves, as streams were more free to elongate. Thus the formation of vortices, especially of this size, is a clear characteristics of gliding in a GUV and it is due to the confinement and different topology of the system with respect to planar GUVs.

Rarely, but sometimes, at high density, the vortex is as big as the vesicle's circumference, effectively forming a GUV-spanning polar band (Fig. 2.19.D and E). This appears in equirectangular projection as a constant flow of mass in one direction. As explained in the next session, polar bands mostly arise by comet-streams at high density merging together.

2.5.3.3 High density patterns and jamming

At high density ($c_0 = 600 nM$, $O \approx 3.0$, i.e. close to O_{iso}) patterns can still form, including vortices and bands spanning the whole GUV. However, because of the high density, we also witness the formation of jammed situation in which the filaments all hinder each others' motion

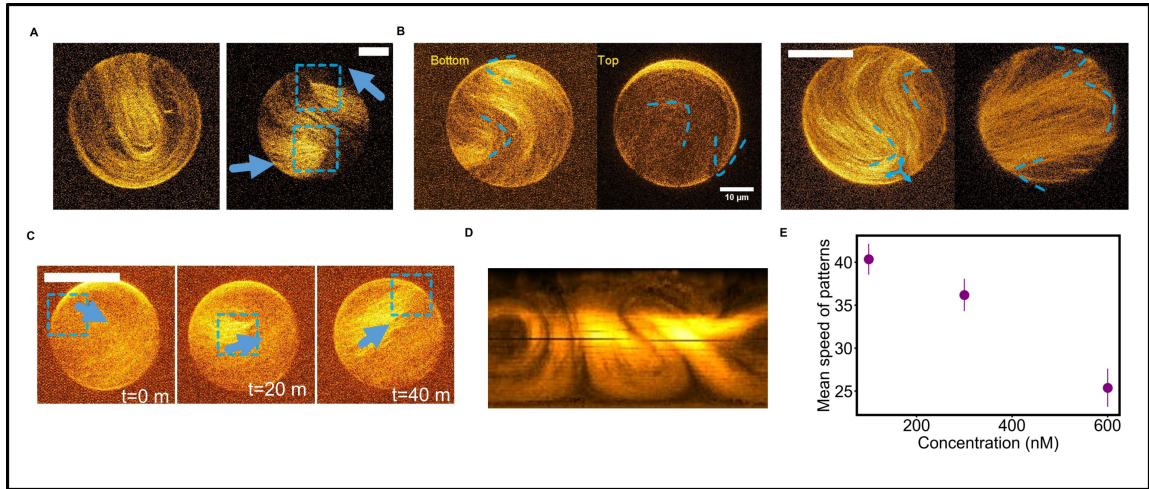


Figure 2.21: **Defects configurations in GUVs** A) Filaments at high density (600 nM) can end up in a jammed case, fully covering the surface, occasionally evolving into a couple of comet-streams that move in the GUV. In this latter case, comets can further merge or instead move independently. B) In the jammed case, topological constraints start playing a role again. Actin filaments can assemble into the well-known $4 \times \frac{1}{2}$ defects configuration (left) but $-1/2$ defects can also appear, in which case to maintain a total charge of $+2$ an additional $+1/2$ defect is required (right). C) If actin filaments manage to escape jamming, comet streams move and evolve along the membrane's surface. They can either form a band or glide as two separate comets as in (A, right) D) Equirectangular projection of a GUV in jammed state at $c_0 = 600$ nM E) Jamming is also visible as the mean speed of patterns lowers as the concentration is increased. Arrows indicate the direction of motion of patterns. Scale bars are 20 μ m.

so that the patterns evolve very slowly. When this happens, topological constraints on the alignment of filaments on a spherical surface can start playing a role again forcing the patterns in a given configuration. Figure 2.21 shows several example of GUVs in the high density case.

A sphere fully covered with filaments must have a total nematic charge of $+2$. This can be in principle realized by having a GUV-spanning vortex, each of cores of the vortices providing a charge of $+1$. This conformation would both satisfy topological requirements and allow filaments to glide easily. However, unless the vesicle quickly relaxes in this configuration (i.e., in a band) it might get arrested in other configurations which prevent effective motion due to steric interactions. In what we described as the jammed case, indeed, filaments assemble in conformations resembling the standard $4 \times \frac{1}{2}$ defects conformation, with approximately 2 positive defects on each hemisphere (Fig. 2.21.B (left)). We also observe the formation of $-1/2$ defects in fully covered GUVs, which force the appearance of a further $+1/2$ defect to maintain a constant charge of 2 (Fig. 2.21.B (right)). Such configuration hinders filaments' motion as each stuck comet-stream is acting as an obstacle for the other ones.

Because of activity filaments still accumulate in defects as much as they can, and hence the nematic does not always homogeneously covers the surface and small empty areas are visible. Yet the defect-like structure is still visible. Should fluctuations or variations in the density allow the defect to move, comet-streams form and start gliding along the membrane again. We witness often the formation of 2 comets, each coming from the merging of 2 positive defects,

that glide along the membrane. Should they meet, they assemble in a vortex or in a band, if they are gliding in the same direction, they just bend and keep traveling otherwise (Fig. 2.21.A (right) and C). Clearly the $2 \times \frac{1}{2}$ defect conformation is not expected in the passive case as the total charge is not equal to +2 but rather to +1. Comet-streams, as already seen in Figure 2.16, if allowed to move, can still assemble in a vortex.

The fact that as the surface coverage σ is increased patterns slow down is visible in Figure 2.21.E which shows a plot of the average speed of comet-like patterns (computed manually, see Methods) as the concentration is increased. This indicates that as the density of filaments increases, confinement and topology start dictating stronger and stronger constraints and play a bigger role.

2.5.4 Discussion

In this section we have observed the formation of patterns in a system of actin filaments gliding in a spherical topology, i.e. on the surface of a GUV. While the microscopic dynamics (and indeed, most of the qualitative observations) is expected to be the same as that in the previous Section about gliding on an SLB, some major difference should be underlined.

Firstly, the system is now in a confined setting. The GUV has a linear size (the radius) only 20 times the mean filaments' length. Additionally, the total number of filaments inside the GUV is relatively small, which we can extract from the O parameter for a vesicle of radius R as $N_f \approx 4\pi R^2 O / L^2$. Using $R \approx 15 \mu m$ and $O = 0.5 - 3$ we get $N_f \approx 2500 - 15000$. As a comparison, on a standard field of view on SLB one gets $N_f \approx 11000$ for the lower density case ($\sigma = 0.7$ filaments/ μm^2). This means that the filaments are much more likely to interact and indeed we notice a small shift in the critical aggregation threshold. Confinement also forces elongated structures of the order of the radius to loop on each other and therefore vortexing (with radii more enhanced as those observed on a SLB) is enhanced. Structures that would not loop on a planar surface now do.

Secondly, the new topology introduces constraints on the alignment of filaments at high density. While the nematic defects observed on SLBs were transient and only due to local high density and accumulation of filaments, here their presence is rather dictated by the conservation of a total charge of +2. The constraint is not fully enforced because of activity, which causes separation of filaments in space and hence does they do not fully cover the surface. However, due to the slow speed and high concentration, it can still play a role by for example simply forcing the $4 \times \frac{1}{2}$ defects configuration.

Both points (confinement and topology) seem to lead to a jamming of the structures much sooner than expected. The $4 \times \frac{1}{2}$ defects' conformation that the system is forced to assume is particularly difficult to relax, whereas on the SLB even at high surface densities comet could still move relatively free and merge into thicker streams. A band-like structure is instead here only seldom observed.

This system also allows to study the behavior of polar particles in a curved geometry. Previous works had indeed highlighted that polar bands would emerge but they were considering either theoretical model or spherical particles [Sknepnek and Henkes 2015; Shankar, Bowick, and Marchetti 2017]. The effect of steric interaction between filaments extends those results: while we do see vortex and band-like behavior, we explore a broader morphology here.

All together, these results indicate how confinement affects pattern formation in the case of cytoskeletal filaments. While not directly comparable to known processes *in vivo*, it is reasonable to believe that the cytoskeleton of cells is indeed affected in similar way by confinement and these results could shed light on processes such as cytokinesis and development. Additionally, cell layers are also often assemble on curved surfaces and might exhibit similar collective motion.

2.6 Gliding in a nematic

In the previous sections we have discussed how a microscopic nematic symmetry can be biased towards collective polar order if one introduces steric interactions. In particular, we discussed the effect of defects in trapping and rectifying filaments' motion. Those defects, however, were active defects, in the sense that they were composed of moving filaments and thus only transient. Also, while their conformation was perfectly resembling that of a nematic defect, they were isolated in space rather than actually part of a nematic material and hence could escape topological constraint such as their creation and annihilation in pairs. Here instead we develop a variation of our experimental gliding system so that filaments are forced to glide in a nematic material that fully covers the surface and contains passive defects. Such a nematic is self-assembled using depletion interactions. We observe the effect this has on the collective order of the active filaments forced to follow the local nematic director.

From another point of view, this system also attempts to mimic the fact that filaments, *in vivo*, move in a complex environment, whose response and effect on the motion of filaments can act as a mechanical cue for the self-organization of the cytoskeleton. While most work until recently focus on active particles moving in an isotropic homogeneous environment, recently some focus has started to shift on the role of complex (e.g., porous, elastic or gel-like) surroundings in shaping pattern formation and the particles' microscopic dynamics [Zhou et al. 2014; Patteson et al. 2015; Genkin et al. 2017; Bhattacharjee and Datta 2019; Turiv et al. 2020; Martínez-Calvo, Trenado-Yuste, and Datta 2021]. Joined with the previous section about the role of spherical confinement, this final part of the chapter aims at understanding the role of environmental conditions on pattern formation in cytoskeletal systems.

2.6.1 Experimental system

We vary the experimental system described in section 2.4 about gliding actin by coating a SLB with biotin-functionalized kinesin motors which propel short ($\approx 2.0 \mu m$), stabilized, fluorescent microtubules. The precise composition and setup is given in Methods 4.4. Again, upon ATP addition filaments are observed moving with a speed of $\approx 300 nm/s$ but do stop and align upon collision. Being rigid filaments, differently from actin, microtubules however align less efficiently, easily getting stuck against each other. Importantly, in these conditions, microtubules glide on the SLB but only transiently form clusters that form and disappear over time (Fig. 2.22.D). No stable pattern is observed even at $\sigma \approx 0.08 MTs/\mu m^2$ which is comparable to the conditions at which actin was starting to align more (see previous Sections).

We then also further sediment on the surface short, stabilized passive actin filaments which form a 2D nematic material on the surface. Fig. 2.22.A shows a full schematic of the system.

Over the course of the first 10 – 15 minutes the actin filaments self-assemble in a nematic material (Fig. 2.22.B, C, E). The formation time is estimated from the saturation of the order parameter S , computed as explained in Methods 4.5. The nematic material also features $\pm 1/2$ nematic defects (Fig. 2.22.E), inside which microtubules are forced to glide (Fig. 2.22.F). We can tune the properties of the nematic material by varying the actin filaments' length (as before, using the severing protein gelsolin, see Methods) and total concentration. We can also tune the number of microtubules gliding in the system by varying their incubation time. Unless specified

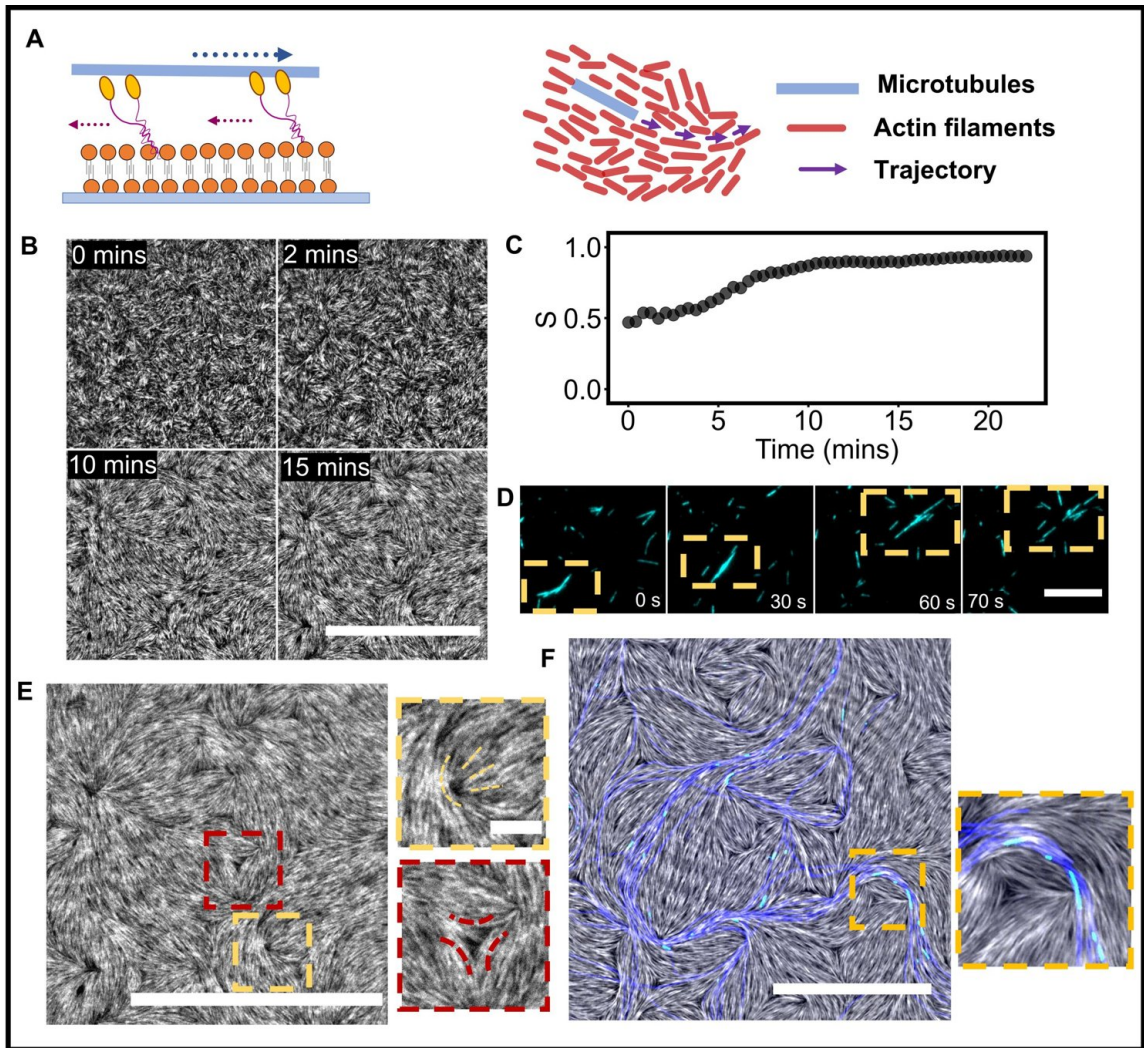


Figure 2.22: **Filaments align with the nematic and follow its trajectories.** A) Schematic of the system: biotinylated-Kinesin is bound to a SLB. Microtubules are bound to the kinesins and glide on the surface, which is finally crowded with short stabilized actin filaments forming a nematic. B) Self-assembly of the actin nematic over time ($1 \mu\text{m}$, with $0.5 \mu\text{m}$ filaments), also measured computing the order parameter S over time (C), starting from when observation is started at the TIRF microscope. D) Microtubules gliding on a bilayer even at $\sigma \approx 0.07$ MTs/ μm^2 only aggregate transiently. Clusters form and disappear. E) The actin nematic is passive and features both $+1/2$ and $-1/2$ nematic defects F) microtubules gliding inside a nematic align with the local director and follow it over time (MT in cyan, actin in red, MTs' time projection in blue indicating the trajectory). Scale bar are $50 \mu\text{m}$, except in the defects' and the individual MTs close ups where it is $5 \mu\text{m}$.

otherwise, actin nematics are assembled using $1 \mu\text{M}$ actin, using filaments with a mean length of $\approx 0.5 \mu\text{m}$. Fig. 2.22.C shows a snapshot with microtubules gliding in the nematic and their trajectory over time. The microtubules gliding inside the nematic material are found to align with the local nematic director. We can thus investigate what is the resulting behavior when

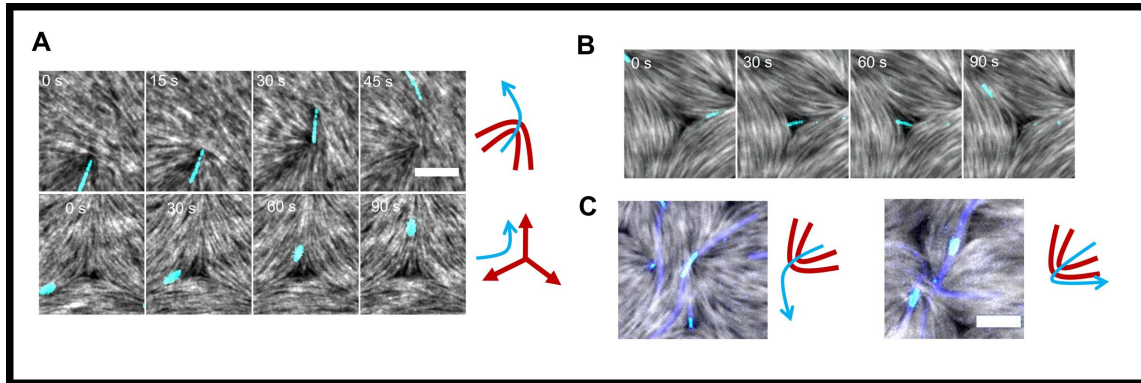


Figure 2.23: **Behavior of microtubules at defects** A) Microtubules gliding in a $+1/2$ defects are converged in the core and then escape it, realigning with the nematic director afterwards (top). Microtubules gliding close to a $-1/2$ defect are bent by the distortions due to the defect itself. B) Occasionally, microtubules can cross a $-1/2$ defect's core and then realign with the nematic director. C) Depending on the filaments' length (left, $0.25 \mu\text{m}$, right $1.5 \mu\text{m}$) microtubules are trapped for different times and align more or less efficiently after escaping the defects. Scale bars are $5 \mu\text{m}$.

filaments glide with a superimposed nematic field that affects their orientation⁷.

2.6.2 Microtubules align in the nematic material and follow its distortions

We first study the behavior of microtubules at low surface density ($\sigma \approx 0.003 \text{ MTs}/\mu\text{m}^2$, $O \approx 0.012$). As long as the microtubules (MTs) are oriented in the same direction of the local nematic director \hat{n} , they will keep gliding along it, only slightly displacing the actin filaments they interact with. The actin nematic is on average unchanged when filaments glide into it in an aligned state. On the other hand, if microtubules find themselves misaligned with the local director, a torque acts on them forcing microtubules to re-align. In this case, MTs are able to locally distort the actin nematic in order to align. The nematic material however quickly relaxes back to its original state. The alignment of microtubules with the local director also means that, if the nematic is locally distorted, the microtubules will follow its distortions and hence an aligning torque is always acting on the microtubules every time a distortion is present (i.e., $|\nabla\hat{n}| \neq 0$, as the gradient of the director vector describes distortions in the nematic). Thus the microtubules motion is affected by the local environment via a spatially varying torque that aligns them with the passive actin filaments.

2.6.2.1 Behavior of gliding microtubules at nematic defects

Particularly interesting is the case of microtubules interacting with a passive nematic defect.

As in defects a nematic director is not defined, microtubules could in principle choose a new direction when they approach one. What instead happens in the case of $-1/2$ defects is that microtubules do not actually reach the core of the defect but rather follow the nematic distortion

⁷Most of these experiments have been carried out together with Lukas Neumann under my supervision. He deserves a good deal of the credit!

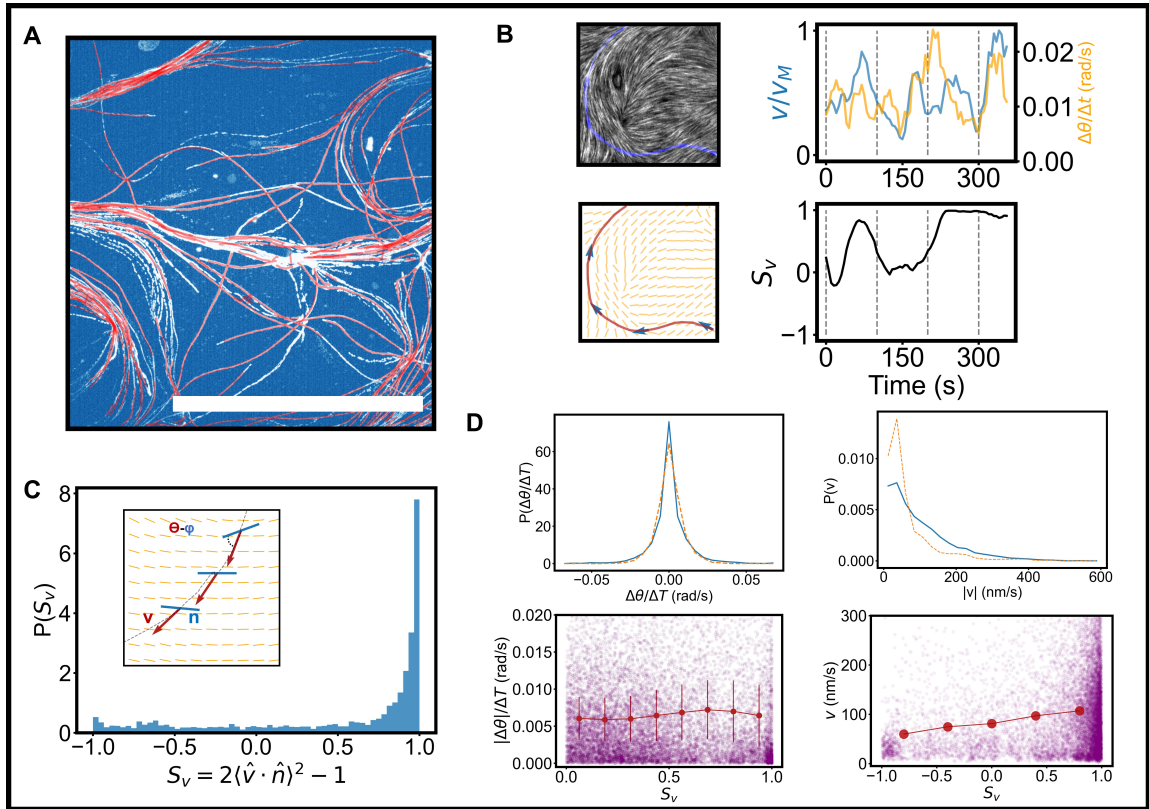


Figure 2.24: **Tracking of microtubules moving in a nematic** A) Overlay of experimental (white) and extracted (red) trajectories showing good agreement. Scale bar is $100 \mu\text{m}$. B) Example trajectory, showing how MTs can change direction abruptly if they meet a defect but yet recover alignment with the nematic over time. The nematic field n , the alignment S_v and the speed and torque over time are also shown. C) Histogram of alignment of MTs with the nematic, showing a peak for $S_v \approx 1$ i.e. that MTs are on average aligned. D) Speed and torque as a function of S_v indicating an increase in speed but no apparent increase in the torque if the MTs are aligned. Histograms show the variability of speed and torque for $S_v \approx 1$ (dashed orange) and $S_v < 0.75$ (blue).

induced by it, thus going around the defect's core on the side (Fig. 2.23.A). Only rarely do microtubules cross the defect's core directly and in this latter case they immediately after re-align with the director field (Fig. 2.23.B). Conversely, positive defects, as already discussed in the previous sections, have a wedge-shaped conformation that can lead to up-concentration of filaments in its core. In facts, what we observe is that MTs entering a $+1/2$ defect either get stuck in its core, unable to escape for long times, or manage to leave it and then successively align with the neighboring nematic director. Figures 2.23.A and B show examples of microtubules leaving a $+1/2$ defect and then aligning with the nematic director. The behavior at $+1/2$ defects will be particularly relevant in the following sections.

The interaction of MTs with nematic defects can also be tuned by changing the actin concentration and length: longer actin filaments ($\approx 5 \mu\text{m}$) are harder to displace and trap microtubules more efficiently in $+1/2$ defects, whereas shorter ($\approx 0.25 \mu\text{m}$) filaments, while still able

to reorient microtubules, are short enough that microtubules can escape defects more easily by momentarily displacing the nematic (Fig. 2.23.C). Yet, once the nematic has formed, we observe only minor local rearrangements of the nematic material itself as MTs glide into it at the chosen concentrations (see Fig. 2.30), with filaments exiting from $+1/2$ defects having to locally push passive filaments to re-align.

2.6.2.2 Tracking of individual microtubules

To understand the microscopic rules of the system, we analyze the trajectories of gliding microtubules at low density by either tracking individual MTs. We start by analyzing the trajectories of individual MTs.

By tracking (see Methods 4.5), we can extract, for each MT labelled i , its position \mathbf{r}_i , velocity \mathbf{v}_i and orientation $\hat{\mathbf{p}}_i$. Fig. 2.24.A shows an example of trajectories extracted from the tracking analysis superimposed to the experimental time projection of gliding microtubules, obtained by averaging the microtubules' intensity over time, showing good agreement.

Additionally, we can extract the nematic director field $\hat{\mathbf{n}}(\mathbf{r})$ using the method described in Methods 4.5 and correlate it with the MTs' orientation. To quantify how microtubules align with the nematic, we compute the average alignment of microtubules with the nematic field, using the definition of order parameter given in equation 1.16, but using the MT's orientation $\hat{\mathbf{p}}_i$ as local director, i.e.

$$S_v = 2(\hat{\mathbf{p}}_i \cdot \hat{\mathbf{n}}(\mathbf{r}_i))^2 - 1 \quad (2.5)$$

Figure 2.24.B shows an example trajectory, together with its instantaneous torque, speed and alignment with the nematic. This latter varies over time, as the microtubule changes its local environment and becomes momentarily misaligned, but it is quickly restored to $S_v \approx 1$. This trajectory also shows that microtubules can indeed cross regions of the nematic in which they are misaligned, but that there must be a restoring force, due to steric interactions with the nematic, that push the filaments back to the aligned state. As mentioned above, abrupt changes in the alignment with the nematic mostly occur when microtubules cross a $+1/2$ nematic defect, with the filament able otherwise to adapt to other local distortions in the nematic material thanks to some re-aligning torque. Finally, an effect of the local alignment on the MTs' speed is also visible, as filaments slow down in area of high misalignment.

We then analyzed multiple trajectories (at an actin concentration of $0.75 \mu M$) together to extract more information. Fig. 2.24.C and D show the results. Microtubules do indeed align strongly with the nematic as seen from the histogram of S_v being peaked at $S_v \approx 1$ (Fig. 2.24.C). This means that the torque present, which aligns MTs to the local nematic director, is strong enough to keep the microtubules aligned most of the time. We can also estimate the torque itself, computed as the difference in orientation over different frames, and find a distribution peaked at 0 with a standard deviation $\sigma_\tau \approx 0.03$ rad/s. From the tracking data we can also compute a mean speed of $|v| \approx 100 nm/s$. Both the torque and the speed have a slight dependance on the alignment with the nematic, with MTs gliding aligned with the actin gliding faster and receiving more torque than filaments misaligned. Notably, while the mean value does not change much as the alignment varies, the standard deviation of the distribution

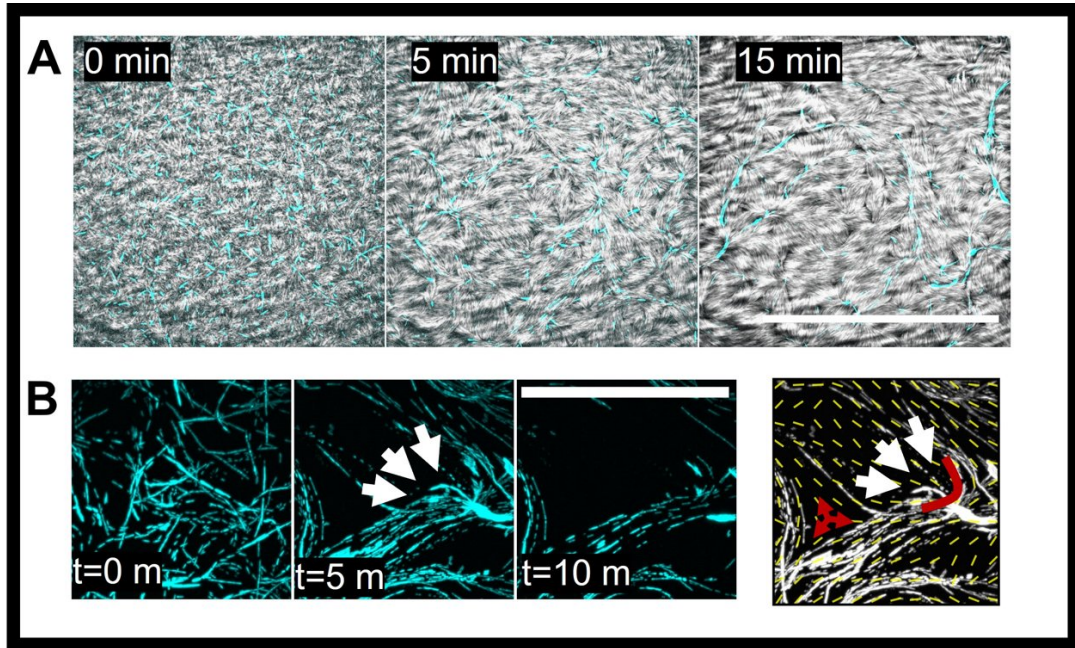


Figure 2.25: **Microtubules gliding in a nematic form macroscopic lanes** A) Snapshots right after ATP and actin addition at $\sigma = 0.08 \text{ MTs}/\mu\text{m}^2$. As the nematic material starts forming, microtubules quickly assemble into lanes from an initially isotropic state. B) Time projections of 30 seconds of motion at different time points, showing how initially isotropic trajectories get shaped by the nematic field over time and accumulate into lanes. The last panel shows the nematic field superimposed to the trajectories at $t = 5\text{m}$ and the positions of defects. White arrows show the general direction of motion. A $+1/2$ defects acts as a gate to accumulate filaments in the lane. Scale bars are $50 \mu\text{m}$.

of torque and speed does, with misaligned microtubules behaving in a more varied way than aligned ones (Fig. 2.24.D)

Microtubules moving in a misaligned state ($S_v < 0$) move at a speed of $\approx 50 \text{ nm/s}$ whereas aligned microtubules ($S_v > 0.8$) move at a mean speed of up to 200 nm/s . Thus the nematic also forces the MTs to move in a medium of locally varying effective mobility, as the drag acting on the microtubule depends on its relative orientation with the local nematic director.

2.6.3 Defects and nematic distortions break the global symmetry

Thus it appears clear that the nematic material, by imposing an orientation, can affect the motion of microtubules by its distortions. Because MTs follow the nematic director, one would expect a global nematic symmetry as locally both the orientation \hat{n} and the opposite $-\hat{n}$ are equivalent. Additionally, one could expect that filaments are on average homogeneously dispersed in the nematic. However, even looking at low density trajectories, one immediately notices that microtubules tend to aggregate along specific trajectories.

We then increased the MT surface density to ($\sigma \approx 0.03 - 0.08 \text{ MTs}/\mu\text{m}^2$) and observed the behavior of active filaments using time-projections of the microtubules' intensity to visualize the filaments' flow. At high density, the effect of the presence of a nematic in selecting specific

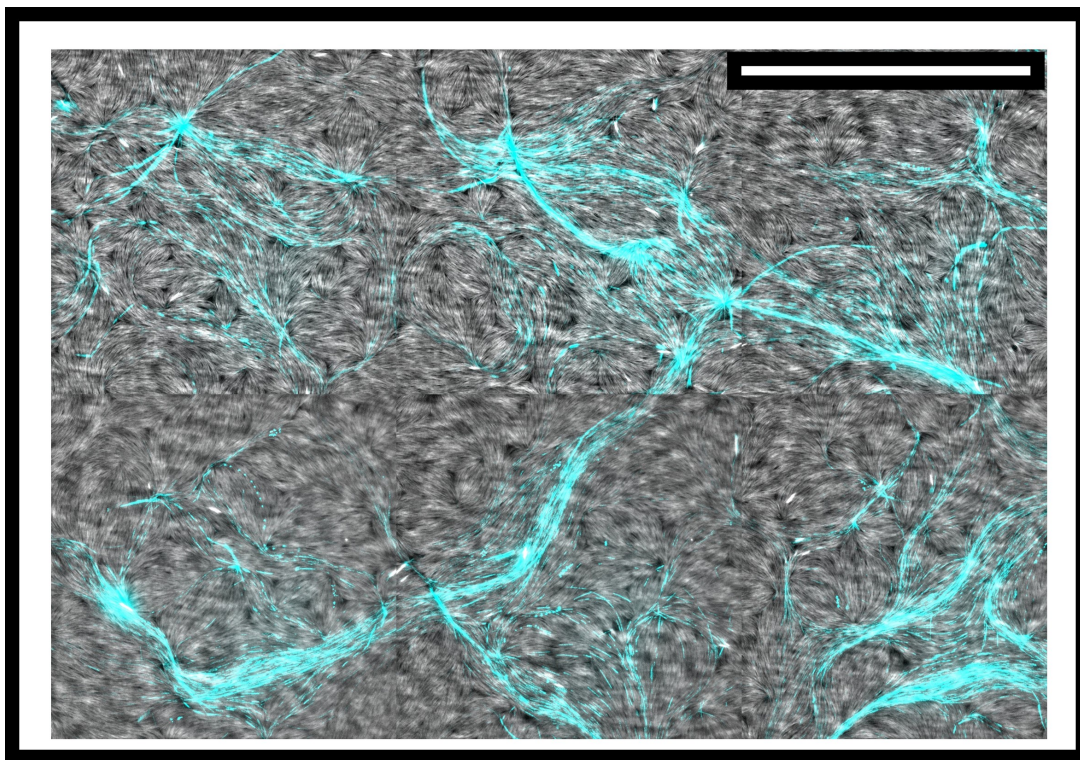


Figure 2.26: **Over time, microtubules assemble into macroscopic structures** Time projections of trajectories of microtubules, obtained by the mean intensity over time. After 45 minutes, the microtubules have assembled into macroscopic structures including vortices and lanes. Such structures are mediated by the nematic material. Scale bar is $50 \mu m$. Conditions are $1 \mu M$ actin at $0.5 \mu m$ length and $\sigma = 0.03$ microtubules/ μm^2 .

trajectories is even more clear. Figure 2.25.A indeed shows how upon formation of the nematic, the microtubules, initially homogeneous in space, quickly assemble into elongated structures. This indicates that the presence of the nematic field leads to the rearrangement of microtubules into ordered structures. Strikingly, indeed, in the absence of a nematic but at the same surface density, MTs align only transiently and do not aggregate into lanes (see Fig. 2.29.B). Also notice that this filament density, assuming microtubules have a length of $\approx 2 \mu m$, corresponds to a O -parameter of $O \approx 0.3$, i.e. much lower than O_{iso} and than the aggregation threshold for gliding actin filaments discussed in Section 2.4. This means that the presence of the nematic field significantly lowers the aggregation threshold. This is because, as we will further see, lanes are not due to direct MT-MT interaction but rather to the nematic field directing MTs' motion.

By looking in detail at the formation of lanes in the initial times, it appears clear how microtubules follow the nematic director until they are forced to accumulate along the same field lines, after which filaments keep traveling together. For example, the fact that some areas end up devoid of filaments, which all accumulate along main directions is mediated by the nematic field and its defect, especially $+1/2$, that act as one-way gates from different portions of space (Fig. 2.25.B). There is afterward no other trajectory compatible with the nematic field that brings filaments back in the original position so that it remains empty.

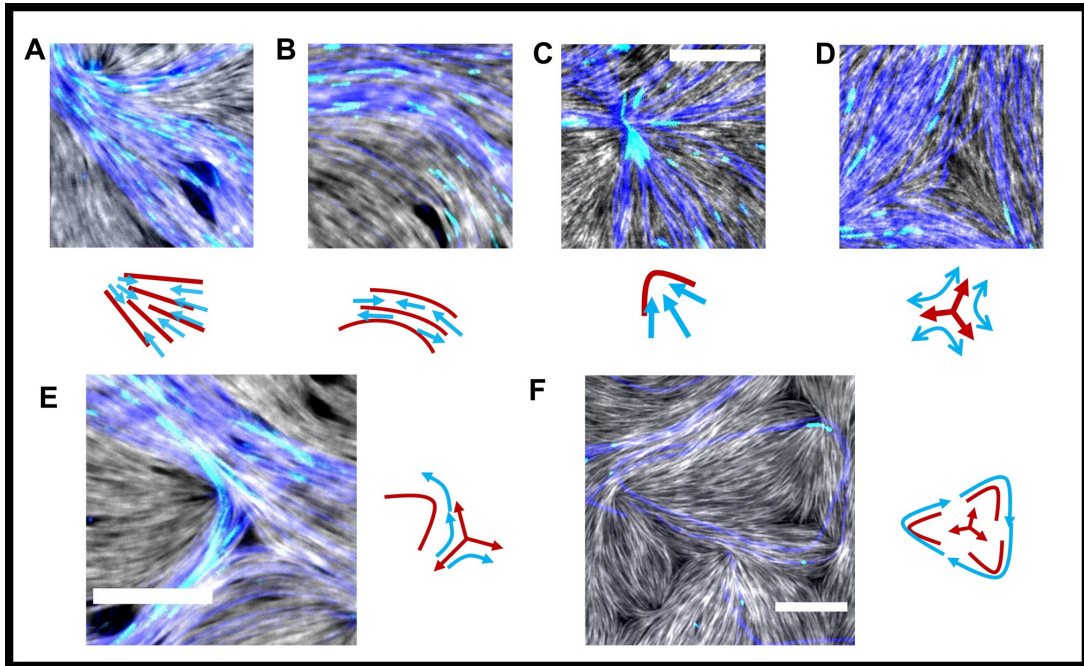


Figure 2.27: **Distortions and defects alter the microtubules' motion.** A-B Splay (A) and bend (B) in the nematic affect the flow of microtubules. While bend distortions only change the flow's orientation, splay can accumulate or disperse the microtubules' density. C-D) Both positive (C) and negative (D) defects affect the flow. Negative defects mostly act as sources of bend deformations, whereas positive, due to their splay, up-concentrate microtubules. E-F) different conformations of defects can alter the microtubules' flow according to the distortions they generate in the nematic material. Composite conformations of $+1/2$ and $-1/2$ defects can create loops (F) or channel microtubules in a given direction preferentially (E). Actin is shown in grey, microtubules in cyan and time projections of the MT's motion in blue. Data are taken from different experiments at $1 \mu M$ actin with length of $0.5 \mu m$. Scale bars are $10 \mu m$.

Over time, the system assembles into macroscopic lane-like patterns. Time-projections of the microtubule flow on a big sample area clearly indicates that microtubules form collective structures much bigger than the individual filament's size, including vortices and lanes of different thickness, all mostly concentrated along main trajectories shaped by the nematic field (Fig. 2.26).

2.6.3.1 Microtubule flow follows distortions in the nematic

To better understand the pattern formation process, we then look more in detail at the microtubules' flow in presence of distortions and defects in the nematic as they appear to somehow break the local spatial symmetry by acting as wedges which rectify the particles' motion.

Again, microtubules appear to mostly follow the nematic director field even at high density. The MTs' flow is indeed shaped by nematic distortions and follows both splay and bend deformations (Fig. 2.27). The microtubules' speed v can be thought of as mostly being proportional to the nematic director \hat{n} i.e. $v = \pm v_0 \hat{n}$, the sign being undefined due to the nematic nature of the director. This also implies that splay in the nematic corresponds to splay in the flow as

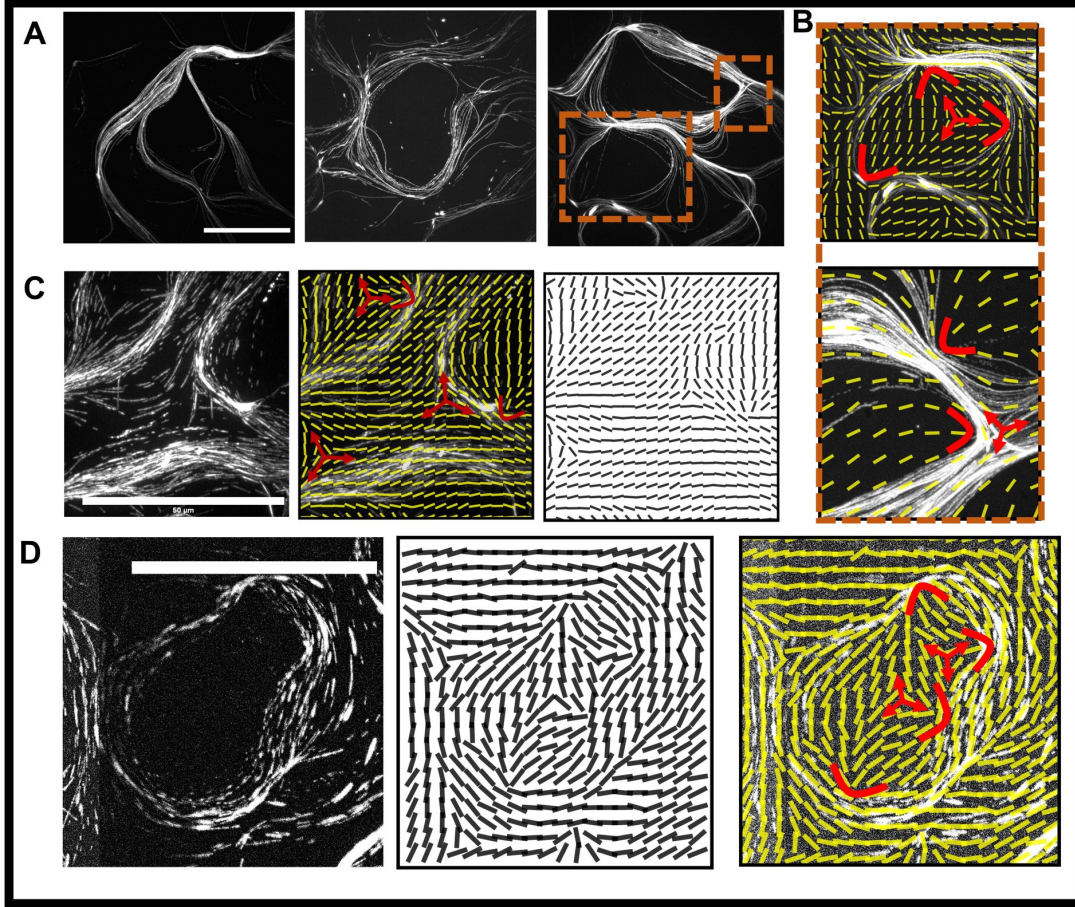


Figure 2.28: **The nematic field and defects shape microtubule lanes** A) Time projections of different patterns emerging, including lanes and loops. B) Details take from the third panel of (A), showing the defect conformation leading to some structures. Notably, the looping configurations with $N = 1$ negative defects is visible, and the gating one (two close defects of opposite charge) already seen in Fig. 2.27.E. C) Detail from Fig. 2.26 showing how a single $-1/2$ defect in the center can deform lanes at a distance. Again, the gating configuration $-1/2$ and $+1/2$ is present. D) Another detail from Fig. 2.27.E showing a looping configuration and the corresponding nematic field. This time, a looping configuration with $N = 2$ is present. Data from $1 \mu M$ actin with length $0.5 \mu m$ and $\sigma \approx 0.007$ MTs/ μm^2 . Scale bars are $50 \mu m$.

$\hat{n} \cdot \nabla \hat{n} = v_0^2 \mathbf{v} \cdot \nabla \mathbf{v}$ and indeed funnel-like splay deformations of the nematic field are found to also converge/diverge the flow of microtubules. Both convergence and divergence of the flow are present. However, because of the funnel-shape, more microtubules will enter it on one side than the other so the net effect is convergence of the flow and up-concentration of the microtubules at the base of the funnel (Fig. 2.27.A). Bend deformations also change the flow's direction but do not change the local concentration of particles (Fig. 2.27.B)

Also in this case, again, nematic defects play a main role in shaping the MTs' flow. Negative defects mainly diverge the flow, sending some microtubules in one direction and some in another one (Fig. 2.27.D). More strikingly instead, $+1/2$ nematic defects not only have a splay-

dominated funnel shape, that converges the microtubules flow, but they also strongly break the flow's symmetry as microtubules can only enter them on one direction, the other one being protected by a mostly-perpendicular arrangement of filaments that shields it. In facts, what we observe is that the MTs' flow entering a nematic defect is converged towards the defect's core, with microtubules escaping it re-aligning afterward in another direction as already observed at low density (Fig. 2.27.C).

Defect's also play a less local role in shaping the flow as the distortion they induce on the nematic can be long-ranged. Figure 2.27.D for example shows microtubules being bent by a $-1/2$ defect whose core is several microns away but which still influences distortions in the field at a distance. Additionally, specific conformations of nematic defects can act together in shaping the flow, for example three $+1/2$ defects with a $-1/2$ defect at the center lead to the formation of closed loops, while $+1/2$ and $-1/2$ defects can act together to shape the flow. Thus also $-1/2$ defects do not only bend the flow but can also help indirectly to reshape it in a more complex way.

This allows for the final patterns to be very diverse depending on the local conformation of the nematic material. Figure 2.28 shows additional time projections, together with the underlying nematic conformation. Structures forming are very varied but some recurring patterns can be found. For example, the same defects' conformation as in Figure 2.27.F can be observed also for this macroscopic flow, leading to looping of microtubules around a three $+1/2$ defect triangle with a $-1/2$ defect in the center (Fig. 2.28.A). More in general, as the total charge enclosed in a loop, by definition of charge, has to be of $+1$ (because the MT did a full rotation of 2π), looping configurations of half integer defects must be composed of N negative defects surrounded by $N + 2$ positive ones, for a total charge of $N \times (-\frac{1}{2}) + (N + 2) \times (+\frac{1}{2}) = +1$. In general, $N \geq 0$. In the previous case, it was $N = 1$. Figure 2.28.D shows another loop, this time with $N = 2$. Also the configuration of 2.25.B that acted a one-way gate, with a $+1/2$ and $-1/2$ defect and flow passing in between, is often observed (see Fig. 2.28.B, bottom, or C).

Thus more complex defect's configurations can shape the formation of lanes by selecting main directions of motion.

2.6.4 Microtubules gliding in a nematic form polar lanes

Another striking features of the lanes we observe is that they are often *polar*. To understand how defects can shape the flow, consider the simple ideal case of an isolated $+1/2$ defect whose main axis resides along the x-axis with a core in the origin, as depicted in Fig. 2.29.A. Filaments gliding left-to-right towards the core will be accumulated by the wedge-like shape of the defect into the core itself ($x = 0$). However, if filaments are also able to leave the core, due to their self-propulsion, then they would find themselves misaligned with the local nematic as they have crossed the defect core, where no alignment is defined, and find themselves in a region of space with completely different local director ($x > 0$). They will then re-align with the local director. In the case of a purely symmetric defect, as both directions are equivalent, filaments will choose either the $+y$ or the $-y$ direction with equal probability. In this case the result would be separation of the filaments in space, with accumulation in the $x > 0$ section of the plane but with nematic symmetry along the $\pm y$ direction. The opposite motion, i.e. a flow going right-to-left, is inhibited because the defect's shape acts as a barrier, allowing filaments to enter the

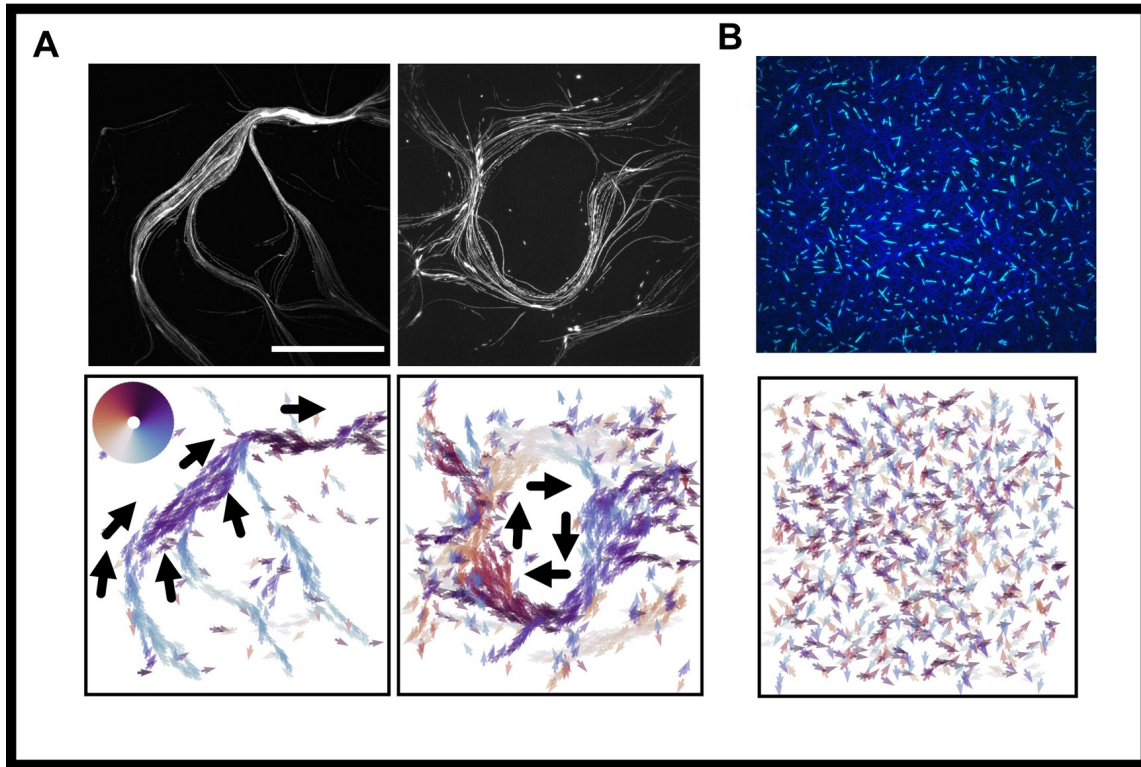


Figure 2.29: **Polarity of observed structures** A) Two different structures (same as 2.28.A) with the corresponding microtubule flow extracted by microscopy images and color coded according to the orientation (see inset). Polar domains are clearly visible as domains of similar color. Black arrows indicate the local direction of the flow for clarity. Data from $1 \mu M$ actin with length $0.5 \mu m$ and $\sigma \approx 0.007 \text{ MTs}/\mu m^2$. B) In the same conditions but without passive nematic, microtubules move isotropically in space and in orientation space (MTs in cyan, projections in blue). In the case without actin, observed speed are around $\approx 300 \text{ nm/s}$. No net flow is observed. Scale bar is $50 \mu m$.

defect only in one direction.

Indeed, as microtubules glide in the actin nematic, even at low density, MTs follow the same trajectories *in the same direction*. Instead, if the density is high enough, they aggregate into lanes, often with *polar* symmetry. Thus defects and distortion can not only influence the spatial distribution of filaments but also their orientation in space. This is due to the asymmetry in splayed conformations of the nematic that both converge and diverge the flow but capture filaments preferentially on the diverging side, a behavior which is especially efficient in the case of $+1/2$ nematic defects. Indeed, this latter play a fundamental role, as they already did in the case of gliding actin filaments, in the polarity sorting of microtubules. Additionally, if due to distortions coming from other points of the nematic, the nematic configuration also breaks the $\pm y$ symmetry, e.g. if the defect axis is oriented at some angle different than 90° with the nematic director right after the defect's core (see Fig. 2.30.A), then a given direction of motion can be selected and the resulting motion is not only separated in space but also with a defined orientation, i.e. polar rather than nematic.

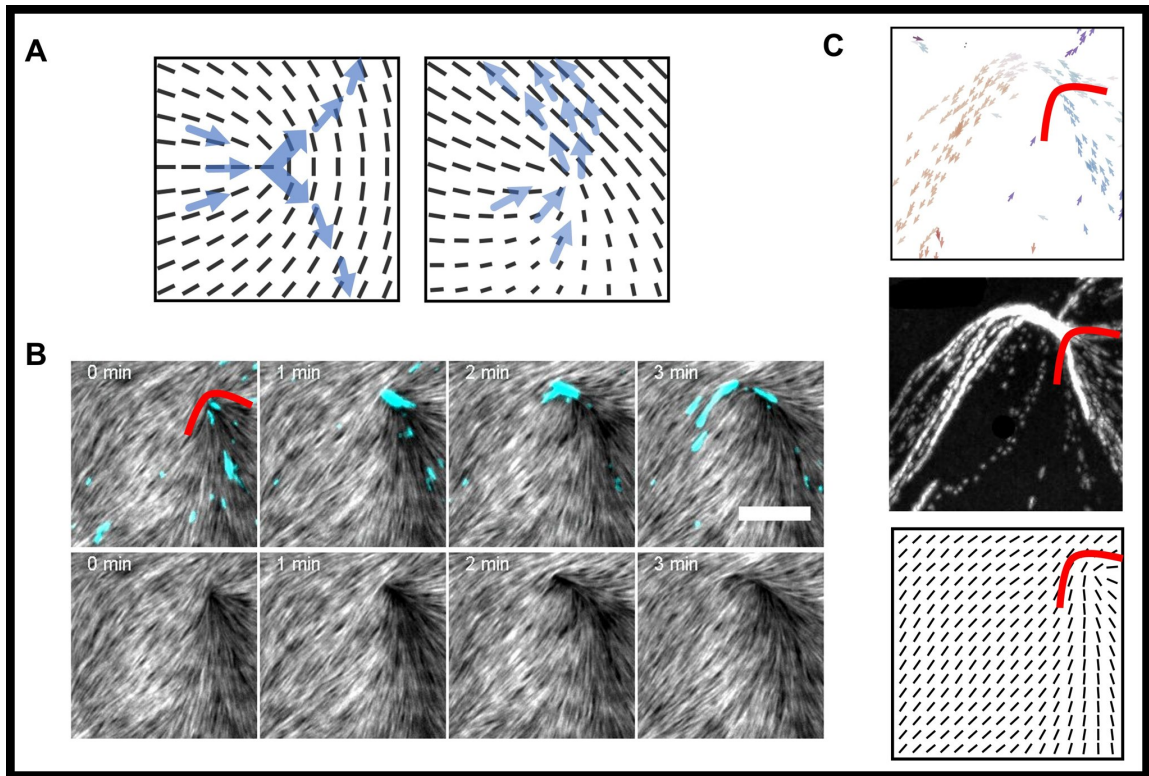


Figure 2.30: **Nematic defects mediate the polarity sorting of microtubules** A) Scheme of defect-based polarity sorting. A symmetric nematic defect can up-concentrate particles in space but does not violate orientational symmetry. An asymmetric defect in which the defect's axis is not perpendicular to the nematic field after the core can instead push filaments preferably in one direction. B) A $+1/2$ nematic defect up-concentrating MTs in its core and then expelling them in one direction (top). The nematic deforms locally but then relaxes back (bottom) C) This results, at high density, in a net flow biased in one direction after exiting the defect. For reference, the time projected trajectories and the nematic field are also shown and the position of the defect is marked. Scale bars are $5 \mu m$.

Positive $+1/2$ defects, similarly to what observed in the previous section, act as efficient polarity sorting conformations, which both accumulate the filaments due to their splay and then release them in a preferred direction dependent on the relative orientation of the defect's axis and the nematic direction right after the defect's core. This indicates that in general, the orientation field imposed by the passive actin nematic breaks both the spatial and the orientational symmetry, forcing filaments to accumulate in lanes and to be oriented in the same direction.

2.6.5 Effect of filaments' length, concentration and sedimentation

We also varied the actin filaments' length and concentration to study its effect on the pattern formation. The results are summarized in Figure 2.31.

Both an increase in length and concentration are expected to change the material properties

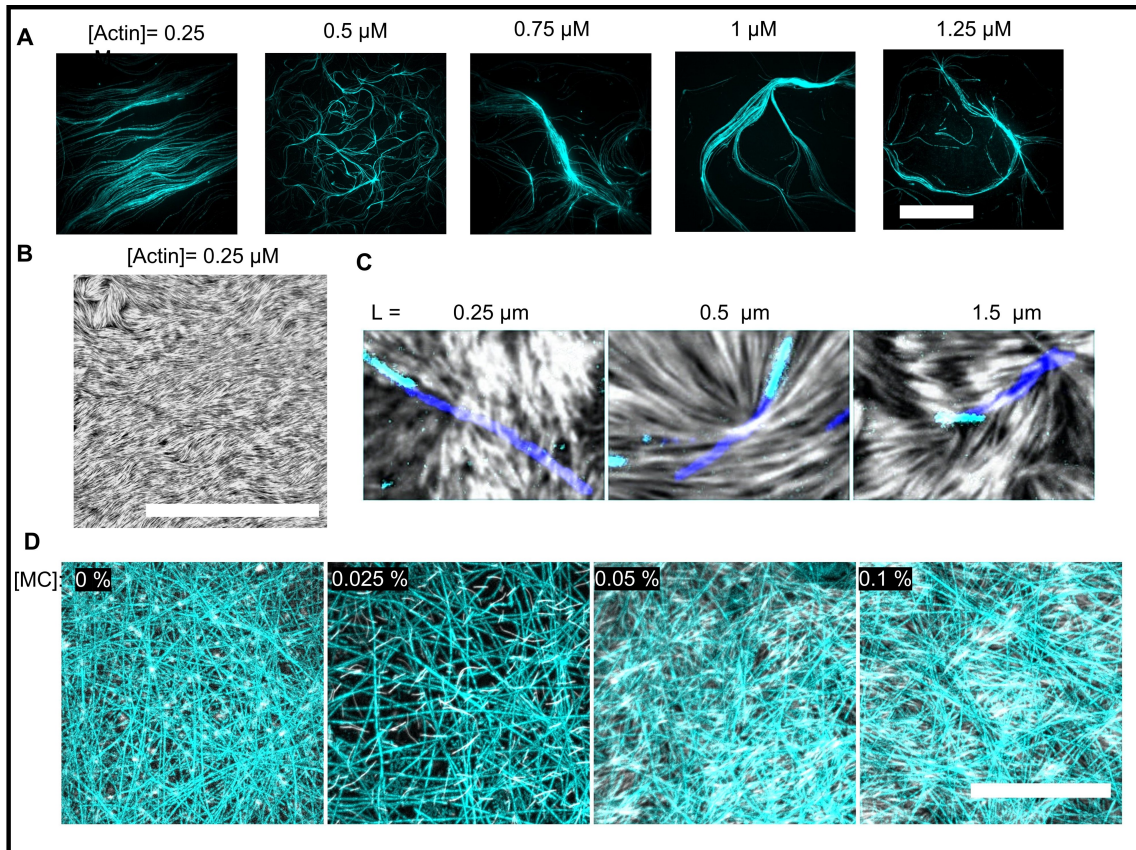


Figure 2.31: **Effect of the actin nematic on patterns** A) As the actin concentration is increased, patterns become thinner but still form, as long as a nematic is present. MT density is kept around $\sigma = 0.05 \text{ MTs}/\mu\text{m}^2$. Scale bar is $50 \mu\text{m}$. B) A nematic field aligned by the MTs at low actin density, with defects segregated on the side. Corresponding trajectories are shown in A, left most panel. Scale bar is $50 \mu\text{m}$. C) Varying the actin filaments' length affects the behavior of MTs in defect. For short filaments, MT escape defects easily. For long filaments, MTs are trapped in defects. Scale bar is $2 \mu\text{m}$. D) Varying the MC concentration, hence the amount of actin sedimented (in red) does not lead to pattern formation unless a stable nematic forms. MTs trajectories (in cyan) remain uniform if the concentration of MC is below 0.2 %. Scale bar is $25 \mu\text{m}$. MT density is kept around $\sigma = 0.02 \text{ MTs}/\mu\text{m}^2$.

of the actin nematic. What we observe, is that increasing the actin concentration (from $0.25 \mu\text{M}$ to $1.5 \mu\text{M}$), as long as a nematic form, has no clear effect on the formation of patterns. On the lower density side, filaments are displaced much more effectively as the elastic feedback on the nematic material is lower so it does not relax back to its initial state. In this case, the nematic can be affected by the MTs' motion. The result is that the nematic locally aligns with the microtubules (shown on the right in Fig. 2.31.A), giving rise to an aligned nematic material (Fig. 2.31.B). Lanes of MTs form and travel within it. Interestingly, in this case, the symmetry is nematic, as due to the absence of defects and distortions microtubules are not polar sorted. Also interestingly, defects are still visible but are pushed on the side of the MTs' trajectories. On the high density case instead, the nematic aligns filaments more strongly and

patterns appear to be thinner, as they are focused more effectively (Fig. 2.31.A) Similarly, changing the filaments' length (from $0.25 \mu m$ to $1.5 \mu m$), as already mentioned, only has an effect on the filaments' behavior at defects, with longer filaments trapping more efficiently. As filaments always eventually escape, this has no clear effect on pattern formation (Fig. 2.31.C).

More interestingly, we varied the MC concentration to vary the sedimentation of filaments on the surface. The results clearly show that if a stable, not varying with time nematic material does not form (i.e., if the concentration of MC is below 0.2 %) no patterns emerge. Indeed, at low MC concentration, only few filaments are sedimented and MTs just ignore them. At intermediate concentration, the presence of filaments hinders the MTs' motion that change direction more often but do not converge on a pattern. For the concentration of $MC \approx 0.05 - 0.1 \%$ instead, a nematic starts forming but is not stable in time. Also in this case, no patterns emerge (Fig. 2.31.D).

This results further prove that it is the coupling with a stable nematic that leads to emergence of polar patterns. As long as MTs are able to move and to escape defects, polar patterns will form if the nematic does not vary over time.

2.6.6 Theoretical and computational models describe the experiments well

To better understand the role of the local alignment with the nematic director of MTs, we developed two approaches: on one side, we simulate a minimal model of particles moving in a nematic field; on the other, we try to heuristically predict where the lanes will form starting from the field itself and its deformations⁸. Both approaches can be tested directly on experimental data as we can extract the nematic field \mathbf{n} from experiments. In both cases, results are strikingly accurate in predicting, starting only from the field's conformation, both where lanes of microtubules will form and in which direction they will move.

2.6.6.1 Simulation scheme

We model filaments as $n = 500$ point particles that persistently move in 2D in a given direction with velocity $v\hat{\mathbf{u}}$, where $\hat{\mathbf{u}} = (\cos(\theta), \sin(\theta))$ is the particle's own orientation and $v = 100 \text{ nm/s}$. To mimic the tendency to align to the nematic, particles interact with an external nematic field $\hat{\mathbf{n}}(\mathbf{r}) = (\cos(\phi(\mathbf{r})), \sin(\phi(\mathbf{r})))$ through a torque $\tau = A \sin(2\theta - 2\phi(\mathbf{r}))$ forcing the particle to align with the nematic. Finally, particles can also interact with each other through another aligning torque if they are closer than $\delta = 1 \mu m$. Thus the equation of motion for the position \mathbf{r} and the orientation angle θ are given, for each particle i , as

$$\frac{d\mathbf{r}_i}{dt} = v\hat{\mathbf{u}}_i \quad (2.6)$$

$$\frac{d\theta_i}{dt} = A \sin(2[\phi(\mathbf{r}_i) - \theta_i]) - s \sum_{j \neq i, r_{ij} < \delta} \sin(2[\theta_j - \theta_i]) + \sqrt{\frac{2v}{L_p}} \xi \quad (2.7)$$

⁸Both the simulations and the heuristic model here presented were developed in collaboration with Timo Krüger and Ivan Maryshev, from Prof. Erwin Frey's group at the Ludwig-Maximilian-Universität.

where ξ is a rotational Brownian noise term with a prefactor giving a path persistence length of $L_p = 100 \mu m$. Clearly, A represents the strength of the coupling with the nematic field and s the strength of the particle-particle interaction. A can be also thought of as a proxy for the actin nematic's concentration (or for the actin filament's length) as that mostly only affects the strength of the nematic alignment of MTs. Notice that if $s = 0$ (no interaction) particles behave as independent point-particles and only feel the torque by the nematic field. We assume that the particles follow the nematic field but that the nematic field is constant, as observed, except minor local deformations, in experiments. We generate the scalar field $\phi(\mathbf{r})$ either simulating it or by extracting the nematic field from TIRF images (see Methods 4.5)

As we only have access to a finite section of the full nematic, particles reaching the edge of the field are eliminated and inserted again randomly on the edge of the field to mimic incoming microtubules. The first 10 % of their trajectory is then eliminated from analysis to allow them to equilibrate.

2.6.6.2 Q-tensor based approach

We also developed a heuristic argument explaining why some trajectories and directions are selected and use it to predict trajectories using only information contained in the nematic field, or rather, in the nematic tensor \mathbf{Q} (see Section 1.3.1 for its definition). This approach relies on the observation that $+1/2$ defects mediate polar sorting by expelling microtubules preferentially in one direction, while otherwise MTs would move along the nematic director. We can then, from the divergence of the tensor \mathbf{Q} , obtain a polarity field able to predict what direction MTs will follow after they cross a $+1/2$ defect and then just elongate streamlines along the nematic field \mathbf{n} starting from a seeding position right after the defect. Thus this polar streamline heuristic prediction will consist of identifying this starting point and a preferred direction.

More in detail, for a given nematic field $\hat{\mathbf{n}}$ we compute the \mathbf{Q} -tensor. Defects' cores $\mathbf{r}^{+1/2}$ are identified as explained in Methods 4.5. For each point in the nematic field \mathbf{n} we can also define a polarity field $\mathbf{p} = (p_x, p_y)$ extracted from the divergence of the \mathbf{Q} -tensor with each component given by

$$p_\alpha = -\partial_\beta Q_{\alpha\beta} \quad (2.8)$$

where repeated indices ($\alpha, \beta = x, y$) indicate a sum, hence

$$\mathbf{p} = -(\partial_x Q_{xx} + \partial_y Q_{xy}, \partial_x Q_{yx} + \partial_y Q_{yy}) \quad (2.9)$$

The divergence of a tensor being a vector, it is, in this case, the only quantity able to describe polarity in the system, as, instead, both \mathbf{n} and its corresponding tensor would have nematic symmetry instead. The field $p(\mathbf{r})$ indicates the net direction filaments would tend to in a given region in the presence of distortions in the field. It somewhat summarizes in it both bend and splay deformations and returns a vector, i.e. it extracts the direction imposed by distortions in the nematic [Vromans and Giomi 2016; Pearce and Kruse 2021].

We then compute the field $\hat{\mathbf{p}} = \mathbf{p}/|\mathbf{p}|$ as the (normalized) divergence of \mathbf{Q} . In particular, in $+1/2$ defects, it can be used to define a (vector) defect axis predicting in which direction particles entering the defect will accumulate [Vromans and Giomi 2016]. More in detail, for

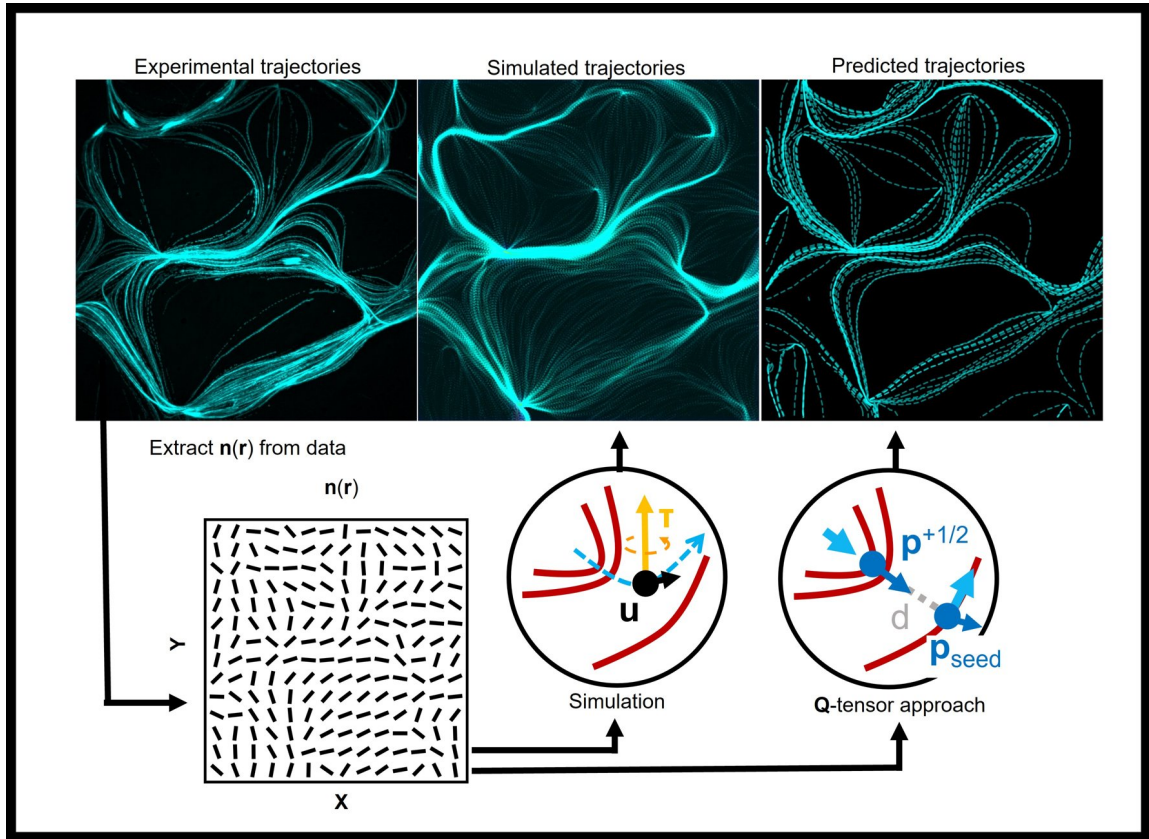


Figure 2.32: **Simulations and arguments based on the presence of $+1/2$ defects** By extracting the nematic field $\mathbf{n}(\mathbf{r})$ from experiments we can use simulations and heuristic arguments to understand how trajectories converge in specific portions of space and compare them with experimental results. We run simulations (top, middle) based on alignment of the particles on the local nematic field. The simulated trajectory (in cyan) evolves based on particles traveling in the nematic with a given speed in the presence of an aligning torque τ that forces them to follow the nematic field (as explained in main text). We also predict trajectories (top, right) by seeding starting points for streamlines (in cyan) in specific positions of the nematic field starting from the position $\mathbf{r}^{+1/2}$ of positive defects and shifting them by a quantity along their main axis $d\hat{\mathbf{p}}^{+1/2}$. This new seeding position is set as starting point of a stream with a direction chosen according to the quantity $\hat{\mathbf{p}}^{seed}$ as explained in the main text. In both cases, we recover with good agreement the experimental trajectories (top, left) of MTs. In this Figure we use as a benchmark the nematic field already shown in Fig. 2.28.A and B, at $1 \mu M$ Actin and $0.5 \mu m$ length. Each field of view is roughly $140 \times 140 \mu m^2$).

each defect, we compute its main axis $\hat{\mathbf{p}}^{+1/2}$ as the (normalized) value of the polarity field $\hat{\mathbf{p}}(\mathbf{r})$ averaged in a small region around the defect's core, i.e.,

$$\hat{\mathbf{p}}^{+1/2} = \frac{\langle \hat{\mathbf{p}}(\mathbf{r}) \rangle_{\mathbf{r} \approx \mathbf{r}^{+1/2}}}{|\langle \hat{\mathbf{p}}(\mathbf{r}) \rangle_{\mathbf{r} \approx \mathbf{r}^{+1/2}}|} \quad (2.10)$$

We can use all this ingredients to predict where microtubules will form lane. We make the following assumptions:

1. Filaments move following the nematic director unless they hit a $+1/2$ defect. A positive

defect will accumulate them and eject them along its axis $\hat{\mathbf{p}}^{+1/2}$.

2. When reaching the core of a $+1/2$ defect in position $\mathbf{r}^{+1/2}$, because of self-propulsion, we expect the filament be ejected from it and end up at a distance d from the defect's core, along the defect's axis. Filaments thus end up in position $\mathbf{r}_{seed} = \mathbf{r}^{+1/2} + d\hat{\mathbf{p}}^{+1/2}$. This position will act as a seed for further motion.
3. Filaments ejected from the defects immediately align with the local nematic field $\mathbf{n}(\mathbf{r}_{seed})$ at the seeding position. Clearly, filaments would actually start aligning as soon as they leave the defect, so the distance d corresponds roughly to the mean distance traveled by a MT before realigning with the field after leaving a defect.
4. The direction the filament chooses between the two available ones (i.e., $\pm\mathbf{n}(\mathbf{r}_{seed})$) is given by the relative orientation between the polarity field $\hat{\mathbf{p}}$ at position \mathbf{r}_{seed} and the nematic director \mathbf{n} at the same position, i.e., the microtubule will attempt to turn as little as possible so the chosen direction along $\pm\mathbf{n}$ will be the one that is at a smaller angle with respect to $\hat{\mathbf{p}}$.

Operatively, we can then, for each identified defect i with a core in position $\mathbf{r}_i^{+1/2}$ with polarity axis $\hat{\mathbf{p}}_i^{+1/2}$, place imaginary particles at a seed position $\mathbf{r}_{seed} = \mathbf{r}_i^{+1/2} + d\hat{\mathbf{p}}_i^{+1/2}$ where $d = 2.5 \mu m$ is a phenomenological length indicating how much filaments overshoot a defect's core and it corresponds to roughly the length of one microtubule.

The particle then aligns with the local nematic field $\pm\mathbf{n}(\mathbf{r}_i)$. However, we can also define a precise orientation based on the polarity field $\hat{\mathbf{p}}_{seed} := \hat{\mathbf{p}}(\mathbf{r}_{seed})$, as the microtubules will align in the direction $\hat{\mathbf{a}}$ given by

$$\hat{\mathbf{a}} = \text{sign}(\mathbf{n} \cdot \hat{\mathbf{p}}_{seed})\mathbf{n} \quad (2.11)$$

i.e. with the direction of the nematic director with a smaller angle with $\hat{\mathbf{p}}_{seed}$. This assumption is justified by the fact that microtubules will bend preferentially according to the relative distortion between the defect's axis (and its projection on the seeding position $\hat{\mathbf{p}}_{seed}$) and the nematic field right after the defect's core as observed in experimental data. From then on, starting from the seed, particles just evolve along the nematic director unless they meet another $+1/2$ defect or leave the edge of the nematic field.

Following this approach, we are then able to predict the main trajectories just from the nematic field $\hat{\mathbf{n}}(\mathbf{r})$ by identifying $+1/2$ defects, computing the polarity of the lanes using the argument above and evolving the motion along the nematic field lines. Of course, this method fails to predict trajectories starting from defects outside the field of view and introduces trajectories coming from defects that are never visited by microtubules. Still, it allows to predict the experimental trajectories in almost all analyzed cases.

2.6.6.3 Results

Figure 2.32 shows a scheme of both approaches and an example of the results in terms of trajectories obtained compared with experimental ones. In both cases, the trajectories identified

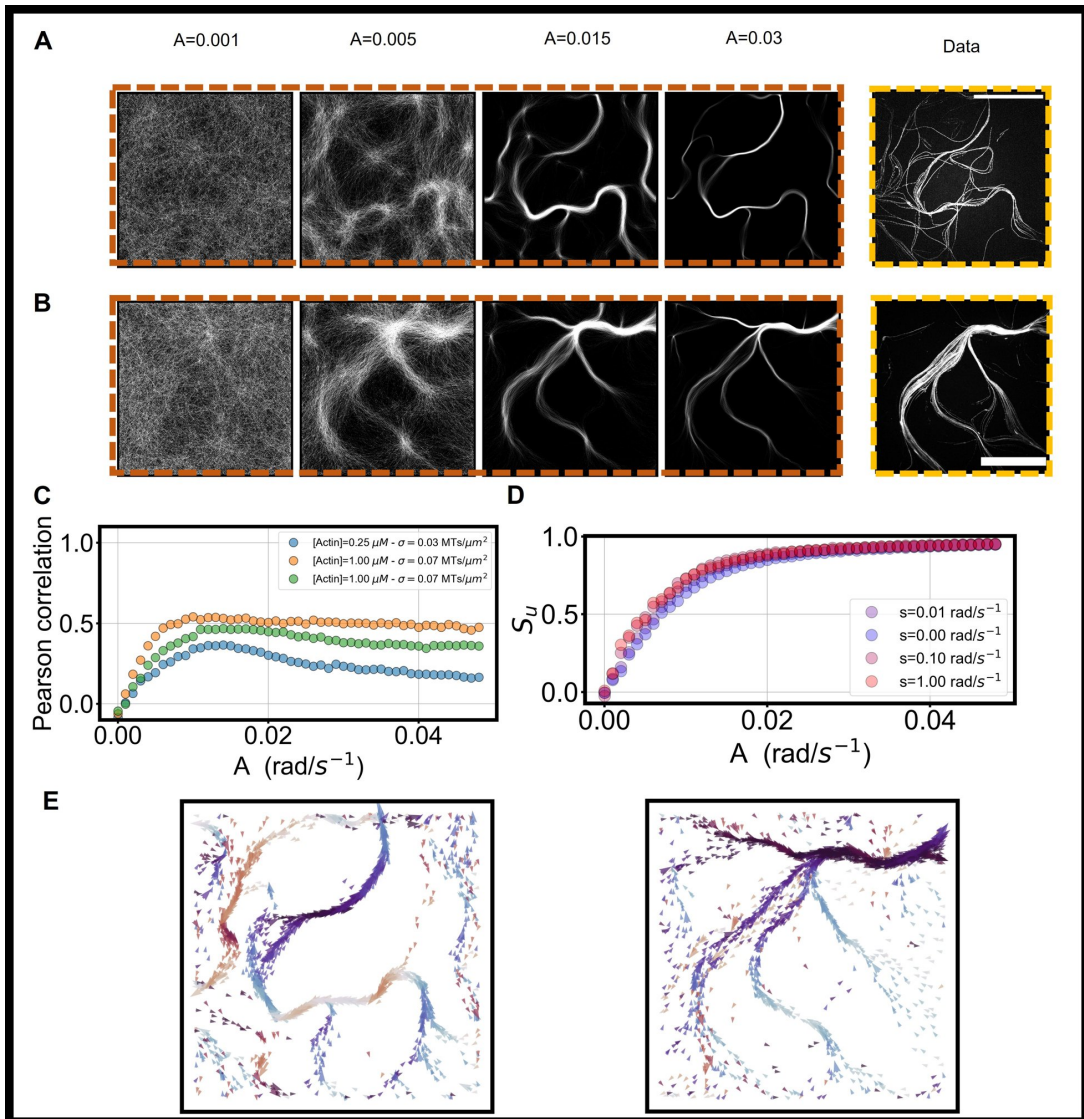


Figure 2.33: **Simulations of particles in a nematic field** A-B) Simulations (left) compared to experiments (right) of the same nematic field. As the parameter A is increased simulations show the system evolves from an isotropic to a laning state. Final conformations resemble experiments both at low (A , $\sigma = 0.003 \text{ MTs}/\mu\text{m}^2$) and high density (B, $\sigma = 0.007 \text{ MTs}/\mu\text{m}^2$). C) Comparing simulated and experimental data with the Pearson correlation coefficients shows that already at small values of the parameter A the simulations converge to the experimental data. At high A lanes become too 'thin' and the correlation coefficient can lower. Visual agreement remains. All datasets are at $1 \mu\text{M}$ Actin D) Adding interaction to the system, summarized by the parameter s does not influence the behavior of particles which still align strongly with the nematic field for $A > 0.01 \text{ rad/s}^{-1}$ regardless of s . Field used is the same as in E, right E) Simulations also recover the formation of polar structures, as shown by the orientation of the mean flow over time in a given position. Polar domains can be clearly seen, with particles all going in one direction same as in experiments. To be compared with Fig. 2.29 for the corresponding experimental data. Scale bars are $50 \mu\text{m}$ and again each field of view is roughly $140 \times 140 \mu\text{m}^2$.

correspond to the ones observed in experiments, suggesting the following arguments: first of all, the accumulation in lanes, i.e. phase separation in space, and the emergence of favored directions are not an effect of collective activity nor of the shape of the particles, but it is rather a direct result of the presence of a nematic field which forces the particles to align. Indeed, despite the field not having apparently any distinct symmetry, the presence of distortions and defects still shapes the microtubules' flow. Moreover, the information about the final state is contained in the nematic field and does not require any assumptions about the particles' motion if not the fact that particles align with the field and that they are able, due to their self-propulsion, to escape $+1/2$ defects along their axis before immediately re-aligning.

From simulations we can also extract the behavior of the system for different values of the couplings A and s . As A is increased, the system changes from an isotropic distribution up to a laning behavior consistent with experimental results. The experimental trajectories can be easily recovered both at high and low density (Fig. 2.33.A, B). We further quantify the similarity between observed and simulated trajectories by generating images with the time-projections from the simulations and computing its similarity with the original data using Pearson's correlation coefficient (see Methods 4.5 and Fig. 2.33.C).

We can also compute the mean value of the alignment between particles and field $S_u = 2\langle(\hat{\mathbf{u}}\cdot\mathbf{n})^2\rangle - 1$ averaged over all particles in the simulations and observe that for $A \approx 0.01 \text{ rad/s}^{-1}$ already most of the particles are aligned with the nematic field in simulations Fig. 2.33.D). These results hold for both experimental trajectories at low and high density, indicating that the used microtubules' density do not play a significant role in shaping the final patterns. Indeed, even the variation of the coupling s in simulations does not affect the results consistently. This is interesting as microtubules are sometimes seen interacting in experiments, especially when colliding in a $+1/2$ defect's core. However, such interaction is transient and does not lead to long-term effects as eventually the leading contribution to the formation of patterns still is the coupling with the nematic field.

Simulations also show the formation of polar lanes (Fig. 2.33.E) matching the experimental ones (compare with Fig. 2.29). Thus also the polar sorting is not an effect of the microtubules' density or interaction, but again, is only due to the presence of an external aligning field which, despite a microscopic nematic symmetry, leads to polar patterns. Additionally, the emergence of polar states is found stable even after motion reversal in simulations: by evolving the simulated system until lanes are forming and then abruptly flipping all the velocities $\mathbf{v} \rightarrow -\mathbf{v}$ it is observed that lanes first disassemble, as the local splay is now diverging rather than converging, but soon enough re-form in the same position and with the same polarity, indicating that the selection of a preferred polar direction is not due to fluctuations during equilibration. Instead, where polar lanes form, the selected direction is the only stable one. To further strengthen this latter point, we again remind that the \mathbf{Q} -tensor approach also allows to compute the polarity of the observed structures based only on the asymmetry between a $+1/2$ -defect's axis and the nematic field in its vicinity, which is the only relevant feature and it is completely a property of the nematic field. This latter approach also identifies correctly the main trajectories, indicating that $+1/2$ defects acts as funnels for the particles and that only trajectories at the end of such funnels are amplified, while the local polarity is given by the relative orientation of the defects and the nematic field. Apart from this, MTs just follow the nematic field and its distortions

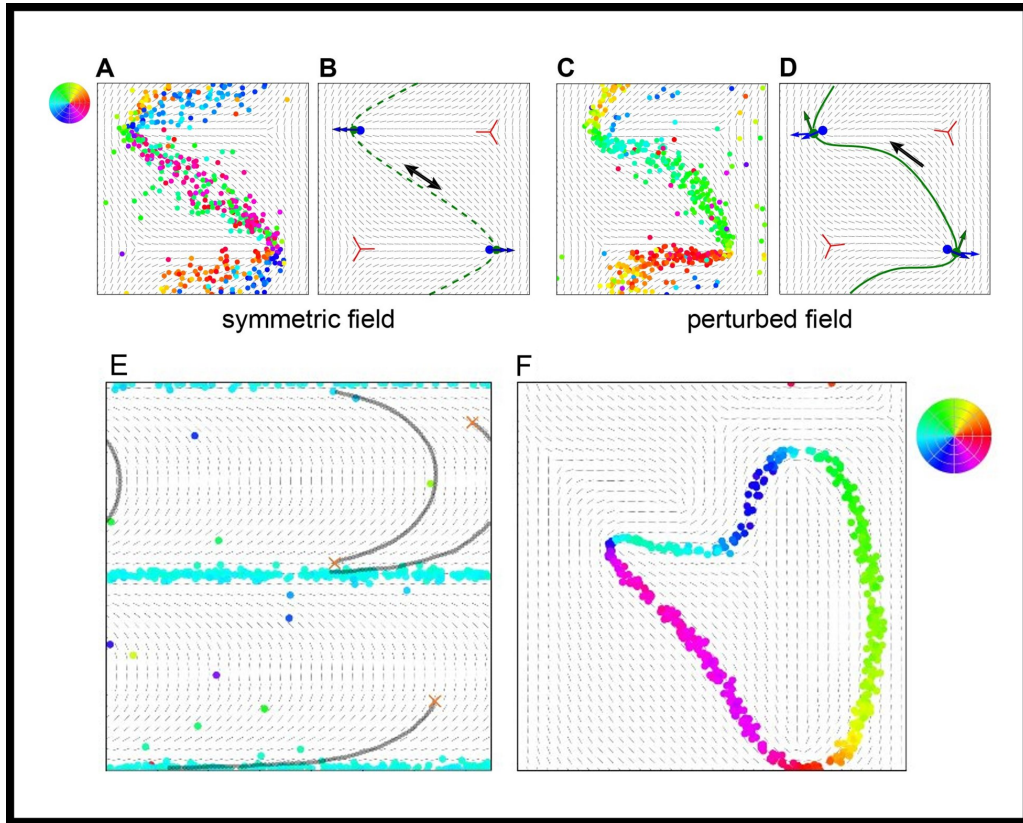


Figure 2.34: **Simulation and prediction out of artificial fields** A-B) A symmetric arrangement of defects leads to lanes with nematic symmetry both in simulations and using the \mathbf{Q} -tensor approach (B). C-D) Skewing the conformation so that the defects are off-axis with respect to the polarity field \mathbf{p} leads instead to polar lanes. E) A field based entirely on splay without defects can lead to polar lanes (see also [Turiv et al. 2020]). However, it is unrealistic in the case of self-assembled nematics where defects play the main role. F) Randomly-generated nematic fields recover most of the behaviors observed in experiments, including the looping conformations, in this case with $N = 1$ negative defect. Orientations are color-coded as shown by the color wheel.

and here defects' play again a role in shaping the MT's flow as shown already (see again Fig. 2.27 for example). We then also generate some specific defects' conformation to further test the two approaches. Figure 2.34 shows the main results. First of all, we simulated a field with 2 couples of $\pm 1/2$ defects in two different configurations shown in Figure 2.34.B and C. In the case in which defects are perfectly symmetrical (B), both simulations and the \mathbf{Q} -tensor based approach predict the formation of lanes made of particles accumulated by the $+1/2$ defects but such lanes result nematic. This is because, due to symmetry, $\hat{\mathbf{p}}_{seed}$ is perfectly perpendicular to the field \mathbf{n} at all points along the axis $\hat{\mathbf{p}}^{+1/2}$. Conversely if a perturbation is added so that the $+1/2$ defects' axis are skewed then along $\hat{\mathbf{p}}^{+1/2}$ one has $\hat{\mathbf{p}}_{seed} \cdot \mathbf{n} \neq 0$ and hence not only a lane arises but it is polar. This further proves the role of defects and their symmetry in creating polar structures. It is worth mentioning that the divergence of the \mathbf{Q} -tensor contains both the effect of bend and splay deformations. Pure, defect-less splay configurations are indeed possible. They can concentrate particles and lead to the formation of the polar stream [Turiv

et al. 2020]. To show it, we can generate splay-dominated conformations, see for example the results for $\mathbf{n} = (\cos(\pi y/L), -\sin(\pi y/L))$ in Figure 2.34.E. Bend deformations, on the contrary, can lead to the nematic stream (not shown) but not to polar sorting. However, in a realistic self-assembled passive nematic, deformations are typically localized around the defects, which are often more energetically favored than pure bend/splay. While splay and bend play both a role in experimental nematic fields, their behavior can be summarized by only considering the presence of $\pm 1/2$ defects and thus no patterning or formation of (possibly energetically unfavorable) splay-only based conformations is necessary to drive the flow along specific trajectories, as self-assembled defects are enough.

We further tested our approach to strengthen our understanding of the system by simulating artificial nematic fields. Fields are generated by evolving an (initially random) conformation according to the variation of the elastic Landau-DeGennes energy given by Equation 1.27 using however the one-constant approximation and writing it in terms of the tensor \mathbf{Q} (see Methods 4.5). Again, randomly simulated fields containing defects lead to the formation of polar lanes, with simulations and \mathbf{Q} -tensor based arguments agreeing on the outcome. We note that random generated fields indeed sometimes contain specific defects configuration observed in experiments, including for example the formation of the $N \times (-\frac{1}{2}) + (N + 1) \times (\frac{1}{2})$ configuration leading to loops, such as the one shown in Figure 2.34.F (for $N = 1$) which perfectly resemble observed conformations in the experimental setup (see for instance Fig. 2.28).

2.6.7 Discussion

In this section we proved that if particles move in a complex environment their motion can be severely affected. In particular, we studied the case where particles move under the constraint that they must follow the field lines of a passive nematic material. We proved, both by experiments, simulations and theory, that in this case there exist trajectories which act as attractors of the motion, i.e. in which most microtubules end up regardless of their initial conditions. Interestingly enough, such trajectories have a defined polarity, i.e. all particles moving in them have roughly the same orientation. Additionally, we identified in splay-based distortions of the field the origin for such behavior and in particular in $+1/2$ nematic defects. Nematic defects can also act together in shaping the field conformation such that microtubules loop or are preferentially gated in a given direction. Finally, using simulations and theoretical approach, we have identified several details of the system, including the minimum necessary alignment strength necessary, the role (or the lack of role) of particle-particle interaction and how much the information about the main trajectories is stored in the field itself. It turns out, that trajectories can be easily predicted by running a simple simulation model and/or by an approach based on seeding streamlines close to $+1/2$ defects. In this latter context, positive defects again act as gates for tuning polar order or rather as lenses that focus trajectories along specific streamlines, whereas the rest of the evolution of the trajectories is due to defect-based distortions in the field, due also to $-1/2$ defects. This all proves that whatever the microscopic details of the particles' motion, as long as a (even small) alignment with a nematic field is present, their motions can be predicted and possibly tuned.

This suggests strategies to control the microtubules' (or any active particle's in a nematic environment) trajectory, for example by patterning the surface with a given configuration of

defects. Previous studies had identified defects and splay as a up-concentrating and polarity sorting mechanism [Genkin et al. 2017; Turiv et al. 2020] in the case of wet active matter (swimming bacteria). Here we further prove that even a randomly self-assembled field is capable of such and that it works also for dry active matter, where hydrodynamics does not play any role and the field configuration is stable in time. Self-assembled nematics, containing defects, are much easier to assemble and do not require any patterning. Additionally, defect-based distortions are energetically more favorable than pure-splay ones. Indeed, actin nematics have been already studied [Murrell and Gardel 2012] as also was their interplay with microtubules in terms of rigidity [Zhang et al. 2018]. This system might then also serve to study the interplay between the actin and the microtubule cytoskeleton and how that affects their motion and activity [Farhadi et al. 2018].

The fact that a nematic environment could lead to the accumulation of particles moving in it in specific positions of space and with a given orientation might be a mechanism that the cytoskeleton and biological system in general use to regulate its self-organization. There exist a number of biological processes which take advantage of local nematic environments, such as the formation of the mitotic spindle, in which microtubules are locally aligned and motors move on them, or the self-organization of the organism *Hydra* which is able to decide, during development, where to grow a foot and where to grow a head depending on the positioning of nematic defects of a nematically-aligned actin meshwork [Maroudas-Sacks et al. 2021]. Additionally, bacterial colonies when forming biofilms and epithelial cells are also known to aggregate into nematic material, which would suggest on the one side, that they might exploit their nematic director as a mechanical cue to interact with each other and transport nutrients. On the other hand, this results also suggest strategies to target biofilm growth with efficient drug delivery based on the nematic order of the colony itself [Doostmohammadi et al. 2018].

An open question remains, what would be the behavior of microtubules in a different topology, e.g. inside a GUV, where topological constraints fix the total charge of the defects to +2 and would thus lead to topologically protected trajectories, keeping a constant amount of charge inside. Again, as we have seen, topology and confinement might lead to unexpected results while also better mimicking a realistic situation. This issue will definitely be further explored in the near future.

2.7 Conclusions of Chapter 2

This chapter has dealt with the self organization of cytoskeletal filaments gliding under different conditions. In particular we have addressed three main aspects of self-organization: the role of steric interaction and flexibility (Section 2.4), the role of confinement in spherical geometries (Section 2.5) and the role of a complex environment, in the form of a nematic material (Section 2.6).

A feature all this system feature is that, due to the presence of steric interactions, filaments assemble into polar structures, despite a microscopic nematic symmetry. In the case of actin gliding on a SLB or in a GUV, the steric interaction lead to the formation of elongated polar structures. Under confinement, such structures assembled into vortices that act as stable attractors. On the other hand, in the case of MTs gliding in a nematic material, steric interaction are necessary to enforce an alignment torque between the material and the MTs, so that specific trajectories, encoded in the field conformation, were selected leading to accumulation of microtubules along specific lanes. This suggests that steric interaction must be carefully considered when SPRs systems are modeled. Despite this, only recently have systems featuring them been studied [Jung et al. 2020; Moore et al. 2020].

Another feature shared by these systems is the fact that topological defect-like conformation have been confirmed as a very efficient polar-sorting conformation. This effect has never been observed before, if not in [Genkin et al. 2017] where it only lead to up-concentration of particles in the core rather than in polar structures. Here, a difference must be underlined between the actin system, in which defects were transient, and the MT system, in which defects were stable. In the former case, defects were acting as wedge-like obstacles, trapping filaments, polar sorting them and only after the disappearance of defect releasing them in the form of a comet-like stream. In the latter case, instead, defects were actually acting as a polarity-funnel, not only upconcentrating filaments in the core but also ejecting them again in the nematic field. As nematic-like structures featuring defects are ubiquitous, these results suggest strategies to better understand their role and to exploit it for efficient matter transport. Examples include epithelial cells in which defects can lead to the expansion of the tissue in 3D, bacteria forming bio-films or clusters, the cytoskeleton of *Hydra* during development, etc. see Doostmohammadi et al. 2018 for a comprehensive review.

All in all, these results again confirm the actin and microtubules gliding assay as a powerful and versatile yet simple systems to explore the formation of collective patterns in biology, and in physics in general. In addition, membranes (SLBs and GUVs) provide the possibility of studying them in new conditions (strong steric interactions, confinement, etc) which not only might mimic more closely what happens *in vivo* but also allow us to explore new physical behaviors such as the formation of polar systems composed of cytoskeletal filaments.

Chapter 3

Pushing on a membrane

Active microtubule fluids and their confinement inside lipid vesicles

Contents

3.1	Introduction	105
3.2	Active microtubule fluids (AMFs)	107
3.3	The interplay of activity and connectivity in AMFs	113
3.4	AMFs under confinement and active GUVs	128
3.5	An active microtubule fluid deforms lipid vesicles	133
3.6	Conclusions of Chapter 3	150

3.1 Introduction

In the previous Chapter, we have discussed gliding filaments as a form of self-organizing system composed of cytoskeletal filaments. Indeed, motors walking on filaments or, depending on whether they can freely move or not, pushing them is one of the main processes cells use to regulate their activity. Additionally, we have mostly studied two-dimensional systems (despite an hint at different topologies and despite the presence of a complex environment). Finally, we have claimed that the class of processes we were studying were part of the so-called *dry* active matter, i.e., composed of elements that interact locally and for which hydrodynamic interactions play a negligible role.

In this chapter, we reverse some of these elements. We are going to explore the behavior of active fluids composed of cytoskeletal filaments, specifically microtubules. Active microtubule fluids are a relatively recent class of bio-materials composed, in general, by microtubules and microtubule-associated motors and crosslinkers. Despite technically being rather an active gel composed of filaments, motors and crosslinkers, because the activity leads to a continuous re-arrangement of the microscopic structure these systems are often classified as fluids and

described by hydrodynamic theories. Their basic mechanism is still based on an energy input provided by molecular motors (specifically, the processive motor kinesin-401). However, this time, the motors will be freely diffusing, will bind on two filaments at the same time and propel them using each filament as an anchor for pushing the other one. This results in a *bulk* fluid (or active gel) of microtubules (hereafter named active microtubule fluid or AMF) that is inherently in three dimensions and is producing macroscopic flows. It is then an example of *wet* active matter, in which different parts of the system affect each other by long range interactions.

The aim of this chapter is first to describe and characterize AMFs. We will do that by reviewing their main properties and then by studying a particular system more in details, attempting to understand how one can go from a microscopic motor-filament-crosslinker interaction to the formation of macroscopic flow. In the second part of the Chapter, instead, we will go back to a membrane-based system, specifically GUVs, and encapsulate inside them an AMF. This latter system is a counterpart to the gliding-in-GUVs system we discussed in Section 2.5: the AMF indeed is completely detached from the membrane and moves in bulk. Because of its extensile activity and because of confinement however, it will affect the membrane (pushing on it) and it will be affected by the membrane (collapsing on its surface during extension). The interplay between this two processes leads to large deformations of the GUV membrane and, in turn, to a rearrangement of the AMF inside it. We will study both the membrane and the MT separately and attempt to understand their connection.

One of the fundamental factors on which AMFs' popularity is based is the fact that they attempt to mimic the self organization of biological systems based on microtubules' extensility (e.g., the mitotic spindle that separates chromosomes in cells). However, they are often studied in bulk, in great quantity and in un-physiological conditions. Their interaction with membranes and their confinement inside cell-like containers is instead poorly studied. Here we make a first step towards an integration between two popular model system (AMFs and GUVs) in order to study cytoskeletal active systems in a more realistic setting.

3.1.1 Chapter outline

In this Chapter we first revise the main microtubule based systems that form AMFs. This is done in the first Section of the Chapter. We then proceed to describe two main results about microtubule fluids: first, in Section 3.2 we attempt to bridge the microscopic description of the system with the most common hydrodynamic theory, using an experimental system composed of microtubules, kinesin clusters and a peptide derived from the protein anillin which is found to bundle microtubules. We complement experimental results with simulations. Finally, in Section 3.5 we use the same system, encapsulating it inside GUVs, meaning imposing some (elastic!) confinement, to study both the membrane deformations and the effect confinement has on the fluid and to try to connect the two again using a simulated system.

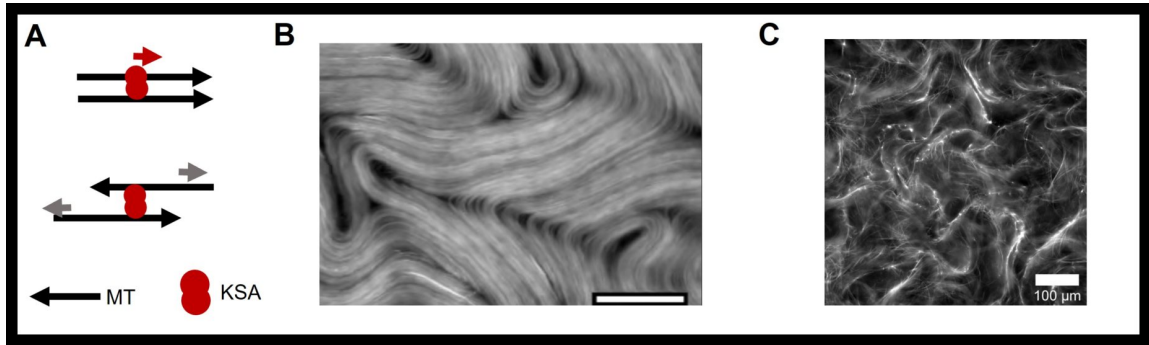


Figure 3.1: **Schematic of AMFs:** A) A KSA (Kinesin cluster) can walk on polarly oriented microtubules, but instead extends anti-polar couples. B) At high MT density, an active nematic material is formed, featuring active defects. Taken from [Sanchez et al. 2012]. B) At low MT density, but in the presence of crosslinkers, active extending bundles form.

3.2 Active microtubule fluids (AMFs)

3.2.1 Basic mechanism

The basic mechanism of the here presented active microtubule fluids (AMFs) is kinesin-derived extensile stress. As already discussed in Section 1.2.1.2, kinesins are a plus-end directed, processive motor found in dimer form that binds to a single MT. In order to form an active fluid, two kinesin (specifically, kinesin-401) dimers are bound together using a biotin-streptavidin tag forming a tetramer or cluster (KSA). In this form, kinesin can bind to two microtubules, with the following interaction rule: if both microtubules are oriented in the same direction (polar couple), the tetramer will walk on both microtubules at the same time while the microtubules themselves are not moving; if however the tetramer binds to two microtubules oriented in opposite directions (anti-polar couple) then each dimer of the cluster will try to move in an opposite direction toward the plus-end of their own filament. Since each dimer is however kept in place by the other one, this actually results in the microtubule pair extending, with each filament moving in opposite direction while the motors do not move. This results in microtubules moving in the direction of their minus end. The mechanism is sketched in Figure 3.1.A. In the right conditions, this process can go on over time resulting in collective large scale flow whose properties reside in several factors including the motors' and ATP concentration, the filaments' length, the amount of interaction between microtubules etc. [Henkin et al. 2014; Chandrakar et al. 2018]. This latter factor (i.e. interaction between filaments) is going to be fundamental in the following: indeed, if there is a lack of interaction between MTs, that must be kept close enough so that motors can bind, the system can not form collective flow. On the other hand, however, exceeding in the amount of filament-filament interaction introduces friction in the system, as motors have to work against the microscopic bonds.

There are two main class of AMF systems: a dense one, in which filaments are above the Onsager isotropic-nematic threshold and therefore align locally, giving rise to a nematic material; a dilute one, in which filaments aggregate into long bundles that the KSAs extend and buckle. In this latter case the system phase-separates into an empty phase and a nematic

phase (the bundles) thanks to the presence of connectivity between filaments.

3.2.2 Active nematics

Active nematics are composed of short microtubules ($1 - 10 \mu m$, depending on the system), Kinesin-II clusters (or some other, possibly strongly-crosslinking MT-associated motor¹) and, if necessary, a depletant or a MT-crosslinker that forces the MTs together.

Such systems can be realised in 2D (pushing the microtubules on the bottom using a depletion force [Sanchez et al. 2012], see Fig. 3.1.B) or in 3D (using passive elongated particles such as *fd*-viruses to force the system above the nematic transition, which would otherwise require a too high amount of microtubules) [Duclos et al. 2020]. When the MT density is above the ordering threshold indeed the systems form a nematic material with the microtubules locally aligned. However, as discussed in Section 1.3.4, there are specific points in which no order can be defined because of an alignment mismatch i.e. there are nematic defects. In 2D defects are point while in 3D defects are lines². The striking characteristics of active nematics are that, because of the energy input at the microscopic scale, the system is dynamic and rearranges continuously, generating active flows but maintaining the nematic order. Defects in particular are found to be active and move. In 2D, $+1/2$ defects are found to move at high speed while $-1/2$ defects do not. Additionally, because of the energy input that can overcome the elastic barrier of defect formation, defects can nucleate (in pairs, as the total charge must be conserved) or annihilate (again, in pairs). When constrained on a surface with spherical topology, 2D active nematics are found to form defects such that the total sum is $+2$ (as dictated by topological constraints) which therefore can never annihilate and move on the surface of the sphere keeping a fixed distance between them [Keber et al. 2014]. In 3D, the systems forms closed defect lines (disclination lines) that again can shrink and disappear or can nucleate as their total charge is 0 [Duclos et al. 2020].

Microtubules-based active nematics have then inspired a great number of experimental systems all based on the formation of nematic materials with an activity input at the micron scale, which includes diverse systems from swimming bacteria to crawling cells [Doostmohammadi et al. 2018].

3.2.3 Bundled active networks

If the MT concentration is below the nematic threshold *but* the interaction between particles is strong enough, MTs can assemble into bundles much longer than the average MT length [Henkin et al. 2014; Chandrakar et al. 2018; Nasirimarekani et al. 2021]. If a bundle contains anti-polar couples, they will extend and strain the bundle, which eventually buckles (because of an instability to bending in the case of active stress) and two shorter bundles are formed that can join other bundles so that the cycle goes on. These systems have been originally named bundled active networks (BANs) but are now mostly regarded as AMFs in general. The formation of bundles of aligned filaments, means that the system is nematic but only on a local

¹Motors can indeed also crosslink when walking on the filament, therefore, as discussed in the next sections, the separation between *activity* and *crosslinking* is a subtle one

²They *could* be points also in 3D, but point-like defects in 3D are not observed.

scale, i.e. that it phase separates into a disordered gas of filaments (outside the bundles) and a very ordered nematic phase inside the bundles (Fig. 3.1.C) as expected for interacting filaments at low density [Dogic et al. 2004]. BANs will be the main MT-based system of this Chapter.

3.2.4 Hydrodynamic theories: an overview

To describe AMFs (and active fluids based on local nematic alignment in general) one usually recurs to hydrodynamic theories [Ahmadi, Liverpool, and Marchetti 2005; Baskaran and Marchetti 2008; Marchetti et al. 2013; Shankar et al. 2018; Shankar and Marchetti 2019; Maryshev et al. 2019]. By postulating a microscopic interaction describing the way filaments, motors and crosslinkers interact one can then coarse-grain them and obtain equations which are not in terms of individual components but in terms of, usually, the concentration ρ , its flow \mathbf{v} and the local orientation of filaments \mathbf{p} . The local orientation can be summarized in the nematic \mathbf{Q} tensor introduced in 1.3.1 so that the active force acting on the system is proportional to the local order times a constant α describing the activity, i.e. $\sim \alpha \mathbf{Q}$. This assumption is based on the fact that, where there is nematic alignment there is activity. However, such an approach neglects the fact that locally, despite the order being nematic, there might be a fraction of filaments bound in parallel which do not contribute to the activity.

Of course the quality of the model will depend on the quality of the microscopic description and on the quality of the coarse-grain and its assumptions. In the following, we will challenge the most-used assumption that the flux of particles is a function of the local *nematic* order and show that *polar* contributions inside the system oppose activity. The reason for this resides in the fact that, microscopically, only *anti-polar* couples contribute to the energy input of the AMF and in their being less stable than polar ones if not enough cross-linking is provided to the system.

3.2.5 The microscopic origin of extensile activity

If a AMF contains enough filaments that motors manage to bind and form couples continuously, there is in principle no need for additional ingredients in the system. However, especially in dilute conditions, microtubules would not form bundles or even couples if not every now and then by chance and thus there is a need for some kind of interaction keeping MTs together. This is often supplied in the form of a MT-specific crosslinker, such as PRC-1, or using a depletant such as PEG or Methylcellulose and exploiting the depletion interaction.

Still, a simple picture in which crosslinkers keep the filaments attached while motors propel them is unsatisfactory for a number of reasons, including the fact that motors, when forming a couple and walking on it processively, also transiently act as crosslinkers and the fact that the interaction between microtubules, due to both motors and crosslinkers, also introduces friction in the system that the motors must overcome. Motor clusters, moreover, also affect differently the formation of polar couples, which they stabilize by walking on them and keeping them in fixed relative position, and of anti-polar ones, which are unstable as the motors dissolve them by extending them.

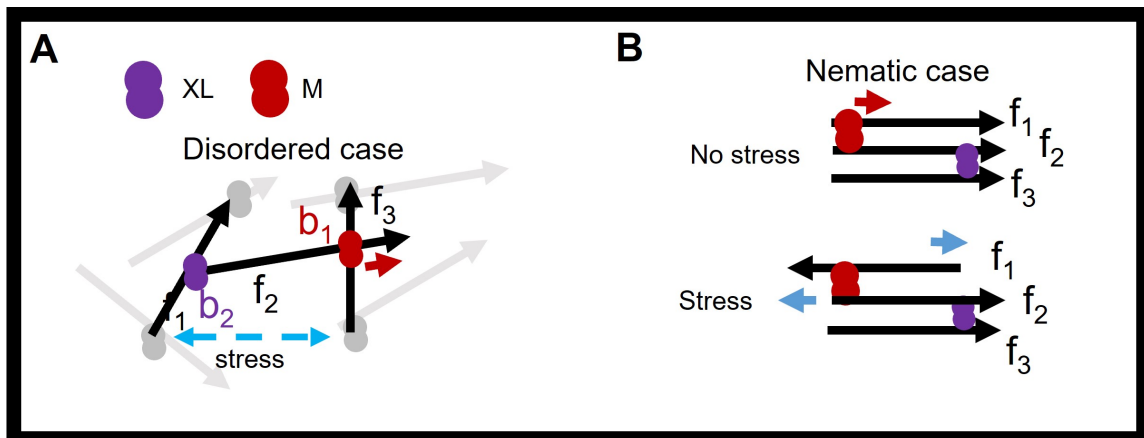


Figure 3.2: **Schematic of the χ parameter.** A) In a disperse network, the stress acting on it can be computed by counting active configurations. A motor (red) and a crosslinker (purple) together on a filament, if connected to the rest of the network (shown in gray) can exert stress depending on their relative position as the motor will try to walk and while the crosslinker will try to resist. B) In a nematic case, where activity arises from anti-polar couples, it is not enough to consider the configuration of motors and crosslinkers but also the relative polarity of the filaments.

The χ parameter In the following we will introduce an experimental system and some numerical simulation in the attempt to explain the emergence of activity in active MT fluids starting from the microscopic interaction between filaments, crosslinkers and motor clusters. Before doing that, it is worth going through the microscopic mechanism by which active fluids behave. The following model has been developed to describe filaments/motors/crosslinkers network in general and spawns from a big number of work on the activity of cytoskeletal networks [Bendix et al. 2008; Köhler and Bausch 2012; Prost, Jülicher, and Joanny 2015]. However we are going to discuss, after having introduced it, its validity in the case of AMFs.

Let us consider in a sparse, disordered, network of rigid filaments a configuration formed by three rigid, polar filaments f_1 , f_2 and f_3 and two binding elements b_1 and b_2 , which can bind the filaments together. The binding elements can be either a plus-end directed motor (able to move at a constant speed v_0) or a crosslinker, and they are positioned on the fibers at a relative distance a . We imagine the configuration is designed such that b_1 bridges f_1 and f_2 while b_2 bridges f_1 and f_3 . If the configuration is connected to the rest of the network by other binding elements, a change in the relative distance of the binding element b_1 and b_2 will be equivalent to a strain exerted on the whole network that would rather resist the change. The situation is sketched in Figure 3.2.A. Should b_1 and b_2 both be crosslinkers, their relative distance over time would not change as they are unable to move, so such a configuration produces no stress. The same, if both binding elements are motors, as they would both move towards the same plus end at the same speed without affecting the relative distance of the filaments. Therefore, the only configurations that will lead to a change in relative position of the binding elements, and therefore to a strain, are those containing one motor and one crosslinker. The motor will move on (for instance) f_2 and drag filament f_3 with it, while the crosslinkers will provide some resistance and filament f_1 will not move, resulting in stress in the system. If the motor is

closer to the plus-end than the crosslinker, the relative distance will grow at speed $\dot{a} = v_0$, hence extending the configuration, and otherwise it will shrink at speed $\dot{a} = -v_0$, hence contracting the configuration. Starting from this line of reasoning, a measure of the expansion (or contraction) rate of the system can be derived [Belmonte, Leptin, and Nédélec 2017], defined as

$$\chi = \frac{\sum_i p_i \dot{a}_i}{\sum_i p_i a_i} \quad (3.1)$$

where p_i indicates the probability of a given configuration (for example, of having a motor and a crosslinker at a distance a on the given filaments) and a_i the relative distance of the elements in such configuration. This values can be computed for a sparse network if the number of filaments and binding elements are known. The parameter χ is related to the expansion rate of the system volume V , as it can be shown $\dot{V} = \chi/3$. Hence $\chi > 0$ indicates extensile activity and $\chi < 0$ indicates contractile activity.

If the only possible configurations are the one mentioned above, only motors/crosslinkers couples are going to change relative position and hence for their configuration $\dot{a}_i = \pm v_0$, where the sign depends on their relative position. We can formulate then a statistical model by calling then the probability of finding each configuration, at a relative distance a , $p_{xx}(a)$, $p_{mm}(a)$, $p_{mx}(a)$ and $p_{xm}(a)$ where the subscripts indicate whether the two binding elements are a motor (m) or a crosslinker (x) and by convention the second subscript indicates the element closer to the plus-end. Using the approximation that $\dot{a} = \pm v_0$ for motor/crosslinker couples, depending on their order and 0 otherwise, we get:

$$\chi = \frac{v_0 \int da' p_{xm}(a') - v_0 \int da' p_{mx}(a')}{\int da' a' (p_{xx}(a) + p_{mm}(a) + p_{mx}(a) + p_{xm}(a))} = \frac{v_0 \int da' (p_{xm}(a') - p_{mx}(a'))}{\langle a \rangle} \quad (3.2)$$

from which one sees immediately that if $p_{xm}(a) = p_{mx}(a)$, for example if both are uniformly distributed along the filament, there can not be any extensile (or contractile) behavior ($\chi = 0$). So the extensile behavior of AMFs must reside in an asymmetry between motors and crosslinkers' distribution along a filament³.

The antenna model Such an asymmetry is indeed present if one takes into account the fact that motors can bind anywhere on the MT, but then move persistently on the filament towards the plus-end and thus there is a flux of motors on the filament increasing their density towards one end (antenna model, [Belmonte, Leptin, and Nédélec 2017; Mohapatra, Goode, and Kondev 2015]). Assuming motors move at a constant speed v_0 and have a rate of attachment k_{on} and of detachment k_{off} then one gets that the probability $f_m(x, t)$ of finding a motor at time t in position x along the filament is given by the probability that a new motors attaches there plus the probability of a motor being at time $t - dt$ in $x - v_0 dt$ that now reaches position x , which however must not detach for a time dt , hence

$$f_m(x, t) = k_{on} dt + f_m(x - v_0 dt, t - dt)(1 - k_{off} dt) \quad (3.3)$$

which we can expand for small dt and retain terms only of order dt obtaining

³We not that in the case of flexible filaments, this does not hold as filaments are allowed to buckle under stress.

$$\frac{df_m(x, t)}{dt} = k_{on} - k_{off}f_m(x, t) - v_0\partial_x f_m(x, t) \quad (3.4)$$

and by imposing a steady-state $\dot{f}_m = 0$ we finally get

$$v_0\partial_x f_m(x, t) = \frac{k_{on}}{v_0} - \frac{1}{\lambda}f_m(x, t) \quad (3.5)$$

where we used the run length $\lambda = v_0/k_{off}$ defined in .

The final solution is, imposing $f_m(x=0) = 0$ and assuming the filament is infinite

$$f_m(x, t) = \frac{k_{on}}{k_{off}}(1 - e^{-\frac{x}{\lambda}}) \quad (3.6)$$

which is also valid for a filament of length L , assuming the motors detach immediately at l , but has to be normalized accordingly. We also notice here that we assumed an infinite reservoir of motors and that they bind-unbind with a given kinetic. If a motor, once unbound, has the probability of re-binding with a rate k_r that amounts to an effective increase in the run-length given by $\lambda_{eff} = v_0/(k_{off} - k_r)$.

The antenna model shows that in the case of processive motors, assuming a uniform crosslinking density, one can recover an asymmetry in the xm and mx couples and obtain an extensile activity with $\chi > 0$.

Polar and antipolar pairs If one microscopic origin of extensility resides in the asymmetry between motors and crosslinker, the second one resides in the formation of anti-polar pairs of filaments, which are the only conformation that the motors can displace. If the network is sparse, the previous theory holds. However, in the case of nematic alignment, the relative orientation also plays a role in the generation of stress. For example, in the previous example, if f_1 , f_2 and f_3 are all aligned in the same direction, while it is true that the relative distance between a motor and a crosslinker changes over time such a change does not affect the filaments' conformation, which stay aligned. The motors will move along the two polarly aligned filaments without propagating any stress. On the other hand, if f_1 is oriented differently from f_2 and f_3 then a motor can extend the pair actually providing an extensile stress (Fig. 3.2.B). Because anti-polar couples form differently than polar couples (see next Section), as motors react differently on them, and because crosslinkers can mediate the formation of couples by stabilizing filaments, all these considerations must be adapted in the case of AMFs. This point will be the main object of the following Section.

3.3 The interplay of activity and connectivity in AMFs

Here we introduce an experimental system⁴ together with simulations, to shed light on the role of crosslinkers in the formation of extensile activity. In particular, we show that the behavior of an AMF can be tuned by the amount of crosslinkers present in the system. Clearly and trivially, a different amount of crosslinkers provides a different amount of friction, so the system is expected to slow down if too many are present.

On the other hand, a too low amount will not be enough to keep filaments together in a stable conformation. However, this is only part of the picture. What we will show, is that crosslinkers actually regulate the amount of anti-polar (and hence active) pairs inside the system and therefore a description purely based on the nematic order (polar and anti-polar indifferently) is unsatisfactory. This Section represents a further attempt to study, with a tunable experimental system and simulations, how one can bridge a microscopic description (of filaments, motors and binding elements) together with a macroscopic one (global flow) when local alignment (in particular, anti-polar one) is fundamental [Fürthauer et al. 2019; Lemma et al. 2020; Striebel, Graf, and Frey 2020].

3.3.1 Experimental system

We assemble a AMF using short, fluorescent, stabilized microtubules ($1.5 - 2 \mu m$) and kinesin clusters. Unless otherwise specified, we use 0.4 mg/ml MTs and 60 nM KSA. As a crosslinker, we add varying amount of a peptide derived from the protein anillin (ANLN) which we found bundles microtubules in a concentration-dependent way. Energy is provided in form of 2 mM ATP and kept constant using an ATP-regeneration system. The solution is then flowed into a small channel carved in parafilm and observed with an epifluorescence microscope. See Methods 4.6 for a full description.

3.3.2 Experimental results

First, we verify that ANLN bundles MTs. As we increase the ANLN concentration c_A indeed, bigger and longer bundles appear (Fig. 3.3.A, B).

The precise mechanism by which ANLN bundles MTs is at the moment unknown but we expect it to be an un-specific electrostatic interaction due to the high pI of the ANLN peptide ($pI \approx 10$ as measured from the ammino-acid sequence) that pushes MT together due to their negative charge. Still, the smooth concentration dependent effect ANLN has on microtubules makes it a useful tool in studying the effect of filament-filament interaction in a tunable way.

We then provide activity in the form of KSA. As we add kinesin clusters, the motors act on antipolar pairs and start extending the bundles. The resulting steady state depends on the ANLN concentration: if the ANLN is below a threshold of approx. $c_A < 0.8 \mu M$ the bundles dissolve and no large scale activity is observed; if $0.8 \mu M < c_A < 2 \mu M$ the systems starts moving and forms an active state resembling an active nematic material; if $c_A > 2 \mu M$ the

⁴This system has been presented to me by, and developed further with, Remi Boros and John Berezney, from Zvonimir Dogic's group at UCSB/Brandeis. I also thank again Ivan Maryshev (LMU) for more theoretical discussions on this subject.

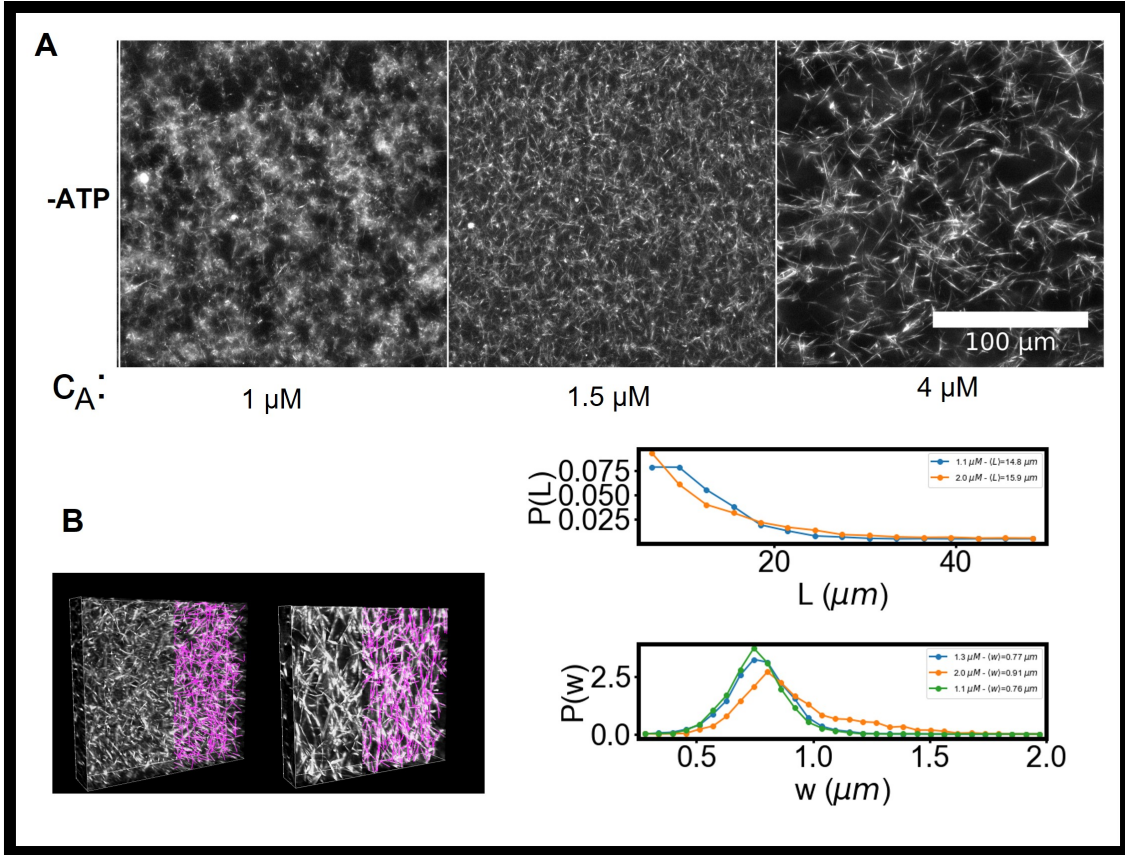


Figure 3.3: **ANLN bundles microtubules in a concentration dependent way** A) In the absence of ATP, as c_A is increased, the microtubules bundle. B) ANLN also tunes the network properties such as the mean bundle length and width. Each curve is at a different ANLN concentration (top: $c_A = 1.1 \mu M$ and $2.0 \mu M$, bottom: $c_A = 1.1 \mu M$, $1.3 \mu M$ and $2.0 \mu M$). Width and length are measured using SOAX [Xu et al. 2015].

system coalesces in thicker bundles whose speed decreases as the ANLN concentration is raised. Figure 3.4.A shows snapshots of the AMF at different values of c_A . These results indicate that ANLN, with respect to native MT crosslinkers such as PRC-1, allows a finer control over the bundling of microtubules probably due to the weak interaction it introduces that can be better controlled. For this reason, we keep using it in the following. We note here that results do not qualitatively change using PRC-1, as shown further on.

We monitor the behavior by computing the optical flow of the images over time which is equivalent to following the mass flow in the system (see Methods 4.7). We can hence verify that there is a sharp transition to activity at $c_A \approx 0.8 \mu M$, with the flow increasing linearly up to a maximum at $c_A \approx 2 \mu M$, before starting a slow decay as $c_A > 2 - 3 \mu M$. Hence the morphology of the system (disordered, quasi-nematic, bundled) correlates with the system's activity and both are tuned with the ANLN concentration (Fig. 3.4.B). We attribute the presence of a threshold in c_A to the fact that the fluid requires a minimum amount of crosslinking before collective flow is able to emerge. Below such threshold, motors extend the initial bundles but

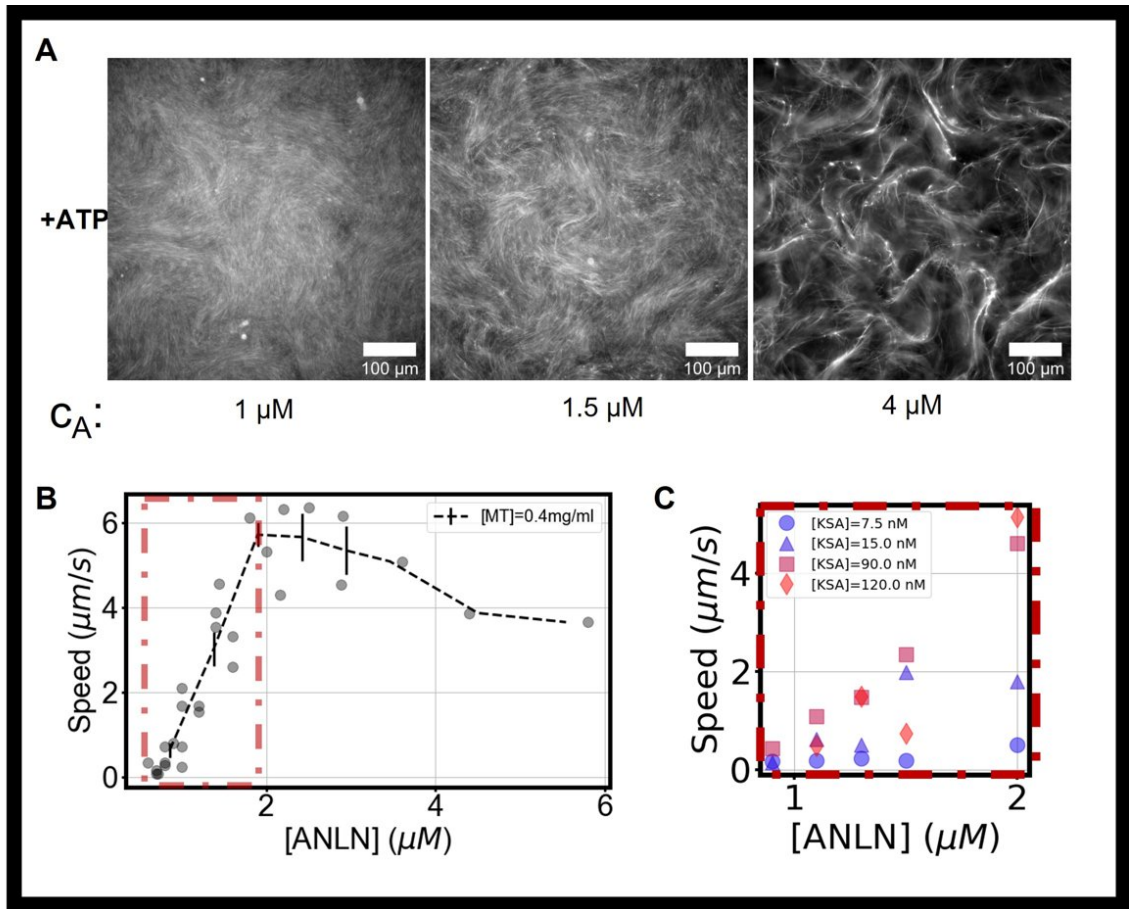


Figure 3.4: **ANLN tunes the morphology and activity of a AMF.** A) Upon ATP addition, the system evolves in a state whose morphology depends on c_A B) The mean flow speed as a function of c_A shows a sharp increase which eventually plateaus and the decreases C) Magnification of the sharp-increase area marked in red in panel C, now at different KSA concentrations

stable moving bundles can not re-form due to the lack of crosslinking.

To further test the behavior of the system, we can also tune the motors' concentration at fixed c_A or the ATP concentration. The former experiment shows that while a minimum number of motors is required for collective flow, a too high amount actually hinders it (Fig. 3.4.C). If the KSA is too low, the system will not show any activity. A threshold in activity is thus also present. Otherwise, adding motors will lead to an higher and higher speed and to a slight decrease of the connectivity threshold, consistent with the fact that motors also provide some connectivity. Similar results (both the presence of a threshold and a slow-down at high crosslinkers' densities) have been found in related systems [Henkin et al. 2014; Chandrakar et al. 2018]. This has been recently connected to the motors' crosslinking activity [Chandrakar et al. 2018]. The ATP-concentration data instead show that, as ATP tunes both the motors' processivity (i.e. their crosslinking ability) and their speed (see Section 1.2.1.2) we observe again a crossover between a low-ATP, slow, bundled state (where connectivity dominates) and a faster,

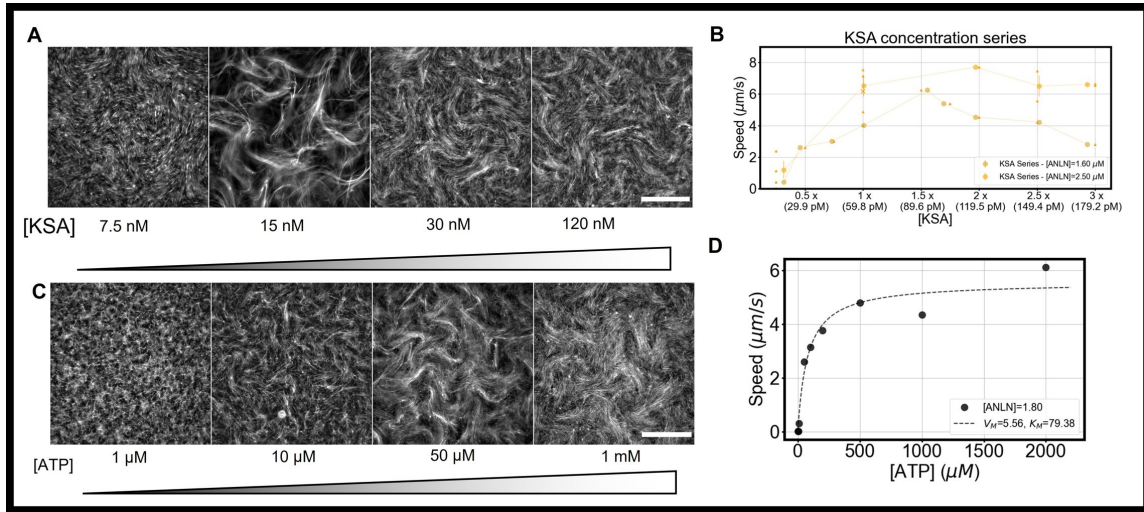


Figure 3.5: **ATP and KSA series** A-B) Morphology and dynamics of the AMF as KSA is varied. A too high or too low amount of KSA will slow the system down or will be insufficient for macroscopic flow. At intermediate KSA, the system is active. C-D) Morphology and dynamics as ATP is varied. At low ATP, activity is present but the system is slow and appears mostly composed of bundles. Increasing the ATP up to saturation leads to a faster and more nematic-like morphology. Both these results confirm the interplay between activity and connectivity. Scale bars are $100 \mu m$. All experiments are at $c_A = 1.8 \mu M$.

more nematic-like state where ATP is high enough that activity dominates. This proves that in the interplay between activity and connectivity can not be reduced to a simple crosslinkers and motors model in general, as they both interact in an entangled way (Fig. 3.5). This effect happens at fixed motors concentration c_A , their activity and connectivity being modulated by ATP.

Finally, we vary both the total microtubules' concentration and the microtubules/motors ratio. The results are qualitatively always the same, with a minimum amount of crosslinkers necessary for activity to arise and a decay in activity instead present at high c_A . However, the position of the threshold and the maximum speed are modulated by all factors (Fig. 3.8.A), proving once more how all parameters are entangled. Increasing the numbers of microtubules also lowers the activity threshold, most likely as the system is denser and therefore less crosslinkers are necessary to keep the filaments together. Instead, decreasing the number of motors per filament lowers the maximum speed. On the other hand, lowering the microtubules' concentration shifts the system further away for the ordering threshold and therefore more crosslinkers (per filament!) are necessary to keep the microtubules stably together.

In all the experiments carried out with fixed KSA concentration but varying c_A , it appears clear that ANLN is having a role in the formation of the active system. It is however not clear which one precisely. On the one hand, we can expect that at very low c_A the microtubules are not interacting enough and are disperse, only transiently binding to motors, whereas at high c_A a too high friction might be present that slows the system down. Why however does one notice a crossover from a low to a high activity mode close to $c_A \approx 0.8$ is not clear and also unclear is how this increase can be so smooth. One can still ask: what is the role crosslinkers

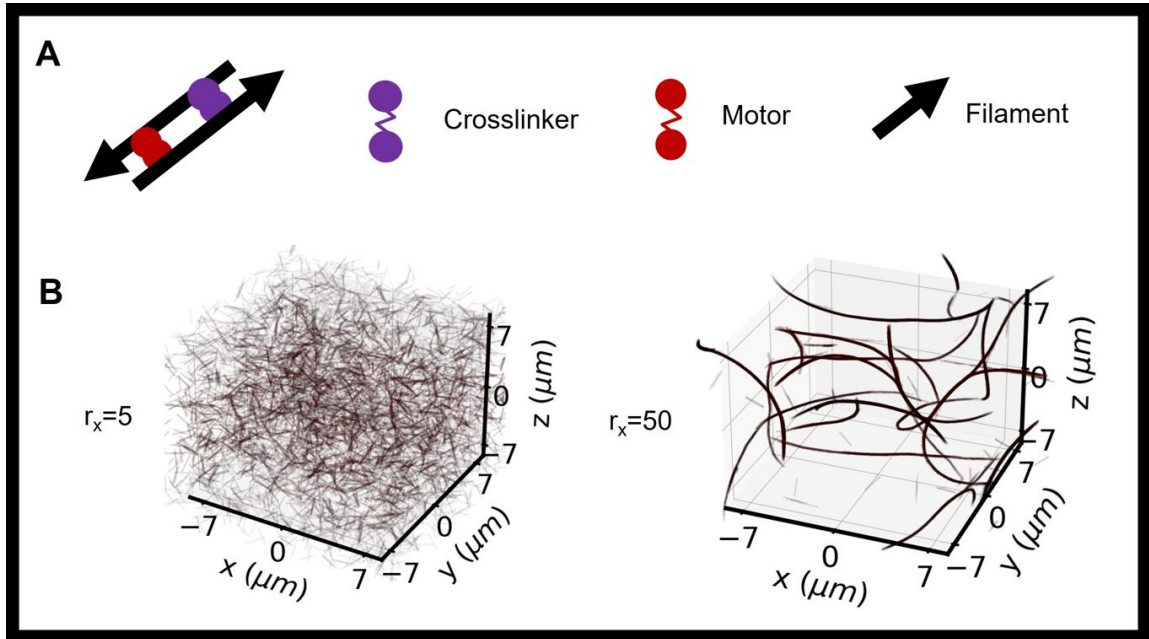


Figure 3.6: **Cytosim simulations recover the behavior of the AMF** A) Schematic of Cytosim simulations. N rigid filaments in a box of volume V with motors and crosslinkers. Motors and crosslinkers are modeled as springs which bind on the filaments. Motors can move on filaments. B) Snapshots of simulations ($N = 8000$, $r_m = 36$) at $r_x = 5$, showing no formation of bundles, and $r_x = 50$ showing formation of bundles which extend and buckle.

play in stabilizing the collective activity of a AMF at constant motors' concentration? How can this counter-intuitive effect be possible, in which adding a crosslinker, which we expect to lower activity, instead slightly modulates an *increase* in activity?

Starting from the discussion in Section 3.2.5 we have a hint that the effect of ANLN must be related in allowing for extensile conformations to be more stable, i.e., it must affect the formation of stable anti-polar pairs.

3.3.3 Cytosim simulations

3.3.3.1 Description of the model

To shed further light on the microscopic role of crosslinkers, we ran simulations using the open-source software Cytosim [Nedelec and Foethke 2007]. The system is modeled as N rigid polar rods of length L and (steric) diameter d in a box of volume V with periodic boundary conditions. N_x crosslinkers and N_m motors are also present. Crosslinkers and motors are modeled as springs that can bind two filaments together and are characterized by their on- and off-rates. Motors can also move towards the plus-end of the filaments with unloaded speed v_0 that is however modulated by the force acting on them according to the force-speed relationship described by Equation 1.11. Both motors and crosslinkers are characterized by a given spring constant and equilibrium length and can detach under strain. The precise values, together with a sample

code, are described in Methods 4.8.

We can also define the filament-to-crosslinker and filament-to-motors ratios

$$r_x = N_x/N \quad r_m = N_m/N$$

and the volume fraction

$$\Phi = N \frac{\pi L d^2}{V}$$

We set the volume fraction to resemble experimental values by setting:

$$L = 1.5 \mu m, d = 25 nm, \Phi \approx 7 \cdot 10^{-4} \text{ and } r_m = 36, v_0 = 0.6 \mu m/s.$$

Figure 3.6 shows a schematic of the simulation and snapshots at different values of r_x .

From the simulations we can extract a number of information. As an activity measure we choose different observables including

$$\alpha = -\frac{\langle \mathbf{n} \cdot \mathbf{v} \rangle}{v_0} \quad (3.7)$$

where \mathbf{n} and \mathbf{v} are respectively a filament's orientation and speed, averaged over all filaments and over time too. The parameter α describes the relative amount of speed in the filaments' main axis direction. If the filament is diffusing, we expect $\alpha \approx 0$ whereas if the filament is propelled by a motor at unloaded speed we expect $\alpha = 1$.

We also observe the mean squared displacement (MSD) of filaments as a function of r_x and extract the scaling exponents β , defined as the exponents of

$$\langle (\mathbf{r}(t + \tau) - \mathbf{r}(t))^2 \rangle_t \sim \tau^\beta \quad (3.8)$$

where \mathbf{r} is the position of filaments and the average is run on all filaments over the full simulations (except an initial equilibration time). We compute β both at short ($\tau < 10 s$) and long ($\tau > 30 s$) times. The former gives an indication about whether MTs are diffusing, the second one whether they move at longer times and if their motion is ballistic or diffusive on longer timescales.

3.3.3.2 Simulation results

We now analyse the main results of the simulations. We use as reference values close to the experimental case ($N = 8000, V = 8000 \mu m^3, r_m = 36$).

Activity The main result is that, as in experiment, the system does not exhibit collective motion if $r_x < r_x^t \approx 10$ i.e. if the number of crosslinkers is below a given threshold value. Additionally, as r_x is further increased, the systems eventually slows down. The same behavior is observed for different values of the volume fraction Φ and of the motors' fraction r_m , with the threshold value depending on those parameters ($r_x^t = r_x^t(\Phi, r_m)$). Interestingly, two phases can be observed. In the first one ($0 < r_x < r_x^t$) the activity lowers as r_x is increased and the systems seems to gelate, forming long immobile bundles. Thus the initial addition of crosslinkers actually hinders motion and decreases diffusivity rather than allowing collective

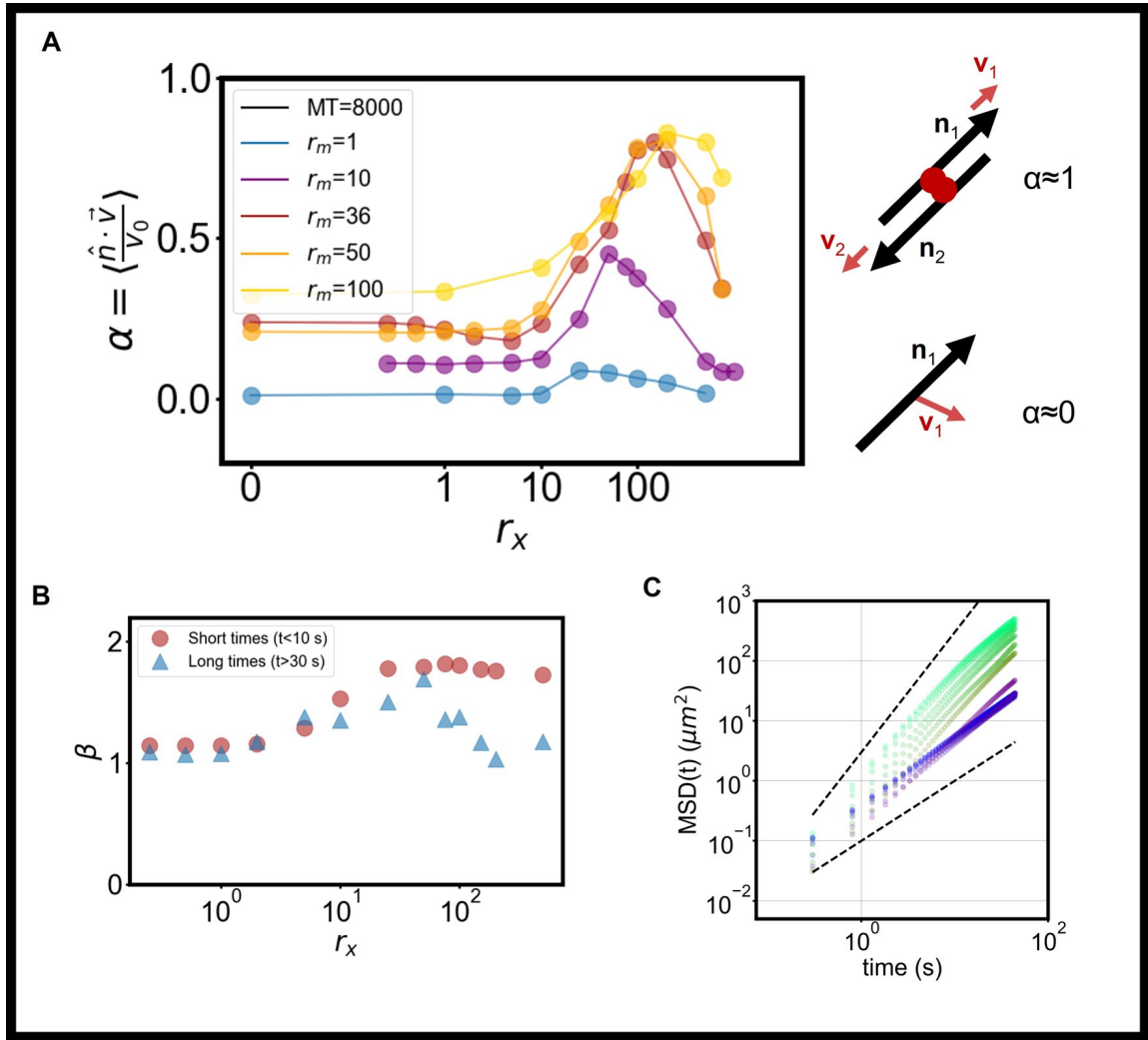


Figure 3.7: **Cytosim simulations recover the behavior of the AMF** By measuring the activity parameter α , indicating the fraction of filaments moving along their axis, and the coefficient β of the MSD at short (circles) and long (triangles) times we can characterize the behavior of the system. A) The parameter α , which is 1 for filaments sliding along their axis and 0 for filaments diffusing or not moving as shown in the scheme, is computed at different values of r_m , from 1 (blue) to 100 (yellow). As motors increase, the activity gets higher and the peak shifts slightly. A small decrease in activity is seen between $r_x = 1$ and $r_x \approx 10$. B) MSD scaling parameter β also indicates a transition from diffusive to ballistic at $r_x \approx 10$ (shown for $N = 8000$, $r_m = 36$). C) MSD curves (with diffusion and ballistic scaling), color-coded using the color-map shown in Fig. 3.12.

flow. However, once $r_x > r_x^t$ the system very quickly increases in activity and collective flow emerges, with bundles breaking and becoming unstable under buckling due to extensile stress. Again, however, as the number of crosslinkers is increased, the systems slows down as too many crosslinkers hinder motion. This latter point was also studied in [Lera-Ramirez and Nedelec 2019] for only two microtubules binding to a different amount of motors and crosslinkers, with the conclusion that the filaments' speed decreases as crosslinkers increase. However, the initial

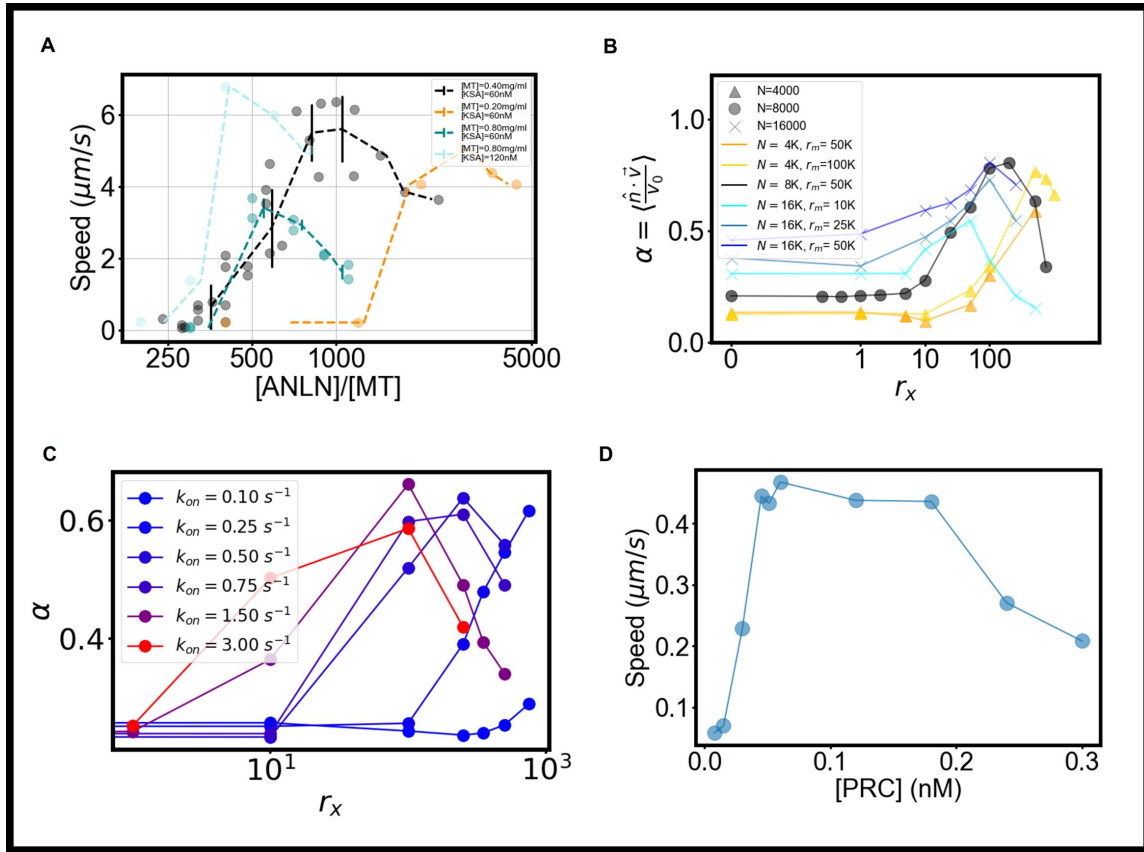


Figure 3.8: **Experiments and simulations in different conditions** A) As we change the ratio of motors to microtubules and of crosslinkers to microtubules, the results look qualitatively the same (with the presence of a threshold activity) but both the position of the threshold and the mean flow speed are modulated. B) Cytosim simulations recover all trends. Plots are color coded so that similar conditions have the same color. C) Cytosim simulations allow to also mimic the behavior of different crosslinking strength by changing the attachment rate k_{on} . Results show that stronger crosslinkers require a smaller amount (lower r_x) for activity to arise and at the same time the decrease in activity at high r_x is shifted to lower values. The initial transition is also sharper. D) A stronger crosslinker mimics the behavior of the MT-native crosslinker PRC-1 that requires smaller amounts to bind MTs and leads to a sharper transition to activity.

decay of the speed we observe and the consequent increase as r_x grows is a direct consequence of the collective (but dilute) state of the system and can not be captured by single-filaments' models.

We can track the activity of the system plotting different activity parameters such as α and β . All parameters show the same general behavior, however slightly differ since both are biased in different directions: α does not take into account the transverse motion due to buckling, the flow is hindered by diffusion at low r_x while the MSD only considers local activity and gives no information about the collective flow at short times. On the other hand, α indicates the presence of extensile activity and hence that filaments are moving slower with respect to each other at high r_x . Instead, β indicates that filaments are diffusive below $r_x \approx 1$, then slowly start

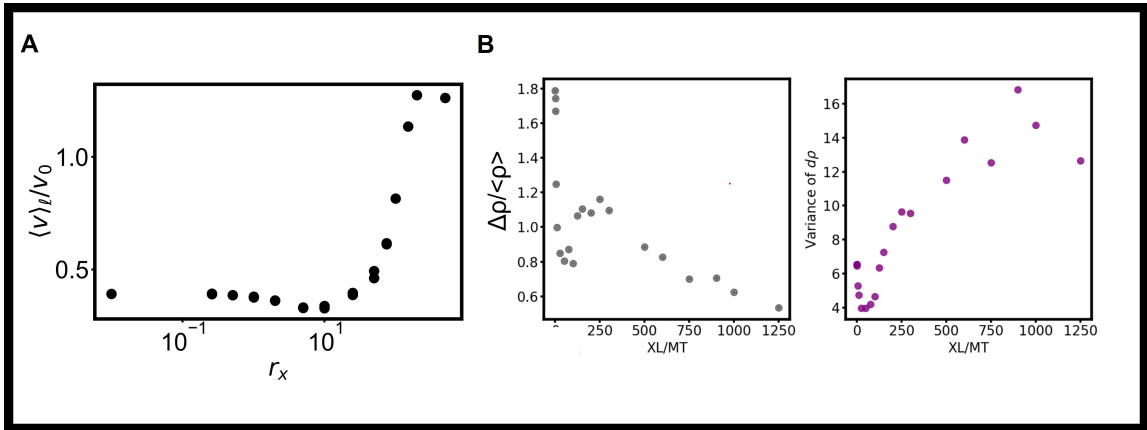


Figure 3.9: **Different activity measures** A) Flow of microtubules averaged in space. B) Variation of filaments' density in space and its variance. Both measures indicate a similar behavior, i.e., that the system, as r_x increases, first starts to gelate, the transitions to an active state and eventually slows down due to friction from the crosslinkers.

moving persistently at short times as r_x increases. Above $r_x \approx r_x^t$ the local motion of filaments is ballistic, as filaments slide relative to each other and only a small slow-down is visible at high r_x . Instead, their long-time motion at high r_x is diffusive again as the bundles start buckling.

All measures concur that at $r_x \approx r_x^t$ a transition takes place from a slowing-down regime to a global motion one. The results are summarized in Figure 3.7. The results mimic closely the behavior of the experimental AMFs. In particular, we manage to replicate an increase (and then decrease) of activity (α) depending on the concentration of crosslinkers r_x . Additionally, we also recover the behavior of experiments where the motors/crosslinkers ratio or the microtubules/motors ratio is varied (Fig. 3.8.B). Simulations also allow to model different kinds of crosslinkers. We thus also change the attachment rate k_{on} of the simulated crosslinkers and show that in all cases we observe the same behavior, again with the activity threshold shifting towards lower values if the crosslinker is stronger ($k_{on} \approx 3 \text{ s}^{-1}$). This results confirm that our conclusions will hold also for different kinds of crosslinkers, and indeed a measurement carried out with the native MT-crosslinker PRC-1, one of the most used one [Duclos et al. 2020; Chandrakar et al. 2018], shows the expected trend, with a threshold in activity and a decrease at high concentration of the AMF's speed (Fig. 3.8.C, D).

Different activity measures replicate the result We also compute different quantities from simulation to get a broader picture of the system's behavior. In particular, we compute the flow $|v|_l$ (as the mean speed of filaments averaged over time inside a box of length $l = 2 \mu\text{m}$) or the mass flow $\Delta\rho$ (as the variation in number of filaments entering or leaving a region in space, specifically, again a box of side l). These quantities are more related to the experimentally observable one as they rely on macroscopic features of the system rather than microscopic ones. They all confirm that there are two phases as r_x vary: one in which the activity lowers slightly (as if the system were gelating) and one in which activity kicks in again, until reaching a maximum value and then decreasing again. While the first part is not easily visible in experiments due to

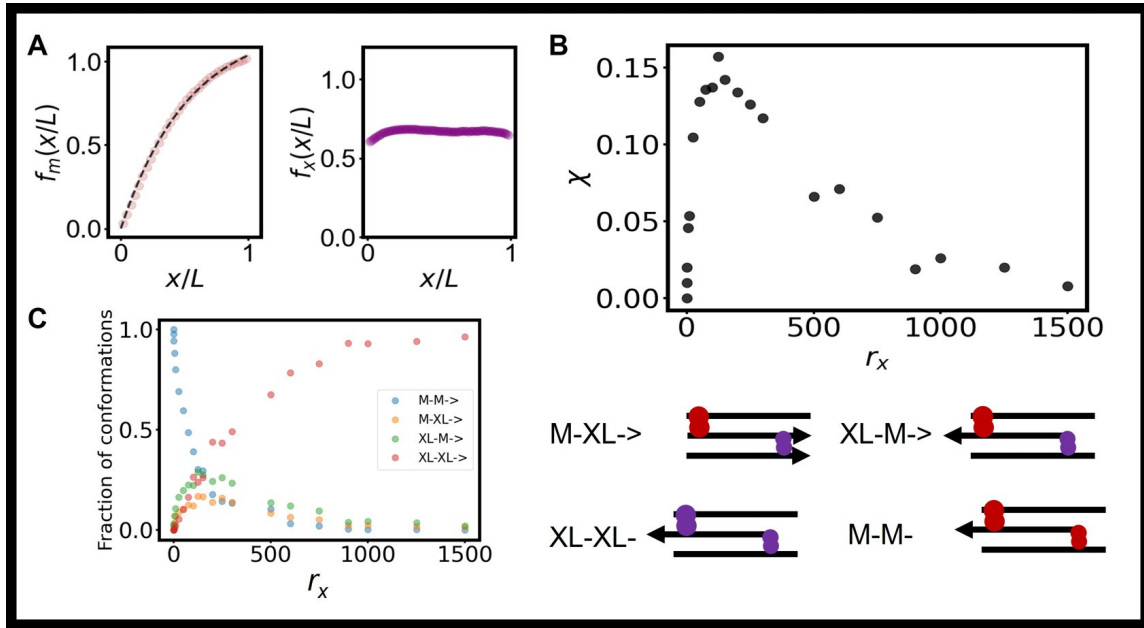


Figure 3.10: **Antenna model and χ computed out of Cytosim simulations** A) Distribution of motors f_x and crosslinkers f_m on a filament ($N = 8000$, $r_m = 36$, $r_x = 200$). The motors follow the antenna model fit. B) Computation of χ shows no correlation with activity, increasing immediately as r_x is increased. C) Probability of obtaining each configuration (M is for motors, X for crosslinker, arrows indicate the filament's plus end) needed to compute the χ parameter as r_x changes. As r_x increases, crosslinkers start binding. At $r_x \approx 10 - 50$ this allows motor-crosslinker couples to form. At high r_x , crosslinkers take much of the available configurations. On the right, all configurations are sketched. According to [Belmonte, Leptin, and Nédélec 2017] M-M and XL-XL are neutral, XL-M is extensile and M-XL is contractile. However, nematic order changes everything.

time and space resolution, the second part of the curve mimics experimental results.

The flows simply slows down and then increases again. It reaches a speed slightly higher than v_0 due to transverse motion of microtubules extending and buckling or individual microtubules diffusing (with a diverging speed $\approx \sqrt{D/dt}$, dt being the simulation time interval). The mass density instead starts at a very high value due to diffusion and then gradually decreases until activity kicks in. Its variance is also strongly amplified by activity. These results are summarized in Figure 3.9.

3.3.3.3 Activity and (anti)polar order

The point then is, why is a minimum amount of crosslinking required for activity to arise. We sought the answer in the microscopic behavior of the system.

Motors' and crosslinkers' distribution The first question is, whether activity arises from high values of the coefficient χ which we have shown to in turn depend on the relative distribution of binding elements along the filament. We first tested whether motors follow the antenna model (see Section 3.2.5 for definitions). Figure 3.10.A shows the distribution of crosslinkers f_x and motors f_m along a filament. Clearly, while crosslinkers are uniformly distributed (let alone

minor fluctuations at the tips) motors indeed follow an antenna model-like exponential distribution, which is appropriately fit using the distribution computed in equation 3.6 normalized in $0 < x < L$ and using the value of the run-length λ set in the simulations. Thus there is an asymmetry of the motors' distribution towards the plus end. The resulting χ coefficient, computed counting the fraction of configurations between motors and crosslinkers observed during the simulations and then according to the definition 3.1 is indeed positive ($\chi > 0$) indicating extensibility (see Methods 4.8 and Fig. 4.5 for more details on how χ is computed from simulations). However, it does not follow the same behavior as activity, see Figure 3.10.B. To get a closer look we can compute the fraction on all total configurations of each specific configuration taken into account to compute χ (i.e., subdivided in motor-motor, crosslinker-crosslinker and motor-crosslinker/crosslinker-motor configurations, depending on the vicinity of to the plus end). It shows that there is indeed a bigger peak of the active (at least, according to [Belmonte, Leptin, and Nédélec 2017]) crosslinker-motor configuration at $r_x \approx r_x^t$ so we *do* expect our activity measure to be peaked there (Fig. 3.10.C). However, χ increases immediately as soon as $r_x > 0$ due to the increase in active couples, something which is not reflected in the system's real large scale activity (summarized in the plot of α in Fig. 3.7, which instead lags behind). The reason is that the theory, developed for sparse networks, does not hold anymore in the case where filaments are locally nematically aligned, as in this latter case it is not the relative position of motors and crosslinkers which counts, but also the relative orientation of the fibers. Figure 3.2 showed already why this is true: in the disordered case, the motor drags a filament with him towards the plus end regardless of their relative orientation whereas in the nematic case the motor can choose to walk if the filaments are polar and no stress is added to the system. On the other hand, the χ parameter captures well the decrease in activity if r_x is increased, due to the increase of crosslinker-crosslinker configurations. Thus the quantity χ measures (at best) only the general tendency towards extensibility of the system and, on the other hand, the amount of friction in the system. The former is always present as all configurations are neutral in the nematic case except those of motors bound to antiparallel couples. This, summed to the asymmetric distribution of motors on filaments, introduce a net bias towards extensile behavior, so we do expect $\chi > 0$, but the parameter *does not* predict whether the system will be globally active and it also does not guess *how* active it is, just that it is extensile. To obtain a better measure, we then need to look at the polarity in the system.

Formation of polar couples Because microscopically activity arises from the (anti-)polar order, we set out to compute the number of motors bound in an (anti-)polar way⁵. We look for motors such that they are bound to two filaments with orientation $\hat{\mathbf{p}}_1$ and $\hat{\mathbf{p}}_2$ with $\hat{\mathbf{p}}_1 \cdot \hat{\mathbf{p}}_2 < -\cos(\pi/6)$ and compute the fraction of anti-polarly bound motors $\sigma_{\uparrow\downarrow}$. We can do the same with $\hat{\mathbf{p}}_1 \cdot \hat{\mathbf{p}}_2 > \cos(\pi/6)$ to obtain the fraction of polar-bound motors $\sigma_{\uparrow\uparrow}$. Similarly, we define the respective fractions of crosslinkers $\gamma_{\uparrow\downarrow}$ and $\gamma_{\uparrow\uparrow}$ bound to anti-polar and polar couples.

By plotting $\sigma_{\uparrow\downarrow}$ and $\sigma_{\uparrow\uparrow}$ (Figure 3.11.B), one sees immediately that, while polar couple start appearing as soon as crosslinkers are added, anti-polar ones only start growing if r_x is big enough.

⁵In this section, we show graphs for $N = 8000$, $r_m = 36$. Qualitatively same results are obtained at all relevant parameters.

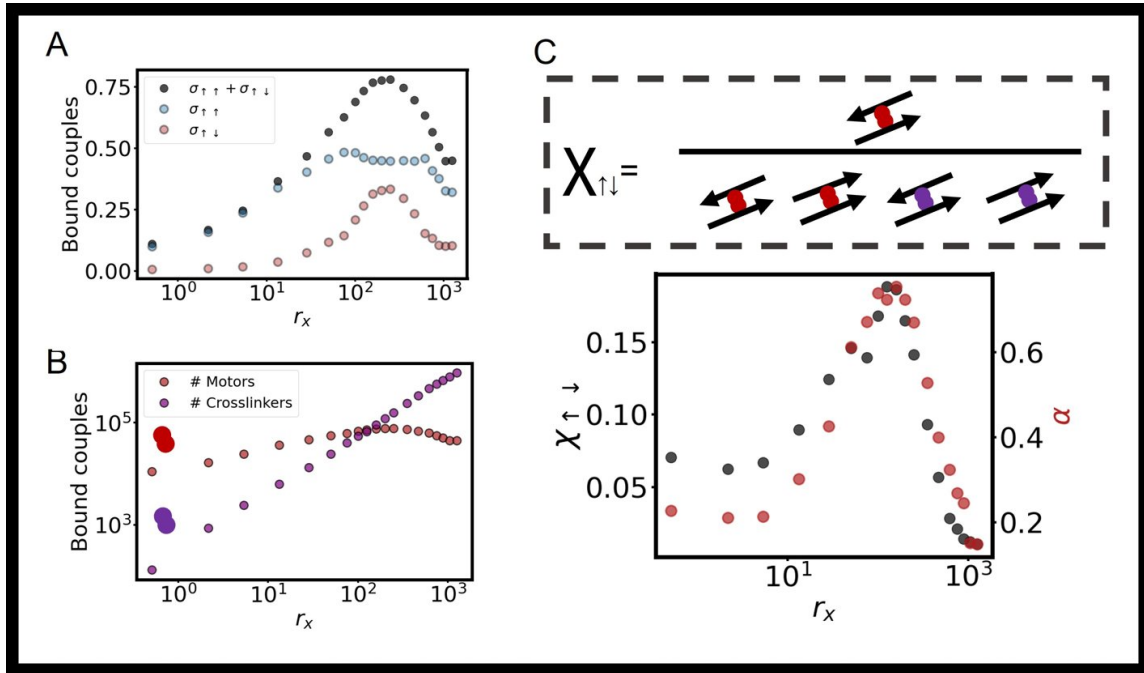


Figure 3.11: **Formation of (anti)polar couples correlates with activity** A) Fraction of motors bound to filaments pairs which are polar ($\sigma_{\uparrow\uparrow}$) or anti-polar ($\sigma_{\uparrow\downarrow}$). The two quantities behave differently for low r_x , as crosslinkers do not manage to stabilize anti-polar (extensile) couples. B) Total number of motors and crosslinkers bound to a couple of filaments as a function of r_x . Plot is in log-log scale. C) As r_x is increased, the total number $N_{\uparrow\downarrow} = N_m \sigma_{\uparrow\downarrow}$ of motors bound in anti-polar state divided by the total number of binding elements bound to a filament pair ($\chi_{\uparrow\downarrow}$, in black) correlates with the onset of activity (α , in red), reproducing both the low and the high r_x behavior.

We attribute this behavior to the fact that anti-polar couples are less stable under motor activity, as they are dissolved by extensile activity. This results in a slower increase of number of bound motors with respect of crosslinkers, which instead bind very fast as they never destabilize couples (Figure 3.11.A). Thus, only when enough crosslinkers are present that stable polar couples can form can motor-based extensile activity be generated. Thus crosslinkers play two roles: on the one hand, they keep microtubules together long enough that couples can form and, provided enough crosslinkers are present, they make it so that anti-polar couples become stable and resist over time; on the other hand, crosslinkers propagate the stress between different parts of the system (see below).

At the same time, however, crosslinkers and polarly-bound motors also cause drag, slowing down the filaments' motion. We then expect such a drag to always be present when a binding element is attached to a filaments' couple irrespectively of the couple's orientation.

We thus take inspiration from the definition of χ as a function of the configurations of the system given above (Equation 3.1 and define a measure of extensile activity in nematic systems as

$$\chi_{\uparrow\downarrow} = \frac{N_m \sigma_{\uparrow\downarrow}}{N_m(\sigma_{\uparrow\uparrow} + \sigma_{\uparrow\downarrow}) + N_x(\gamma_{\uparrow\uparrow} + \gamma_{\uparrow\downarrow})} \quad (3.9)$$

i.e. as the ratio of the total number of motors bound anti-polarly ($N_m \sigma_{\uparrow\downarrow}$), which provide activity, divided by the total number of elements bound, which provide drag. Figure 3.11.A shows a plot of the parameter $\chi_{\uparrow\downarrow}$ as a function of the number of crosslinkers and is directly compared with the activity α : both the initial slow-down in activity, its increase and the final decrease are correctly predicted using $\chi_{\uparrow\downarrow}$ as an observable, indicating again that activity in nematic systems only arises from anti-polar couples propelled by motors. The initial decrease in activity can be attributed to an increase in crosslinking which is not compensated by anti-polar motor couples. Similarly, another feature of $\chi_{\uparrow\downarrow}$ is being able to describe the final loss in activity not only in terms of drag but also in reduction of the total number of motors bound if the crosslinking on the filament is too strong.

We can extend the above reasoning to the behavior of filaments rather than binding elements. To do that, we count filaments which are bound to another filaments in a polar (anti-polar) way. Specifically, we define the parameter $N_{\uparrow\uparrow}$ ($N_{\uparrow\downarrow}$) as the number of filaments bound to a filament oriented in the same (opposite) direction. Again, as r_x changes, after an initial increase in $N_{\uparrow\uparrow}$ (which again, correlates with the initial slowing down of the system), there is a sudded increase in $N_{\uparrow\downarrow}$ exactly when activity kicks in. This is also reflected on the behavior of the nematic order parameter S (defined, as usual, as $S = 2\langle \cos(\theta)^2 \rangle - 1$ where $\cos(\theta)$ is the angle between filaments) and the polar one ($S_p = \langle \cos(\theta) \rangle$). Parameters are averaged in small boxes of side $l = 2 \mu m$. While the nematic order is always high ($S \approx 1$) as filaments bind together, the polar order changes from polar ($S_p > 0.$), in the presence of polar couples, to less polar ($S_p \approx 0$) indicating the formation of anti-polar pairs which start activity. It is for this reason that theories describing the system purely in terms of the nematic order can fail to account for the modulation in activity due to crosslinking, which again stabilize antipolar (active) couples [Maryshev et al. 2019]. This description also shows that as activity slows down, the formation of polar couples is again favored, probably because the motors become unable to break couples efficiently and the system arrests in a highly polar state again. These results are summarized in Figure 3.12.A and B.

3.3.3.4 Formation of filaments' cluster

Crosslinkers play another role in the generation of macroscopic activity, i.e., they allow filaments to bind continuously as motors break them. In other words, in the active state, the system is composed of bigger cluster of filaments all connected to each other so that activity can percolate in the system, whereas at low r_x the system dissolved in individual filaments. This is of course only possible if enough crosslinkers are present to guarantee that this happens. We can then count the number of microtubules in each cluster and see that, while at low r_x clusters dissolve (and multiply in number), at higher ones clusters become bigger (and only a few of them are present at any time). Again, looking at the number of clusters as a function of r_x a sharp transition is visible at $r_x \approx r_x^t$ indicating a critical number of clusters so that activity can propagate to larger scale (Fig. 3.12.C and D).

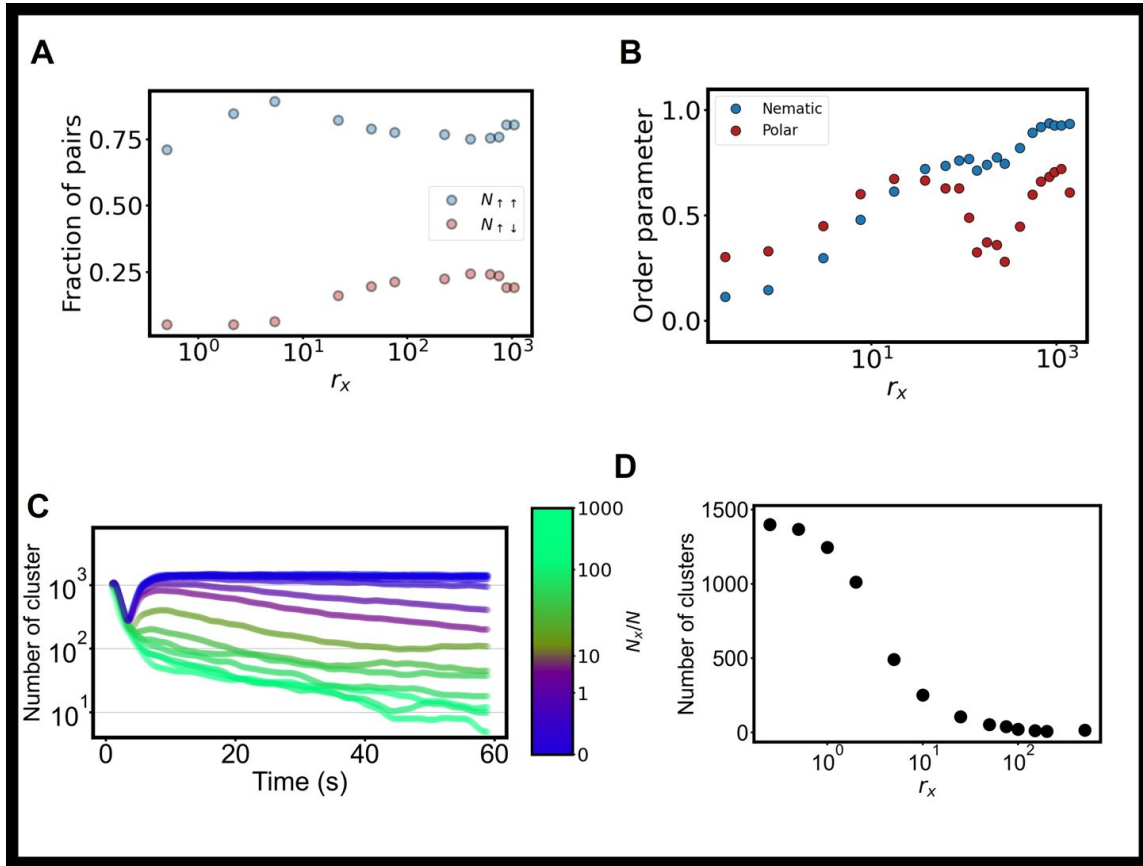


Figure 3.12: **Polar and nematic order of filaments and cluster formation** A) The fraction of filaments' couples bound in an polar (blue) or antipolar (red) fashion changes depending on the amount of crosslinkers B) The local polar and nematic order is also affected, indicating that nematic order is not a good descriptor of activity, as the polar contribution needs to be accounted for and changed in a non-trivial way with the amount of crosslinkers. Activity actually correlates with negative polar order (i.e., with anti-polar couples forming). C) Activity is also related to the formation of clusters. Over time, clusters form and dissolve (at low r_x) or grow (at high r_x). Colorbar indicates value of r_x , from blue to green. D) The number of clusters as a function of r_x again shows a sharp decrease around the activity threshold, indicating that the number of clusters is a relevant parameter to describe the system.

3.3.4 Discussion

This section had the aim to shed light on what actually is the role of crosslinkers in shaping AMFs i.e., active microtubule fluids based on kinesin-based extensile activity. This latter requires microtubules to be aligned anti-polarly.

There is in general interest, at the moment, in understanding how to bridge the microscopic dynamics with the macroscopic flow. Recently, it has even been shown how a system of motors and rigid filaments can switch from extensile to contractile activity depending on the motors used and the amount of interaction between filaments, underlining the importance of the microscopic dynamics in shaping the collective behavior [Lemma et al. 2021]. Several computational and

theoretical results are indeed already available to study active cytoskeletal fluids and attempt to bridge this gap, often with the help of Cytosim simulations [Gao et al. 2015; Roostalu et al. 2018; Rickman, Nédélec, and Surrey 2019]. In [Belmonte, Leptin, and Nédélec 2017] a theory to explain the contraction/extension of network was devised. In [Lera-Ramirez and Nedelec 2019] the microscopic microtubule-motor interaction was also investigated in the case of two microtubules with a variable number of motors. In [Striebel, Graf, and Frey 2020; Fürthauer et al. 2019] the microscopic origin of collective flow was also investigated and the role of crosslinkers elucidated. Several experimental systems are also available to study the assembly of AMFs and the importance of MT-MT interaction [Chandrakar et al. 2018; Nasirimarekani et al. 2021].

Another important point is that we study a dilute system, in which nematic order is only local. Most of the studied system, for which predictive theories exist, are instead in a more dense state (e.g., [Striebel, Graf, and Frey 2020; Fürthauer et al. 2019] are at a packing fraction 250 times closer to the Onsager isotropic-nematic threshold than the system we study). However, dilute systems of active MTs have important biological analogues in the cytoskeleton, including the formation of the mitotic spindle ([Dalton et al. 2021]) and beating cilia or flagella ([Sanchez et al. 2011; Vilfan et al. 2019]). Recently, indeed, they have been further studied, showing interesting rheological properties and, more importantly, showing the importance of crosslinking to obtain stable structures and even indicating the importance of gelation-like transitions for collective flow to emerge [Dalton et al. 2021; Gagnon et al. 2020]. Here we add to this confirming the role of crosslinking in mediating the formation of gel-like clusters but also underline their role in the stabilization of antipolar pairs.

Yet, most of the macroscopic descriptions neglect this fact and just start from a \mathbf{Q} -tensor dependent term which is assumed to be proportional to activity. The assumption usually made, that the activity is proportional to the nematic order must however be handled with care. Indeed, depending on the concentration of crosslinkers, the same nematic order can be composed of different fractions of polar and anti-polar couples, only the latter providing an energy input, breaking the assumption that nematic order is proportional to the polar (or anti-polar) one.

Here, we have studied more in details this fact, using Cytosim simulations, together with an experimental AMF which replicates the main results (i.e. a modulation of activity as a function of crosslinkers). Simulations have allowed to clarify the microscopic structure of the AMF. The main result is that indeed activity is proportional to the amount of anti-polar couples present in the system (but inversely proportional to the friction of the system, too). However, this quantity is *not* directly proportional to the system's nematic order, which is something that should instead, at least in similar conditions to the ones explored here, more explicitly taken into account.

3.4 AMFs under confinement and active GUVs

In the previous Section we have described the general behavior of AMFs in bulk and underlined the role of crosslinking in shaping the system. However, again, we need to address the fact that biological systems, in which microtubule- (and actin-)based structures behaving similarly to AMFs exist (the main example being the mitotic spindle but also the formation of motile cilia, see e.g. [Sanchez et al. 2011]), usually are confined within the cellular membrane. The previous chapter has elucidated how anchoring to the membrane can have an effect on the formation of ordered structures and confinement can also play a big role. Here, we discuss instead what happens if a bulk AMF is encapsulated inside a GUV. This system is peculiar for a particular reason: GUVs are yes closed (i.e., the system is confined) but they are also elastic and can change shape. Deformability of the membrane and control over its mechanics is a necessary condition for most of the behaviors of cells, such as crawling (forming filopodia), adhering (forming focal adhesions) and navigating complex environments during migration. It is, once more, the cytoskeleton that drives such deformations [Pollard and Cooper 2009]. Thus the ability to control and/or study the behavior of AMFs inside GUV confinement represents a crucial step towards linking the cytoskeletal active behavior (the AMF) with the membrane mechanical properties. In this section we review, on the one side, the behavior of AMFs under confinement. On the other, the behavior of GUVs containing an active system and how that affects the GUVs' deformation and fluctuation. In the next Section, by encapsulating an AMF inside a GUV, these two aspects will converge in the same system.

3.4.1 The role of confinement for AMFs

First, we need to frame better the already known effect that confinement has on AMFs in general. Because of the complex hydrodynamic interactions between different parts of an AMF, confinement can indeed tune many of their properties by providing boundary conditions.

Confinement inside small channels, with their height much smaller than the sides, has shown how an AMF can be tuned from a disordered flow (as the one discussed in the previous Section) to an ordered one, in which there is net mass transport in one direction. The behavior of bundles at the edges of the channel has been directly connected to the emergence of such coherent flow: microtubules are forced to align in a precise way on the boundary, which propagates into the bulk and, if the geometrical ratios are tuned right, this effect can be relevant. Geometrical properties of confinement are indeed also important [Wu et al. 2017]. A similar effect has also been connected to the presence of long-wavelength unstable modes that drive the buckling transition so that tuning the geometrical aspect of confinement affects the transition from disorder to order [Strübing et al. 2020; Chandrakar et al. 2020].

AMFs have also been confined in (rigid) droplets leading to the emergence of asters and vortices, again driven by the alignment of MTs at the boundary [Suzuki et al. 2017; Juniper et al. 2018].

In the case of active nematics, where topological constraints play a role as confinement can fix the total topological charge, the nucleation rate of defects can also be tuned using different geometries [Norton et al. 2018; Hardoüin et al. 2019].

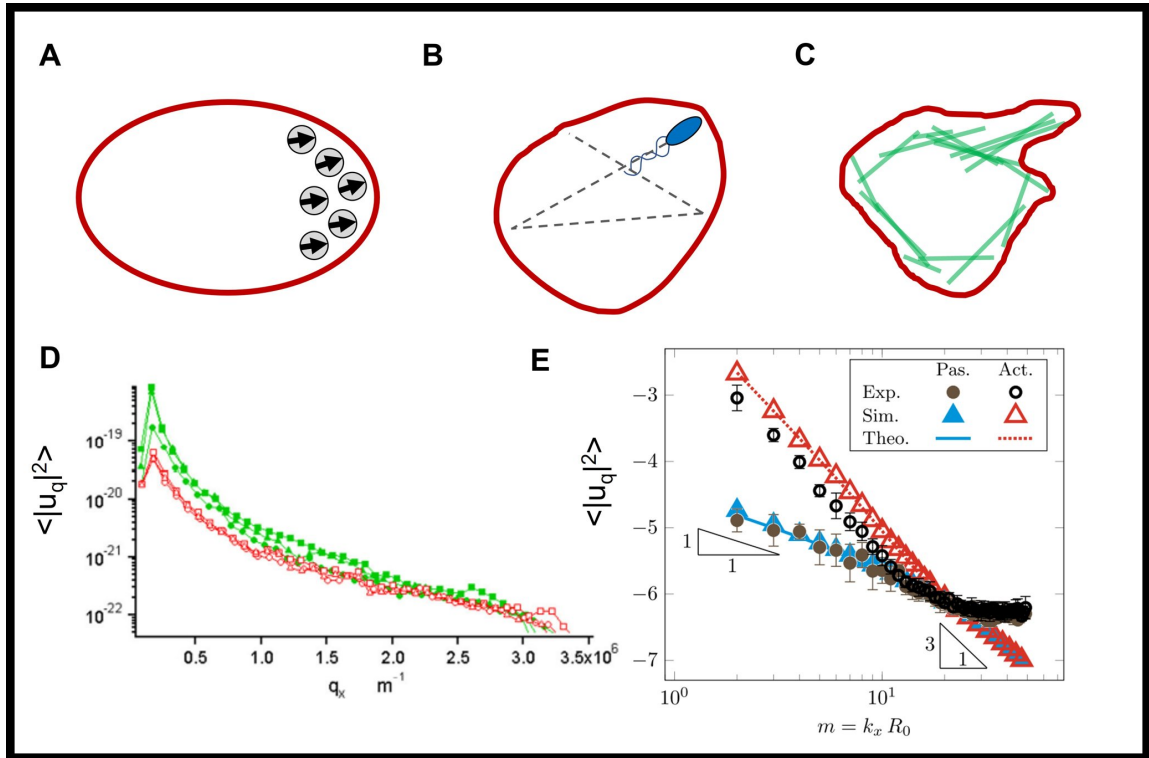


Figure 3.13: **Examples of active GUVs** A) Encapsulating self-propelled particles inside a GUV can give rise to non-spherical shapes as particles accumulate in convex deformations (adapted from [Vutukuri et al. 2020] B) Encapsulating motile bacteria can give rise to shape deformations as the bacteria travel inside the GUV (adapted from [Takatori and Sahu 2020] C) Binding the cytoskeleton to a GUV can give rise to membrane deformations too. C) Comparing an active (green) and a passive (red) spectrum as a function of the wavelength q_x shows how the two spectra have the same scaling but the active one shows passive-like yet enhanced fluctuations (taken from [Faris et al. 2009]. D) Spectra from [Takatori and Sahu 2020] as a function of the mode number m showing how active (empty dots) and passive (full dots) spectra can differ greatly. A model (triangles) recovers both the active and the passive scaling.

However, most of these works are realized in rigid and relatively macroscopic confinement. The aim of this chapter is an extension towards deformable confinement.

3.4.2 Active GUVs

In the recent years, some works have appeared aiming at studying the behavior of *active* membranes, i.e. membranes whose mechanical modes are excited by active processes. A big number of works has been devoted to study the influence of ion channels and pumps embedded in the membrane using flicker spectroscopy i.e. the study of the membrane's fluctuation spectrum compared to the one of a passive one which can be analytically computed as shown in Section 1.4.3.2 (we refer in general to Section 1.4.3.2 for an overview on flicker spectroscopy).

A passive membrane is indeed defined by its bending rigidity and its tension. It was instead shown that GUVs containing active proteins were exhibiting out-of-equilibrium fluctuations

that could be measured and did not fit the expected behavior of a passive GUV [Pécrcéaux et al. 2004; Faris et al. 2009; Almendro-Vedia et al. 2017]. Interestingly, most of the peculiarity of proteins-containing membranes had been already predicted by the first attempts at modelling their behavior [Prost and Bruinsma 1996]. In all cases, the ability of GUVs to deform, and how that was affected by the presence of an active process, could be exploited to extract information about the active process itself. These early experiments and theoretical models about actively fluctuating GUVs have in common the fact that the scaling of the GUV’s fluctuations is still power-law like but can be renormalized to a passive one by assuming the active process leads to a reduction in the bending rigidity or, from a different point of view, as if the active GUV was instead a passive one immersed in a thermal bath at high temperature (see Fig. 3.13.D). A reduction in (effective) tension has also been measured by micropipette aspiration [Girard, Prost, and Bassereau 2005]. However, this is not true from all points of view. Interestingly, for example, the time correlations of the membrane’s fluctuations can also be affected by active processes in a way that does not correspond to any equilibrium picture. Flicker spectroscopy, allowing access to not only the spatial fluctuations but also their temporal behavior, also allows to study how one can learn about the timescales of the active process itself, which does not in general follow an effective temper, something we will explore more in depth further on [Bouvrais et al. 2012].

This kind of approach has been further expanded to understand, both *in vitro* and *in vivo* whether the cytoskeleton, and its dynamics, also has an effect on the membrane’s fluctuation (see Fig. 3.13.C). Work on red blood cells has shown that indeed their membrane fluctuates out of equilibrium due to the presence of a cytoskeletal meshwork which continuously attaches and detaches to the membrane [Betz et al. 2009; Turlier et al. 2016]. This latter set of experiments also clearly show the non-equilibrium nature of active fluctuations. More recently, artificial systems composed by encapsulating a membrane-binding actin cytoskeleton in GUVs showed clear membrane deformations. GUVs represent indeed a powerful tool to study how cell-like confinement affects cytoskeleton-related processes and how they in turn can affect the deformation of the membrane [Loiseau et al. 2016; Simon et al. 2019; Allard et al. 2020; Gat et al. 2020]. Differently from droplets, indeed, GUVs are elastic and deformable which allows to study the mechanical deformations induced by the cytoskeletal systems they contain.

Another important contribution in this context has been the encapsulation of an active nematic inside a GUV [Keber et al. 2014]. The nematic assembled on the GUV’s membrane and formed a $4 \times \frac{1}{2}$ defect’s configuration. Because of topological constraint, the total charge had to be +2 so those defects could not disappear and instead traveled along the membrane in a definite configuration minimizing the elastic energy. Upon deflation of the vesicle, active tube-like deformations appeared at the four positions where defects were present. In this case, the pressure on the GUV membrane was defined by topological constraints.

Only recently has flicker spectroscopy also been applied to systems (not related to the cytoskeleton) that show massive membrane fluctuations induced by activity. Such systems, due to the relative simplicity of their modeling, have improved our understanding of GUV deformations in the presence of active forces. Encapsulating synthetic self-propelled particles (which convert chemical fuel, e.g. consuming H_2O_2 , into persistent motion) inside a GUV leads to huge deformations that can make the vesicle deviate from the equilibrium spherical

shape. Using a GUV system, a phase diagram connecting the activity of the particles and their number to the final shape of the vesicles. While the presence of only a few particles leads to enhanced fluctuations and (depending on their activity) the formation of tubes and tethers on the membrane, as their packing fraction is increased the GUVs settle to a final shape which resembles a prolate i.e. it is clearly non spherical [Vutukuri et al. 2020] (see Fig. 3.13.A). This is due to a feedback between the pushing of particles on the membrane hat can deform and hence, because of its convex shape, accumulate further particles. This work clearly showed how the deformations of the vesicle can act as a feedback on the active process.

A similar system has been realized by encapsulating swimming bacteria [Takatori and Sahu 2020]. Again, by swimming and hitting the membrane, bacteria induce strong deformations of the shape of the GUV (see Fig. 3.13.B). Both systems exhibit enhanced fluctuations at large wavelength and a scaling of the fluctuations spectrum which differs from the equilibrium one (but is surprisingly close to the scaling observed when the membrane contains active proteins). In the latter case (see Fig. 3.13.E), a model has been developed by assuming that each bacterium, of linear size a , applies a pressure $p \approx \frac{2a}{\lambda}$ on a membrane with tension λ and bending rigidity K_b . The contact lasts τ_c seconds and two contacts are separated by a time $\tau_T \approx 2R_0/v_0$ (i.e., the time it takes a bacterium to travel through the whole GUV). This leads to a height fluctuation spectrum for a squared, planar membrane of side $L = 2\pi R_0$, of the form:

$$\langle |h(k)|^2 \rangle = h_p(k) + N \frac{\tau_c}{\tau_T} \frac{a^4 p^2}{(k_B T R_0)^2} e^{-(ak)^2} h_p^2 \quad (3.10)$$

where k is the absolute value of the wave vector, N is the number of bacteria inside the GUV and $h_p(k) \approx k_B T / (\lambda k^2 + K_b k^4)$ is the passive fluctuation spectrum. This shows that the fluctuations of the GUV are enhanced in the active case by a factor $\propto e^{-(ak)^2} / (\lambda k^2 + K_b k^4)^2$ which is not a power law (due to the presence of the exponential) and hence have a definite scale set by a . If however we neglect the exponential (which is ≈ 1 anyway at low modes if $a \approx 1 \mu m$ and $R_0 \approx 10 \mu m$) and assume the membrane is tension dominated we get a correction that scales as $\sim 1/k^4$ which is observed by both [Takatori and Sahu 2020] and [Vutukuri et al. 2020] but also comparable to previous works. This is probably due to the bending-dominated correction decaying very fast and thus only the tension-dominated part being resolved. While based on strong assumption, this model helps to understand how, poking actively on a membrane, can lead to an enhancement of its fluctuations. For example, this further indicates that the effective temperature picture for active GUVs is flawed or at least incomplete as low modes can be strongly affected by activity. Additionally, as already mentioned, the time scale of the membrane fluctuation can strongly differ from the equilibrium one.

All in all, these result show that we can use the fluctuation spectrum to extract information about the way an active system affects (and is affected by) a membrane. We are now going to apply this approach to a GUV system containing an AMF. Differently from [Keber et al. 2014] we are not going to encapsulate an active nematic but rather an active-bundles system. This means that the system will be in bulk and will affect the membrane (by extending and pushing on it). As the system is in bulk and not globally nematic, the positioning of the contact points with the membrane where stress is higher will not be dictated by topological constraints. Additionally, due to the GUV's linear size $R_0 \approx 20 \mu m$ being much smaller than the average

bundle size ($\approx 100 \mu m$) the bundles themselves will be affected by the elastic boundaries. For this same reason, we expect the model by [Takatori and Sahu 2020] to not be accurate as due to the elongated shape of the bundles the contact points will be strongly correlated with each other. This all will be the aim of the next Section.

3.5 An active microtubule fluid deforms lipid vesicles

In this Section we show the results of the system hinted at above, i.e. a bundled AMF inside a GUV. We will both study the deformations induced by the bundles on the GUV but also the feedback due to the elastic confinement felt by the MTs' dynamics. In particular, we will show that the membrane deformations follow an enhanced fluctuations scaling analogous to previous observations. However, because of activity, the correlation times of such perturbations are not simply due to membrane's mechanics but rather to the engulfed AMF. Hence the active system is decoupling the mechanical response in space (the fluctuations spectrum) with the one in time (the correlation of the fluctuations). Additionally, we will study, with the help of a simulated model, the behavior of MTs under confinement, the positioning of the bundles and the way they push on the membrane and are in turn also affected by it.

3.5.1 Experimental system

We use the cDICE technique (See Methods 4.2.0.2) to encapsulate an AMF inside a GUV. The membrane composition is chosen to be 98 % EggPC, 2 % DSPE-PEG(2000) to avoid protein adsorption on the membrane and 0.05 % TexasRed-DHPE for fluorescent imaging. The inside solution consists of Alexa647-labelled, GMP-CPP stabilized microtubules (at a concentration c_{MT}), KSA (at a concentration c_K) and ANLN (at a concentration c_A) in M2B. Additionally, the mix contains an ATP regeneration system (CPH/CPK), a scavenging system to reduce oxidation (POC) and 4 mM ATP. In these conditions the system is active for at least 1-2 hours. The precise description of the system is given in 4.6.

The vesicles are harvested and imaged with confocal microscopy. Both 3-dimensional stacks and time series of only the equatorial plane are recorded in both the microtubule and the membrane channel.

3.5.2 GUVs deform due to pushing of microtubules bundles

When an AMF is confined inside a GUV, MT-bundles form that poke on the membrane and deform it. At the same time, the presence of the membrane forces the microtubule bundles to break and re-form. While occasionally the microtubules manage to push on the membrane and use its excess area to generate tube-like protrusions, most of the times the membrane rather globally deforms, dramatically changing shapes.

Fig. 3.14 shows confocal images of a vesicle deforming every 5 seconds. Notice the amount of different conformations explored by the GUV, from oval-shaped (00:20 s), to triangle-shaped (00:35 s) to squared shape (00:40 s), and so on. Protrusions are also visible for example at 00:40 s or 1:10 s. The deformations are fast with each shape being stable for approximately 5-10 seconds. Inside the GUV, also the microtubules continuously change conformation.

We produce vesicles in different conditions and observe that their behavior is only slightly affected by the internal composition, the main difference being that at higher crosslinking / lower density of microtubules, longer thicker bundles are present (Fig. 3.15.A). If enough activity and microtubules are present, the AMF behaves as a fluid of bundles that extend and

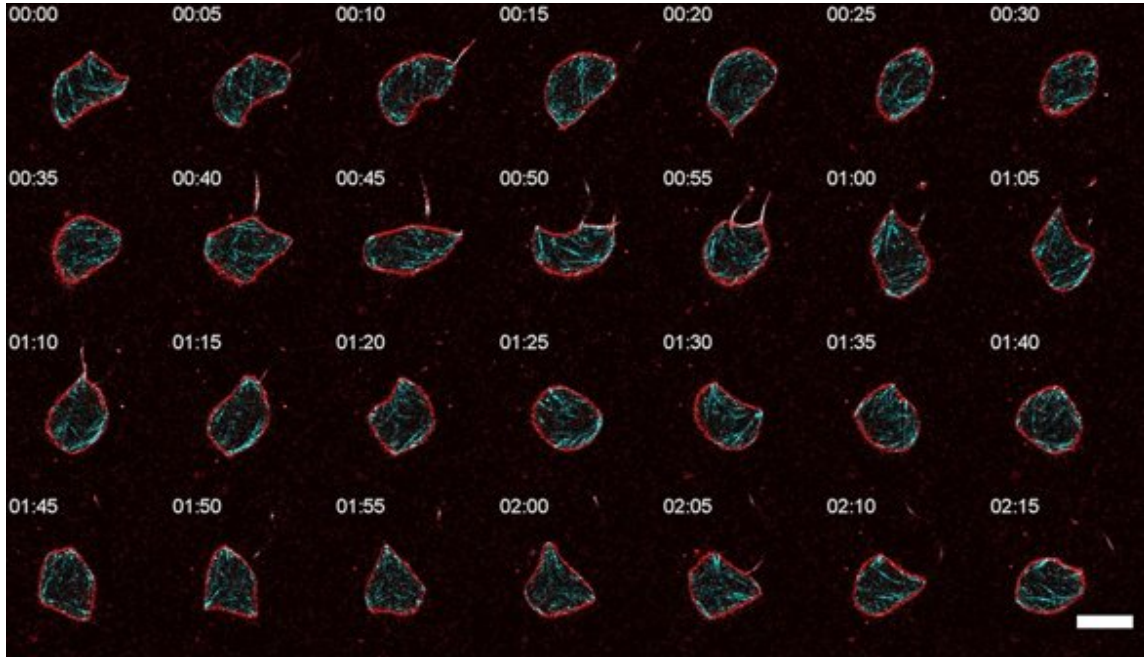


Figure 3.14: **Deformation of a GUV containing microtubules:** Equatorial plane of a GUV registered every 5 seconds for a total of 2 minutes and 15 seconds. Conditions are: $c_{MT} = 0.8$ mg/ml, $c_K = 120$ nM, $c_A = 1.5$ μ M. Scale bar is 50 μ m. Notice the amount of different conformations in such little time.

hit the membrane. The deformations are three-dimensional and strongly correlated to the MT organization inside the GUV (Fig. 3.15.B).

By looking more closely at the deformations, one notices how the microtubules assemble in bundles that push on the membrane and deform it. Two main deformations can be seen: when bundles are directly, radially poking against the membrane, they form tubes. Tubes protrude and retract. However, bundles can also align with the membrane and buckle due to their instability. When this happens, they deform the membrane due to the extension of the buckling pivot, which leads to smoother deformations. This is summarized in Fig. 3.15.C.

This two different main kinds of deformation are both present in all samples, especially due to the variability intrinsic to the cDICE method and in the encapsulation of such an active mixture. However, one can, up to some point, modulate it by changing the properties of the AMF e.g. by tuning the MTs' concentration, as in conditions when short thick bundles form then poking is the main deformation mode whereas buckling requires longer bundles (Fig. 3.15).

3.5.2.1 Analysis of the deformations

To analyze the deformations, we extract the GUVs' contour on the equatorial plane starting from confocal images (see also Methods 4.7), as shown in Figure 4.4. Briefly, the images are thresholded, a first contour is found using a Python script to obtain the center of the GUV, and then refined by looking for the maximum intensity values in an angular segment of width $d\alpha = 0.1$ radians with a spacing of $d\theta = 0.01$ radians. From this analysis, the $\{x(t), y(t)\}$

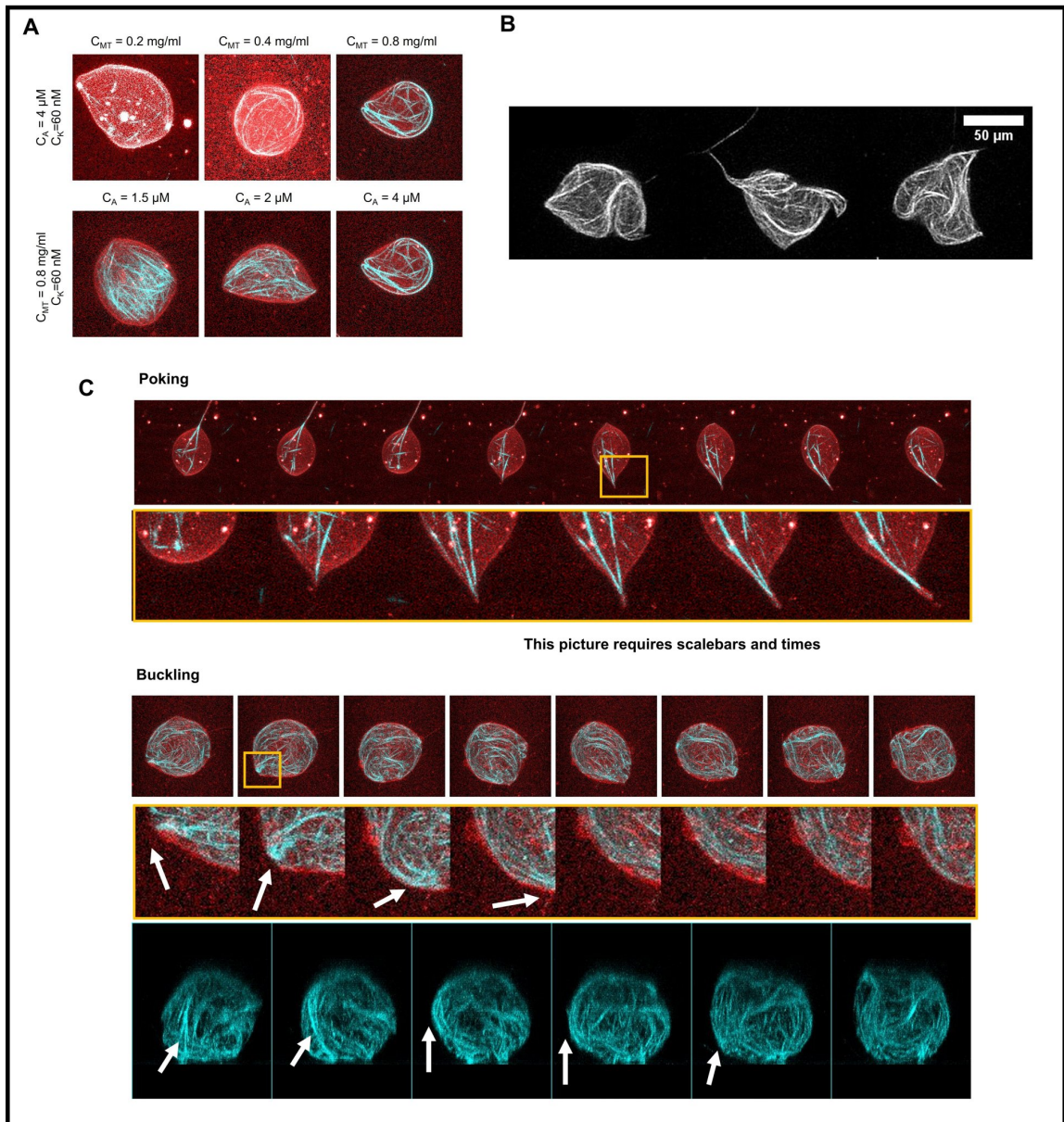


Figure 3.15: **Microtubules deform a GUV's membrane in different ways:** A) By varying the composition of the AMF we can slightly tune the behavior of the GUV. B) Top and side views of a GUV deforming and the underlying microtubules organization (conditions: $c_{MT} = 0.8$ mg/ml, $c_K = 120$ nM, $c_A = 2.0$ μM). C) Membranes can deform in two main ways: bundles can poke directly at the membrane forming tubes (top, conditions: $c_{MT} = 0.2$ mg/ml, $c_K = 60$ nM, $c_A = 2.5$ μM). MTs can also buckle against the membrane generating large deformations (bottom, conditions: $c_{MT} = 0.8$ mg/ml, $c_K = 120$ nM, $c_A = 1.5$ μM). Close ups and behavior of the microtubules is also shown.

positions of the contour can be extracted and also converted in polar coordinates, obtaining a representation $R(\phi, t)$ of the GUV.

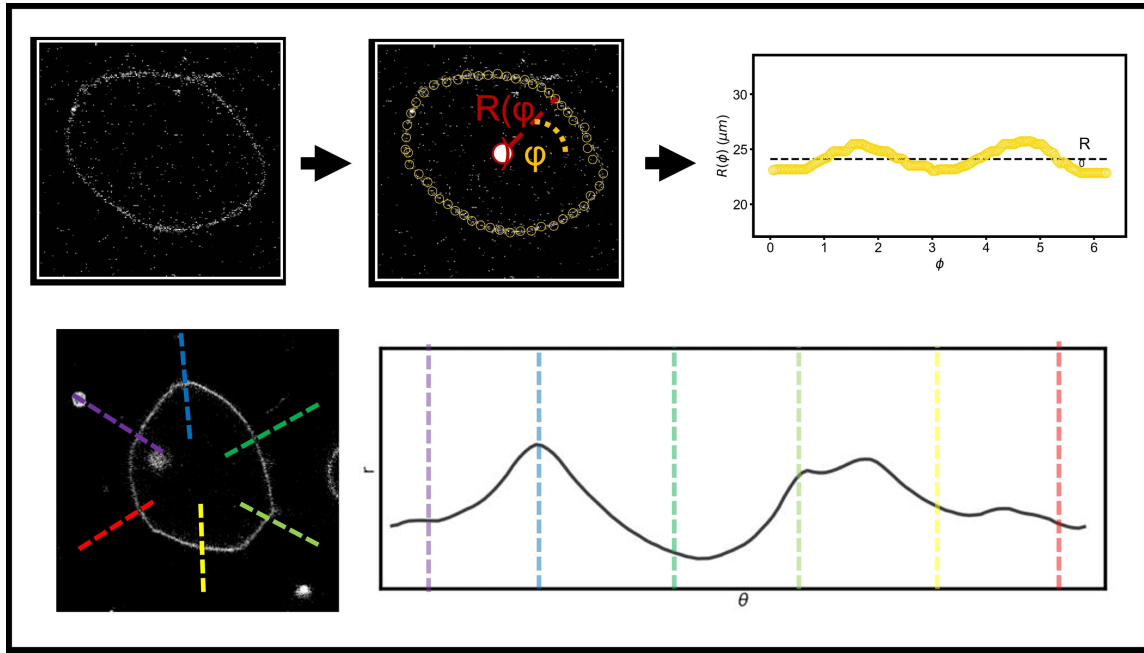


Figure 3.16: **Contour analysis of active GUVs** By identifying high intensity position on the equatorial plane we can obtain a contour in polar coordinates $R(\phi, t)$. Bottom picture shows a GUV with some marked positions and the same position as they appear on the reconstructed polar contour.

From this analysis we can compute both the local curvature k (Fig. 3.17.A) and the distance of each point of the membrane from the center with respect to the expected one $\Delta R = R - R_0$, where R_0 is the mean radius of the GUV. Curvature is computed by fitting the best circle to a shifting window of 20 points along the contour by a least squared method. Active GUVs exhibit a non-gaussian distribution of curvature, which is not centered at the expected one ($k_0 \approx 1/R_0$) the peak being shifted towards lower curvatures. This is because the membrane has to compensate for higher deformations resulting in curvatures as high⁶ as $k \approx 3k_0$. A big peak is at $k = 0$ is also visible, indicating that the membrane is often locally flat. This is similar to what observed for simulated membranes in the presence of active forces and hints at the fact that the GUV continuously changes shape and is not oscillating around a spherical shape [Paoluzzi et al. 2016]. Indeed, also the radial displacements ΔR show huge variations, as high as 40 % with respect to the mean R_0 , as already observed in active GUVs [Vutukuri et al. 2020; Takatori and Sahu 2020] (Fig. 3.17.B). A kymograph of the deformations over time also indicates that deformations are correlated in time and space, with perturbations travelling along the membrane. Such behavior is different with that of a passive GUV, which instead shows a Gaussian distribution of curvatures around $k_0 = 1/R_0$ and $\Delta R \approx 10\%$ at most.

Having described the deformations of a GUV containing an AMF, the question is then how does the MT-based activity affect the vesicle's deformation and, *vice versa*, how does confinement affect the AMF.

⁶For this analysis, contours are smoothed so that very high curvatures, e.g. tubes, are not considered.

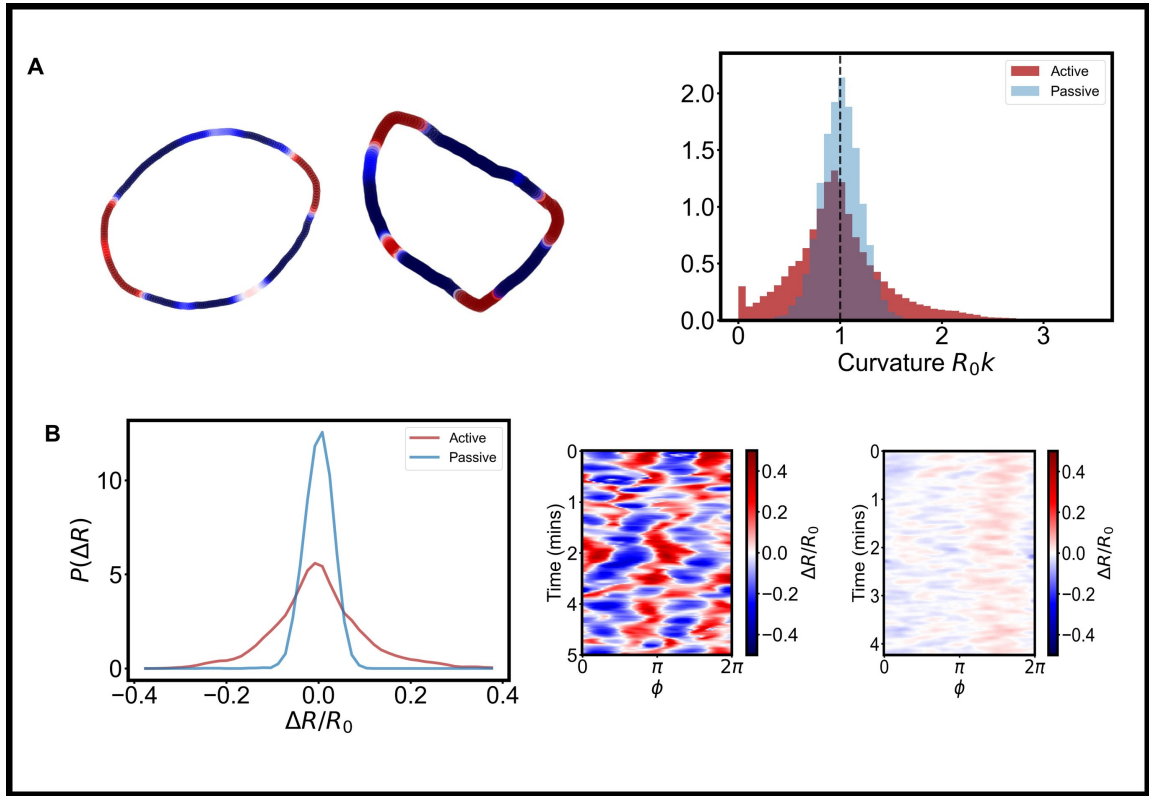


Figure 3.17: **Radial deformations of an active GUV** A) Examples of active GUVs exhibiting high curvature and histogram of curvature over time. Curvature in the contour plots is color coded, with blue being $k = 0$ and red being $k \approx 3/R_0$. The histogram show the distribution of curvature along an active and a passive GUV over the course of a ≈ 2 minutes time interval. While a passive GUV has curvature normally distributed around the mean radius ($k \approx k_0 = 1/R_0$) the active one exhibits a non-equilibrium distribution, with one peak at $k \approx 0$ and longer tails for $k > 1/R_0$ and $k < R_0$. The modal curvature is also not corresponding to k_0 anymore. B) Kymograph showing the radial fluctuations $((R(t) - R_0)/R_0)$ around the mean R_0 over time for an active GUV (left). Deformations as big as $\pm 40\%$ are visible. Additionally, the perturbations appear to be correlated in time and space, showing the presence of small membrane waves. In comparison, a passive one exhibits only minor fluctuations (right).

3.5.3 Spectral behavior of the GUV membrane

To obtain information about the membrane's deformation, we perform flicker spectroscopy, i.e., we image the equatorial plane of the GUV at high speed (35 to 250 ms time interval between frames, with an integration time smaller than 30 ms) to obtain the position of the membrane on the plane $R(\phi, t)$ at time t at an angle ϕ with respect to the contour's center⁷. We can then decompose the contour in Fourier modes using the expansion

⁷This part of this work has been conducted in collaboration with Hammad Faizi from Petia Vlahovska's group at Northwestern University.

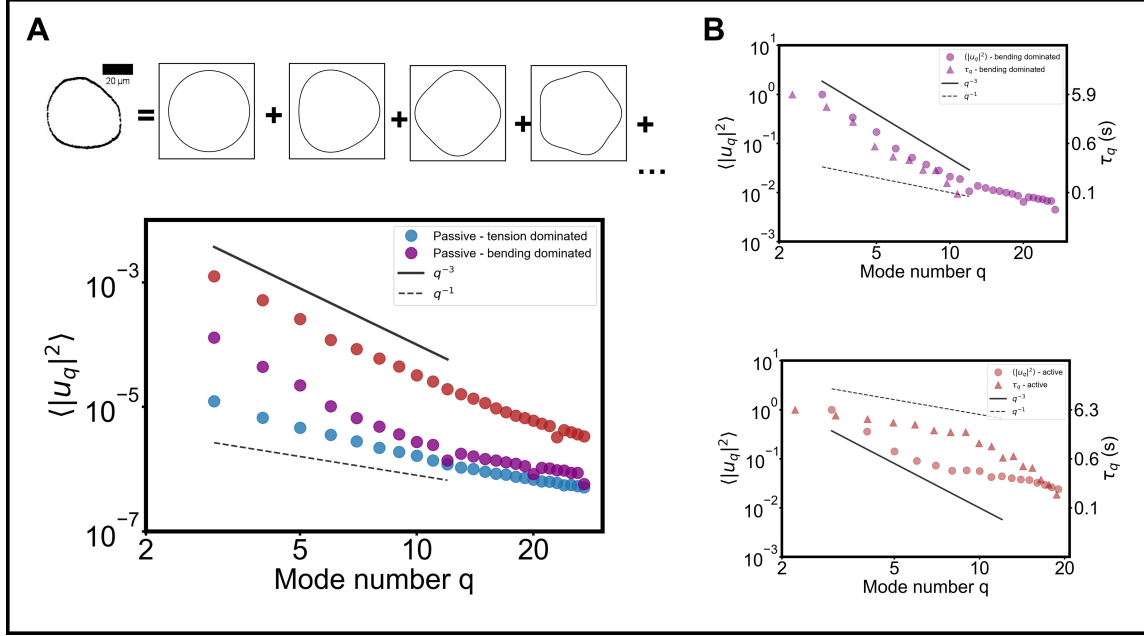


Figure 3.18: **Flicker spectrum of active and passive GUVs:** A) Contours are expanded in Fourier series to obtain the fluctuation spectrum of each mode. Passive GUVs (blue and purple) exhibit an equilibrium spectrum, with a crossover mode q_c that can be tuned by choosing appropriate sizes for the GUV and obtain spectra for both the bending and the tension dominated regime. Active spectra (red) are in all cases ≈ 1 order of magnitude above passive ones and exhibit a clear $\sim 1/q^3$ scaling, as indicated by the solid line. B) However, the time correlations τ_q , which for a passive one should scale like the spectra (top), are now decoupled (bottom), scaling as $\sim 1/q$, indicating that the spatial and temporal scales are now separated. The active GUV is at $c_{MT} = 0.8$ mg/ml, $c_A = 2 \mu M$, $c_K = 120$ nM. Passive GUVs only contain M2B buffer.

$$R(\phi, t) = R_0 \left(1 + \sum_{q=1}^{q_M} a_q(t) \cos(q\phi) + b_q(t) \sin(q\phi) \right) \quad (3.11)$$

where R_0 is the mean radius, q_M is the highest resolved mode and $a_q(t)$ and $b_q(t)$ are Fourier coefficients. The detailed procedure is explained in 4.7.

This allows to separate the behavior of the membrane at each separate wavelength $\ell_q = 2\pi R_0/q$. Indeed from the Fourier coefficients we can compute the absolute value

$$c_q(t) = \sqrt{a_q^2(t) + b_q^2(t)} \quad (3.12)$$

and then the fluctuations over time of $u_q(t) := c_q - \langle c_q \rangle$, namely the variance, is given by

$$\langle |u_q(t)|^2 \rangle = \langle c_q^2 \rangle - \langle c_q \rangle^2 \quad (3.13)$$

We recall that for a passive membrane, due to the equipartition theorem, we must have (see Section 1.4.3.2⁸) that

⁸By taking the expansion as sines and cosines of $R(\phi, t)$ we have implicitly taken the real part, as $R(\phi, t)$ is of

$$\langle |u_q(t)|^2 \rangle \approx \frac{k_B T}{K_b(q^3 + \bar{\lambda}q)} \quad (3.14)$$

where K_b is the bending rigidity and $\bar{\lambda} = \lambda R_0^2 / K_b$ is an effective tension. The above equation will serve as a passive reference case.

Figure 3.18 shows the spectrum of an active GUV. It is compared with those of two passive ones with different sizes to tune the value of $\bar{\lambda}$ and hence the crossover mode at which the scaling changes from bending dominated ($\sim 1/q^3$ as if $\bar{\lambda} \approx 0$) to tension dominated ($\sim 1/q$ as if $K_b \approx 0$).

In the case of a AMF-containing GUV, the fluctuation spectrum is found to scale as $\sim 1/q^3$ at low modes. While such a scaling is consistent with a low-tension GUV ($\lambda \approx 0$), active fluctuations are one order of magnitude higher than the respective passive case. This indicates that the vesicle is fluctuating with increased strength at relatively smooth wavelengths and that, possibly because of the extensile nature of the AMF, the vesicle is in a tense state and bending rigidity is the leading term. However, while the fluctuation spectrum is indeed consistent with a picture at which tension is reduced and the vesicle fluctuates as if immersed in a bath of increased temperature, the complete picture is more complicated.

Indeed, one can look at the time evolution of modes computing the correlation function averaged over time

$$C_q(\tau) = \frac{1}{2} \langle a_q(\tau + t)a_q(t) + b_q(\tau + t)b_q(t) \rangle_t \quad (3.15)$$

In the purely passive case, we expect

$$C_q(\tau) \sim e^{-\tau/\tau_q} \quad (3.16)$$

and notably, the correlation time of each mode τ_q is expected to have the exact same scaling of the fluctuation spectrum i.e.

$$\tau_q \propto \frac{1}{(q^3 + \bar{\lambda}q)} \quad (3.17)$$

This is indeed the case for the observed passive GUVs. In contrast, active GUVs containing an AMF exhibit a completely different scaling, with fluctuations at low modes scaling as $\sim 1/q^3$ but correlation times scaling as $\sim 1/q$ or slower, indicating that a thermal bath picture does not account for the observed results and that the time correlation of each mode, i.e. the mean time each mode is excited, is decoupled from the amplitude fluctuation of each mode.

course real, of the more general complex expression for the Fourier series i.e. $R(\phi, t) = \text{Re}[R_0 + \sum_{q=-q_M}^{q_M} f_q e^{iq\phi}]$ from Equation 1.4.3.2. It can be proven by equating the two terms that f_q is a complex number given by $f_{\pm q} = a_q \mp ib_q$ so that in all cases $|f_q| = \sqrt{a_q^2 + b_q^2} = c_q$. The two definitions are equivalent, so that the variance of c_n is the same as the variance of f_q .

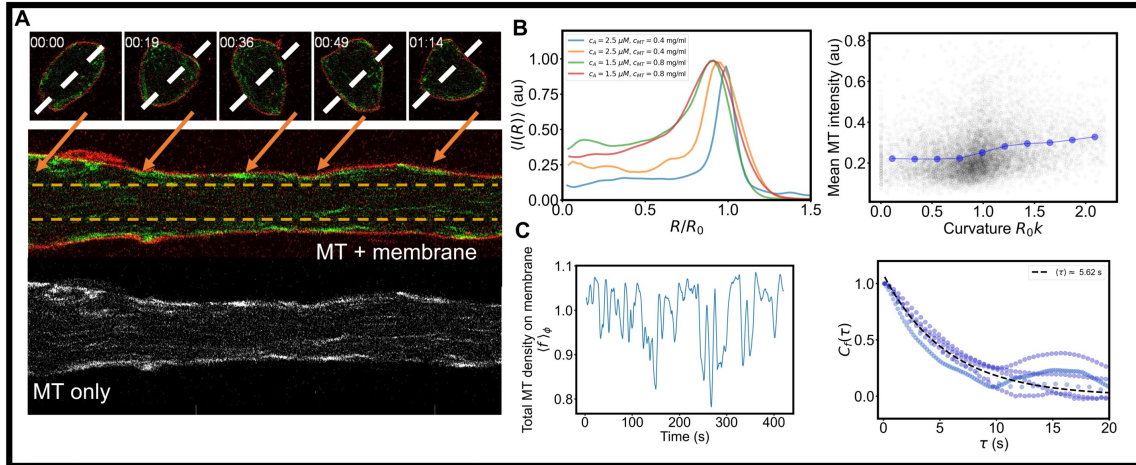


Figure 3.19: **Radial distribution of microtubules:** A) A kymograph shows accumulation of the microtubules along the membrane. Some temporal modulation of the MT density is also visible. B) Microtubules accumulate on the membrane, as measured by the radial distribution of the MT intensity across different samples, and have the tendency to accumulate in areas of high curvature. Left: Each curve is from a different GUV, conditions are $c_{MT} = 0.4$ mg/ml, $c_A = 2.5$ μM (blue and orange) and $c_{MT} = 0.8$ mg/ml, $c_A = 1.5$ μM , motors' concentration is kept at 60 nM for 0.4 mg/ml (120 nM for 0.8 mg/ml). Right: black points come from different GUVs, blue curve is the mean. C) Temporal behavior of the microtubule density near the membrane $f(\phi, t)$ (see Section 3.5.4.3) averaged along all membrane showing that the total MT intensity at the equatorial plane along the membrane changes over time, with a correlation time of ≈ 5.6 s. Conditions are $c_{MT} = 0.8$ mg/ml, $c_A = 2$ μM , $c_K = 120$ nM.

3.5.4 Analysis of the active forcing

3.5.4.1 Computing the active forcing

Clearly the decoupling must be due to the presence of an active forcing term that excites the membrane, i.e. the activity of microtubules. A precise microscopic picture would have to include how the microtubules are pushing against the membrane, and we will analyze this in the following simulation-based sections, but from an experimental point of view that analysis is unfeasible. We then use as a proxy for the active forcing the microtubules fluorescence intensity (in polar coordinates) $I(r, \phi, \theta) \propto \rho(r, \phi, \theta)$ that we assume proportional to the MTs' density ρ . That the forcing only depends on the density of microtubules and not on their orientations and/or the amount of locally present motors (KSA) here is a strong assumption that we nonetheless make.

3.5.4.2 Radial distribution of the microtubules

First of all, we can compute the distribution in space of microtubules, by analyzing the microtubules' density (intensity) $I(r, \phi, \theta)$ from images and averaging across the angular part to extract the radial distribution of microtubules, i.e. $I(R) = \langle I(r, \phi, \theta) \rangle_{\theta, \phi}$. We also apply a threshold to the intensity I to isolate microtubules from the background. The result (Fig. 3.19) clearly shows that microtubules accumulate on the membrane, as was also clear from microscopy

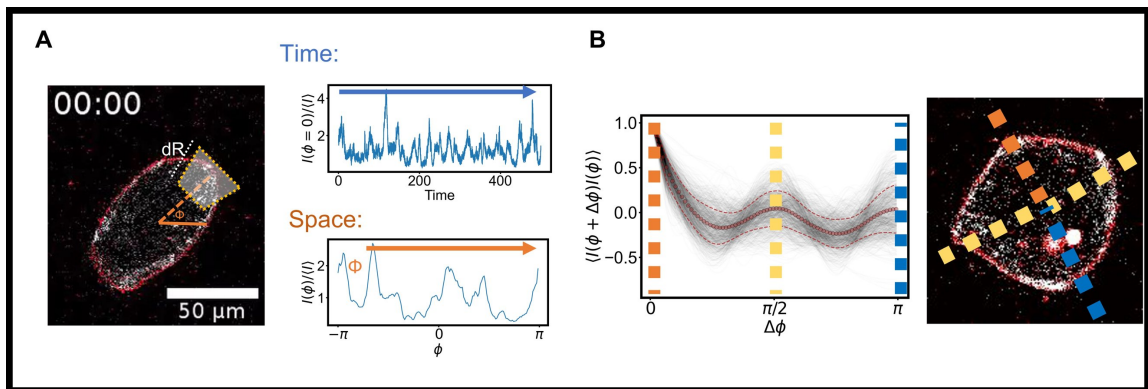


Figure 3.20: **Extraction of the membrane-near active forcing $f(\phi, t)$** : A) Starting from the equatorial plane images, we extract the intensity of microtubules f in a small area close to the membrane's position to obtain the active forcing pushing on the membrane. From this we can recover the behavior of MTs over time and space and connect it to membrane deformations. B) The MT intensity is correlated along the membrane, with visible correlation peaks seen at $\Delta\phi \approx \pi/2$ and $\Delta\phi \approx \pi$, indicating that bundles do not act as point forces but have a distinct organization. This is sketched in the picture reporting high intensity of microtubules at a quarter and at a half of the GUV perimeter, as shown by the correlation function.

images. The $I(R)$ function is indeed peaked at $R \approx R_0$, R_0 being the mean radius of the vesicle over time as extracted from the Fourier decomposition. Variations from R_0 in both directions are due to the intense radial fluctuations (Fig. 3.19.B). The accumulation of MTs at the membrane is due to the extensile nature of the AMF, that has a natural tendency to go towards the periphery. However, the presence of an elastic confinements stops it and forces it to rearrange. In particular, we notice microtubules have a slight tendency to accumulate in high curvature convex regions as expected for active particles.

However, a closer look at the MT time traces indeed shows that microtubules continuously reach and leave the membrane, i.e., they have a clear temporal dependency (Fig. 3.19.C), with the total density of microtubules near the membrane being modulated in time. The correlation function of the density shows a correlation time of roughly 6 seconds, consistent across datasets. Of course the equatorial plane projection misses the complex three-dimensional spatial organization of microtubules (seen for instance from the 3D images in Figure 3.15.B) which we will address further on with simulations.

3.5.4.3 Spectral behavior of the active forcing

From the radial distribution we realize that the microtubules accumulate on the membrane and that such a membrane-near MT density also has a temporal evolution. This suggests that we can extract information about the membrane's deformation by extracting the active forcing only in proximity of the membrane and analyse its temporal behavior.

Specifically, we observe a GUV with high resolution on the equatorial plane and compute from experiments the quantity

$$f(\phi, t) = \langle I(r, \phi, \theta = \text{equator}) \rangle_{R(\phi, t) - dR < r < R(\phi, t)} \quad (3.18)$$

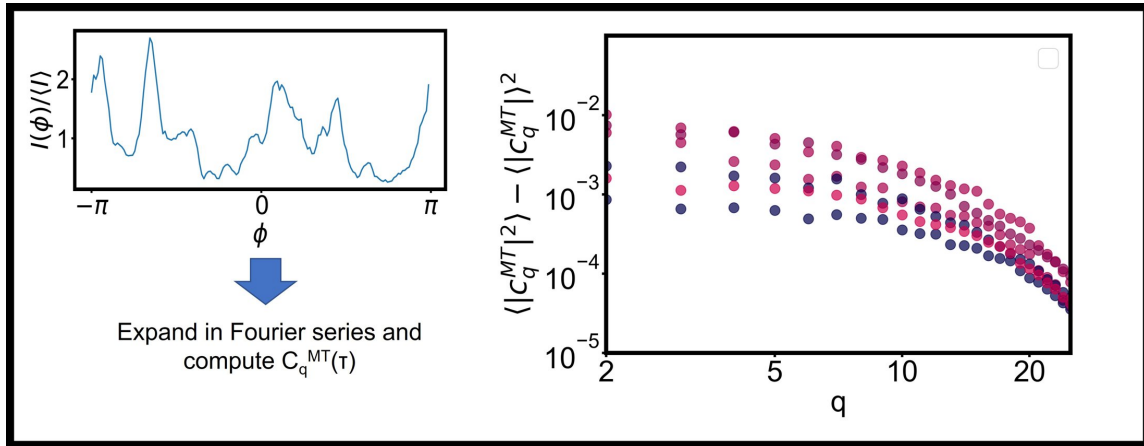


Figure 3.21: **Spectral behavior of the membrane-near active forcing** $f(\phi, t)$: The fluctuation spectrum of the forcing $f(\phi, t)$ does not follow the same scaling as the membrane but rather an exponential one, coherent with the fact that microtubules move for a given time across the membrane and then disappear. Indeed, the microtubule fluctuations are enhanced at $q < 5$, indicating low-mode distributions of the forcing, which decays as q increases.

i.e. the microtubule intensity averaged at each angle ϕ but only in a shell around the membrane's local position $R(\phi, t)$ of thickness dR , i.e., in proximity of the membrane. dR is chosen to be $2 \mu m$. This allows to estimate the active forcing $f(\phi, t)$ of the microtubules directly on the membrane. Additionally, of course, we can also expand f in a Fourier series following the same procedure we utilized for the membrane to obtain both the amplitude and the temporal fluctuations of the forcing f at each wavelength ℓ_q

$$f(\phi, t) = f_0 \left(1 + \sum_{q=1}^{q_M} a_q^{MT}(t) \cos(q\phi) + b_q^{MT}(t) \sin(q\phi) \right) \quad (3.19)$$

and allows for comparison between the microtubules' and the membrane's spectral behavior.

From this we obtain the fluctuation spectrum of the absolute value $c_q^{MT}(t) = \sqrt{(a_q^{MT}(t))^2 + (b_q^{MT}(t))^2}$ of the forcing, i.e., roughly, the density fluctuations of MTs at a given scale. The results, shown in Fig. 3.21. It shows the MT density along the membrane fluctuates with an exponential scaling. This already hints that confinement is setting a definite length-scale, given by the exponential at around $q \approx 5$, whereas a bulk AMF would rather expected to follow a power-law (see also Fig. 3.23) [Wensink et al. 2012; Doostmohammadi et al. 2017; Alert, Joanny, and Casademunt 2020; Alert, Casademunt, and Joanny 2021].

We then compute the correlation function $C_q^{MT}(\tau) = 1/2 \langle a_q^{MT}(\tau + t)a_q^{MT}(t) + b_q^{MT}(\tau + t)b_q^{MT}(t) \rangle_t$ using the same procedure as above but using f as input instead of R , and compare it with the previously computed correlation function $C_q(\tau)$ for the membrane.

The result shows that the time correlation of the membrane matches closely that of the microtubules, indicating that the time evolution of the membrane deformation are driven by the forcing f whereas its amplitude fluctuation are controlled by a mechanical response, imposing a $\sim 1/q^3$ scaling and not the exponential one of MTs. This can be further visualized by comparing

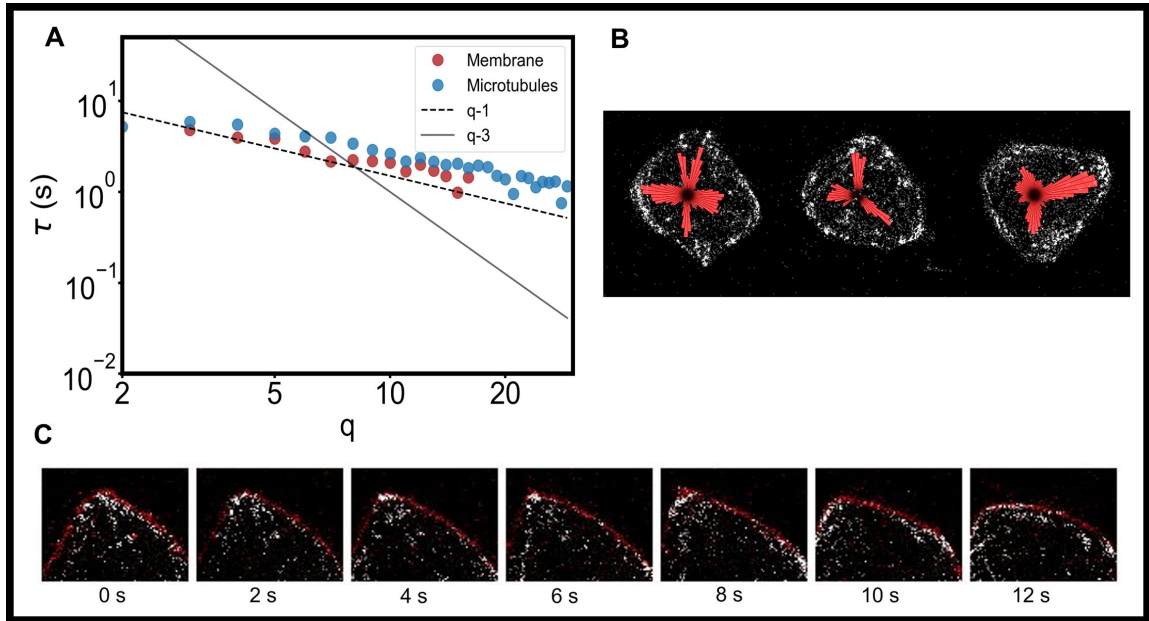


Figure 3.22: **Comparison of the spectral behavior of microtubules and membrane:** A) Microtubules fluctuate with the same correlation as the membrane, indicating that membrane deformations are indeed caused by the local pushing due to microtubules, i.e., it is the microtubules organization which fixes the time coherence of membrane fluctuations, whereas the fluctuations of the membrane are also tuned by the membrane mechanics. B) The organization of the microtubules correlates also with the membrane fluctuations. Vesicles showing deformations peaked at a given wavelength also exhibit a microtubules' density (red bars) with the same symmetry. C) Microtubules fix the membrane correlation. As long as microtubules are present, the membrane remains deformed. The picture show a ≈ 10 seconds long deformation driven by the presence of microtubules.

the microtubules' distribution in (angular) space with the membrane deformation, showing that microtubules accumulate where the deformation is stronger (Fig. 3.22.B) and that they also fix the duration of the deformation, which lasts as long as microtubules are present (Fig. 3.22.C).

3.5.5 Effect of confinement on the AMF

It is clear that confinement in an GUV is strongly affecting the behavior of bundles, which are forced to poke or buckle against the membrane. This hints that microtubules will spend an increased amount of time in a given position with respect to a bulk fluid as they accumulate against the GUV. This effect is clear as already seen in the microtubules accumulating at the membrane and buckling against it. This results, as shown, in the membrane fluctuating with a timescale which is fixed, at each wavelength, by the dynamics of the AMF. There is hence a feedback between the membrane, which confines the microtubules, and the microtubules, which deform the membrane. The feedback is clearly seen in the time correlation of the microtubules which spend ≈ 10 s at low-modes configurations (while the real-space correlation time is about ≈ 5 s) and have a distinct spatial organization (see again Figures 3.19.C and 3.20.B). This needs to be compared with the bulk behavior of the AMF. To do that we start from microscopy images of a bulk AMF ($c_A = 4 \mu\text{M}$, $c_K = 120 \text{ nM}$, 0.8 mg/ml MTs) and compute the intensity-intensity

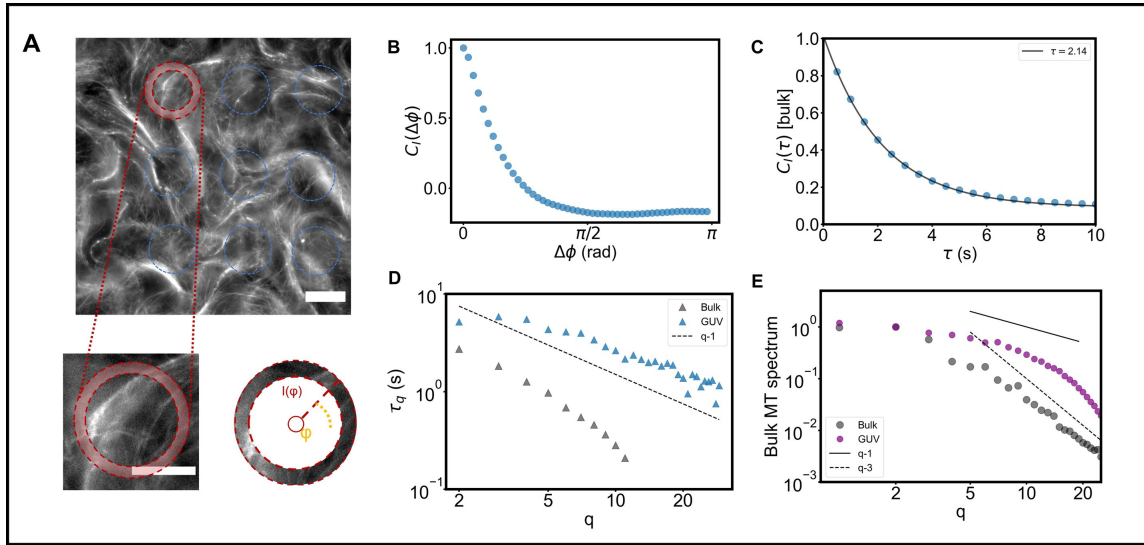


Figure 3.23: **Comparison of the behavior of the AMF in bulk and in GUVs:** A) By analyzing the microtubule intensity of a 3D bulk fluid ($c_{MT} = 0.8$ mg/ml, $c_A = 4$ μ M, $c_K = 120$ nM) inside virtual circles with roughly the same size of a GUV ($R_0 \approx 25$) we show the effect of confinement on the AMF. B-C) Both the time and spatial correlation of the bulk AMF is decreased with respect to that of a confined one. Compare with Figures 3.20.B and 3.19.C D-E) Also the spectral behavior of the bulk fluid is different from that of a confined one, with both the q -scaling of the time correlation and of the membrane fluctuation decaying faster. This indicates that confinement enhances the time and space persistence of microtubules. Scale bars are 25 μ m.

time correlation function $C_I(\tau) = \langle I(x, y, t + \tau)I(x, y, t) \rangle_{x, y}$ starting from epifluorescence microscopy images, where the mean is carried out over all pixels of the image inside virtual circular shells of internal radius 25 μ m and external one 27 μ m i.e. with a size comparable to a GUV. (Fig. 3.23.A). The result is a correlation time of ≈ 2 s and no visible correlation in space (Fig. 3.23.C-D). Starting from the same images, we also extract the spectral behavior of MTs by computing the bulk forcing $f_b(\phi, t)$ by expanding in Fourier series the intensity of microtubules in the circular shell. We average over multiple independent circles in the image and obtain a fluctuation and a time correlation spectrum which differs from that of MTs in confinement: correlation times are enhanced at each scale, as it was in real-space total correlation, and the fluctuation spectrum shows reduced fluctuation as over time microtubules decorrelate fast at all scales in the absence of confinement (Fig. 3.23.D-E).

Thus, due to the presence of a soft membrane, against which MTs can accumulate, deforming it and thus further getting trapped in position, the correlation times of the AMFs are enhanced in the GUV system. The same is also true for the spatial correlation of microtubules along the membrane, which shows distinct peaks under confinement (see again Fig. 3.20) whereas no peak can be detected by computing the correlation $C_I(\Delta\phi) = \langle I(\phi + \Delta\phi t + \tau)I(\phi, t) \rangle_t$ over time around circular shells in the bulk (Fig. 3.23.C).

Additionally, in the bulk fluid, by computing the velocity-velocity correlation function for the extracted flow field, one finds a correlation length $\ell_{act} \approx 150$ μ m which is bigger than the GUVs' mean diameter but roughly in the same order of magnitude. There is then a kind

of match between the GUV size and the correlation length of the active system. Some more additional comments can be also added here. First of all, the fact that under confinement low modes are enhanced in the forcing spectrum might be connected with the fact that only at low modes is the effect of confinement felt by the bundles. Indeed, the forcing fluctuations are enhanced up to $q \approx 5 - 7$ corresponding to a wavelength $\ell_q \approx 2\pi R_0/q \approx R_0$ i.e., comparable in size with the GUV's radius. This is also coherent with the model hinted at presented in Takatori and Sahu 2020 in which the fluctuation spectrum of the forcing was found to be $\sim e^{-(aq)^2}$ where a is the typical contact area. In this case, because deformations are due to bundles buckling, then $a \approx R_0$, comparable with the GUV radius and the bundles' buckling length. This sets a precise scale on the fluctuations spectrum of microtubules which is absent in the bulk.

3.5.6 Simulations of an AMF inside a GUV

To gain a better understanding of the behavior of active GUVs containing an AMF we performed simulations. This analysis is still in progress, but preliminary data already replicate they main feature of the experimental system and indicate the possibility of gaining a deeper understanding of the system.

We simulate GUVs containing an active fluid of microtubules to obtain further information about the behavior of the membrane and the bundles⁹. These results are promising but still preliminary and we present here a quick overview.

GUVs are simulated¹⁰ as an elastic mesh whose nodes can diffuse [Vutukuri et al. 2020; Peterson, Baskaran, and Hagan 2021]. MT bundles are simulated as N_f active filaments composed of a chain of monomers, which move inside the GUV. Each monomer has a linear size σ and the chain has a total length $L = N_m\sigma$, where N_m is the number of monomers. The value σ fixes the length-scale of the simulations whereas time is measured in units of a simulation time τ . Monomers are connected by an angular potential¹¹ which results in the chain having a bending stiffness κ_b that can be tuned. We thus neglect to simulate individual filaments and only simulate active bundles, with an effective bending rigidity, whereas their breaking and reassembling is simulated by the fact that bundles can bend and also change direction. Each monomer of the chain indeed moves with speed v and reverses its speed every τ_r units of time. The GUV radius is set to $R_0 = 25\sigma$.

Speeds are set in units of σ/τ . The bundles active force is summarized by the parameter α , in units of $k_B T/\sigma$, that represents the active force acting on the bead so that, for a single bead its speed is given by $v = \mu\alpha$ where $\mu = 0.1$ is a mobility coefficient low enough that the dynamics is overdamped (see Section 1.1). This means that beads move at a speed of $(\alpha/10)\frac{\sigma}{\tau}$. For example, an activity of $\alpha = 50$ indicates $v = 5\sigma/\tau$ and hence it takes the bead 10τ to cross the diameter of the GUV. Starting from this, the system is simulated using an overdamped Langevin scheme. Each simulation time step is $10^{-3}\tau$.

⁹This part of this work has been conducted in collaboration with Matt Peterson and Sarvesh Uplap from Aparna Baskaran's and Michael Hagan's group at Brandeis University.

¹⁰Details of the simulations, except for the fact that in this case bundles reverse their direction, can be found in Peterson, Baskaran, and Hagan 2021.

¹¹Using a *fene* bond from LAMMPS with an angular potential added to it. We also refer to LAMMPS units (style lj) system for units conversion.

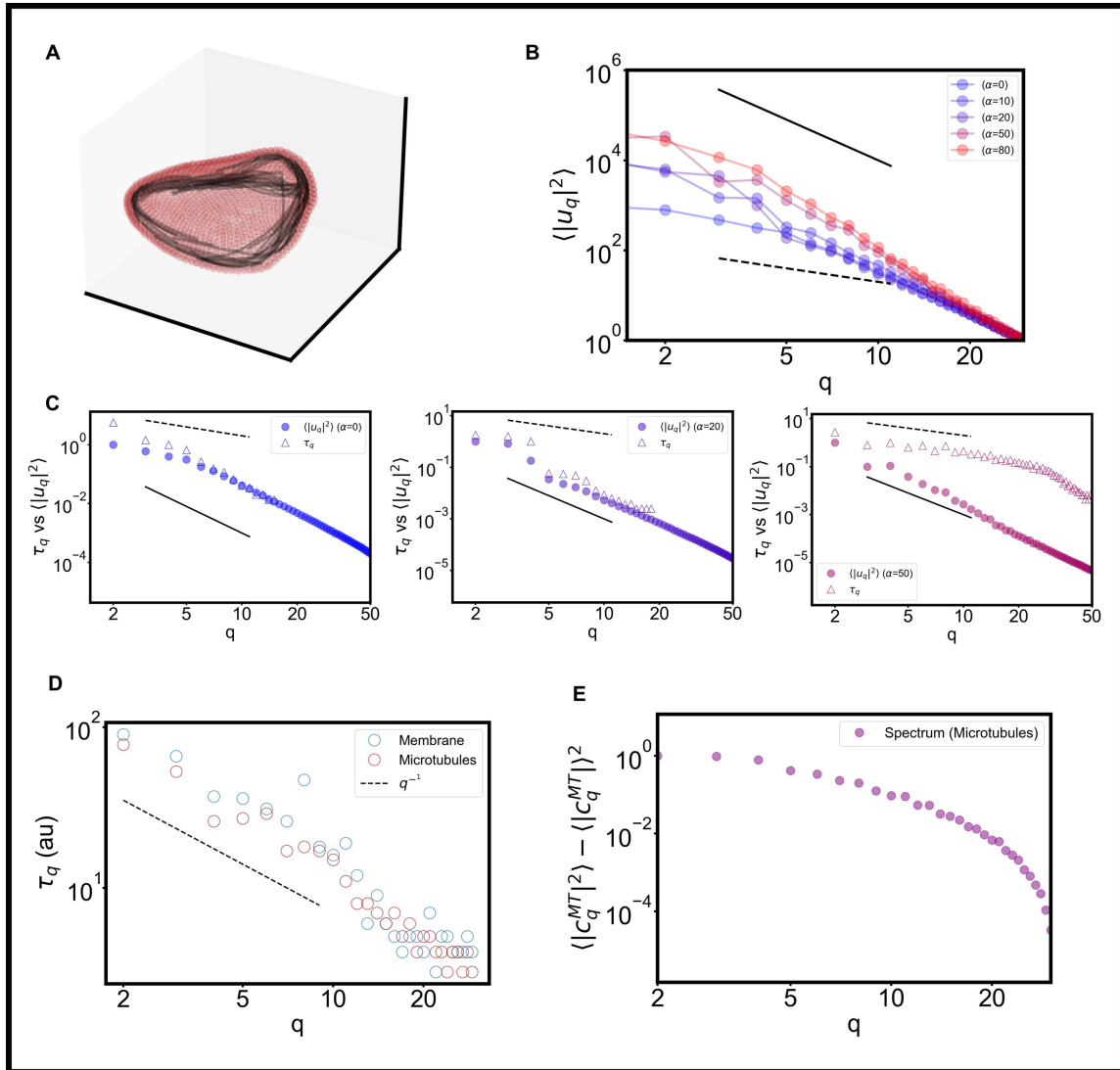


Figure 3.24: **Simulations confirm experimental results:** A) We simulated GUVs containing active bundles. B) As activity α of the bundles is increased, the fluctuations' spectrum also is enhanced and tends towards the $\sim 1/q^3$ scaling. B) Similarly, the membrane's fluctuation spectrum becomes detached from the time correlation τ_q in an activity-dependent way. D) The microtubules and the membrane fluctuation times are superimposable. E) The MT fluctuation spectrum is exponential.

By using a normalized system of units, we get the relative values of all quantities in the simulation units σ and τ . We can verify that they match experimental ones by fixing these two. As bundles in experiments move at $\approx 2 \mu\text{m}/\text{s}$ and thus it takes them 25 s to cross the GUV diameter (assuming $R_0 \approx 25 \mu\text{m}$), this implies $\tau \approx 2.5$ s. If we also set $\sigma = 1 \mu\text{m}$ then bundles are in the $50 - 100 \mu\text{m}$ range, the GUV has a radius of $25 \mu\text{m}$, speeds are in the $0 - 2 \mu\text{m}/\text{s}$ range depending on α and the integration time is 2.5 ms. This is close enough to experimental values.

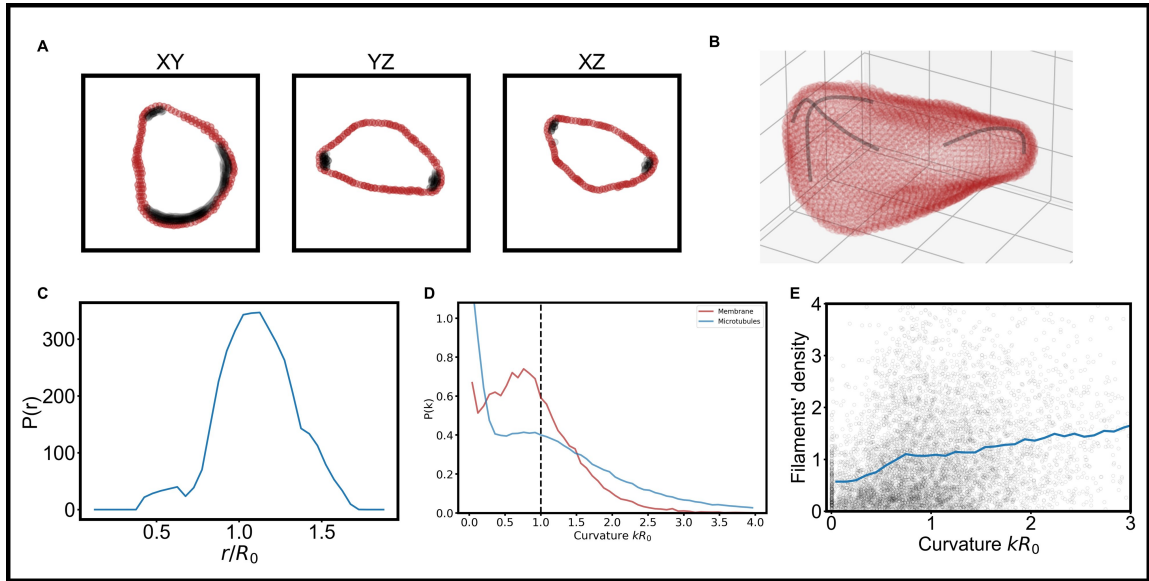


Figure 3.25: **Curvature and density of filaments:** A) Microtubules accumulate at the membrane where high-curvature deformations are present and have a distinct 3D organization as shown from these snapshots of the same simulated GUV at different planes. B) Bundles curve along the membrane, fixing its curvature and, in return, being affected by it. This is shown here by isolating only a few bundles out of all the present ones. C) As in experiments, simulated bundles accumulate on the membrane D) Membrane and bundles curvature. Bundles deviate strongly from their equilibrium elongated shape due to activity and confinement and especially show a peak at $k \approx 1/R_0$ indicating an effect due to the GUV. E) Bundles accumulate in areas of higher curvature. Compare with Figure 3.19

We first of all verify that we can recover the experimental results (Fig. 3.24). Upon activation of the bundles, they start pushing against the membrane deforming it. We extract the fluctuation spectrum by expanding the contour of the mesh on the equatorial plane as a Fourier series, from which we extract both the Fourier coefficients $u_q(t)$ and the correlation times τ_q . As expected, in the passive case the time scale as the spectrum whereas as activity increases ($\alpha \approx 20 - 50$) the spectra show the experimental $\sim 1/q^3$ scaling whereas correlation times again scale as $\sim 1/q$. We also see that as α is increased the fluctuations' order-of-magnitude increases accordingly. Additionally, we also can compute the fluctuation spectrum of the filaments' density along the membrane, replicating an exponential decay similar to that of $f(\phi)$, and prove that again the microtubules fix the correlation time of membrane deformations, while at the same point confinement forces them to follow a non power-law, hence not scale-free, behavior.

With simulations we however also have full control over the behavior of the individual microtubules. We can monitor their position along the membrane and their curvature (Fig. 3.25.A-B). Again, we verify that filaments because of activity accumulate on the membrane (whereas in the passive case they do not). The radial distribution of filaments is obtained from the position $\mathbf{r}_i = (x_i, y_i, z_i)$ of the monomers as $r = |\mathbf{r}|$. The number of filaments with a distance from the center of the GUV between r and $r + \Delta r$ (with $\Delta r = 1 \mu m$) normalized by the volume of the spherical shell $\approx r^2$ is then plotted against r obtaining the distribution in

Figure 3.25.C. Additionally, the curvature of the bundles (obtained as $k = |\mathbf{n} \times \mathbf{t}|/|\mathbf{t}|^3$, where \mathbf{t} is the tangent vector along the bundle and $\mathbf{n} = \nabla \mathbf{t}$ is the normal one) is also plotted and shows a peak at $k \approx 1/R_0$ indicating that confinement inside a GUV, as expected, has an effect on the behavior of the bundles. Indeed, bundles appear to buckle, as in experiments, along the membrane and thus have a comparable curvature. The curvature of the membrane (computed along the GUV contour on the equatorial plane¹²) is compared to that of simulated bundles in Figure 3.25.D. Finally, we also check that active bundles have the tendency to accumulate in high-curvature areas of the membrane as expected for active particles and as observed, although with a lower signal, in experiments.

Simulations also allow to study the behavior of the system as activity increases. As already mentioned, we notice an increase in the fluctuations' amplitude as activity is increased. This hints that, as the bundles become more active different modes start to fluctuate, with low-activity mostly affecting the low modes whereas high activity affects an increasing number of higher modes. This will also be further investigated by studying the behavior of the simulated GUVs not only as activity changes but also tuning the bundles' rigidity and length, to see the effect this has on the excitation of the low fluctuation modes, as we expect small flexible bundles to feel the confinement less.

Additionally, we now have access to the three-dimensional behavior of the membrane. This means that we can decompose both the membrane and the microtubules' density in spherical harmonics and check whether, in the process of projecting on the equatorial plane, some information about the dynamics is lost by averaging over the three-dimensional modes. Thus the ongoing work on this system consists indeed in better understanding how is the bundles' 3D conformation affected by confinement and how, given an active forcing due to the microtubules, does the membrane react in its fluctuations.

3.5.7 Discussion

AMFs have brought a lot of attention on themselves thanks to their ability to replicate biologically-related phenomena, but also as a tool to study cytoskeleton-based active fluids. However, cellular systems are, of course, confined inside the cell and hence to understand how this modifies the behavior of an AMF is of utter importance. Indeed, several studies have attempted to study the behavior of AMFs, and active systems in general, under strong or elastic confinement recently [Paoluzzi et al. 2016; Hardoüin et al. 2019; Chandrakar et al. 2020; Takatori and Sahu 2020; Vutukuri et al. 2020]. Strong confinement has been shown to change drastically the behavior of AMFs, leading to coherent flow [Wu et al. 2017]. Elastic confinement has however been mostly unexplored in the field of AMFs.

Here we have shown that encapsulating an AMF inside a GUV leads to large shape fluctuations. Interestingly, instead of reaching an equilibrium shape with all pressures balanced the vesicle continuously deforms, driven by the microtubules, changing shape over time. This indicates that, due to the nematic extensile behavior of microtubules, the force the AMFs impart is changing over time without settling. This is also due to confinement that forces microtubules inside a finite volume, with size comparable to the bundles' length, leading to accumulation on

¹²For the moment, the analysis is limited to the 2D curvature of the membrane as in experiments.

the membrane and enhanced fluctuations in time and space. MTs travel across the membrane with a definite timescale which we found also fixes the timescale of membrane fluctuations. While the membrane is forced, by area conservation and resistance to bending, to accommodate its shape to deal with the AMF-based pressure, resulting in fluctuations which still decay similarly to the passive one, albeit with different order of magnitudes, the prolonged presence of microtubules on the membrane leads to an uncoupling of the time behavior and the spatial behavior, the former being now dominated by MTs' activity rather than mechanics. Microtubules fix the timescale of the fluctuation.

At the same time, MTs are affected by confinement and hence force to organize according to the membrane's shape. They indeed accumulate in high-curvature areas, in which they can get trapped for a long time, resulting in high correlation times at high mode, until the conformation becomes unstable due to buckling and velocity reversal and they travel through the bulk until they reach a new temporary conformation. Buckling of the bundles is also affected by the membrane and, in turn, is the source of the membrane's deformation in the first place. Additionally, one main effect of confinement is to set a length-scale for the otherwise scale-free AMF which is reflected both in an exponential-like scaling of their fluctuations and in peaks of the intensity correlation along the GUV's equator. Hence simple models with point forces, such as the one in Takatori and Sahu 2020, will have to be revisited to account for this behavior in which bundles collectively push over a wide area (set by their buckling curvature).

This Section represents an attempt to disentangle all of these effects and understanding how the feedback works. We did this, by analyzing separately the behavior of microtubules and that of membrane, underlining where they differ and where they behave similarly.

The ability of MTs to deform a vesicle, if understood, can lead to the development of deformable micro-robots [Sato et al. 2017], to the replication of biological processes such as cilia-based motility but can also serve as a model systems to study the influence of active forces, in a more realistic and complex settings than those already presented [Takatori and Sahu 2020; Vutukuri et al. 2020], on deformable membranes.

3.6 Conclusions of Chapter 3

In cells, shape deformations are often based on the actin cytoskeleton, whose complex regulation is hard to replicate *in vitro* due to the huge number of processes involved. While its contraction is now relatively well understood [Bendix et al. 2008; Köhler and Bausch 2012; Belmonte, Leptin, and Nédélec 2017] its ability to also grow, expand, deform and assemble into ordered structures is more complex hence less clear. We did address some of these concerns in Chapter 2, whereas here we circumvented the problem by focusing on a microtubule-based system, which was already known to show self-organization into an active fluid. While, for the above reason, this means that we lack biological MT-based analogues, by abstracting and focusing on general mechanisms we have attempted to understand, in general, how the self-organization of active fluids can be regulated by crosslinking and activity and, more importantly, what is the effect of an active fluid under cell-like confinement.

In the first Section, we focused on how the microscopic behavior affects the macroscopic one. This highlights some of the possibility cells have to tune the macroscopic dynamics of the cytoskeleton by making local, microscopic changes, i.e. (de)activating crosslinkers and motors. Small changes can have a strong effect and can be based on subtle changes, for example in the local polarity of filaments (which, for example, plays a central role in the formation of the mitotic spindle).

In the second Section instead, we focused on the macroscopic behavior of an AMF under confinement. Having learned how to tune it, how is the final result affected by cell-like (elastic) confinement. The AMF-in-GUV systems allows to study at the same time the membrane, and its deformations, and the AMF, and its modulations in time and space, trying to understand if the energy input due to the AMF affects the vesicle at all scales or whether some specific length- and time-scales are more affected than other ones.

The ability to tune, control, encapsulate and study AMFs in cell-like confinement can allow the development of more complex and refined experimental systems, able to replicate in controlled conditions the phenomenal plasticity of cells' deformations, necessary for basilar processes, from motility to reproduction.

Conclusions

The cytoskeleton, despite its name, does not behave as a simple scaffold but is rather an active, ever-changing machinery that provides as much change as it provides structure. At the same time, to change shape, for a cell, also means to deform their membrane. Cells indeed separate themselves from the outside world thanks to their membrane. However, same as the cytoskeleton, it would be misleading to consider the cell membranes as simply a rigid, protective barrier as it instead is a dynamic, continuously morphing structure. Cells can indeed tune their shape from amoebic-like to spherical like, can protrude finger-like structures, can engulf outside elements and so on. The cytoskeleton, on its part, is what drives these changes.

The general aim of this thesis has been to elucidate, on the one side, how, due to the presence of a membrane and in general of a complex environment, the cytoskeleton must cope with constraints (of different kind, from steric to topological) to be able to assemble in the desired structure. On the other hand, the presence of the cytoskeleton leads to sometimes violent changes in the membrane conformation which in turn affect the cytoskeleton that produced it in the first place. To disentangle and control separately all of these feedbacks we have exploited *in vitro* model systems containing a cytoskeletal component (actin, microtubules, motors...) and a lipid membrane and we have combined them in different ways to isolate the relevant contributions and to explain them in simple terms. The main results can be summarized as follows: first of all, the fluidity of the membrane can lead to unexpected effects on the organization of the cytoskeleton. In particular, different than on a solid substrate, friction is decreased and thus exerting forces is more challenging. In this context, steric interactions can become relevant and lead to unexpected emerging patterns. At the same time, if steric interactions are relevant, then so are the constraints dictated by topology on the alignment of elongated particles (filaments) and hence the local alignment (or, when absent, nematic defects) start playing a role. This result has been studied in depth in Chapter 2.

The second main result is the effect of confinement, set by the presence of the cell membrane. Even when undeformed, the spherical topology of the cell can have an effect on the formations of patterns. Additionally however, when deformed by the cytoskeleton, it can lead to feedback loops in which the deformation enhances further build-up of pressure, leading to a complex crosstalk between the cell's mechanics and the force-generating units (i.e. motors and filaments). We studied this in Chapter 3, where we also showed how while membrane's mechanics still is relevant (in maintaining the cell intact, in the first place) their behavior in time is completely dictated by the active process it contains (which however, again, is in turn influenced by confinement).

These results have several implications. First of all, some of these effects are often neglected,

whereas we have proved that they can result in non-trivial behavior. Second, while lacking a precise biological analogue, they are simple enough to generalize, suggesting that all we discussed (steric effects leading to polar sorting, nematic constraints shaping the flow, active forces deforming the membrane according to specific mode-dependent rules) surely has been exploited by cells at some point or another. Third, and finally, this opens up new possibility along the path of reconstituting a full cell, or a minimal version of it, able to assemble its skeleton into predefined patterns, to deform and move, to adapt and, in short, sooner or later, to do what all cells do: live.

Chapter 4

Materials and Methods

Contents

4.1	Materials: buffer, proteins and reagents	153
4.2	Experimental model systems of lipid membranes: SLBs and cDICE GUVs	157
4.3	Microscopy	160
4.4	Gliding assays	161
4.5	Data analysis for gliding filaments	162
4.6	Active microtubule fluids	167
4.7	Data analysis for active microtubule fluids	167
4.8	Cytosim simulations	169

4.1 Materials: buffer, proteins and reagents

Buffers

FB and FB25 buffers

F-Buffer (FB) is 2 mM Tris (pH 7.5), 2 mM $MgCl_2$, 0.5 mM ATP, 0.2 mM $CaCl_2$, 100 mM KCl. 1 mM DTT is added before use. F25-Buffer (FB25) is exactly the same as FB but with only 25 mM KCl. This buffer is used when actin and myosin have to be mixed without exceeding 60 mM KCl in total, which is known to impair Myosin's binding to actin.

AB and ABT buffers

Assay-Buffer (AB) is 25 mM Imidazole (pH 7.4), 25 mM KCl, 4 mM $MgCl_2$, 1 mM EGTA. 1 mM DTT is added right before use. AssayTris-Buffer (ABT) is exactly the same as AB but 50 mM Tris is used instead of Imidazole.

M2B and MIX buffers

M2B is 80 mM Pipes (pH 6.8), 2mM $MgCl_2$ and 1 mM EGTA. MIX, which is added at the end when Kinesin is present, is 3.2 mM $MgCl_2$ taken from a 67 mM stock in M2B.

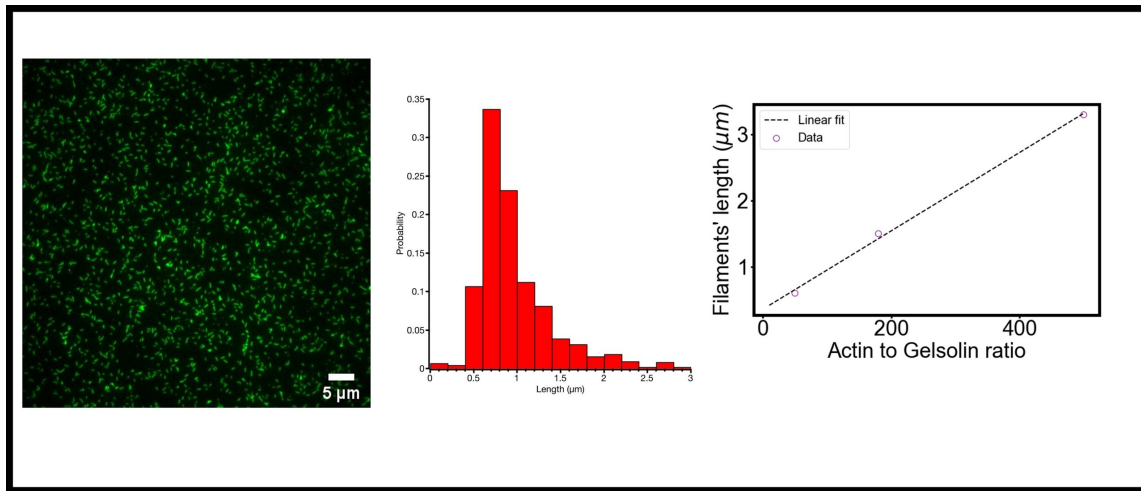


Figure 4.1: **Gelsolin affects the actin filaments' length** Different gelsolin to actin ratio lead to different mean filaments length, as computed from TIRF images. A histogram for an actin:gelsolin ratio of 1:100 is shown, together with linear fit to compute different expected lengths based on the ratio.

Proteins and reagents

Actin

Actin was purified from rabbit skeletal muscle. No rabbits were directly involved in the study. Monomeric actin was stored at 4 °C in G-Buffer (2 mM Tris, 0.2 mM ATP, 0.2 mM CaCl₂, 0.2 mM DTT, and 0.005 % NaN₃ at pH 8.0). In the following, G-Actin refers to actin in monomer state, F-Actin to polymerised actin.

Stabilized actin filaments To polymerize actin filaments and stabilize them to avoid de-polymerization, the desired concentration of actin is incubated in FB together with 1mM DTT and a phalloidin, which stabilizes the filaments. Phalloidin is added at half the actin concentration and can be fluorescently labelled with Alexa-488 or Alexa-647 (Thermofisher). The mixture is kept at room temperature for \approx 30 minutes and then kept on ice and used within the week.

Length regulation with Gelsolin To regulate the length of actin filaments, G-Actin is incubated with phalloidin and gelsolin in a given ratio $r = [\text{Actin}]/[\text{Gelsolin}]$ in FB25. The more gelsolin is present, the shorter the resulting actin filaments. Actin filaments shortened by gelsolin are used within a week. Figure 4.1 shows the mean length of actin filaments as gelsolin is added in different ratios, as measured from TIRF images of sedimented filaments.

Myosin/HMM

Myosins were purified from rabbit's skeletal muscles. HMMs were prepared by dialyzing ground rabbit skeletal muscle against the Myosin-buffer (0.6 M KCl, 10 mM KH₂PO₄, and 2 mM DTT) at 4 °C (77). Biotin-HMMs were prepared by incubating HMM with NHS-biotin.

Removal of inactive heads To remove inactive heads, 2 μ M HMM is incubated with 10 μ M F-Actin polymerised in FB25 to avoid an excess of KCl which is known to reduce Myosin's affinity to actin. The mix is supplemented with 1 mM DTT and 2 mM ATP, left on ice for 5 minutes and then centrifuged at 350.000 x g, 4 °C, 25 minutes. Inactive heads bind actin filaments in the rigor state and accumulate in the pellet. The supernatant is extracted and used within the day.

Lipids

Lipids are purchased from Avanti or ThermoFisher. In particular DOPC, Egg-PC, DSPE-PEG(2000) and DSPE-PEG(2000)-biotin are purchased from Avanti. Instead, TexasRed-DHPE is purchased from ThermoFisher. All lipids are dissolved in chloroform and stored at -20 °C

Actin-binding proteins

Gelsolin Gelsolin was purified from adult bovine serum (Sigma Aldrich). The freshly defrosted serum was supplied with 50 mM Tris-HCl (pH 8.0) and 0.2 mM PMSF. Then, the serum proteins were precipitated with 35down by centrifugation. The pellet obtained by the second precipitation was washed twice with a buffer containing 25 mM Tris-HCl (pH 8.0) and 50subsequently dialyzed against a buffer containing 25 mM Tris-HCl (pH 8.0), 45 mM NaCl and 1 mM EGTA. Gelsolin was purified by ion-exchange chromatography on a diethylaminoethyl cellulose column by washing first with the same buffer, then with a buffer containing 30 mM NaCl and finally eluted with a buffer containing 25 mM Tris-HCl (pH 8.0), 30 mM NaCl and 2 mM CaCl₂.

Anillin (ANLN) for microtubule active fluids

Anillin (ANLN) is an actin-binding protein that bundles filaments. We use it as an (unspecific) microtubule crosslinkers. We clone ANLN using the following (His-Tag containing) amminoacid sequence¹:

```
MGSSHHHHHSSGLVPRGSHMDPFTEKLLERTRARRENLQKKMADRPTAGTRTAAL
NKRPREPLLEANHQPPAPAEAAKPSKSPSKRRCSDNASTPDAGAENKQPKTPEL
PKTELSAVASHQQLRATNQTTPQVSLSSDKELTASDVKDASSVKTRMQKLADQRRY
WDNNVSPSSPPAHVPPKDIIVSPPKQIPDVGNDTPVGRRRGRFANLAATIGSWED
DLSHPFVKPNKQEKPGTACLSKESTTSSASASMNSRSVKQDTTSCSQRPKDITVN
KAVCSGQLKNILPASKPASSVASTEVSQKSKPLAIKSPTVVTSKPNENVLPASSL
KPVSANSSPQKTERPASRIYSYQSASARNELNNNTPVQTQQKDKVATSGGVGKSF
LERFGEKCEHSPAPLNQGHRTAVLTPNTKSIQERLLKQNDISSTALEHHHHHHH
```

We use a pET28b(+) vector. Plasmids are amplified with chemically competent E. coli XL-1 blue cells for DNA production and E. coli BL-21 CodonPlus for protein expression, both purchased from Agilent Technologies.

Kinesin/microtubules/PRC-1

Small, GMPCPP-stabilized, Alexa-647 labeled microtubules, biotin-Kinesin401 and KSA (two Kinesin401 connected by a streptavidin linker) are obtained from Brandeis' University's Material Research Science and Engineering Center (MRSEC) and kindly prepared by Dr. Shibani Dalal. PRC-1 was a gentle gift of Dr. John Berezney (Brandeis University). Microtubules is thawed right before used and kept at room temperature.

Other material

Methylcellulose, PEG (35 kDa), silicon oil (50 cSt, product number 4020.1), mineral oil (product number M3516) are purchased from Sigma. Methylcellulose (40 kDa, 400.000 cps) is dissolved to 2 % w/w in water by heating ca. 80% of the water volume to 80°, dissolving MC until the solution is clear and then letting it mix at 6°. Only then is the remaining necessary water added. MC stock solutions are left in a rotor at 6° and used within the week. PEG is dissolved to 2 % w/w in water.

Coverslips (in mm²: 18x18, 24x25, 24x60) are purchased from Roth.

¹I deeply thank Dr. Philip Walter Bleicher for the cloning of ANLN!

Scavenging systems (GOC and POC)

We use Glucose-oxidase and catalase (GOC) or pyranose-oxidase and catalase (POC) as oxygen removal scavenging systems.

GOC is 10 U/mL glucose-oxidase and 1 kU/mL catalase.

POC is 10 U/mL and 1kU/mL catalase. POC, differently from GOC, does not lead strong to a time-dependent pH lowering and is more suitable for most application.

As a substrate, a final concentration of 0.66 % glucose is used. Glucose-oxidase, pyranose-oxidase, catalase and glucose are dissolved in PBS and snap-frozen at a 50 x more concentrate aliquots and thawed and mixed at the last moment.

ATP regeneration system (CPK/CPH)

As an ATP regeneration system we use creatine-phosphokinase (18.2 units/mL CPK) and creatine-phosphate (CPH, 9 mM) (Sigma). Stock solutions (at 66x the final concentration) are dissolved in 90 mM Tris (pH 8.3) and 44 mM Boric acid and frozen at -80 °. When doing the buffer, the pH should automatically reach ≈ 8.3 . Do NOT use Tris-HCl.

4.2 Experimental model systems of lipid membranes: SLBs and cDICE GUVs

We here describe the precise methods used to produce supported lipid bilayers (SLBs) and giant unilamellar vesicles (GUVs) using the technique cDICE. Both techniques are used in the results Chapter and are therefore explained in detail here.

4.2.0.1 Supported lipid bilayers

Supported lipid bilayers (SLB) are a model system for membranes whose advantages resides in its simplicity, tunability and in the fact that, being flat, it allows high-resolution TIRF microscopy. We prepare SLBs according to published protocols with only minor modifications [Murrell and Gardel 2012; Sciortino and Bausch 2021].

Preparation of small unilamellar vesicles

To prepare SUVs, the chosen concentration of lipids are added to a glass vessel and evaporated with a gentle nitrogen streams. The formed lipid film is the kept in a vacuum chamber for at least 3 hours to evaporate the remaining chloroform. After that, lipids are dissolved in PBS to a final concentration of 1 mM, gently vortexed and then sonicated for 45 minutes. The lipid solution is then extruded using an Avanti MiniExtruder with a 100 nm membrane for 20 times and then kept on ice or at -6°C . SUVs are used within the week.

Cleaning of glass slides

In order to form a supported lipid bilayer (SLB) a fundamental step is cleaning coverslips and making the strongly hydrophilic. This can be achieved in two ways:

Fast cleaning with UV/Ozone Coverslips are first immersed in 2% Hellmanex, sonicated for 30 minutes and extensively washed with millipore water (ddH_2O). Then they are immersed in 3 mM KCl and again sonicated for 30 minutes. Finally, they are washed in ddH_2O , then 100% ethanol and stored in ethanol. Right before use, the coverslips are dried with a nitrogen stream and kept for 6 minutes in a UV/Ozone cleaner (Jelight, Model 30). A chamber is then assembled and the SUVs are added immediately.

Piranha cleaning First, coverslips are precleaned by sonicating them in 3 mM NaOH for 30 minutes and then washing with $dd - H_2O$. Then, they are immersed for 2 minutes in Piranha solution, as described below. The ‘‘Piranha’’ solution is a mixture of Sulphuric acid and Hydrogen-Peroxide. Due to its very reactive nature it is a dangerous preparation which we suggest to perform carefully, as it is prone to explode if mishandled. Hydrogen peroxide and sulphuric acid are mixed in a 1:2 ratio. To avoid high local concentration of peroxide, which would cause the solution to explode, this latter is added to sulphuric acid and never vice versa. The so made solution instantaneously becomes very hot and it must be handled with care. No organic material nor metals must be insterted in the solution. Coverslips are inserted in a glass container, which is then put in a 60°C bath to avoid heat shocks. The Piranha solution is poured on top. Coverslips are extracted with ceramic tweezers after 2 minutes and washed abundantly with ddH_2O . They are then stored in ddH_2O and used within the week. Prior to use, the coverslip is dried with nitrogen and used immediately.

After three hours, as the solution lost reactivity, it is discarded appropriately.

Formation of the SLB

SUVs are diluted to 0.5 mM and are incubated in a $\approx 50 \mu\text{L}$ chamber composed of a hydrophilic coverslip and a glass slide separated by three layers of molten parafilm. SUVs are incubated for 10 minutes then washed with an at least 10 x volume excess with PBS. Finally, the chamber is washed two times with the buffer in which the experiment will take place. The rest of the experiment is performed by adding material to the chamber, washing if necessary. Right before imaging the chamber is sealed with vacuum grease and observed with TIRF microscopy. The fluidity of the SLB is checked using FRAP measurements (see 4.5).

Notes on the formation of SLBs

SLBs are very sensible to heat shocks and buffer exchanges. Buffer should be exchanged gradually and after removing all unburst SUVs with extensive washing after incubation. All solutions added to the SLB must be at room temperature, same as the SLBs. Degassing solutions before adding them to the SLB improves sensibly the final quality.

Some proteins or buffers might be very sensible to the coverslip cleaning. Piranha solution is the most effective way in our opinion but should be performed with care.

Several alternative methods exist to produce SUVs including tip-sonication and heat-thaw cycles of the lipid mix. Each method has pros and cons and must be carefully chosen depending on the experiment needed.

4.2.0.2 cDICE: continous droplet interface crossing encapsulation

Continous droplet interface crossing encapsulation (cDICE) [Abkarian, Loiseau, and Massiera 2011; Van de Cauter et al. 2021] is a technique to generate giant unilamellar vesicles (GUVs) containing the desired reaction mix in a fast, controlled way and using a small amount of materials. Briefly, a capillary is filled with the reaction mix and inserted in a rotating chamber with an applied pressure (using an Elveflow pump). The pressure leads to the formation of droplets at the capillary tip which then, due to centrifugal forces, detaches and crosses several layers containing lipids that cover its surface.

Preparation of the chamber

A cylindrical chamber is made by cutting Petri dishes or by 3D-printing. The chamber has a 3 cm (diameter) hole in the center to allow capillary insertion and small hole at the side to extract vesicles. This latter hole is capped with an Eppendorf-tube cap. The total diameter of the chamber is approximately 1.5 cm high and has a diameter of 8 cm. See Fig. 4.2.A for a picture of the chamber.

Preparation of the lipid/oil mix

First, an oil mix is prepared containing 80 mL of silicon oil and 14 mL of mineral oil are mixed together. The desired ratio of lipid is then mixed directly in 600 μL of decane and then 9.4 mL of the oil mix is added on top, with slight vortexing. The final concentration is 10 mM lipids.

Preparation of capillaries

Capillaries (1 mm diameter, 8" long) are cut in two steps. First, they are cut in two halves with smaller tips using a Flaming Brown Micropipette Puller (Sutter Inst. CO.) using specific settings (Heat: 820, Pull: 80, Velocity: 40, Time: 100). Then, the tip is adjusted to the desired size using a small glass bead attached to a resistor. By applying a voltage difference across the resistor, the resistor expands, the beads warms up and is stuck to the capillary at the desired position, chosen using a microscopic scale. Removing the voltage causes contraction of the resistor and rupture of the capillary. Capillaries are cut to a 40 μm diameter tip, unless specified otherwise, as measured with a 20 x objective, but their diameter can be adjusted to obtain GUVs of different size. The capillaries are then passivated by dipping them for one minute in 65% nitric acid, then washed with ddH_2O , dried with nitrogen, dipped again in a 90% Methanol, 9% ddH_2O and 1% (Chloromethyl)trimethylsilane for 30 seconds and thouroughly dried again. Especially the silane needs to be removed as best as possible to avoid clogging. This makes the capillary tip hydrophobic and avoids protein adsorption. Finally, the capillaries are dried at 70 ° C for at least 3 hours. Afterwards, they are bent in an L-shape with an open flame to make it easier inserting them into the chamber.

Encapsulation procedure

First of all, the osmotic pressure of the reaction mix is measured with a Gondotec osmometer. If the mix contains proteins which react fast or degrade fast they are added at the very and or the experiment is carried out in a cold room. A glucose-buffer solution is made such that its osmotic pressure is roughly the same as the reaction mix

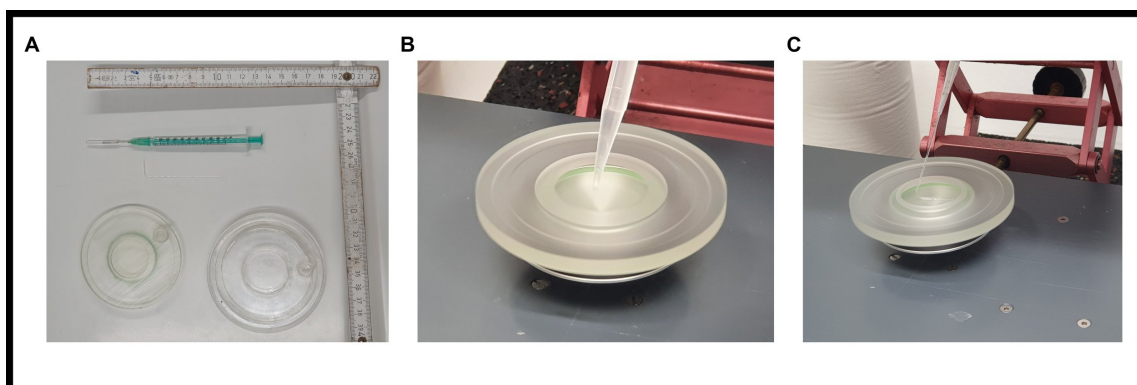


Figure 4.2: **cDICE setup** A) Size and shape of the cDICE chamber, both 3D-printer and made out of Petri dishes, and capillary. Ruler for reference. The syringe and tubing is used to flow the mix inside the capillary. The hole to extract GUVs is also visible. B) the chamber is put on a rotating motor and the solutions are added sequentially inside with a pipette. C) Finally, the capillary is inserted in the decane solution and pressure is applied to form GUVs.

($\approx 10 - 20$ mOsm/Kg higher). The chamber is placed on a motor and set to rotate at 1800 rpm. In the following order, 1 mL of glucose-buffer mix, 3.5 mL of lipid-oil mix and 1 mL of decane are inserted in the chamber. The reaction mix is then flown inside a capillary, the capillary is inserted in the chamber and the pressure necessary to generate droplets is applied (roughly, 30 – 100 mbar). See Fig. 4.2.B and C for a picture of the procedure. Should droplets not form on the capillary's tip, gently shaking the capillary or even cutting the tip can help, especially with viscous (e.g. MC) solutions. Of course this might change the expected GUVs' radius.

The droplets then detach from the capillary, cross the decane solution, enter the lipid-oil solution where they are covered by lipids, cross the oil mix/outside mix interface where an additional layer of lipid is zipped on the droplet creating the necessary bilayer and eventually accumulate in the outside glucose-buffer mix. When the capillary is empty (roughly 5-15 minutes) vesicles are extracted and observed in a chamber, with its bottom slide passivated with 10 mg/ml bovine serum albumine (10 minutes incubation and then washed with the same glucose-buffer mix as the one the vesicles are in). If necessary, the outside solution is modified by adding (osmotically balanced) additional ingredients, such as buffer, salts, proteins or methylcellulose to increase viscosity and reduce GUVs' diffusion.

Vesicle deflation

To deflate vesicles, the vesicles are added to the chamber but left exposed to air for 5-15 minutes to allow evaporation and hence increased osmolarity of the outside solution. A more controlled but slower way is to separate to chambers with a membrane: a bottom chamber (which will be observed) contains the GUVs, a top chamber contains a glucose solution with increased osmolarity (up to 400 mOsm/Kg more than the initial one) [Maan, Loiseau, and Bausch 2018].

Notes on the cDICE method

Several factors affect the quality of the GUVs resulting from a cDICE preparation, including humidity (lipids should be mixed in a dry environment), choice of buffers (some buffers change the lipid adsorption kinetics resulting in aggregates or poor yield) and choice of the mineral and silicon oil. In this work, for example, ABT was found to be more efficient than AB when encapsulating actin. Also the choice of the scavenging system (pyranose-oxidase rather than glucose-oxidase) changed the yield dramatically. Once a good balance between these components is found, cDICE can be a good, reliable method.

4.3 Microscopy

TIRF imaging

Total internal reflection fluorescence (TIRF) microscopy allows high-resolution visualization of 2-dimensional samples. SLB experiments are carried out preferentially with TIRF microscopy. We use a Leica DMI8 TIRF microscope with infinity scanner using a 100x NA 1.47 oil objective. Images are recorded at 2048 x 2048 pixels.

Confocal imaging

Confocal allows visualization of 3D samples by acquiring planes at different height with good z -resolution. We use confocal for GUVs experiments. We use a Leica DMI5 with a 63x NA 1.4 objective. We use the confocal with its resonant scanning settings to allow higher speed and visualize multiple vesicles in the same experiment or individual ones with good time resolution. The pinhole, unless specified, is set to 1.5 Airy units, the resolution to 512 x 512 or alternatively 256 x 256 pixels when time resolution is needed.

3D stacks of images are visualized and post-processed using Fiji/ImageJ. Equirectangular projections are used using the Map2-3D software [Sendra et al. 2015].

Epifluorescence imaging

Epifluorescence images of GUVs are acquired at a Leica Thunder (DMI8 with thunder module) microscope using a 63x objective (oil) NA 1.47.

4.4 Gliding assays

This section contains the actual experimental methods utilized in this work. We refer to the above illustrated procedures for finer details about the preparations of individual material.

Actin gliding assay on glass

To perform a gliding assay, first coverslip are covered with a (sticky) collodion film. Coverslips ($24 \times 24 \text{ mm}^2$) are fully dipped in a 0.2 % collodion solution in isoamylacetate (from Sigma) and left to dry under a hood overnight. To perform the assay, first a chamber is assembled using one layer of parafilm as spacer. Motors (HMM) are diluted to $\approx 0.025 \text{ mg/ml}$ in AB buffer and incubated in the chamber for 3 minutes. Motors will stick to the collodion surface. To avoid unspecific binding of actin, the chamber is then passivated by washing with 5 mg/ml BSA in AB. Finally, the desired concentration of $\approx 5 \mu\text{m}$ long, fluorescent, phalloidin-stabilized actin filaments (see 4.1. As a starting point, use 50 nM of actin) are incubated for 3 minutes to allow binding to the motors. At this stage, it can be checked whether filaments adhere on the surface and whether the density is high enough using epifluorescence microscopy. Then the chamber is washed with AB and finally 2 mM ATP with a scavenging system (GOC) and 1 mM DTT in AB is added to the chamber to start motion. The chamber is then imaged with tirf or epifluorescence microscopy at $\approx 250 \text{ ms} - 1 \text{ s}$ time interval. If necessary, MC is added to the chamber to increase the motors' processivity.

By tuning the amount of motors on the surface or the amount of actin filaments one can get different results. A too low amount of motors will cause filaments to detach upon ATP addition. A too high amount of motors or a too high amount of inactive heads lead to filament fragmentation and a high number of immobile filaments. A high density of filaments ($\approx 5 - 20 \text{ filaments}/\mu\text{m}^2$) give rise to the patterns described in Section 2.3.

Actin gliding on SLBs

Small actin filaments ($5 \mu\text{M}$) are prepolymerized with gelsolin in a ratio gelsolin:actin = 1:370, leading to $\approx 2 \mu\text{m}$ long filaments, and phalloidin. A SLB containing 99.5 % Egg PC and 0.5 % DSPE-PEG(2000)-biotin is prepared on a Piranha-etched coverslip, separated from the top by a stack of three parafilm layers. HMM motors are pre-cleaned to remove inactive heads, then incubated on ice for 10 minutes with streptavidin in a 1:1 ratio in AB. After washing unburst SUVs, the chamber is washed with AB and 200 nM streptavidin-functionalized HMM are inserted and incubated for 5 minutes. After that, the chamber is rinsed and incubated with the desired concentration of actin filaments for 5 minutes, after which the chamber is flushed with AB. Finally, a reaction mix containing 2 mM ATP and 0.2 % methylcellulose in A Buffer is inserted in the chamber. To avoid oxidation damage, a scavenging system (GOC) with glucose is also present. The chamber is sealed and observed with a TIRF microscope. In experiments with high actin density, actin is added directly in the final reaction mix and sedimented over time.

Actin gliding in GUVs

Actin and motors are prepared as above. A reaction mix is prepared containing the desired concentration of actin filaments (of the chosen length) and streptavidin-functionalized HMM, 4 mM ATP, 2 mM DTT, 30 mM sucrose, POC with glucose (0.66 %), 0.3% methylcellulose and an ATP regeneration system (CPK/CPH) in ABT. Actin is added at the very end. Before the beginning of the encapsulation procedure (cDICE) the osmotic pressure of the mix is measured by preparing 50 μL of solution including actin. After that, an outside glucose solution is prepared and the cDICE encapsulation is carried out. The lipid composition of the GUV membrane is 95% EggPC, 5% DSPE-PEG(2000)-biotin and 0.05% TexasRed-DHPE. Vesicles are then extracted, mixed with a glucose solution containing methylcellulose to a final concentration of 0.5% methylcellulose to avoid diffusion and flown in a BSA-passivated chamber. Vesicles are observed with confocal microscopy with 512×512 pixels resolution and a time interval of approx. 30-60 seconds.

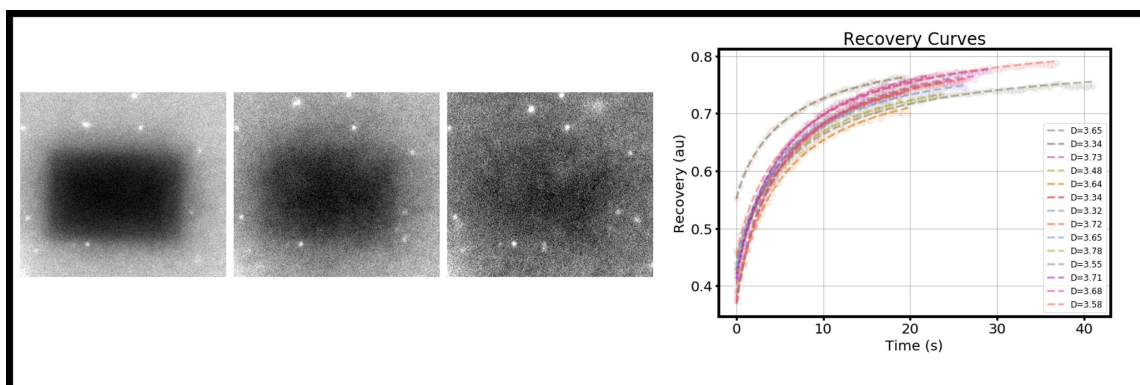


Figure 4.3: **FRAP experiments on EggPC SLBs** Example of a FRAP experiment, showing recovery of the fluorescent signal, and curves fitted as explained in 4.5 to extract the diffusion coefficient (in units of $\mu\text{m}^2/\text{s}$). 14 different curves are shown.

Microtubules gliding in an actin nematic

A SLB containing 99.5% Egg PC and 0.5% DSPE-PEG(2000)-biotin is prepared on a Piranha-etched coverslip, separated from the top by a stack of two parafilm layers. A stock solution of short actin filaments is prepared as above with gelsolin:actin ratio varying from 1:10 to 1:500. 100 nM biotin-Kinesin401 is incubated in a 1:1 ratio with streptavidin in M2B and incubated in the chamber for 3 minutes and then washed with M2B. Subsequently, the desired concentration of microtubules (from 1.6 to 8 ng/ml) is incubated for 1 to 3 minutes and then washed with M2B. Finally, a reaction mix containing the desired concentration of actin together with methylcellulose, 2 mM ATP, an ATP-regeneration system (CPH/CPK), a scavenging system (GOC) with glucose and MIX in M2B is inserted and the chamber is sealed. An actin nematic forms in the first 10-15 minutes. Unless specified otherwise, the actin concentration is set to $0.75 \mu\text{M}$ and the MC concentration to 0.25%, while the actin filaments' length is fixed to $\approx 0.5 \mu\text{m}$ (1:75 gelsolin:actin ratio). The system is observed with TIRF microscopy with 2048x2048 pixels resolution (15.5 pixels per micron) with a time interval of 5 seconds.

4.5 Data analysis for gliding filaments

The following section contains the procedures utilised to analyse data. Custom scripts are made in Python3, simple image analysis is also performed with Fiji/ImageJ (REFS).

Fluorescence recovery after photobleaching (FRAP) experiments

FRAP to estimate the diffusion coefficient of SLBs

To estimate the diffusion coefficient from FRAP experiments, we use the technique from [Goehring et al. 2010]. A rectangular ROI is bleached using high-intensity laser illumination and its recovery is imaged. To obtain the diffusion coefficient, the center of the bleached region is identified, the intensity of the image is fitted with the curve suggested in the reference to obtain the initial condition taking into account non-instantaneous bleaching. The mean intensity over time of the full image is then measured and fitted again using the recovery function suggested in [Goehring et al. 2010] to obtain the diffusion coefficients.

For a standard EggPC bilayer we obtain a diffusion coefficient of roughly $D \approx 3\mu\text{m}^2/\text{s}$. See Figure 4.3.

FRAP to estimate polarity of active actin structures

To estimate the asymmetry in the recovery of active actin structures, a rectangular region along the structure is bleached with a high-intensity laser and the recovery is imaged. The intensities I_L and I_R over time at

opposite edges of the region along the filaments' direction are measured and the asymmetry parameter $p = |I_L - I_R|/(I_L + I_R)$ is measured and averaged over the first 15 s of recovery. Perfectly symmetric recovery (nematic motion) would yield $p = 0$, whereas perfectly asymmetric recovery (polar motion) yields $p = 1$.

Estimate of surface concentration from TIRF images

We compute the surface concentration in gliding assays or in sedimentation issues, the filaments are sedimented on the surface with 0.2 % Methylcellulose or bound to motors and counted in regions of interest of variable size. The mean over the ROI size is then taken as the mean concentration.

Analysis of structures forming on a SLB

Collision statistics The density of filaments is computed by manually counting the number of filaments in at least five independent square regions of side $5 \mu\text{m}$, when the filaments' distribution is still uniform in space. To measure the incoming and outgoing angle of binary collisions, the orientation of each filaments is defined by their velocity. Orientations are measured from the raw data with Fiji's line selection. The difference between the two orientations, shifted in a $(0, 180)^\circ$ interval, is then plotted. Only collisions lasting more than 15 s are analyzed, and the orientation of the filaments is computed right before collision and either after the two filaments are clearly detached or, in the case of persistent alignment, after they have been in contact at least 10 s.

Histogram of densities To estimate the local density and compute its distribution, images are first preprocessed with a Gaussian filter to eliminate background intensity, and then, an automated thresholding algorithm is applied to set the background to zero. Images are normalized by the total integrated intensity, which is assumed to be proportional to the total density and thus should be kept constant. Finally, the intensity of the image is integrated inside regions of size $4.8 \mu\text{m} \times 4.8 \mu\text{m}$, each separated from the other by $2.4 \mu\text{m}$. The distribution of such values is then computed.

Curvature of streams and vortices Streams and vortices are manually selected with a segmented line with Fiji. To compute the local curvature, a spline fit with a two-pixel interval is performed to the selected line and the best fitting radius is computed by a Python script, considering at each point the five closest points for the fit. The same line selections are used to compute the length distribution of streams by integrating the geometric distance between points of the spline fits.

Estimate of the thickness of streams To estimate the number of filaments in a stream, firstly the background of the images is set to 0 and the transverse intensity profile of several individual filaments (20 to 30 for each frame) is measured. The same is done for streams in the frame. The integral intensity of each stream is divided by the mean integral of the filaments' profile yielding an estimate of the number of filaments composing the transverse size of streams. The measurement is repeated for different frames in the steady state of the system. The profiles are measured manually using Fiji's line tool and the analysis is carried out afterwards with a Python script.

Estimate of GUV radius

Epifluorescence microscopy images showing GUVs are opened with Fiji and circles (GUVs) are manually identified and measured with an ellipse fit. The radius is computed as the mean between the max and the min half-axis of the ellipse.

Estimate of speed of patterns

To estimate the speed of patterns, comet-looking shapes and high-fluorescence intensity points on Z-projections of confocal stack are identified manually and their (x, y) position on the GUV is marked. The GUV radius R and

center (x_c, y_c) are also identified. From the planar coordinate, the z position is estimated as

$$z = \sqrt{R^2 - (x - x_c)^2 - (y - y_c)^2}$$

The speed is then computed as the euclidean distance between consecutive points divided by the time interval. For each GUV several patterns are measured and for each concentration several GUVs are measured.

Tracking of microtubules and computation of flow

Tracking of MTs To track microtubules, TIRF microscopy images are thresholded and contours in the images are identified using a python routine (in the library OpenCV). Contours with aspect ratio smaller than 2 and area smaller than $0.2 \mu m^2$ are eliminated. For each contour with save the length of the main axis, its aspect ratio, its area, its orientation and the position of its center of mass. The positions of the center of mass of each contour is in a list $\mathbf{r}_i(t) = (x_i(t), y_i(t))$. For each couple of consecutive time frames, with time difference ΔT , we compute the distance matrix

$$D(t, t + \Delta T)_{ij} = \sqrt{(x_i(t + \Delta T) - x_j(t))^2 + (y_i(t + \Delta T) - y_j(t))^2} \quad (4.1)$$

and then we assign a position j at time $t + \Delta T$ to the same trajectory at a position i at time t

1. j and i have both not been assigned to a trajectory before
2. D_{ij} is smaller than $d_m \approx 3 \mu m$
3. j is the contour closest to i ($D_{ij} = \min(D_{il})$ amongst all values of l)
4. There is no other contour k at time t closest to j ($D_{ij} = \min(D_{kj})$ amongst all values of k)
5. The relative change in area, aspect ratio and length of the contour j with respect to i is smaller than 30%

At each frame, all contours are found, either assigned to a contour at the previous time-step or, otherwise, set as the possible start of a new trajectory.

The resulting trajectories are eventually cleaned (removing short trajectories, of less than 10 time-points, or trajectories that did not move of at least $10 \mu m$) and if possible merged together (two trajectories at time t_1 and $t_2 > t_1$ are merged if $t_2 - t_1 < 3$, the change in aspect ratio, length and area is not higher than 30% and the distance between the final point at t_1 and the initial point at t_2 is smaller than $5 \mu m$).

For each contour i then we can extract its position \mathbf{r}_i , its orientation $\hat{\mathbf{p}}_i = (\cos(\theta_i), \sin(\theta_i))$ with θ_i being the result of an elliptical fit on the contour perimeter allowing to find the orientation of the main axis. From the contour, one can also extract its length L_i and aspect ratio k_i . Contours with $k_i < 2$ are discarded. Additionally, we can also find, for each microtubule labeled as i , the local nematic director as $\hat{\mathbf{n}}_i = \langle \hat{\mathbf{n}}(\mathbf{r}) \rangle_{|\mathbf{r}_i - \mathbf{r}| < \Delta r}$ where $\Delta r \approx 400 nm$. Extraction of the nematic field is explained below in 4.5.

We can also compute the speed as $\mathbf{v}_i(t) = \frac{1}{\Delta T}(\mathbf{r}_i(t + \Delta T) - \mathbf{r}_i(t))$ and the angular speed $\omega_i(t) = \frac{1}{\Delta T}(\theta_i(t + \Delta T) - \theta_i(t))$ with $\Delta T = 5 s$ being the time interval of the acquisition. Using the speed we can fix the MT's orientation, since both $\hat{\mathbf{p}}_i$ and $-\hat{\mathbf{p}}_i$ are equivalent in the ellipse fit, using the condition that $\hat{\mathbf{p}}_i \cdot \mathbf{v}_i > 0$. The angular speed is used as a proxy for the torque $\tau_i(t)$ actin on the microtubules as $\tau_i(t) = \mu(L)\omega(t)$ with $\mu(L)$ being a mobility coefficient depending on the length which we neglect.

From the trajectories and these other data, we can extract several other parameters explained in main text (see Section 2.6).

Flow of MTs At higher densities, as tracking become unfeasible, we use an optical flow algorithm to extract the microtubules' motion. Two consecutive frames are analyzed using Python's optical flow algorithm (in the library OpenCV) and the flow field $\mathbf{v} = (v_x(x, y), v_y(x, y))$ is extracted for each pixel. From the flow at each frame we can compute the mean flow over time in each position and the local polarity of the flow. Flow in points below threshold, where no MTs are present, are set to 0.

The mean flow is computed as an average over the total time T i.e. $\mathbf{v}_m = \langle \mathbf{v} \rangle_T$ whereas the average local polarity is an average over the flow orientation i.e. $\hat{\mathbf{p}} = \langle \mathbf{v}/|\mathbf{v}| \rangle_T$ and then normalized as $\hat{\mathbf{p}} = \mathbf{p}/|\mathbf{p}|$. Null vectors are not considered.

Extraction of local nematic alignment from microscopy images

To extract the local nematic alignment from TIRF images of filaments, the technique from [Boudaoud et al. 2014] is utilized. The image is divided in squared reagonis of interest (ROIs) with side L pixels and distance between the center of each ROI δ pixels. For all the pixels inside a ROI we find the intensity $I(x, y)$ and compute the gradient $\mathbf{g}(x, y) = \nabla I(x, y) = (g_x, g_y)$. The main assumption is that the local alignment is perpendicular to the intensity gradient \mathbf{g} so that the vector field

$$\mathbf{t}(x, y) = (t_x(x, y), t_y(x, y)) := \left(\frac{g_y(x, y)}{|g(x, y)|}, -\frac{g_x(x, y)}{|g(x, y)|} \right)$$

which is perpendicular to $\mathbf{g}(x, y)$ as $\mathbf{g} \cdot \mathbf{t} = 0$, is also locally oriented as the filaments.

Then to extract the nematic director, one needs to compute a slightly modified version of the \mathbf{Q} -tensor (see Section 1.3.1) using the vector \mathbf{t} instead of the actual field \mathbf{n} .

This tensor, which we name \mathbf{T} , has components

$$\mathbf{T}_{xx} = \langle t_x t_x \rangle$$

,

$$\mathbf{T}_{xy} = \mathbf{T}_{yx} = \langle t_x t_y \rangle$$

and

$$\mathbf{T}_{yy} = \langle t_y t_y \rangle$$

averaged over the ROI. The (normalized) eigenvector of this tensor corresponding to the bigger eigenvalue is the best estimate of the nematic director $\mathbf{n}_0(x_0, y_0)$ where (x_0, y_0) is the center of the ROI.

Operationally, then, having chosen the parameters δ and L

1. The image of the actin nematic is processed with Fiji's pseudo flat-field correction filter
2. The image of the actin nematic is loaded and smoothed with a gaussian filter with standard deviation of a few pixels to remove noise
3. Some points (x_i, y_i) are selected on a grid with spacing δ so that $x_i = n\delta$ and $y_i = m\delta$ with n, m integers so that $x_0, y_0 > L/2$ and $\max(x_i), \max(y_i) < S - L/2$ where S is the image size
4. For each point, all the points (x, y) such that $|x - x_i| < L/2$ and $|y - y_i| < L/2$ are selected. This creates a squared ROI.
5. For each point (x, y) inside the ROI, the discrete gradient of the intensity $I(x, y)$ is computed, resulting in a list of values for the x -component $g_x(x, y)$ and the y -component $g_y(x, y)$
6. The tensor \mathbf{T} is computed as above, averaging $g_x g_x$, $g_y g_y$ and $g_x g_y$ inside the roi
7. The eigenvector \mathbf{v} corresponding to the biggest eigenvalue of \mathbf{T} is normalised and returned $\hat{\mathbf{A}}$
8. The item (x_i, y_i, v_x, v_y) , where v_x and v_y are the components of the eigenvector \mathbf{v} is added to a list
9. Iterating over all positions, a vector field $\mathbf{v}_i(x_i, y_i)$ is returned and constitutes the extracted (discrete) nematic field \mathbf{n}

The results of the procedure is a list of vectors oriented as the nematic director $\mathbf{n}_i = \mathbf{n}(x_i, y_i)$ where (x_i, y_i) are points on the images separated by δ pixels. If $\delta = 1$ there is a vector for each pixel of the image. L is chosen so that it contains enough points to average appropriately but not so many that positions of the image with different alignment interfere.

Computing the order parameter S

Having extracted the field \mathbf{n} we can compute its (mean) order parameter in the following way. For each frame we extract the nematic field $\mathbf{n}_b = (n_x, n_y)$ inside boxes b of side $2 \mu m$ and compute the Q -tensor (defined, in 2D by equation 1.15) as

$$Q_{xx} = 2\langle n_x^2 \rangle - 1 \quad Q_{xy} = Q_{yx} = 2\langle n_x n_y \rangle \quad Q_{yy} = 2\langle n_y^2 \rangle - 1$$

This matrix is diagonalized. The order parameter S_b is the biggest eigenvalue whereas the local nematic director \mathbf{n}_{0b} inside the box is the corresponding eigenvector.

The order parameter of the field is given as the average of S_b taken over all boxes.

Identification of defects and heuristic trajectories

From the nematic field obtained using the method above, we can identify nematic defects using the following method.

Given the nematic tensor \mathbf{Q} defined, in 2D by equation 1.15, we can compute the divergence of it

$$\nabla \cdot \mathbf{Q} = (\partial_x Q_{xx} + \partial_y Q_{xy}, \partial_x Q_{xy} + \partial_y Q_{yy}) \quad (4.2)$$

and because \mathbf{Q} has unitary trace, $Q_{yy} = 1 - Q_{xx}$ so we can switch sign to the final term

$$\nabla \cdot \mathbf{Q} = (\partial_x Q_{xx} + \partial_y Q_{xy}, \partial_x Q_{xy} - \partial_y Q_{xx}) \quad (4.3)$$

and in terms of the vector $\mathbf{n} = (n_x, n_y)$, again using the definition 1.15,

$$\nabla \cdot \mathbf{Q} = (\partial_x(n_x^2 - n_y^2) + \partial_y 2n_x n_y, \partial_x 2n_x n_y - \partial_y(n_x^2 - n_y^2)) \quad (4.4)$$

We compute $\nabla \cdot \mathbf{Q}$ using the (discrete) gradient after having extracted the (discrete) field $\mathbf{n}(\mathbf{r})$ from microscopy images using the definition above. The divergence of \mathbf{Q} is the polarity field \mathbf{p} .

Defect cores are then identified as areas with high values (bigger than 0.1) of the quantity, related to the divergence of \mathbf{Q} ,

$$q = \frac{1}{4\pi} (\partial_x Q_{xi} \partial_y Q_{yi} - \partial_x Q_{yi} \partial_y Q_{xi})$$

which represents a charge density [Maryshev et al. 2020]. Positive defects have high values, negative low (negative) values.

The axis of a $+1/2$ defect is identified as $\hat{\mathbf{p}}^{+1/2} = -\langle \nabla \cdot \mathbf{Q} \rangle / |\nabla \cdot \mathbf{Q}|$ averaged over a region around the defect's core of $0.5 \mu m$. Seeds for heuristic trajectories are planted at a distance of $d = 2.5 \mu m$ (roughly one MT length) from the identified defect's core and the mean polar field \mathbf{p} is computed again in a region of radius $0.5 \mu m$. Having chosen the polarity, lanes are evolved by simply following the streamlines of the field \mathbf{n} with steps of $0.5 \mu m$.

Generation of simulated nematic fields

The Landau-DeGennes energy for nematic material 1.27 can be rewritten in terms of the \mathbf{Q} -tensor and using the one constant ($K_1 = K_2 = K_3 = K$) approximation. From then, the nematic field can be computed up to equilibration following

$$\partial_t Q_{ij} = -\frac{1}{\gamma} \frac{\delta F}{\delta Q_{ij}} = [\alpha - \beta Q_{kl} Q_{kl}] Q_{ij} + \kappa \Delta Q_{ij}$$

, where γ is a friction term (rotational viscosity), κ is Frank's constant K (normalized by γ), α and β are standard Ginzburg-Landau coefficients. Starting from an initial random state, we stop the time evolution of the field before the system reaches an equilibrium homogeneous state and use the output as the pre-imposed director field for our approaches.

Pearson correlation coefficient for simulated images

To compare trajectories extracted from simulations and experimental data, both images containing experimental time projections and simulated images containing, for each pixel, the number of particles that crossed that pixel (i.e., the mean trajectories) are binned on the same 256×256 grid to generate comparable images and to avoid errors due to the different resolution. For each couple of images (the experimental one and the simulated one in a given condition) we compute the Pearson correlation coefficient defined as

$$P = \frac{\sum_{i=1}^{256} \sum_{j=1}^{256} (I_1(x_i, y_j) - \langle I_1 \rangle)(I_2(x_i, y_j) - \langle I_2 \rangle)}{\sigma_{I_1} \sigma_{I_2}}$$

where the sum is carried out on each couple of points (x, y) on the grid, I_1 and I_2 are the intensities of each image at each pixel and σ_{I_1} and σ_{I_2} the standard deviations of the intensity of each image.

4.6 Active microtubule fluids

Bulk

Acrylamide coating

To avoid adsorption of proteins on the coverslip's and/or glass slide's surface, they are passivated using an acrylamide brush using a protocol from Zvonimir Dogic's lab. Briefly, the coverslips and slides are pre-cleaned (sonicating them successively in 2 % Hellamanex, water 0.1 M NaOH and water again, storing them in water at the end) and then incubated in 98.5 % ethanol, 1 % acetic acid and 0.5 % 3-(trimethoxysilyl)propylmethacrylate (silane) for 10-15 minutes to activate the surface. The activating mix is made right before use. After incubation, coverslips are rinsed extensively with *ddH₂O*. Finally they are left (at least 12 hrs) in a 2 % acrylamide solution in water, with the addition of 0.7 mg/ml APS (Ammonium persulfate) and 0.035 % TEMED (105 μ L on 300 mL). The 2 % acrylamide solution is degassed 45 minutes before use. We remind that acrylamide is toxic especially in power form. The acrylamide polymerizes on the slides. Before use, slides are washed in *ddH₂O* and air-dried. The slides are used within a week.

Reaction mix

The desired concentration of stabilized microtubules (usually, 0.4 mg/ml) is mixed together with the desired concentration of KSA, ANLN and ATP together with a scavenging system (GOC) and glucose, an ATP regeneration system (CPK/CPH), 5 mM DTT in M2B with MIX. It is made sure that the final concentration of salts is exactly the one expected for M2B by correcting for dead volume using a 10x M2B preparation. MTs are kept at room temperature and the mix is left to equilibrate for 5-10 minutes before adding them, to avoid depolymerization. The mix is incubated in a small channel carved in parafilm and molten on an acrylamide slide coating. The slide is inserted in an Ibidi chamber with a controlled temperature of 24°C. The system is observed with a Leica Thunder (DMI8 with thunder module) microscope using either a 20 x objective (air) or a 63x objective (oil) NA 1.47.

Encapsulation inside GUVs

The active fluid (with the desired MT, KSA and ANLN concentration) is prepared as above and its osmotic pressure measured. The mix is left to evolve for 5 minutes. In the meantime, a glucose solution with comparable osmotic pressure is also prepared and the cDICE encapsulation is carried out at room temperature as explained above. The capillary diameter is 40 – 50 μ m to allow for bigger vesicles and fast encapsulation. The sample is tightly sealed with vacuum grease to avoid flow. Active vesicles are then observed with confocal microscopy, using a 63x NA 1.4 oil objective and resonant scanner settings. Equatorial planes are measured at 256x256 pixels resolution with time intervals between 35 ms and 250 ms. The pinhole is kept at 1.2 Airy units. Full stacks are measured at either 256x256 or 512x512 pixels resolution with varying time intervals. Both the membrane channel (TexasRed) and the microtubules (Alexa647) are imaged at the same time.

4.7 Data analysis for active microtubule fluids

Optical flow for the speed of AMFs

To compute the optical flow (i.e. the mass flow) from microscopy images, movies are acquired with a Thunder microscope at a framerate fast enough to resolve the flow (500 *ms* to 2 *s*). The images are then smoothed with a gaussian filter and a gaussian background is removed and they are analysed using OpenCV's optical flow implementation in Python3.7.

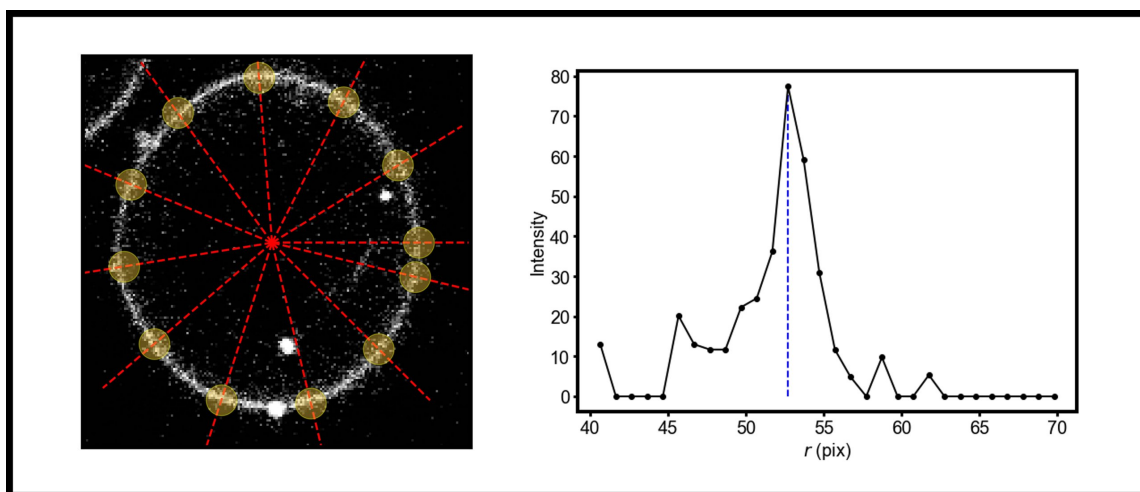


Figure 4.4: **Computation of GUVs' contour:** Schematic of the detection approach. Starting from the center of the GUV, we look for peaks of high intensity along the radial direction. This is repeated for different polar angles ϕ (red lines). The intensity values along the direction are histogrammed (right) and the radial position at which the intensity is maximum (blue line) is isolated (yellow dots). The radial position corresponding to the peak of the histogram is obtained with a parabolic fit close to the maximum intensity value.

GUV-contour detection from confocal images and Fourier decomposition

Contour detection

To detect the contour of GUVs, confocal images of the equatorial plane are smoothed with a gaussian filter and thresholded so that only the lipid bilayer is above threshold. Then contours are detected to find both the inner and the outer contour of the GUV. By that we also find the center of the GUV. Starting from the center, the image is converted in polar coordinates (with radial distance r and polar angle $0 < \theta \leq 2\pi$) and split in angular segments centered at an angle θ_0 rad, separated by a quantity $d\theta = 0.005$ and with width $d\alpha$.

All the pixels with polar angle $\theta_0 - d\alpha/2 < \theta < \theta_0 + d\alpha/2$ are selected and binned radially, obtaining a list of points (r_i, θ_i) where r_i is the distance from the center and θ_i the polar angle. The radial binning is $dr = 0.5 \mu m$. For each bin in the list, the average intensity of the bin $I(r_i, \theta_i)$ is found. The bin (r_M, θ_M) such that the intensity is maximum is selected. This results in a list of points containing, for each angular sector, the distance for which the intensity is maximum which we assume as the position of the membrane at that angle. We then obtained a discretized contour $r(\theta)$ as a list of points (r_M^i, θ_M^i) . Clearly this corresponds to contours positions using the transformation $(x, y) = r(\theta)(\cos(\theta), \sin(\theta))$. The procedure is schematized in Figure 4.4.

Analysis of curvature

To analyze the curvatures, first the contours are smoothed by averaging together 5 consecutive positions and then $N = 20$ points of the contour (corresponding to a circular sector of length $NR_0d\alpha \approx 2.5 \mu m$) are fitted with a circles by minimizing the quantity $r = \sum_i^{20} (x_i - x_0)^2 + (y_i - y_0)^2 - R^2$ (with (x_i, y_i) points of the contour) to obtain the best fit for the curvature center (x_0, y_0) and radius R . The curvature is then computed as $1/R$.

Decomposition in Fourier series

The contour is then decomposed in Fourier modes integrating the definition of the coefficients of the Fourier series as

$$a_n = \frac{1}{\pi} \int_0^{2\pi} r(\theta) \cos(n\theta) d\theta \quad (4.5)$$

$$b_n = \frac{1}{\pi} \int_0^{2\pi} r(\theta) \sin(n\theta) d\theta \quad (4.6)$$

Clearly, $b_0 = 0$ and $a_0 = \frac{1}{2\pi} \int_0^{2\pi} r(\theta) d\theta = 2\langle r(\theta) \rangle_\theta$ is two times the mean radius R_0 averaged over the contour. The term a_0 is then discarded or used to compute R_0 and all the other coefficients are normalized by R_0 . With this definition the Fourier series given in Equation 3.11 can be summed back to obtain $r(\theta)$.

As we have discrete points, we use the trapezoidal rule to compute these integrals. We perform the integrals for modes $n = 0$ to $n = 50$ although there is a loss in resolution above $n \approx 20$.

Analysis of the active forcing

First, starting from microscopy images, the MT channel is threshold-ed to separate the microtubules from the background. Then all the pixels above threshold are selected. Their intensity $I(x, y)$ is proportional to the MT density and their position is used to compute the radial distribution of MTs.

From the membrane channel, the position of the membrane $R(\phi, t)$ at a given time t is extracted as explained above. The microtubules intensity is also converted into polar coordinates as $I(r, \phi, t)$. Then the microtubule forcing is obtained by averaging the microtubules intensity such that, at a given angle ϕ , $f(\phi, t) = \langle I(r, \phi, t) \rangle$ where the average is computed for $R(\phi, t) - 2 \mu m < r < R(\phi, t)$.

Analysis of simulated GUVs and bundles

The simulated membrane is centered in the origin. From the positions $\mathbf{r} = (x, y, z)$ of simulated beads composing a bundle we compute their radial position as $|r| = \sqrt{x^2 + y^2 + z^2}$. This allows to compute their radial distribution. Bundles curvature is obtained as $k = |\mathbf{n} \times \mathbf{t}|/|\mathbf{t}|^3$ where $\mathbf{t} = \nabla \mathbf{r}$ (where the gradient is computed along the bundle, i.e. by ordering the beads according to their position in the filament) and $\mathbf{n} = \nabla \mathbf{t}$. Membrane's curvature, the microtubule forcing and the MT and membrane's fluctuation spectra are computed as above with the difference that the equatorial plane is composed of all beads (MTs) and mesh points (membrane) such that their z position was such that $|z| < 1.5\sigma$.

4.8 Cytosim simulations

In Cytosim [Nedelec and Foethke 2007], one can model easily filaments, motors and crosslinkers and let them evolve with a Langevin dynamics. We refer to the original paper and the most up-to-date documentations for details. The parameters used are summarized in the table below. Cytosim config.cym files (used to run the simulations) are generate with a custom Python 3.7 code that loops through all conditions. Results are then extracted using the ./report.exe utility from Cytosim and analysed with Python.

Filaments are modelled as rigid rods of length $1.5 \mu m$. They have a rigidity of $50 pN/\mu m$ but they are modelled as filaments with a single segment which is tantamount to infinite rigidity. Filaments also have a steric radius of $12.5 nm$. If they are too close, filaments interact with a repulsive linear force with elastic constant of $50 pN/\mu m$. Motors are modelled as springs that move at a speed $v_0 = 0.6 \mu m/s$ on filaments. They have a stall force above which they stop moving and unbind. Crosslinkers (ANLN) is modelled as a spring that can only bind but does detach if the strain is too strong.

The filaments and elements are put in a box of size $L = 20 \mu m$. There are periodic boundary conditions on all sides. Motors, crosslinkers and filaments (if not bound) all diffuse explicitly.

Simulations are then run for $60 - 80 s$ with a time-step of $dt = 0.005 s$ and every 10 frames the configuration of the system is saved. After an initial $1 s$ in which the elements are allowed to bind (setting temporarily $v_0 = 0$) the motors are activated and the simulation is run until the end. The first $30 - 40 s$ are discarded as transient for the following analysis unless stated otherwise

Parameters used in simulations

The table summarizes all the parameters used in the Cytosims simulations.

Parameter	Value	Comments
General		
Box side	10 μm	3D, with periodic boundary conditions
Viscosity	1	Water
$k_B T$		Room temperature
Time step	5 ms	
Steric strength	50 pN/ μm	
Microtubules		
Length	1.5 μm	
Diameter (steric)	25 nm	
Rigidity	Infinite	
Couples (Motors and crosslinkers)		
Rest length	8 nm	
Activity	Bridge	
Stiffness	150 pN/ μm	
Diffusion coefficient	50 $\mu m^2/s$	
Crosslinkers (ANLN)		
Binding rate	0.75 s^{-1}	Unless specified differently
Binding range	200 nm	
Unbinding rate	1 s^{-1}	
Unbinding force	1.5 pN	
Motors (KSA)		
Binding rate	5 s^{-1}	
Binding range	100 nm	
Unbinding rate	0.75 s^{-1}	Set to 0.015 at the beginning
Unloaded speed	0.6 $\mu m/s$	Set to 0 at the beginning
Stall force	6 pN	
Unbinding force	6 pN	
Run length	0.8 μm	Speed / unbinding_rate

Example of a cytosim config.cym file to run simulations

The following example can be used to reproduce results, changing the appropriate parameters (mainly r_x , r_m and N).

```
set simul system
  {
    dim = 3;
    time_step = 0.005; % seconds
    viscosity = 1; %pN.s/um^2
    steric = 1, 50;}
set space cell
  {geometry = periodic 10.0 10.0 10.0;} %periodic box with half-size 10 micron
set fiber microtubule
  {
    rigidity = 50
    segmentation = 1.5
    confine = inside, 400, cell
    steric = 1, 0.025000;}
set hand kinesin %motors are activated later on. Here the speed is set to 0...
  {binding_rate = 5 %$s^{-1}$
    binding_range = 0.1
    unbinding_rate = 0.015
    unbinding_force = 6.0 %pN
    activity = move
    unloaded_speed = 0.0 %um/s - set later
    stall_force = 6.0;}
set couple motor
  {activity = bridge
    hand1 = kinesin
    hand2 = kinesin
    length = 0.08
    stiffness = 150.0
    diffusion = 50
    fast_diffusion = 0;} % If 1, diffusion is not modelled explicitly.
set hand xlink_head
  {binding_rate = 1.0
    binding_range = 0.2
    unbinding_rate = 1
    unbinding_force = 1.5;}
set couple ANLN
  {hand1 = xlink_head
    hand2 = xlink_head
    activity = bridge
    stiffness = 100
    length = 0.08
    diffusion = 50
    fast_diffusion = 0;}
new space cell
%initialize MTs
new 8000 microtubule
{length = 1.5;}
%initialize motors and crosslinkers
new 800000 ANLN % r_x=100
new 288000 motor % r_m=36
%start running for 200 frames to equilibrate the system with motors turned off
```

```
run 200 simul system{nb_frames=10}
export all xlink_state_wKSA.cmo
%turn on motors
change kinesin
      {unloaded_speed=0.60
      unbinding_rate=0.75}
% Save configuration every 200 frames -> 1s
run 12000 simul system{nb_frames=200}
```

Cytosim data analysis

Using the ./report.exe executable from Cytosim we extract for each simulation the filaments' position $\mathbf{r}_i(t)$ and their orientation $\hat{\mathbf{p}}_i(t)$. Additionally, we can extract which binding elements are connected to it and where along the fiber. Finally, also the clusters of fibers (what fiber is connected to which other one) can be extracted automatically. Several custom Python3.7 scripts are used to analyze this data. For all trajectories, the first 10 s are eliminated.

Mean squared displacement The mean squared displacement is found by its definition as

$$\text{MSD}(\tau) = \langle (\mathbf{r}_i(t + \tau) - \mathbf{r}_i(t))^2 \rangle$$

Then $\ln(\text{MSD}(\tau))$ is fitted against $\ln(\tau)$ with a line to obtain its power law scaling as $\sim \tau^\beta$ at different times ($\tau < 10$ s and $\tau > 30$ s) to obtain the parameter β .

Activity measures The speed of fibers is computed as

$$\mathbf{v}_i(t) = \frac{\mathbf{r}_i(t + dt) - \mathbf{r}_i(t)}{dt}$$

where dt is the simulation time interval at which data are extracted (0.1 s). We note that with this definition purely diffusive fibers have an expected speed of $\sqrt{\frac{2D}{dt}} \approx 10 \mu\text{m/s} \gg v_0$ where D is the fibers' diffusion coefficient. This problem, relevant where diffusion is dominant i.e. at low r_x , is a problem for the mean flow but is expected to average out for the parameter α .

The activity parameter α is computed as

$$\alpha = \frac{\langle \mathbf{v}_i \cdot \hat{\mathbf{p}}_i \rangle}{v_0}$$

where v_0 is the motors' unloaded speed.

The flow and the mass flow are computed by creating a $2 \mu\text{m} \times 2 \mu\text{m} \times 2 \mu\text{m}$ grid and averaging at each grid point different quantities. To obtain the flow $|v|_i$ the speed $\mathbf{v}_i(\mathbf{r}, t)$ is averaged inside each grid point and then its absolute value is taken, possibly normalizing by v_0 . For the mass flow, the number of particles inside each box is computed, is normalized by the expected value in a uniform distribution and their variation over time is recorded to compute its mean and variance.

Clusters Clusters can be automatically extracted by Cytosim. We simply plot them at each frame and normalize by the total number of microtubules if necessary.

Polar pairs We select couples of fibers bound with each other using ./report.exe. Then, we simply compute, for each couple (i, j) the quantity

$$\hat{\mathbf{p}}_i \cdot \hat{\mathbf{p}}_j = \cos(\theta_{ij})$$

with θ_{ij} the relative angle. To compute $N_{\uparrow\downarrow}$ and $N_{\uparrow\uparrow}$ fibers with $\theta_{ij} < \pi/6$ are counted as polar couples, whereas if $\theta_{ij} > \pi - \pi/6$ they count as antipolar. For each couple, we can also compute the number of motors or crosslinkers bound to them to compute $\sigma_{\uparrow\uparrow}$, $\sigma_{\uparrow\downarrow}$, $\gamma_{\uparrow\uparrow}$ and $\gamma_{\uparrow\downarrow}$. Of course, due to the presence of unbound motors (crosslinkers) or motors (crosslinkers) bound to only one fiber, $\sigma_{\uparrow\uparrow} + \sigma_{\uparrow\downarrow} < 1$ ($\gamma_{\uparrow\uparrow} + \gamma_{\uparrow\downarrow} < 1$)

Motors and crosslinking positioning The positioning along fibers of bound crosslinkers and motors is recorded for all motors and then histogrammed between 0 and L , L being the fibers' length. The results are then compared with an antenna model as discussed in Section 3.3.3.3.

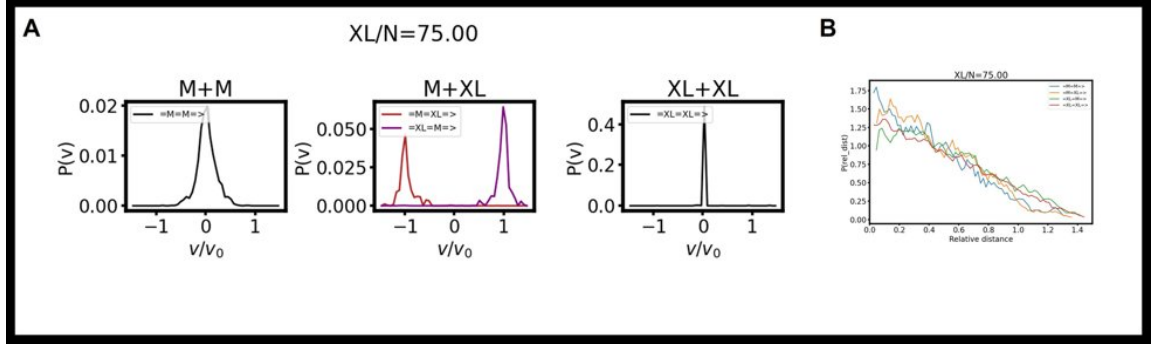


Figure 4.5: **Computation of configurations from Cytosim simulations** A) Histogram of relative speed for each configuration. Motors are marked as M and crosslinkers as XL , arrows in the legend indicate the filament's plus end. As expected, configurations have a peak in relative speed at $0 \mu m/s$ and $\pm v_0$. B) Histogram of relative distances between different configurations. All data at $N = 2750$, $r_x = 75$, $r_m = 36$, $V = 2750 \mu m^3$.

Order parameters Again, the simulation box is divided in a grid and inside each grid point the order parameters are computed using the standard definition of

$$S = 2\langle(\hat{p}_i \cdot \hat{p}_j)^2\rangle - 1$$

and

$$S_p = \langle\hat{p}_i \cdot \hat{p}_j\rangle$$

for all couples (i, j) inside the grid point.

Computation of χ To compute χ we need to count configurations inside the system. We do the following: first, we define as a configuration, according to [Belmonte, Leptin, and Nédélec 2017], triplets of distinct fibers (f_1, f_2, f_3) such that f_1 is bound to f_3 and f_2 is also bound to f_3 . We then look for all couples (b_1, b_2) of motors and crosslinkers bound to f_3 such that b_1 is bound to f_1 (and f_3) and b_2 is bound to f_2 (and f_3). We then divide such configurations in four groups depending on whether b_1 and b_2 are two motors (mm), two crosslinkers (xx) or mixed (xm and mx). The latter couple of configurations depends on which of the two elements is closer to the plus end of f_3 . For all configuration, we also record the relative distance a between b_1 and b_2 and, by looking for the exact same configuration $(f_1, f_2, f_3, b_1, b_2)$ at the next time step $(t + dt)$ we can compute the change in relative distance $\dot{a} = a(t + dt) - a(t)$. We verify that in mx and xm configurations the relative speed distribution is peaked at $\dot{a} = \pm v_0$ whereas xx and mm are very peaked at $\dot{a} = 0 \mu m/s$ (Fig. 4.5.A, B). Configurations which did not survive to the next frame are discarded.

We can finally compute the probabilities $p_{xx}(a)$, $p_{mm}(a)$, $p_{mx}(a)$, $p_{xm}(a)$ of having a given configuration at a given distance by an histogram of all relative distances in a given configuration and by counting the fraction of states in a given configurations on all found configurations.

From then on, χ is computed as defined as

$$\chi = \frac{v_0 \int da' (p_{xm}(a') - p_{mx}(a'))}{\langle a \rangle}$$

where the integral is carried out as a discrete sum.

List of publications

Alfredo Sciortino and Andreas R. Bausch (2021). “Pattern formation and polarity sorting of driven actin filaments on lipid membranes.” In: *Proceedings of the National Academy of Sciences* 118.6, e2017047118. DOI: [10.1073/pnas.2017047118](https://doi.org/10.1073/pnas.2017047118)

P. Bleicher, T. Nast-Kolb, A. Sciortino, Y. A. de la Trobe, T. Pokrant, J. Faix, and A. R. Bausch (2021). “Intra-bundle contractions enable extensile properties of active actin networks.” In: *Scientific Reports* 11.1, p. 2677. DOI: [10.1038/s41598-021-81601-0](https://doi.org/10.1038/s41598-021-81601-0)

P. Bleicher, A. Sciortino, and A. R. Bausch (2020). “The dynamics of actin network turnover is self-organized by a growth-depletion feedback.” In: *Scientific Reports* 10.1, p. 6215. DOI: [10.1038/s41598-020-62942-8](https://doi.org/10.1038/s41598-020-62942-8)

Giacomo Frangipane, Gaszton Vizsnyiczai, Claudio Maggi, Romolo Savo, Alfredo Sciortino, Sylvain Gigan, and Roberto Di Leonardo (2019). “Invariance properties of bacterial random walks in complex structures.” In: *Nature Communications* 10.1, p. 2442. DOI: [10.1038/s41467-019-10455-y](https://doi.org/10.1038/s41467-019-10455-y)

In preparation

Alfredo Sciortino, Lukas Neumann, Timo Krueger, Ivan Maryshev, Erwin Frey, Andreas R. Bausch, *Microtubules gliding in a nematic form polar lanes*

Alfredo Sciortino and Chiao-Peng Hsu, Alice Yu De La Trobe, Andreas R. Bausch, *Polar pattern formation of actin gliding in GUVs*

Alfredo Sciortino and Hammad Faizi, Matthew Peterson, Sarvesh Uplap, Remi Boros, John Berezney, Aparna Baskaran, Michael Hagan, Zvonimir Dogic, Andreas R. Bausch, *An active microtubule fluids deforms GUVs*

Alfredo Sciortino, Ivan Maryshev, Remi Boros, John Berezney, Zvonimir Dogic, Erwin Frey, Andreas R. Bausch *Cytosim simulations of an active fluid reveal the role of crosslinking in stabilizing anti-polar couples*

References

- Abkarian, Manouk, Etienne Loiseau, and Gladys Massiera (2011). “Continuous droplet interface crossing encapsulation (cDICE) for high throughput monodisperse vesicle design.” In: *Soft Matter* 7.10, p. 4610. DOI: 10.1039/c1sm05239j.
- Abkenar, Masoud, Kristian Marx, Thorsten Auth, and Gerhard Gompper (2013). “Collective behavior of penetrable self-propelled rods in two dimensions.” In: *Physical Review E - Statistical, Nonlinear, and Soft Matter Physics* 88.6, p. 062314. DOI: 10.1103/PhysRevE.88.062314.
- Abu Shah, Enas and Kinneret Keren (2014). “Symmetry breaking in reconstituted actin cortices.” In: *eLife* 2014.3, p. 1433. DOI: 10.7554/eLife.01433.001.
- Afroze, Farhana, Daisuke Inoue, Tamanna Ishrat Farhana, Tetsuya Hiraiwa, Ryo Akiyama, Arif Md Rashedul Kabir, Kazuki Sada, and Akira Kakugo (2021). “Monopolar flocking of microtubules in collective motion.” In: *Biochemical and Biophysical Research Communications* 563, pp. 73–78. DOI: 10.1016/j.bbrc.2021.05.037.
- Ahmadi, A., T. B. Liverpool, and M. C. Marchetti (2005). “Nematic and polar order in active filament solutions.” In: *Physical Review E* 72.6, p. 060901. DOI: 10.1103/PhysRevE.72.060901.
- Alert, Ricard, Jaume Casademunt, and Jean-François Joanny (2021). “Active Turbulence.” In: Alert, Ricard, Jean-François Joanny, and Jaume Casademunt (2020). “Universal scaling of active nematic turbulence.” In: *Nature Physics* 16.6, pp. 682–688. DOI: 10.1038/s41567-020-0854-4.
- Allard, A., F. Valentino, C. Sykes, T. Betz, and C. Campillo (2020). “Fluctuations of a membrane nanotube covered with an actin sleeve.” In: *Physical Review E* 102.5, p. 052402. DOI: 10.1103/PhysRevE.102.052402.
- Almendro-Vedia, Víctor G., Paolo Natale, Michael Mell, Stephanie Bonneau, Francisco Monroy, Frederic Joubert, and Iván López-Montero (2017). “Nonequilibrium fluctuations of lipid membranes by the rotating motor protein F₁F₀-ATP synthase.” In: *Proceedings of the National Academy of Sciences of the United States of America* 114.43, pp. 11291–11296. DOI: 10.1073/pnas.1701207114.
- Asakura, Sho and Fumio Oosawa (1954). *On interaction between two bodies immersed in a solution of macromolecules*. DOI: 10.1063/1.1740347.
- Bär, Markus, Robert Großmann, Sebastian Heidenreich, and Fernando Peruani (2020). “Self-Propelled Rods: Insights and Perspectives for Active Matter.” In: *Annual Review of Condensed Matter Physics* 11.1, pp. 441–466. DOI: 10.1146/annurev-conmatphys-031119-050611.

- Bashirzadeh, Yashar and Allen P. Liu (2019). “Encapsulation of the cytoskeleton: towards mimicking the mechanics of a cell.” In: *Soft Matter* 15.42, pp. 8425–8436. DOI: 10.1039/C9SM01669D.
- Baskaran, Aparna and M. Cristina Marchetti (2008). “Hydrodynamics of self-propelled hard rods.” In: *Physical Review E* 77.1, p. 011920. DOI: 10.1103/PhysRevE.77.011920.
- Becco, Ch, N. Vandewalle, J. Delcourt, and P. Poncin (2006). “Experimental evidences of a structural and dynamical transition in fish school.” In: *Physica A: Statistical Mechanics and its Applications* 367, pp. 487–493. DOI: 10.1016/j.physa.2005.11.041.
- Belmonte, Julio M, Maria Leptin, and François Nédélec (2017). “A theory that predicts behaviors of disordered cytoskeletal networks.” In: *Molecular Systems Biology* 13.9, p. 941. DOI: 10.15252/msb.20177796.
- Bendix, Poul M., Gijsje H. Koenderink, Damien Cuvelier, Zvonimir Dogic, Bernard N. Koeleman, William M. Briehar, Christine M. Field, L. Mahadevan, and David A. Weitz (2008). “A quantitative analysis of contractility in active cytoskeletal protein networks.” In: *Biophysical Journal* 94.8, pp. 3126–3136. DOI: 10.1529/biophysj.107.117960.
- Betz, Timo, Martin Lenz, J.-F. Jean François Joanny, and Cécile Sykes (2009). “ATP-dependent mechanics of red blood cells.” In: *Proceedings of the National Academy of Sciences* 106.36, pp. 15320–15325. DOI: 10.1073/pnas.0904614106.
- Bezanilla, Magdalena, Amy S. Gladfelter, David R. Kovar, and Wei-Lih Lee (2015). “Cytoskeletal dynamics: A view from the membrane.” In: *Journal of Cell Biology* 209.3, pp. 329–337. DOI: 10.1083/jcb.201502062.
- Bhattacharjee, Tapomoy and Sujit S. Datta (2019). “Bacterial hopping and trapping in porous media.” In: *Nature Communications* 10.1, p. 2075. DOI: 10.1038/s41467-019-10115-1.
- Blanchoin, Laurent, Rajaa Boujemaa-Paterski, Cécile Sykes, and Julie Plastino (2014). “Actin Dynamics, Architecture, and Mechanics in Cell Motility.” In: *Physiological Reviews* 94.1, pp. 235–263. DOI: 10.1152/physrev.00018.2013.
- Bleicher, P., T. Nast-Kolb, A. Sciortino, Y. A. de la Trobe, T. Pokrant, J. Faix, and A. R. Bausch (2021). “Intra-bundle contractions enable extensile properties of active actin networks.” In: *Scientific Reports* 11.1, p. 2677. DOI: 10.1038/s41598-021-81601-0.
- Bleicher, P., A. Sciortino, and A. R. Bausch (2020). “The dynamics of actin network turnover is self-organized by a growth-depletion feedback.” In: *Scientific Reports* 10.1, p. 6215. DOI: 10.1038/s41598-020-62942-8.
- Boal, David H (2012). *Mechanics of the cell*. English. OCLC: 801405893. Cambridge; New York: Cambridge University Press.
- Boudaoud, Arezki, Agata Burian, Dorota Borowska-Wykręt, Magalie Uyttewaal, Roman Wrzalik, Dorota Kwiatkowska, and Olivier Hamant (2014). “FibrilTool, an ImageJ plug-in to quantify fibrillar structures in raw microscopy images.” In: *Nature Protocols* 9.2, pp. 457–463. DOI: 10.1038/nprot.2014.024.
- Bouvrais, Hélène, Flemming Cornelius, John H. Ipsen, and Ole G. Mouritsen (2012). “Intrinsic reaction-cycle time scale of Na⁺,K⁺-ATPase manifests itself in the lipid-protein interactions of nonequilibrium membranes.” In: *Proceedings of the National Academy of Sciences* 109.45, pp. 18442–18446. DOI: 10.1073/pnas.1209909109.

- Brown, Robert (1828). “A brief account of microscopical observations made in the months of June, July and August, 1827, on the particles contained in the pollen of plants; and on the general existence of active molecules in organic and inorganic bodies.” In: *Phil. Mag.* 4.
- Caldas, Paulo, Mar López-Peigrín, Daniel J.G. G. Pearce, Nazmi Burak Budanur, Jan Brugués, and Martin Loose (2019). “Cooperative ordering of treadmilling filaments in cytoskeletal networks of FtsZ and its crosslinker ZapA.” In: *Nature Communications* 10.1, p. 5744. DOI: 10.1038/s41467-019-13702-4.
- Canham, P. B. (1970). “The minimum energy of bending as a possible explanation of the biconcave shape of the human red blood cell.” In: *Journal of Theoretical Biology* 26.1. DOI: 10.1016/S0022-5193(70)80032-7.
- Cates, Michael E. and Julien Tailleur (2015). “Motility-Induced Phase Separation.” In: *Annual Review of Condensed Matter Physics* 6.1, pp. 219–244. DOI: 10.1146/annurev-conmatphys-031214-014710.
- Cetera, Maureen, Guillermina R. Ramirez-San Juan, Patrick W. Oakes, Lindsay Lewellyn, Michael J. Fairchild, Guy Tanentzapf, Margaret L. Gardel, and Sally Horne-Badovinac (2014). “Epithelial rotation promotes the global alignment of contractile actin bundles during *Drosophila* egg chamber elongation.” In: *Nature Communications* 5.1, p. 5511. DOI: 10.1038/ncomms6511.
- Chandrakar, Pooja, Minu Varghese, S.Ali Aghvami, Aparna Baskaran, Zvonimir Dogic, and Guillaume Duclos (2020). “Confinement Controls the Bend Instability of Three-Dimensional Active Liquid Crystals.” In: *Physical Review Letters* 125.25, p. 257801. DOI: 10.1103/PhysRevLett.125.257801.
- Chandrakar, Pooja et al. (2018). “Microtubule-based active fluids with improved lifetime, temporal stability and miscibility with passive soft materials.” In: *arXiv*.
- Chaté, Hugues (2020). “Dry Aligning Dilute Active Matter.” In: *Annual Review of Condensed Matter Physics* 11.1, pp. 189–212. DOI: 10.1146/annurev-conmatphys-031119-050752.
- Dalton, Benjamin A, David Oriola, Franziska Decker, Frank Jülicher, and Jan Brugués (2021). “A gelation transition enables the self-organization of bipolar metaphase spindles.” In: *bioRxiv*, p. 2021.01.15.426844. DOI: 10.1101/2021.01.15.426844.
- De La Cruz, Enrique M. and Margaret L. Gardel (2015). “Actin mechanics and fragmentation.” In: *Journal of Biological Chemistry* 290.28, pp. 17137–17144. DOI: 10.1074/jbc.R115.636472.
- DeGennes, Pierre Gilles and Jacques Prost (1993). *The physics of liquid crystals*. 2nd ed. Oxford science publications 83. Oxford : New York: Clarendon Press ; Oxford University Press.
- Di Leonardo, R., L. Angelani, D. Dell’Arciprete, G. Ruocco, V. Iebba, S. Schippa, M. P. Conte, F. Mecarini, F. De Angelis, and E. Di Fabrizio (2010). “Bacterial ratchet motors.” In: *Proceedings of the National Academy of Sciences* 107.21, pp. 9541–9545. DOI: 10.1073/pnas.0910426107.
- Dimova, Rumiana and Carlos Marques, eds. (2019). *The giant vesicle book*. Boca Raton, FL: CRC Press, Taylor & Francis Group.
- Dogic, Zvonimir, Kirstin R. Purdy, Eric Grelet, Marie Adams, and Seth Fraden (2004). “Isotropic-nematic phase transition in suspensions of filamentous virus and the neutral polymer Dextran.” In: *Physical Review E* 69.5, p. 051702. DOI: 10.1103/PhysRevE.69.051702.

- Doostmohammadi, Amin, Jordi Ignés-Mullol, Julia M. Yeomans, and Francesc Sagués (2018). “Active nematics.” In: *Nature Communications* 9.1, p. 3246. DOI: 10.1038/s41467-018-05666-8.
- Doostmohammadi, Amin, Tyler N. Shendruk, Kristian Thijssen, and Julia M. Yeomans (2017). “Onset of meso-scale turbulence in active nematics.” In: *Nature Communications* 8.1, p. 15326. DOI: 10.1038/ncomms15326.
- Duclos, Guillaume et al. (2020). “Topological structure and dynamics of three-dimensional active nematics.” In: *Science* 367.6482, pp. 1120–1124. DOI: 10.1126/science.aaz4547.
- Dürre, Katharina, Felix C. Keber, Philip Bleicher, Fridtjof Brauns, Christian J. Cyron, Jan Faix, and Andreas R. Bausch (2018). “Capping protein-controlled actin polymerization shapes lipid membranes.” In: *Nature Communications* 9.1, pp. 1–11. DOI: 10.1038/s41467-018-03918-1.
- Einstein, Albert (1905). “Ueber die von der molekularkinetischen Theorie der Waerme geforderte Bewegung von in ruhenden Fluessigkeiten suspendierten Teilchen (On the movement of small particles suspended in a steady liquid demanded by the molecular-kinetic theory of heat).” In: *Annalen der Physik* 322, pp. 549–560.
- (1908). “The elementary theory of the Brownian motion.” In: *Zeit. f. Elektrochemie* 14, pp. 235–239.
- Elgeti, J., R. G. Winkler, and G. Gompper (2015). “Physics of microswimmers” single particle motion and collective behavior: a review.” In: *Reports on Progress in Physics* 78.5, p. 056601. DOI: 10.1088/0034-4885/78/5/056601.
- Eto, Hiromune, Henri G. Franquelin, Michael Heymann, and Petra Schwille (2021). “Membrane-coated 3D architectures for bottom-up synthetic biology.” In: *Soft Matter* 17.22, pp. 5456–5466. DOI: 10.1039/D1SM00112D.
- Faizi, Hammad A., Cody J. Reeves, Vasil N. Georgiev, Petia M. Vlahovska, and Rumiana Dimova (2020). “Fluctuation spectroscopy of giant unilamellar vesicles using confocal and phase contrast microscopy.” In: *Soft Matter* 16.39, pp. 8996–9001. DOI: 10.1039/D0SM00943A.
- Fardin, M.-A. and B. Ladoux (2021). “Living proof of effective defects.” In: *Nature Physics* 17.2, pp. 172–173. DOI: 10.1038/s41567-020-01084-0.
- Farhadi, Leila, Carline Fermino Do Rosario, Edward P. Debold, Aparna Baskaran, and Jennifer L. Ross (2018). “Active Self-Organization of Actin-Microtubule Composite Self-Propelled Rods.” In: *Frontiers in Physics* 6, p. 75. DOI: 10.3389/fphy.2018.00075.
- Faris, M. D. El Alaoui et al. (2009). “Membrane tension lowering induced by protein activity.” In: *Physical Review Letters* 102.3, p. 038102. DOI: 10.1103/PhysRevLett.102.038102.
- Foster, Peter J., Sebastian Fürthauer, Michael J. Shelley, and Daniel J. Needleman (2015). “Active contraction of microtubule networks.” In: *eLife* 4.DECEMBER2015. DOI: 10.7554/eLife.10837.
- Frangipane, Giacomo, Gaszton Vizsnyiczai, Claudio Maggi, Romolo Savo, Alfredo Sciortino, Sylvain Gigan, and Roberto Di Leonardo (2019). “Invariance properties of bacterial random walks in complex structures.” In: *Nature Communications* 10.1, p. 2442. DOI: 10.1038/s41467-019-10455-y.
- Fürthauer, Sebastian, Bezia Lemma, Peter J. Foster, Stephanie C. Ems-McClung, Che-Hang Yu, Claire E. Walczak, Zvonimir Dogic, Daniel J. Needleman, and Michael J. Shelley (2019).

- “Self-straining of actively crosslinked microtubule networks.” In: *Nature Physics* 15.12, pp. 1295–1300. DOI: 10.1038/s41567-019-0642-1.
- Gagnon, David A., Claudia Dessi, John P. Berezney, Remi Boros, Daniel T.-N. Chen, Zvonimir Dogic, and Daniel L. Blair (2020). “Shear-Induced Gelation of Self-Yielding Active Networks.” In: *Physical Review Letters* 125.17, p. 178003. DOI: 10.1103/PhysRevLett.125.178003.
- Gao, Tong, Robert Blackwell, Matthew A. Glaser, M. D. Betterton, and Michael J. Shelley (2015). “Multiscale modeling and simulation of microtubule-motor-protein assemblies.” In: *Physical Review E - Statistical, Nonlinear, and Soft Matter Physics* 92.6, p. 062709. DOI: 10.1103/PhysRevE.92.062709.
- García-Soriano, Daniela A., Tamara Heermann, Ana Raso, Germán Rivas, and Petra Schwille (2020). “The speed of FtsZ treadmilling is tightly regulated by membrane binding.” In: *Scientific Reports* 10.1, p. 10447. DOI: 10.1038/s41598-020-67224-x.
- Gat, Shachar, Camille Simon, Clément Campillo, Anne Bernheim-Groswasser, and Cécile Sykes (2020). “Finger-like membrane protrusions are favored by heterogeneities in the actin network.” In: *Soft Matter* 16.31, pp. 7222–7230. DOI: 10.1039/C9SM02444A.
- Genkin, Mikhail M., Andrey Sokolov, Oleg D. Lavrentovich, and Igor S. Aranson (2017). “Topological Defects in a Living Nematic Ensnare Swimming Bacteria.” In: *Physical Review X* 7.1, p. 011029. DOI: 10.1103/PhysRevX.7.011029.
- Giardina, Irene (2008). “Collective behavior in animal groups: Theoretical models and empirical studies.” In: *HFSP Journal* 2.4, pp. 205–219. DOI: 10.2976/1.2961038.
- Girard, P., J. Prost, and P. Bassereau (2005). “Passive or Active Fluctuations in Membranes Containing Proteins.” In: *Physical Review Letters* 94.8, p. 088102. DOI: 10.1103/PhysRevLett.94.088102.
- Goehring, Nathan W., Debanjan Chowdhury, Anthony A. Hyman, and Stephan W. Grill (2010). “FRAP analysis of membrane-associated proteins: Lateral diffusion and membrane-cytoplasmic exchange.” In: *Biophysical Journal* 99.8, pp. 2443–2452. DOI: 10.1016/j.bpj.2010.08.033.
- Großmann, Robert, Igor S. Aranson, and Fernando Peruani (2020). “A particle-field approach bridges phase separation and collective motion in active matter.” In: *Nature Communications* 11.1, p. 5365. DOI: 10.1038/s41467-020-18978-5.
- Grover, Rahul, Janine Fischer, Friedrich W. Schwarz, Wilhelm J. Walter, Petra Schwille, and Stefan Diez (2016). “Transport efficiency of membrane-anchored kinesin-1 motors depends on motor density and diffusivity.” In: *Proceedings of the National Academy of Sciences* 113.46, E7185–E7193. DOI: 10.1073/pnas.1611398113.
- Hardouin, Jérôme, Rian Hughes, Amin Doostmohammadi, Justine Laurent, Teresa Lopez-Leon, Julia M Yeomans, Jordi Ignés-Mullol, and Francesc Sagués (2019). “Reconfigurable flows and defect landscape of confined active nematics.” In: *Communications Physics* 2.1, p. 121. DOI: 10.1038/s42005-019-0221-x.
- Helfrich, W. (1973). “Elastic Properties of Lipid Bilayers: Theory and Possible Experiments.” In: *Zeitschrift für Naturforschung - Section C Journal of Biosciences* 28.11-12, pp. 693–703. DOI: 10.1515/znc-1973-11-1209.
- Henkin, Gil, Stephen J. DeCamp, Daniel T.N. Chen, Tim Sanchez, and Zvonimir Dogic (2014). “Tunable dynamics of microtubule-based active isotropic gels.” In: *Philosophical Transac-*

- tions of the Royal Society A: Mathematical, Physical and Engineering Sciences* 372.2029, pp. 20140142–20140142. DOI: 10.1098/rsta.2014.0142.
- Howard, Jonathon (2001). *Mechanics of motor proteins and the cytoskeleton*. eng. Nachdr. OCLC: 247917499. Sunderland, Mass: Sinauer.
- Huber, L., R. Suzuki, T. Krüger, E. Frey, and A. R. Bausch (2018). “Emergence of coexisting ordered states in active matter systems.” In: *Science* 361.6399, pp. 255–258. DOI: 10.1126/science.aao5434.
- Hynes, Thomas R., Steven M. Block, Brian T. White, and James A. Spudich (1987). “Movement of myosin fragments in vitro: Domains involved in force production.” In: *Cell* 48.6, pp. 953–963. DOI: 10.1016/0092-8674(87)90704-5.
- Inoue, Daisuke, Greg Gutmann, Takahiro Nitta, Arif Md. Rashedul Kabir, Akihiko Konagaya, Kiyotaka Tokuraku, Kazuki Sada, Henry Hess, and Akira Kakugo (2019). “Adaptation of Patterns of Motile Filaments under Dynamic Boundary Conditions.” In: *ACS Nano* 13.11, pp. 12452–12460. DOI: 10.1021/acsnano.9b01450.
- Inoue, Daisuke, Bulbul Mahmot, Arif Md Rashedul Kabir, Tamanna Ishrat Farhana, Kiyotaka Tokuraku, Kazuki Sada, Akihiko Konagaya, and Akira Kakugo (2015). “Depletion force induced collective motion of microtubules driven by kinesin.” In: *Nanoscale* 7.43, pp. 18054–18061. DOI: 10.1039/c5nr02213d.
- Jiang, Rui, Steven Vandal, Soohyun Park, Sheereen Majd, Erkan Tüzel, and William O. Hancock (2019). “Microtubule binding kinetics of membrane-bound kinesin-1 predicts high motor copy numbers on intracellular cargo.” In: *Proceedings of the National Academy of Sciences of the United States of America* 116.52, pp. 26564–26570. DOI: 10.1073/pnas.1916204116.
- Jung, Wonyeong, Luke A. Fillenwarth, Atsushi Matsuda, Jing Li, Yasuhiro Inoue, and Taeyoon Kim (2020). “Collective and contractile filament motions in the myosin motility assay.” In: *Soft Matter* 16.6, pp. 1548–1559. DOI: 10.1039/C9SM02082A.
- Juniper, Michael P N, Marian Weiss, Ilia Platzman, Joachim P Spatz, and Thomas Surrey (2018). “Spherical network contraction forms microtubule asters in confinement.” In: *Soft Matter* 14.6, pp. 901–909. DOI: 10.1039/C7SM01718A.
- Kaiser, A., H. H. Wensink, and H. Löwen (2012). “How to capture active particles.” In: *Physical Review Letters* 108.26, p. 268307. DOI: 10.1103/PhysRevLett.108.268307.
- Kamien, Randall D. (2002). “The geometry of soft materials: a primer.” In: *Reviews of Modern Physics* 74.4, pp. 953–971. DOI: 10.1103/RevModPhys.74.953.
- Kaneko, Taikopaul, Suguru Ando, Ken’Ya Furuta, Kazuhiro Oiwa, Hirofumi Shintaku, Hidetoshi Kotera, and Ryuji Yokokawa (2019). “Transport of microtubules according to the number and spacing of kinesin motors on gold nano-pillars.” In: *Nanoscale* 11.20, pp. 9879–9887. DOI: 10.1039/c9nr01324e.
- Kaneko, Taikopaul, Ken’ya Furuta, Kazuhiro Oiwa, Hirofumi Shintaku, Hidetoshi Kotera, and Ryuji Yokokawa (2020). “Different motilities of microtubules driven by kinesin-1 and kinesin-14 motors patterned on nanopillars.” In: *Science Advances* 6.4, eaax7413. DOI: 10.1126/sciadv.aax7413.
- Käs, J., H. Strey, J.X. Tang, D. Finger, R. Ezzell, E. Sackmann, and P.A. Janmey (1996). “F-actin, a model polymer for semiflexible chains in dilute, semidilute, and liquid crystalline

- solutions.” In: *Biophysical Journal* 70.2, pp. 609–625. DOI: 10.1016/S0006-3495(96)79630-3.
- Kayser, Richard F. and Harold J. Raveché (1978). “Bifurcation in Onsager’s model of the isotropic-nematic transition.” In: *Physical Review A* 17.6, pp. 2067–2072. DOI: 10.1103/PhysRevA.17.2067.
- Keber, F. C., E. Loiseau, T. Sanchez, S. J. DeCamp, L. Giomi, M. J. Bowick, M. C. Marchetti, Z. Dogic, and A. R. Bausch (2014). “Topology and dynamics of active nematic vesicles.” In: *Science* 345.6201, pp. 1135–1139. DOI: 10.1126/science.1254784.
- Köhler, Simone and Andreas R. Bausch (2012). “Contraction mechanisms in composite active actin networks.” In: *PLoS ONE* 7.7. Ed. by Harry Mellor, e39869. DOI: 10.1371/journal.pone.0039869.
- Köhler, Simone, Volker Schaller, and Andreas R. Bausch (2011). “Structure formation in active networks.” In: *Nature Materials* 10.6, pp. 462–468. DOI: 10.1038/nmat3009.
- Köhler, Simone, Kurt M. Schmoller, Alvaro H. Crevenna, and Andreas R. Bausch (2012). “Regulating Contractility of the Actomyosin Cytoskeleton by pH.” In: *Cell Reports* 2.3, pp. 433–439. DOI: 10.1016/j.celrep.2012.08.014.
- Köster, Darius Vasco, Kabir Husain, Elda Iljazi, Abrar Bhat, Peter Bieling, R. Dyché Mullins, Madan Rao, and Satyajit Mayor (2016). “Actomyosin dynamics drive local membrane component organization in an in vitro active composite layer.” In: *Proceedings of the National Academy of Sciences* 113.12, E1645–E1654. DOI: 10.1073/pnas.1514030113.
- Kumar, Nitin, Rahul Kumar Gupta, Harsh Soni, Sriram Ramaswamy, and A. K. Sood (2018). “Trapping and sorting active particles: motility-induced condensation and smectic defects.” In: *Physical Review E* 99.3, p. 032605. DOI: 10.1103/PhysRevE.99.032605.
- Langevin, Paul (1908). “Sur la theorie du mouvement brownien (On the theory of Brownian Motion).” In: *C. R. Acad. Sci.* 146, pp. 530–533.
- Lee, Kwonmoo, Jennifer L. Gallop, Komal Rambani, and Marc W. Kirschner (2010). “Self-Assembly of Filopodia-Like Structures on Supported Lipid Bilayers.” In: *Science* 329.5997, pp. 1341–1345. DOI: 10.1126/science.1191710.
- Lekkerkerker, Henk N. W. and Remco Tuinier (2011). *Colloids and the depletion interaction*. Lecture notes in physics v. 833. OCLC: ocn727325895. Dordrecht ; New York: Springer.
- Lemma, Bezia, Noah P Mitchell, Radhika Subramanian, Daniel J Needleman, and Zvonimir Dogic (2021). “Active microphase separation in mixtures of microtubules and tip-accumulating molecular motors.” In.
- Lemma, Linnea M, Michael M Norton, Stephen J. DeCamp, S Ali Aghvami, Seth Fraden, Michael F Hagan, and Zvonimir Dogic (2020). “Multiscale dynamics in active nematics.” In: *arXiv*.
- Lenz, Martin (2014). “Geometrical Origins of Contractility in Disordered Actomyosin Networks.” In: *Physical Review X* 4.4, p. 041002. DOI: 10.1103/PhysRevX.4.041002.
- Lera-Ramirez, Manuel and Francois Nedelec (2019). “Theory of antiparallel microtubule overlap stabilization by motors and diffusible crosslinkers.” In: *Cytoskeleton* 76.11-12, pp. 600–610. DOI: 10.1002/cm.21574.

- Litschel, Thomas and Petra Schwille (2021). “Protein Reconstitution Inside Giant Unilamellar Vesicles.” In: *Annual Review of Biophysics* 50.1, pp. 525–548. DOI: 10.1146/annurev-biophys-100620-114132.
- Loiseau, Etienne, Jochen A.M. Schneider, Felix C. Keber, Carina Pelzl, Gladys Massiera, Guillaume Salbreux, and Andreas R. Bausch (2016). “Shape remodeling and blebbing of active cytoskeletal vesicles.” In: *Science Advances* 2.4, e1500465–e1500465. DOI: 10.1126/sciadv.1500465.
- Lopes, Joseph, David A. Quint, Dail E. Chapman, Melissa Xu, Ajay Gopinathan, and Linda S. Hirst (2019). “Membrane mediated motor kinetics in microtubule gliding assays.” In: *Scientific Reports* 9.1, pp. 1–9. DOI: 10.1038/s41598-019-45847-z.
- Maan, Renu, Etienne Loiseau, and Andreas R. Bausch (2018). “Adhesion of Active Cytoskeletal Vesicles.” In: *Biophysical Journal* 115.12, pp. 2395–2402. DOI: 10.1016/j.bpj.2018.10.013.
- Manneville, J.-B., P. Bassereau, S. Ramaswamy, and J. Prost (2001). “Active membrane fluctuations studied by micropipet aspiration.” In: *Physical Review E* 64.2, p. 021908. DOI: 10.1103/PhysRevE.64.021908.
- Marchetti, M. C., J. F. Joanny, S. Ramaswamy, T. B. Liverpool, J. Prost, Madan Rao, and R. Aditi Simha (2013). “Hydrodynamics of soft active matter.” In: *Reviews of Modern Physics* 85.3, pp. 1143–1189. DOI: 10.1103/RevModPhys.85.1143.
- Maroudas-Sacks, Yonit, Liora Garion, Lital Shani-Zerbib, Anton Livshits, Erez Braun, and Kinneret Keren (2021). “Topological defects in the nematic order of actin fibres as organization centres of Hydra morphogenesis.” In: *Nature Physics* 17.2, pp. 251–259. DOI: 10.1038/s41567-020-01083-1.
- Martínez-Calvo, Alejandro, Carolina Trenado-Yuste, and Sujit S Datta (2021). “Active transport in complex environments.” In.
- Maryshev, Ivan, Andrew B. Goryachev, Davide Marenduzzo, and Alexander Morozov (2019). “Dry active turbulence in a model for microtubule–motor mixtures.” In: *Soft Matter* 15.30, pp. 6038–6043. DOI: 10.1039/C9SM00558G.
- Maryshev, Ivan, Alexander Morozov, Andrew B. Goryachev, and Davide Marenduzzo (2020). “Pattern formation in active model C with anchoring: bands, aster networks, and foams.” In: *Soft Matter* 16.38, pp. 8775–8781. DOI: 10.1039/D0SM00927J.
- Middelkoop, Teije C., Júlia Garcia-Baucells, Porfirio Quintero-Cadena, Lokesh G. Pimpale, Shahrzad Yazdi, Paul W. Sternberg, Peter Gross, and Stephan W. Grill (2021). “CYK-1/Formin activation in cortical RhoA signaling centers promotes organismal left–right symmetry breaking.” In: *Proceedings of the National Academy of Sciences* 118.20, e2021814118. DOI: 10.1073/pnas.2021814118.
- Milner, Scott T. and S. A. Safran (1987). “Dynamical fluctuations of droplet microemulsions and vesicles.” In: *Physical Review A* 36.9, pp. 4371–4379. DOI: 10.1103/PhysRevA.36.4371.
- Mohapatra, Lishibanya, Bruce L. Goode, and Jane Kondev (2015). “Antenna Mechanism of Length Control of Actin Cables.” In: *PLOS Computational Biology* 11.6. Ed. by Sean X. Sun, e1004160. DOI: 10.1371/journal.pcbi.1004160.
- Monzel, C. and K. Sengupta (2016). *Measuring shape fluctuations in biological membranes*. DOI: 10.1088/0022-3727/49/24/243002.

- Moore, Jeffrey M., Tyler N. Thompson, Matthew A. Glaser, and Meredith D. Betterton (2020). “Collective motion of driven semiflexible filaments tuned by soft repulsion and stiffness.” In: *Soft Matter* 16.41, pp. 9436–9442. DOI: 10.1039/D0SM01036G.
- Murrell, Michael P. and Margaret L. Gardel (2012). “F-actin buckling coordinates contractility and severing in a biomimetic actomyosin cortex.” In: *Proceedings of the National Academy of Sciences of the United States of America* 109.51, pp. 20820–20825. DOI: 10.1073/pnas.1214753109.
- Mušević, Igor (2019). “Interactions, topology and photonic properties of liquid crystal colloids and dispersions.” In: *The European Physical Journal Special Topics* 227.17, pp. 2455–2485. DOI: 10.1140/epjst/e2019-800107-y.
- Nasirimarekani, Vahid, Tobias Strübing, Andrej Vilfan, and Isabella Guido (2021). “Tuning the Properties of Active Microtubule Networks by Depletion Forces.” In: *Langmuir* 37.26, pp. 7919–7927. DOI: 10.1021/acs.langmuir.1c00426.
- Nedelec, Francois and Dietrich Foethke (2007). “Collective Langevin dynamics of flexible cytoskeletal fibers.” In: *New Journal of Physics* 9.11, p. 427. DOI: 10.1088/1367-2630/9/11/427.
- Nelson, Philip, Marko Radosavljević, Sarina Bromberg, and David S. Goodsell (2014). *Biological physics: energy, information, life*. eng. OCLC: 931490066. New York, NY: Freeman.
- Norton, Michael M., Arvind Baskaran, Achini Opathalage, Blake Langeslay, Seth Fraden, Aparna Baskaran, and Michael F. Hagan (2018). “Insensitivity of active nematic liquid crystal dynamics to topological constraints.” In: *Physical Review E* 97.1, p. 012702. DOI: 10.1103/PhysRevE.97.012702.
- Onsager, Lars (1949). “The effects of shape on the interaction of colloidal particles.” In: *Annals of the New York Academy of Sciences* 51.4, pp. 627–659. DOI: 10.1111/j.1749-6632.1949.tb27296.x.
- Opathalage, Achini, Michael M Norton, Michael P N Juniper, Blake Langeslay, S Ali Aghvami, Seth Fraden, and Zvonimir Dogic (2019). “Self-organized dynamics and the transition to turbulence of confined active nematics.” In: *Proceedings of the National Academy of Sciences* 116.11, pp. 4788–4797. DOI: 10.1073/pnas.1816733116.
- Paoluzzi, Matteo, Roberto Di Leonardo, M. Cristina Marchetti, and Luca Angelani (2016). “Shape and Displacement Fluctuations in Soft Vesicles Filled by Active Particles.” In: *Scientific Reports* 6.1, p. 34146. DOI: 10.1038/srep34146.
- Paraschiv, Alexandru, Thibaut J. Lagny, Christian Vanhille Campos, Evelyne Coudrier, Patricia Bassereau, and Anđela Šarić (2021). “Influence of membrane-cortex linkers on the extrusion of membrane tubes.” In: *Biophysical Journal* 120.4, pp. 598–606. DOI: 10.1016/j.bpj.2020.12.028.
- Patteson, A. E., A. Gopinath, M. Goulian, and P. E. Arratia (2015). “Running and tumbling with *E. coli* in polymeric solutions.” In: *Scientific Reports* 5.1, p. 15761. DOI: 10.1038/srep15761.
- Pearce, Daniel J. G. and Karsten Kruse (2021). “Properties of twisted topological defects in 2D nematic liquid crystals.” In: *Soft Matter* 17.31, pp. 7408–7417. DOI: 10.1039/D1SM00825K.

- Pécrcéaux, J., H.-G. Döbereiner, J. Prost, J-F J.-F. Joanny, and P. Bassereau (2004). “Refined contour analysis of giant unilamellar vesicles.” In: *The European Physical Journal E* 13.3, pp. 277–290. DOI: 10.1140/epje/i2004-10001-9.
- Penrose, L. S. (1965). “Dermatoglyphic Topology.” In: *Nature* 205.4971, pp. 544–546. DOI: 10.1038/205544a0.
- Pernier, Julien, Remy Kusters, Hugo Bousquet, Thibaut Lagny, Antoine Morchain, Jean-François Joanny, Patricia Bassereau, and Evelyne Coudrier (2019). “Myosin 1b is an actin depolymerase.” In: *Nature Communications* 10.1, p. 5200. DOI: 10.1038/s41467-019-13160-y.
- Pernier, Julien, Antoine Morchain, Valentina Caorsi, Aurélie Bertin, Hugo Bousquet, Patricia Bassereau, and Evelyne Coudrier (2020). “Myosin 1b flattens and prunes branched actin filaments.” In: *Journal of Cell Science* 133.18. DOI: 10.1242/jcs.247403.
- Perrin, Jean (1912). “Les Atomes (The Atoms).” In.
- Peruani, Fernando, Andreas Deutsch, and Markus Bär (2006). “Nonequilibrium clustering of self-propelled rods.” In: *Physical Review E - Statistical, Nonlinear, and Soft Matter Physics* 74.3, p. 030904. DOI: 10.1103/PhysRevE.74.030904.
- Peterson, Matthew S E, Aparna Baskaran, and Michael F Hagan (2021). “Vesicle shape transformations driven by confined active filaments.” In.
- Phillips, Rob, Jane Kondev, Julie Theriot, and Hernan G. Garcia (2019). *Physical Biology Of The Cell, 2/E*. Garland Science.
- Pollard, Thomas D. (2016). “Actin and Actin-Binding Proteins.” In: *Cold Spring Harbor Perspectives in Biology* 8.8, a018226. DOI: 10.1101/cshperspect.a018226.
- Pollard, Thomas D. and John A. Cooper (2009). “Actin, a Central Player in Cell Shape and Movement.” In: *Science* 326.5957, pp. 1208–1212. DOI: 10.1126/science.1175862.
- Poon, Wilson C K (2013). *From Clarkia to Escherichia and Janus: the physics of natural and synthetic active colloids*, pp. 317–386. DOI: 10.3254/978-1-61499-278-3-317.
- Prost, J and R Bruinsma (1996). “Shape fluctuations of active membranes.” In: *Europhysics Letters (EPL)* 33.4, pp. 321–326. DOI: 10.1209/epl/i1996-00340-1.
- Prost, J., F. Jülicher, and J-F F. Joanny (2015). “Active gel physics.” In: *Nature Physics* 11.2, pp. 111–117. DOI: 10.1038/nphys3224.
- Purcell, Edward M. (1977). “Life at low Reynolds number.” In: *Ann. J. Phys.* 45.
- Pyrpassopoulos, Serapion, Elizabeth A. Feeser, Jessica N. Mazerik, Matthew J. Tyska, and E. Michael Ostap (2012). “Membrane-bound Myo1c powers asymmetric motility of actin filaments.” In: *Current Biology* 22.18, pp. 1688–1692. DOI: 10.1016/j.cub.2012.06.069.
- Rickman, Jamie, François Nédélec, and Thomas Surrey (2019). “Effects of spatial dimensionality and steric interactions on microtubule-motor self-organization.” In: *Physical Biology* 16.4, p. 046004. DOI: 10.1088/1478-3975/ab0fb1.
- Rinaldin, Melissa, Piermarco Fonda, Luca Giomi, and Daniela J. Kraft (2020). “Geometric pinning and antimixing in scaffolded lipid vesicles.” In: *Nature Communications* 11.1, p. 4314. DOI: 10.1038/s41467-020-17432-w.
- Rizzelli, Francesca, Maria Grazia Malabarba, Sara Sigismund, and Marina Mapelli (2020). “The crosstalk between microtubules, actin and membranes shapes cell division.” In: *Open biology* 10.3, p. 190314. DOI: 10.1098/rsob.190314.

- Rodríguez-García, Ruddi et al. (2020). “Mechanisms of Motor-Independent Membrane Remodeling Driven by Dynamic Microtubules.” In: *Current Biology* 30.6, 972–987.e12. DOI: 10.1016/j.cub.2020.01.036.
- Rogez, Benoit, Laeschkir Würthner, Anastasiia B. Petrova, Felix B. Zierhut, Dario Saczko-Brack, Maria-Ana Huergo, Christopher Batters, Erwin Frey, and Claudia Veigel (2019). “Reconstitution reveals how myosin-VI self-organises to generate a dynamic mechanism of membrane sculpting.” In: *Nature Communications* 10.1, p. 3305. DOI: 10.1038/s41467-019-11268-9.
- Roostalu, Johanna, Jamie Rickman, Claire Thomas, François Nédélec, and Thomas Surrey (2018). “Determinants of Polar versus Nematic Organization in Networks of Dynamic Microtubules and Mitotic Motors.” In: *Cell* 175.3, 796–808.e14. DOI: 10.1016/j.cell.2018.09.029.
- Roux, Aurélien, Giovanni Cappello, Jean Cartaud, Jacques Prost, Bruno Goud, and Patricia Bassereau (2002). “A minimal system allowing tubulation with molecular motors pulling on giant liposomes.” In: *Proceedings of the National Academy of Sciences* 99.8, pp. 5394–5399. DOI: 10.1073/pnas.082107299.
- Saito, Ai, Tamanna Ishrat Farhana, Arif Md Rashedul Kabir, Daisuke Inoue, Akihiko Konagaya, Kazuki Sada, and Akira Kakugo (2017). “Understanding the emergence of collective motion of microtubules driven by kinesins: role of concentration of microtubules and depletion force.” In: *RSC Advances* 7.22, pp. 13191–13197. DOI: 10.1039/c6ra27449h.
- Sanchez, Tim, Daniel T.N. Chen, Stephen J. Decamp, Michael Heymann, and Zvonimir Dogic (2012). “Spontaneous motion in hierarchically assembled active matter.” In: *Nature* 491.7424, pp. 431–434. DOI: 10.1038/nature11591.
- Sanchez, Timothy, David Welch, Daniela Nicastro, and Zvonimir Dogic (2011). “Cilia-Like Beating of Active Microtubule Bundles.” In: *Science* 333.6041, pp. 456–459. DOI: 10.1126/science.1203963.
- Sato, Yusuke, Yuichi Hiratsuka, Ibuki Kawamata, Satoshi Murata, and Shin-ichiro Ichiro M. Nomura (2017). “Micrometer-sized molecular robot changes its shape in response to signal molecules.” In: *Science Robotics* 2.4, eaal3735. DOI: 10.1126/scirobotics.aal3735.
- Schaller, Volker, Christoph Weber, Erwin Frey, and Andreas R. Bausch (2011). “Polar pattern formation: hydrodynamic coupling of driven filaments.” In: *Soft Matter* 7.7, p. 3213. DOI: 10.1039/c0sm01063d.
- Schaller, Volker, Christoph Weber, Christine Semmrich, Erwin Frey, and Andreas R. Bausch (2010). “Polar patterns of driven filaments.” In: *Nature* 467.7311, pp. 73–77. DOI: 10.1038/nature09312.
- Schliwa, Manfred and Günther Woehlke (2003). “Molecular motors.” In: *Nature* 422.6933, pp. 759–765. DOI: 10.1038/nature01601.
- Sciortino, Alfredo and Andreas R. Bausch (2021). “Pattern formation and polarity sorting of driven actin filaments on lipid membranes.” In: *Proceedings of the National Academy of Sciences* 118.6, e2017047118. DOI: 10.1073/pnas.2017047118.
- Sendra, G. Hernán, Christian H. Hoerth, Christian Wunder, and Holger Lorenz (2015). “2D map projections for visualization and quantitative analysis of 3D fluorescence micrographs.” In: *Scientific Reports* 5.1, p. 12457. DOI: 10.1038/srep12457.

- Shankar, Suraj, Mark J. Bowick, and M. Cristina Marchetti (2017). “Topological Sound and Flocking on Curved Surfaces.” In: *Physical Review X* 7.3, p. 031039. DOI: 10.1103/PhysRevX.7.031039.
- Shankar, Suraj and M. Cristina Marchetti (2019). “Hydrodynamics of Active Defects: From Order to Chaos to Defect Ordering.” In: *Physical Review X* 9.4, p. 041047. DOI: 10.1103/PhysRevX.9.041047.
- Shankar, Suraj, Sriram Ramaswamy, M. Cristina Marchetti, and Mark J. Bowick (2018). “Defect Unbinding in Active Nematics.” In: *Physical Review Letters* 121.10, p. 108002. DOI: 10.1103/PhysRevLett.121.108002.
- Shi, Xia-qing and Hugues Chaté (2018). “Self-Propelled Rods: Linking Alignment-Dominated and Repulsion-Dominated Active Matter.” In:
- Simon, Camille et al. (2019). “Actin dynamics drive cell-like membrane deformation.” In: *Nature Physics* 15.6, pp. 602–609. DOI: 10.1038/s41567-019-0464-1.
- Sknepnek, Rastko and Silke Henkes (2015). “Active swarms on a sphere.” In: *Physical Review E* 91.2, p. 022306. DOI: 10.1103/PhysRevE.91.022306.
- Smoluchowski, Marian (1906). “On the average path of the gas molecules and its relationship with the theory of diffusion.” In: *Bulletin International de l’Academie des Sciences de Cracovie*.
- Soares E Silva, Marina, José Alvarado, Jeanette Nguyen, Nefeli Georgoulia, Bela M. Mulder, and Gijsje H. Koenderink (2011). “Self-organized patterns of actin filaments in cell-sized confinement.” In: *Soft Matter* 7.22, pp. 10631–10641. DOI: 10.1039/c1sm06060k.
- Stephens, David J. (2012). *Functional coupling of microtubules to membranes-implications for membrane structure and dynamics*. DOI: 10.1242/jcs.097675.
- Striebel, Moritz, Isabella R. Graf, and Erwin Frey (2020). “A Mechanistic View of Collective Filament Motion in Active Nematic Networks.” In: *Biophysical Journal* 118.2, pp. 313–324. DOI: 10.1016/j.bpj.2019.11.3387.
- Strübing, Tobias, Amir Khosravanizadeh, Andrej Vilfan, Eberhard Bodenschatz, Ramin Golestanian, and Isabella Guido (2020). “Wrinkling Instability in 3D Active Nematics.” In: *Nano Letters* 20.9, pp. 6281–6288. DOI: 10.1021/acs.nanolett.0c01546.
- Sumino, Yutaka, Ken H. Nagai, Yuji Shitaka, Dan Tanaka, Kenichi Yoshikawa, Hugues Chaté, and Kazuhiro Oiwa (2012). “Large-scale vortex lattice emerging from collectively moving microtubules.” In: *Nature* 483.7390, pp. 448–452. DOI: 10.1038/nature10874.
- Suzuki, Kazuya, Makito Miyazaki, Jun Takagi, Takeshi Itabashi, and Shin’ichi Ishiwata (2017). “Spatial confinement of active microtubule networks induces large-scale rotational cytoplasmic flow.” In: *Proceedings of the National Academy of Sciences of the United States of America* 114.11, pp. 2922–2927. DOI: 10.1073/pnas.1616001114.
- Suzuki, Ryo and Andreas R. Bausch (2017). “The emergence and transient behaviour of collective motion in active filament systems.” In: *Nature Communications* 8.1, p. 41. DOI: 10.1038/s41467-017-00035-3.
- Suzuki, Ryo, Christoph A. Weber, Erwin Frey, and Andreas R. Bausch (2015). “Polar pattern formation in driven filament systems requires non-binary particle collisions.” In: *Nature Physics* 11.10, pp. 839–843. DOI: 10.1038/nphys3423.

- Takatori, Sho C. and Amaresh Sahu (2020). “Active Contact Forces Drive Nonequilibrium Fluctuations in Membrane Vesicles.” In: *Physical Review Letters* 124.15, p. 158102. DOI: 10.1103/PhysRevLett.124.158102.
- Tanida, Sakurako, Ken’ya Furuta, Kaori Nishikawa, Tetsuya Hiraiwa, Hiroaki Kojima, Kazuhiro Oiwa, and Masaki Sano (2020). “Gliding filament system giving both global orientational order and clusters in collective motion.” In: *Physical Review E* 101.3, p. 032607. DOI: 10.1103/PhysRevE.101.032607.
- Toyoshima, Yoko Yano, Stephen J. Kron, Elizabeth M. McNally, Kenneth R. Niebling, Chikashi Toyoshima, and James A. Spudich (1987). “Myosin subfragment-1 is sufficient to move actin filaments in vitro.” In: *Nature* 328.6130, pp. 536–539. DOI: 10.1038/328536a0.
- Tsitkov, Stanislav, Yuchen Song, Juan B. Rodriguez, Yifei Zhang, and Henry Hess (2020). “Kinesin-Recruiting Microtubules Exhibit Collective Gliding Motion while Forming Motor Trails.” In: *ACS Nano* 14.12, pp. 16547–16557. DOI: 10.1021/acsnano.0c03263.
- Turiv, Taras et al. (2020). “Polar jets of swimming bacteria condensed by a patterned liquid crystal.” In: *Nature Physics* 16.4, pp. 481–487. DOI: 10.1038/s41567-020-0793-0.
- Turlier, H., D. A. Fedosov, B. Audoly, T. Auth, N. S. Gov, C. Sykes, J.-F. F. Joanny, G. Gompper, and T. Betz (2016). “Equilibrium physics breakdown reveals the active nature of red blood cell flickering.” In: *Nature Physics* 12.5, pp. 513–519. DOI: 10.1038/nphys3621.
- Van de Cauter, Lori, Federico Fanalista, Lennard van Buren, Nicola De Franceschi, Elisa Godino, Sharon Bouw, Christophe Danelon, Cees Dekker, Gijsje H. Koenderink, and Kristina A. Ganzinger (2021). “Optimized cDICE for Efficient Reconstitution of Biological Systems in Giant Unilamellar Vesicles.” In: *ACS Synthetic Biology* 10.7, pp. 1690–1702. DOI: 10.1021/acssynbio.1c00068.
- Van Der Schoot, Paul (2018). *Molecular Theory of Nematic Liquid Crystals*. Tech. rep.
- Vicsek, Tamás, András Czirók, Eshel Ben-Jacob, Inon Cohen, and Ofer Shochet (1995). “Novel Type of Phase Transition in a System of Self-Driven Particles.” In: *Physical Review Letters* 75.6, pp. 1226–1229. DOI: 10.1103/PhysRevLett.75.1226.
- Vicsek, Tamás and Anna Zafeiris (2012). “Collective motion.” In: *Physics Reports* 517.3-4, pp. 71–140. DOI: 10.1016/j.physrep.2012.03.004.
- Vilfan, Andrej, Smrithika Subramani, Eberhard Bodenschatz, Ramin Golestanian, and Isabella Guido (2019). “Flagella-like Beating of a Single Microtubule.” In: *Nano Letters* 19.5, pp. 3359–3363. DOI: 10.1021/acs.nanolett.9b01091.
- Vromans, Arthur J. and Luca Giomi (2016). “Orientational properties of nematic disclinations.” In: *Soft Matter* 12.30, pp. 6490–6495. DOI: 10.1039/C6SM01146B.
- Vutukuri, Hanumantha Rao, Masoud Hoore, Clara Abaurrea-Velasco, Lennard van Buren, Alessandro Dutto, Thorsten Auth, Dmitry A. Fedosov, Gerhard Gompper, and Jan Vermant (2020). “Active particles induce large shape deformations in giant lipid vesicles.” In: *Nature* 586.7827, pp. 52–56. DOI: 10.1038/s41586-020-2730-x.
- Weber, Christoph A., Ryo Suzuki, Volker Schaller, Igor S. Aranson, Andreas R. Bausch, Erwin Frey, and David A Weitz (2015). “Random bursts determine dynamics of active filaments.” In: *Proceedings of the National Academy of Sciences* 112.34, pp. 10703–10707. DOI: 10.1073/pnas.1421322112.

- Weitz, Sebastian, Andreas Deutsch, and Fernando Peruani (2015). “Self-propelled rods exhibit a phase-separated state characterized by the presence of active stresses and the ejection of polar clusters.” In: *Physical Review E - Statistical, Nonlinear, and Soft Matter Physics* 92.1, p. 012322. DOI: 10.1103/PhysRevE.92.012322.
- Wensink, H. H. and H. Löwen (2012). “Emergent states in dense systems of active rods: From swarming to turbulence.” In: *Journal of Physics Condensed Matter* 24.46, p. 464130. DOI: 10.1088/0953-8984/24/46/464130.
- Wensink, Henricus H., Jörn Dunkel, Sebastian Heidenreich, Knut Drescher, Raymond E. Goldstein, Hartmut Löwen, Julia M. Yeomans, H. Lowen, and Julia M. Yeomans (2012). “Meso-scale turbulence in living fluids.” In: *Proceedings of the National Academy of Sciences of the United States of America* 109.36, pp. 14308–14313. DOI: 10.1073/pnas.1202032109.
- Wu, Kun-Ta, Jean Bernard Hishamunda, Daniel T. N. Chen, Stephen J. DeCamp, Ya-Wen Chang, Alberto Fernández-Nieves, Seth Fraden, and Zvonimir Dogic (2017). “Transition from turbulent to coherent flows in confined three-dimensional active fluids.” In: *Science* 355.6331, eaal1979. DOI: 10.1126/science.aal1979.
- Xu, Ting, Dimitrios Vavylonis, Feng Ching Tsai, Gijsje H. Koenderink, Wei Nie, Eddy Yusuf, I. Ju Lee, Jian Qiu Wu, and Xiaolei Huang (2015). “SOAX: A software for quantification of 3D biopolymer networks.” In: *Scientific Reports* 5.1, pp. 1–10. DOI: 10.1038/srep09081.
- Yang, Yingzi, Vincent Marceau, and Gerhard Gompper (2010). “Swarm behavior of self-propelled rods and swimming flagella.” In: *Physical Review E - Statistical, Nonlinear, and Soft Matter Physics* 82.3, pp. 1–13. DOI: 10.1103/PhysRevE.82.031904.
- Zhang, Li and Amy Shaub Maddox (2010). “Anillin.” In: *Current Biology* 20.4, R135–R136. DOI: 10.1016/j.cub.2009.12.017.
- Zhang, Rui, Nitin Kumar, Jennifer L. Ross, Margaret L. Gardel, and Juan J. de Pablo (2018). “Interplay of structure, elasticity, and dynamics in actin-based nematic materials.” In: *Proceedings of the National Academy of Sciences* 115.2, E124–E133. DOI: 10.1073/pnas.1713832115.
- Zhou, Shuang, Andrey Sokolov, Oleg D. Lavrentovich, and Igor S. Aranson (2014). “Living liquid crystals.” In: *Proceedings of the National Academy of Sciences of the United States of America* 111.4, pp. 1265–1270. DOI: 10.1073/pnas.1321926111.

List of Figures

1.1	Depletion force Big objects immersed in a bath of smaller objects feel an attractive force. This is because by aggregating together bigger objects can decrease the volume that was previously inaccessible to the smaller ones, thus increasing their entropy. The same phenomenon is present in the case of elongated objects (e.g., filaments) in a bath of smaller polymers (e.g, PEG or methylcellulose).	8
1.2	Scheme of the Vicsek model as an example of agent-based model A) Scheme of the Vicsek model [Vicsek et al. 1995]. Particles with a given self-propulsion speed interact locally with their neighbors and change their speed accordingly. B) Pattern forming in the Vicsek model: at high activity collective bands form, at low activity the phase is isotropic.	9
1.3	Cytoskeletal filaments Cell contains different kinds of cytoskeletal filaments. Microtubules (left) are rigid and mainly used for cargo transport. Actin (center) is a semiflexible and mainly use for plasticity and dynamics of the cytoskeleton. Intermediate filaments (right) are flexible and perform a variety of different roles we do not discuss here. Image from [Käs et al. 1996] . .	12
1.4	Cytoskeletal motors A) Motors are composed by a head (binding filaments) and a tail (binding cargo or other motors) B) Motors can coordinate to walk on filaments and they always move in a specific direction given by the filaments' polarity. C) Motors can assemble into multi-motors minifilaments. D) Motors stuck on a solid substrate propel filaments instead of walking on them. This technique (gliding assay) can be used to study motors' properties. D) Example of the ATP-based cycle of myosin: without ATP, the motor is bound to the filament in a given position (red bar). Upon ATP binding, the motors detaches and then hydrolyzes the ATP into ADP-Pi. This leads to a conformational change. Upon dissociation of the ATP the motor binds again, now in a new position (blue bar) and eventually recovers its initial configuration so the cycle can start over. F) Micrograph of a myosin (left) and a kinesin (right) dimers, from [Schliwa and Woehlke 2003]	16
1.5	Reconstitution of cytoskeletal networks Both actin (A) and microtubules (B) networks can be reconstituted <i>in vitro</i> using a mixture of filaments, motors and crosslinkers. In A, an actin network will contract due to the presence of motors. In B, microtubules assemble in an active fluid composed of extensile bundles (see Section 3.2). Scale bars are 100 μm . C) Example of a reconstituted GUV containing an actin cortex, from Maan, Loiseau, and Bausch 2018.	21
1.6	Scheme of the hard-rod model and the isotropic-nematic transition top) The hard-rod model features elongated object with a main orientation $\pm n$ and an aspect ratio D/L . Rods can not occupy the same volume as each other. At high enough density, rods self assemble into an ordered, nematic state with mean alignment $\pm n_0$. bottom) If rods are not aligned (high orientational entropy), a big portion of space (shaded area) is unavailable for other rods (resulting in lower translational entropy). Conversely, if they align, the excluded volume is much smaller. This explains the clash between orientational and translational entropy leading to order.	25
1.7	Splay, twist and bend deformations Scheme of the three main deformations allowed for a nematic material.	30
1.8	An actin nematic with topological defects Actin filaments form a lyotropic nematic. When self-assembled, the system can be quenched using depletants so that topological defects of charge $\pm 1/2$ appear.	32

1.9	Lipid assembly: A-C) Different assemblies of lipids including a micelle, an inverted micelle (A), a bilayer (B) and a vesicle (C). Lipids' hydrophilic heads are in red and hydrophobic tails are in grey. D) Examples of a FRAP experiment on a supported bilayer showing the bilayer is fluid. D) Confocal snapshot of an empty vesicle.	36
1.10	Deformations of membranes: Membranes can be deformed in different ways. They can be for instance stretched (change in area or in thickness) (A) or bent, for example to form GUVs, giving rise to a curvature $1/R$ to which corresponds an energy penalty (B).	38
1.11	Fluctuations of membranes: A) Membranes fluctuate due to thermal motion. This gives rise to undulations bringing the membrane at a given height h with respect to the equilibrium $h = 0$. B) We can decompose undulations of a GUV in Fourier series to obtain a fluctuation spectrum. To each mode q indeed a different energy e_q corresponds. C) The final spectrum plotted for two vesicles having same tension and bending rigidity but different radius, leading to changes in the crossover mode $\bar{\lambda}$. The $1/q$ and $1/q^3$ scaling are shown for reference.	41
2.1	Self-propelled rods: A) An example of SPR, a particle with an orientation \mathbf{p} and a self propulsion speed v . B, C) Alignment and repulsion dominated interactions: on the left (alignment-dominated) particles can cross each other but align due to some interaction; on the right (repulsion dominated) particles must stop upon collision.	48
2.2	Actin gliding assays: A, B) Schematics of two different kind of alignments, a very weak one and a slightly stronger one. A) In the case of weak alignment between filaments, the resulting order is polar, featuring density waves moving in the same direction (scale bar: $50 \mu m$). B) If alignment is slightly strengthened, the resulting order is nematic and lanes form (scale bar: $50 \mu m$). C) Filament-filament collision statistics for an actin gliding assay with (red) and without (blue) PEG, from [Suzuki and Bausch 2017]. Polar waves and nematic lanes in A and B are labelled with the same color to indicate to which alignment statistic they correspond. D) Rings formed by gliding actin in the presence of fascin, from [Weber et al. 2015].	50
2.3	Microtubules gliding assays: A) Microtubules forming an array of vortices, from [Sumino et al. 2012]. Scale bar is $2 \mu m$. B) Microtubules assembling in nematic lanes, from [Inoue et al. 2015]. Scale bar is $50 \mu m$	52
2.4	Microtubule gliding on a membrane: A microtubule gliding on a membrane moves but its speed is decreased as motors slip on the membrane. This also means that colliding microtubules stop as motors are unable to provide enough force to make filaments crawl over each other.	55
2.5	Schematics of the system and microscopic behavior A) Motors are bound to a SLB and push short actin filaments. Because of slippage of the motors on the membrane, filaments stop upon collision and align. On glass instead, filaments interact weakly. B) Filaments colliding align due to the modification of the substrate. Upon collision, filaments stop, align and then keep moving (Scale bar: $5 \mu m$). C) Multiple filaments can stop and aggregate against obstacles (Scale bar: $2 \mu m$).	57
2.6	Collision statistics for gliding filaments on a SLB A) By measuring multiple collisions, we show that the interaction is strongly nematic, with filaments aligning at $\theta_{out} \approx 0^\circ$ or 180° whatever the incoming angle θ_{in} . B) Time evolution of example collisions. Filaments collide, stop, fluctuate and eventually align.	58
2.7	High density pattern formation of gliding actin on a SLB As the surface density of filaments is increased, collective structures appear, featuring streams and vortices of filaments. A) as the density is increased, patterns start forming (Scale bars: $20 \mu m$) B) time series of the formation of structures at $O = 2.6$, showing aggregation into lanes and vortices (Scale bar: $50 \mu m$).	60
2.8	Formation and structure of streams and vortices A) Schematics of seeds, streams and vortices. B-C) Close up of a stream and a vortex forming. Filaments accumulate in streams at $\sigma = 0.83$ filaments/ μm^2 . Seeds join and leave the stream. Vortices can appear and disappear and sometimes join a close-by stream. (B) A vortex can form by a stream looping on itself due to collisions with other streams (B). Scale bars are $10 \mu m$. D-G) Details: small seeds of filaments can collide and form streams (D, E, G) or vortices (F). (Scale bars: $10 \mu m$) Scale bar is $10 \mu m$	61

2.9	Quantification of structure formation on SLBs A) Thickness distribution and mean thickness in terms of filaments' number as a function of the concentration of filaments. Streams become longer and thicker. B) Vortices (dashed) and streams (thick) radii of curvatures. This indicates that vortices have diameters much bigger than the individual filaments' size. C) The formation of structures leads to a separation of the filaments density in space over time, from uniform in space to either high or zero. This is visualized by snapshots at different times (left) and by a histogram of the fluorescence intensity at the same times (right) for $\sigma = 0.83$ filaments/ μm^2 . See Methods 4.5 for details.	62
2.10	Phase diagram of structures on SLB: As the filaments' length and concentration is changed, the formation of structures is affected. Higher concentrations lead to longer, more stable, thicker patterns. Longer filaments lead to more vorticity.	63
2.11	High density sedimentation leads to nematic-like structures comprising $\pm 1/2$ defects A) Sedimenting $1 \mu M$ of actin over time leads to the appearance of a very dense, nematic-like phase and a low density, almost empty phase (Scale bar: $50 \mu m$). B) In the high density phase, where alignment mismatches are present in the dense phase, nematic defects of charge $\pm 1/2$ are present. (Scale bar: $10 \mu m$) C) Time series of defects formation and dissolution (Scale bar: $5 \mu m$). Nematic defects in this case can appear (middle frame) and dissolve over time as they are not constrained by conservation of the total charge since they are isolated in space. Negative defects disappear, positive defects turn into polar comets.	64
2.12	Nematic wedges accumulate and polar sort filaments A) Formation of a $+1/2$ nematic defect and successive accumulation and ejection of polar filaments. The intensity along the dashed line is plotted, with the intensity at time 0 as a reference, showing accumulation and then motion of filaments. B) schematics of accumulation of filaments in a nematic wedge and successive ejection of a polar comet. On the right, the $+1/2$ defect conformation is shown highlighting the splay- and bend-dominated areas.	65
2.13	Asymmetric fluorescence recovery indicates polarity By performing FRAP experiments we can measure the polarity of observed structures. A-C) FRAP experiments indicating asymmetric recovery for a vortex (A), a stream, including its kymograph (B) and a comet lane (C). D) schematics of the measurement: the recovery of the bleached region is measured at two opposite positions I_L and I_R and the parameter p is computed. Both p (black), I_L (blue) and I_R (red) are shown in the plot. E) results of the computation of p , indicating that all structures at all densities have asymmetric recovery and are hence polar. Scale bars: $10 \mu m$	67
2.14	Mechanism of polarity sorting due to steric interaction A) Already at the single filament collision, there is a bias towards polar order due to filaments colliding polarly moving afterwards in the same direction for a longer time. B) Steric interactions lead to accumulation of filaments against obstacles. All accumulated filaments have the same polarity and when the obstacle vanishes move in the same direction. C) Even at low density, defect-like trapping conformations can be observed (Scale bar is $10 \mu m$).	68
2.15	Schematics of the GUV-filaments system and examples A) We bind HMM inside spherical GUVs using biotin-streptavidin. Upon ATP addition, the filaments assemble into patterns visible as clear bands on the equatorial plane of the GUV. B) Control experiments show instead no organization of the actin, but only accumulation on the membrane in the presence of PEG. C) Microscopy images of GUVs at 100, 300 and 600 nM, indicating the formation of patterns. At low density, only small streams are visible. At higher density, vesicles with vortices and more complex patterns are visible. D) Radius distribution of GUVs (N=193), showing a mean radius of $\langle R \rangle = 15 \mu m$. Scale bars are $20 \mu m$	70
2.16	Phase diagram of GUVs containing gliding filaments GUVs containing respectively an actin concentration of 100, 150, 300 and 600 nM exhibit different patterns. At low density, streams form. As the density increases, comet-streams start emerging and often converge into a vortex. At 600 nM a fraction of the GUVs is jammed, with GUVs exhibiting a well known $4 \times \frac{1}{2}$ defects conformation. Scale bars are $20 \mu m$	72

2.17	Time series of pattern forming in a GUV A-C) Over time, patterns appear. At low density, streams are present (A). At higher densities, streams form and merge into vortices also form (B, C). D) Fraction of GUVs observed in a given state as the density changes, showing how streams are soon dominated by vortices which however soon turn into a jammed state. Bands are rarely observed. Close ups on the bottom indicate the different structures. A band-forming GUV is shown in Fig. 2.19. The number of analysed GUVs appears in the inset. Scale bars are $20 \mu m$.	74
2.18	Nematic defects and nematic wedges in GUVs Nematic wedge-based polarity sorting is present also in the GUV system. A) Time series of a GUV at $c_0 = 150$ with a nematic wedge forming and turning into a polar stream. B) Nematic wedge forming at $c_0 = 600 nM$. Close up shows both a $+1/2$ and a $-1/2$ nematic defect are present. C) The same GUV as Fig. 2.16.C at $c_0 = 600 nM$ for a vortex. A nematic defect, on the side, turns into a comet-stream and joins the vortex. Scale bars are $20 \mu m$.	76
2.19	Formation of vortices in GUVs A) Equirectangular projections of GUVs at $600 nM$ over time, showing vortex formation. The equirectangular projection allows to see the full formation on a single plane. Merging of streams is evident. B) Snapshot of a vortex and a stream at $300 nM$ and of two different double vortices at $600 nM$. C) A histogram of vortex radii shows a mean radius $R_v \approx 11 \mu m$, much bigger than vortices observed on SLBs. D) At high concentration, GUV-wide vortices (bands) can be observed (experiment carried out with $c_0 = 1 \mu M$ and 0.25% MC). Scale bars are $20 \mu m$. E) Equirectangular projections of a double vortex (top) and a band (bottom) at $600 nM$.	77
2.20	Quantification of formation of vortices in GUVs A) Taking the intensity of actin fluorescence as a function of the polar angle ϕ we can monitor the stream formation and merging into a vortex. A low intensity (uniform) configuration evolves forming two peaks (streams) that merge into a single one (vortex). B) By observing motion of the structure on an equirectangular projection, it appears clear how vortices form by streams moving, colliding, bending and merging. C) The same vortex formation as Fig. 2.19 in the equirectangular projection can be used to compute a kymograph of streams merging in the vortex. The color-coded time scale is consistent within the figure.	78
2.21	Defects configurations in GUVs A) Filaments at high density ($600 nM$) can end up in a jammed case, fully covering the surface, occasionally evolving into a couple of comet-streams that move in the GUV. In this latter case, comets can further merge or instead move independently. B) In the jammed case, topological constraints start playing a role again. Actin filaments can assemble into the well-known $4 \times \frac{1}{2}$ defects configuration (left) but $-1/2$ defects can also appear, in which case to maintain a total charge of $+2$ an additional $+1/2$ defect is required (right). C) If actin filaments manage to escape jamming, comet streams move and evolve along the membrane's surface. They can either form a band or glide as two separate comets as in (A, right) D) Equirectangular projection of a GUV in jammed state at $c_0 = 600 nM$ E) Jamming is also visible as the mean speed of patterns lowers as the concentration is increased. Arrows indicate the direction of motion of patterns. Scale bars are $20 \mu m$.	79
2.22	Filaments align with the nematic and follow its trajectories. A) Schematic of the system: biotinilated-Kinesin is bound to a SLB. Microtubules are bound to the kinesins and glide on the surface, which is finally crowded with short stabilized actin filaments forming a nematic. B) Self-assembly of the actin nematic over time ($1 \mu m$, with $0.5 \mu m$ filaments), also measured computing the order parameter S over time (C), starting from when observation is started at the TIRF microscope. D) Microtubules gliding on a bilayer even at $\sigma \approx 0.07$ MTs/ μm^2 only aggregate transiently. Clusters form and disappear. E) The actin nematic is passive and features both $+1/2$ and $-1/2$ nematic defects F) microtubules gliding inside a nematic align with the local director and follow it over time (MT in cyan, actin in red, MTs' time projection in blue indicating the trajectory). Scale bar are $50 \mu m$, except in the defects' and the individual MTs close ups where it is $5 \mu m$.	83

- 2.23 **Behavior of microtubules at defects** A) Microtubules gliding in a +1/2 defects are converged in the core and then escape it, realigning with the nematic director afterwards (top). Microtubules gliding close to a -1/2 defect are bent by the distortions due to the defect itself. B) Occasionally, microtubules can cross a -1/2 defect's core and then realign with the nematic director. C) Depending on the filaments' length (left, 0.25 μm , right 1.5 μm) microtubules are trapped for different times and align more or less efficiently after escaping the defects. Scale bars are 5 μm . 84
- 2.24 **Tracking of microtubules moving in a nematic** A) Overlay of experimental (white) and extracted (red) trajectories showing good agreement. Scale bar is 100 μm . B) Example trajectory, showing how MTs can change direction abruptly if they meet a defect but yet recover alignment with the nematic over time. The nematic field n , the alignment S_v and the speed and torque over time are also shown. C) Histogram of alignment of MTs with the nematic, showing a peak for $S_v \approx 1$ i.e. that MTs are on average aligned. D) Speed and torque as a function of S_v indicating an increase in speed but no apparent increase in the torque if the MTs are aligned. Histograms show the variability of speed and torque for $S_v \approx 1$ (dashed orange) and $S_v < 0.75$ (blue). . . . 85
- 2.25 **Microtubules gliding in a nematic form macroscopic lanes** A) Snapshots right after ATP and actin addition at $\sigma = 0.08$ MTs/ μm^2 . As the nematic material starts forming, microtubules quickly assemble into lanes from an initially isotropic state. B) Time projections of 30 seconds of motion at different time points, showing how initially isotropic trajectories get shaped by the nematic field over time and accumulate into lanes. The last panel shows the nematic field superimposed to the trajectories at $t = 5m$ and the positions of defects. White arrows show the general direction of motion. A +1/2 defects acts as a gate to accumulate filaments in the lane. Scale bars are 50 μm 87
- 2.26 **Over time, microtubules assemble into macroscopic structures** Time projections of trajectories of microtubules, obtained by the mean intensity over time. After 45 minutes, the microtubules have assembled into macroscopic structures including vortices and lanes. Such structures are mediated by the nematic material. Scale bar is 50 μm . Conditions are 1 μM actin at 0.5 μm length and $\sigma = 0.03$ microtubules/ μm^2 88
- 2.27 **Distortions and defects alter the microtubules' motion.** A-B) Splay (A) and bend (B) in the nematic affect the flow of microtubules. While bend distortions only change the flow's orientation, splay can accumulate or disperse the microtubules' density. C-D) Both positive (C) and negative (D) defects affect the flow. Negative defects mostly act as sources of bend deformations, whereas positive, due to their splay, up-concentrate microtubules. E-F) different conformations of defects can alter the microtubules' flow according to the distortions they generate in the nematic material. Composite conformations of +1/2 and -1/2 defects can create loops (F) or channel microtubules in a given direction preferentially (E). Actin is shown in grey, microtubules in cyan and time projections of the MT's motion in blue. Data are taken from different experiments at 1 μM actin with length of 0.5 μm . Scale bars are 10 μm 89
- 2.28 **The nematic field and defects shape microtubule lanes** A) Time projections of different patterns emerging, including lanes and loops. B) Details take from the third panel of (A), showing the defect conformation leading to some structures. Notably, the looping configurations with $N = 1$ negative defects is visible, and the gating one (two close defects of opposite charge) already seen in Fig. 2.27.E. C) Detail from Fig. 2.26 showing how a single -1/2 defect in the center can deform lanes at a distance. Again, the gating configuration -1/2 and +1/2 is present. D) Another detail from Fig. 2.27.E showing a looping configuration and the corresponding nematic field. This time, a looping configuration with $N = 2$ is present. Data from 1 μM actin with length 0.5 μm and $\sigma \approx 0.007$ MTs/ μm^2 . Scale bars are 50 μm 90

- 2.29 **Polarity of observed structures** A) Two different structures (same as 2.28.A) with the corresponding microtubule flow extracted by microscopy images and color coded according to the orientation (see inset). Polar domains are clearly visible as domains of similar color. Black arrows indicate the local direction of the flow for clarity. Data from $1 \mu M$ actin with length $0.5 \mu m$ and $\sigma \approx 0.007 \text{ MTs}/\mu m^2$. B) In the same conditions but without passive nematic, microtubules move isotropically in space and in orientation space (MTs in cyan, projections in blue). In the case without actin, observed speed are around $\approx 300 \text{ nm/s}$. No net flow is observed. Scale bar is $50 \mu m$ 92
- 2.30 **Nematic defects mediate the polarity sorting of microtubules** A) Scheme of defect-based polarity sorting. A symmetric nematic defect can up-concentrate particles in space but does not violate orientational symmetry. An asymmetric defect in which the defect's axis is not perpendicular to the nematic field after the core can instead push filaments preferably in one direction. B) A $+1/2$ nematic defect up-concentrating MTs in its core and then expelling them in one direction (top). The nematic deforms locally but then relaxes back (bottom) C) This results, at high density, in a net flow biased in one direction after exiting the defect. For reference, the time projected trajectories and the nematic field are also shown and the position of the defect is marked. Scale bars are $5 \mu m$ 93
- 2.31 **Effect of the actin nematic on patterns** A) As the actin concentration is increased, patterns become thinner but still form, as long as a nematic is present. MT density is kept around $\sigma = 0.05 \text{ MTs}/\mu m^2$. Scale bar is $50 \mu m$. B) A nematic field aligned by the MTs at low actin density, with defects segregated on the side. Corresponding trajectories are shown in A, left most panel. Scale bar is $50 \mu m$. C) Varying the actin filaments' length affects the behavior of MTs in defect. For short filaments, MT escape defects easily. For long filaments, MTs are trapped in defects. Scale bar is $2 \mu m$. D) Varying the MC concentration, hence the amount of actin sedimented (in red) does not lead to pattern formation unless a stable nematic forms. MTs trajectories (in cyan) remain uniform if the concentration of MC is below 0.2% . Scale bar is $25 \mu m$. MT density is kept around $\sigma = 0.02 \text{ MTs}/\mu m^2$ 94
- 2.32 **Simulations and arguments based on the presence of $+1/2$ defects** By extracting the nematic field $\mathbf{n}(\mathbf{r})$ from experiments we can use simulations and heuristic arguments to understand how trajectories converge in specific portions of space and compare them with experimental results. We run simulations (top, middle) based on alignment of the particles on the local nematic field. The simulated trajectory (in cyan) evolves based on particles traveling in the nematic with a given speed in the presence of an aligning torque τ that forces them to follow the nematic field (as explained in main text). We also predict trajectories (top, right) by seeding starting points for streamlines (in cyan) in specific positions of the nematic field starting from the position $\mathbf{r}^{+1/2}$ of positive defects and shifting them by a quantity along their main axis $d\hat{\mathbf{p}}^{+1/2}$. This new seeding position is set as starting point of a stream with a direction chosen according to the quantity $\hat{\mathbf{p}}_{seed}$ as explained in the main text. In both cases, we recover with good agreement the experimental trajectories (top, left) of MTs. In this Figure we use as a benchmark the nematic field already shown in Fig. 2.28.A and B, at $1 \mu M$ Actin and $0.5 \mu m$ length. Each field of view is roughly $140 \times 140 \mu m^2$ 97

2.33	<p>Simulations of particles in a nematic field A-B) Simulations (left) compared to experiments (right) of the same nematic field. As the parameter A is increased simulations show the system evolves from an isotropic to a laning state. Final conformations resemble experiments both at low (A, $\sigma = 0.003$ MTs/μm^2) and high density (B, $\sigma = 0.007$ MTs/μm^2). C) Comparing simulated and experimental data with the Pearson correlation coefficients shows that already at small values of the parameter A the simulations converge to the experimental data. At high A lanes become too 'thin' and the correlation coefficient can lower. Visual agreement remains. All datasets are at $1 \mu\text{M}$ Actin D) Adding interaction to the system, summarized by the parameter s does not influence the behavior of particles which still align strongly with the nematic field for $A > 0.01 \text{ rad/s}^{-1}$ regardless of s. Field used is the same as in E, right E) Simulations also recover the formation of polar structures, as shown by the orientation of the mean flow over time in a given position. Polar domains can be clearly seen, with particles all going in one direction same as in experiments. To be compared with Fig. 2.29 for the corresponding experimental data. Scale bars are $50 \mu\text{m}$ and again each field of view is roughly $140 \times 140 \mu\text{m}^2$.</p>	99
2.34	<p>Simulation and prediction out of artificial fields A-B) A symmetric arrangement of defects leads to lanes with nematic symmetry both in simulations and using the \mathbf{Q}-tensor approach (B). C-D) Skewing the conformation so that the defects are off-axis with respect to the polarity field \mathbf{p} leads instead to polar lanes. E) A field based entirely on splay without defects can lead to polar lanes (see also [Turiv et al. 2020]). However, it is unrealistic in the case of self-assembled nematics where defects play the main role. F) Randomly-generated nematic fields recover most of the behaviors observed in experiments, including the looping conformations, in this case with $N = 1$ negative defect. Orientations are color-coded as shown by the color wheel.</p>	101
3.1	<p>Schematic of AMFs: A) A KSA (Kinesin cluster) can walk on polarly oriented microtubules, but instead extends anti-polar couples. B) At high MT density, an active nematic material is formed, featuring active defects. Taken from [Sanchez et al. 2012]. B) At low MT density, but in the presence of crosslinkers, active extending bundles form.</p>	107
3.2	<p>Schematic of the χ parameter. A) In a disperse network, the stress acting on it can be computed by counting active configurations. A motor (red) and a crosslinker (purple) together on a filament, if connected to the rest of the network (shown in gray) can exert stress depending on their relative position as the motor will try to walk and while the crosslinker will try to resist. B) In a nematic case, where activity arises from anti-polar couples, it is not enough to consider the configuration of motors and crosslinkers but also the relative polarity of the filaments. . . .</p>	110
3.3	<p>ANLN bundles microtubules in a concentration dependent way A) In the absence of ATP, as c_A is increased, the microtubules bundle. B) ANLN also tunes the network properties such as the mean bundle length and width. Each curve is at a different ANLN concentration (top: $c_A = 1.1 \mu\text{M}$ and $2.0 \mu\text{M}$, bottom: $c_A = 1.1 \mu\text{M}$, $1.3 \mu\text{M}$ and $2.0 \mu\text{M}$). Width and length are measured using SOAX [Xu et al. 2015].</p>	114
3.4	<p>ANLN tunes the morphology and activity of a AMF. A) Upon ATP addition, the system evolves in a state whose morphology depends on c_A B) The mean flow speed as a function of c_A shows a sharp increase which eventually plateaus and then decreases C) Magnification of the sharp-increase area marked in red in panel C, now at different KSA concentrations</p>	115
3.5	<p>ATP and KSA series A-B) Morphology and dynamics of the AMF as KSA is varied. A too high or too low amount of KSA will slow the system down or will be insufficient for macroscopic flow. At intermediate KSA, the system is active. C-D) Morphology and dynamics as ATP is varied. At low ATP, activity is present but the system is slow and appears mostly composed of bundles. Increasing the ATP up to saturation leads to a faster and more nematic-like morphology. Both these results confirm the interplay between activity and connectivity. Scale bars are $100 \mu\text{m}$. All experiments are at $c_A = 1.8 \mu\text{M}$.</p>	116

3.6	Cytosim simulations recover the behavior of the AMF A) Schematic of Cytosim simulations. N rigid filaments in a box of volume V with motors and crosslinkers. Motors and crosslinkers are modeled as springs which bind on the filaments. Motors can move on filaments. B) Snapshots of simulations ($N = 8000$, $r_m = 36$) at $r_x = 5$, showing no formation of bundles, and $r_x = 50$ showing formation of bundles which extend and buckle.	117
3.7	Cytosim simulations recover the behavior of the AMF By measuring the activity parameter α , indicating the fraction of filaments moving along their axis, and the coefficient β of the MSD at short (circles) and long (triangles) times we can characterize the behavior of the system. A) The parameter α , which is 1 for filaments sliding along their axis and 0 for filaments diffusing or not moving as shown in the scheme, is computed at different values of r_m , from 1 (blue) to 100 (yellow). As motors increase, the activity gets higher and the peak shifts slightly. A small decrease in activity is seen between $r_x = 1$ and $r_x \approx 10$. B) MSD scaling parameter β also indicates a transition from diffusive to ballistic at $r_x \approx 10$ (shown for $N = 8000$, $r_m = 36$). C) MSD curves (with diffusion and ballistic scaling), color-coded using the color-map shown in Fig. 3.12.	119
3.8	Experiments and simulations in different conditions A) As we change the ratio of motors to microtubules and of crosslinkers to microtubules, the results look qualitatively the same (with the presence of a threshold activity) but both the position of the threshold and the mean flow speed are modulated. B) Cytosim simulations recover all trends. Plots are color coded so that similar conditions have the same color. C) Cytosim simulations allow to also mimic the behavior of different crosslinking strength by changing the attachment rate k_{on} . Results show that stronger crosslinkers require a smaller amount (lower r_x) for activity to arise and at the same time the decrease in activity at high r_x is shifted to lower values. The initial transition is also sharper. D) A stronger crosslinker mimics the behavior of the MT-native crosslinker PRC-1 that requires smaller amounts to bind MTs and leads to a sharper transition to activity.	120
3.9	Different activity measures A) Flow of microtubules averaged in space. B) Variation of filaments' density in space and its variance. Both measures indicate a similar behavior, i.e., that the system, as r_x increases, first starts to gelate, the transitions to an active state and eventually slows down due to friction from the crosslinkers.	121
3.10	Antenna model and χ computed out of Cytosim simulations A) Distribution of motors f_x and crosslinkers f_m on a filament ($N = 8000$, $r_m = 36$, $r_x = 200$). The motors follow the antenna model fit. B) Computation of χ shows no correlation with activity, increasing immediately as r_x is increased. C) Probability of obtaining each configuration (M is for motors, X for crosslinker, arrows indicate the filament's plus end) needed to compute the χ parameter as r_x changes. As r_x increases, crosslinkers start binding. At $r_x \approx 10 - 50$ this allows motor-crosslinker couples to form. At high r_x , crosslinkers take much of the available configurations. On the right, all configurations are sketched. According to [Belmonte, Leptin, and Nédélec 2017] M-M and XL-XL are neutral, XL-M is extensile and M-XL is contractile. However, nematic order changes everything.	122
3.11	Formation of (anti)polar couples correlates with activity A) Fraction of motors bound to filaments pairs which are polar ($\sigma_{\uparrow\uparrow}$) or anti-polar ($\sigma_{\uparrow\downarrow}$). The two quantities behave differently for low r_x , as crosslinkers do not manage to stabilize anti-polar (extensile) couples. B) Total number of motors and crosslinkers bound to a couple of filaments as a function of r_x . Plot is in log-log scale. C) As r_x is increased, the total number $N_{\uparrow\downarrow} = N_m \sigma_{\uparrow\downarrow}$ of motors bound in anti-polar state divided by the total number of binding elements bound to a filament pair ($\chi_{\uparrow\downarrow}$, in black) correlates with the onset of activity (α , in red), reproducing both the low and the high r_x behavior.	124

- 3.12 **Polar and nematic order of filaments and cluster formation** A) The fraction of filaments' couples bound in an polar (blue) or antipolar (red) fashion changes depending on the amount of crosslinkers B) The local polar and nematic order is also affected, indicating that nematic order is not a good descriptor of activity, as the polar contribution needs to be accounted for and changed in a non-trivial way with the amount of crosslinkers. Activity actually correlates with negative polar order (i.e., with anti-polar couples forming). C) Activity is also related to the formation of clusters. Over time, clusters form and dissolve (at low r_x) or grow (at high r_x). Colorbar indicates value of r_x , from blue to green. D) The number of clusters as a function of r_x again shows a sharp decrease around the activity threshold, indicating that the number of clusters is a relevant parameter to describe the system. 126
- 3.13 **Examples of active GUVs** A) Encapsulating self-propelled particles inside a GUV can give rise to non-spherical shapes as particles accumulate in convex deformations (adapted from [Vutukuri et al. 2020] B) Encapsulating motile bacteria can give rise to shape deformations as the bacteria travel inside the GUV (adapted from [Takatori and Sahu 2020] C) Binding the cytoskeleton to a GUV can give rise to membrane deformations too. C) Comparing an active (green) and a passive (red) spectrum as a function of the wavelength q_x shows how the two spectra have the same scaling but the active one shows passive-like yet enhanced fluctuations (taken from [Faris et al. 2009]. D) Spectra from [Takatori and Sahu 2020] as a function of the mode number m showing how active (empty dots) and passive (full dots) spectra can differ greatly. A model (triangles) recovers both the active and the passive scaling. 129
- 3.14 **Deformation of a GUV containing microtubules:** Equatorial plane of a GUV registered every 5 seconds for a total of 2 minutes and 15 seconds. Conditions are: $c_{MT} = 0.8$ mg/ml, $c_K = 120$ nM, $c_A = 1.5$ μM . Scale bar is 50 μm . Notice the amount of different conformations in such little time. 134
- 3.15 **Microtubules deform a GUV's membrane in different ways:** A) By varying the composition of the AMF we can slightly tune the behavior of the GUV. B) Top and side views of a GUV deforming and the underlying microtubules organization (conditions: $c_{MT} = 0.8$ mg/ml, $c_K = 120$ nM, $c_A = 2.0$ μM). C) Membranes can deform in two main ways: bundles can poke directly at the membrane forming tubes (top, conditions: $c_{MT} = 0.2$ mg/ml, $c_K = 60$ nM, $c_A = 2.5$ μM). MTs can also buckle against the membrane generating large deformations (bottom, conditions: $c_{MT} = 0.8$ mg/ml, $c_K = 120$ nM, $c_A = 1.5$ μM). Close ups and behavior of the microtubules is also shown. 135
- 3.16 **Contour analysis of active GUVs** By identifying high intensity position on the equatorial plane we can obtain a contour in polar coordinates $R(\phi, t)$. Bottom picture shows a GUV with some marked positions and the same position as they appear on the reconstructed polar contour. 136
- 3.17 **Radial deformations of an active GUV** A) Examples of active GUVs exhibiting high curvature and histogram of curvature over time. Curvature in the contour plots is color coded, with blue being $k = 0$ and red being $k \approx 3/R_0$. The histogram show the distribution of curvature along an active and a passive GUV over the course of a ≈ 2 minutes time interval. While a passive GUV has curvature normally distributed around the mean radius ($k \approx k_0 = 1/R_0$) the active one exhibits a non-equilibrium distribution, with pnc peak at $k \approx 0$ and longer tails for $k > 1/R_0$ and $k < R_0$. The modal curvature is also not corresponding to k_0 anymore. B) Kymograph showing the radial fluctuations $((R(t) - R_0)/R_0)$ around the mean R_0 over time for an active GUV (left). Deformations as big as ± 40 % are visible. Additionally, the perturbations appear to be correlated in time and space, showing the presence of small membrane waves. In comparison, a passive one exhibits only minor fluctuations (right). 137

- 3.18 **Flicker spectrum of active and passive GUVs:** A) Contours are expanded in Fourier series to obtain the fluctuation spectrum of each mode. Passive GUVs (blue and purple) exhibit an equilibrium spectrum, with a crossover mode q_c that can be tuned by choosing appropriate sizes for the GUV and obtain spectra for both the bending and the tension dominated regime. Active spectra (red) are in all cases ≈ 1 order of magnitude above passive ones and exhibit a clear $\sim 1/q^3$ scaling, as indicated by the solid line. B) However, the time correlations τ_q , which for a passive one should scale like the spectra (top), are now decoupled (bottom), scaling as $\sim 1/q$, indicating that the spatial and temporal scales are now separated. The active GUV is at $c_{MT} = 0.8$ mg/ml, $c_A = 2$ μM , $c_K = 120$ nM. Passive GUVs only contain M2B buffer. 138
- 3.19 **Radial distribution of microtubules:** A) A kymograph shows accumulation of the microtubules along the membrane. Some temporal modulation of the MT density is also visible. B) Microtubules accumulate on the membrane, as measured by the radial distribution of the MT intensity across different samples, and have the tendency to accumulate in areas of high curvature. Left: Each curve is from a different GUV, conditions are $c_{MT} = 0.4$ mg/ml, $c_A = 2.5$ μM (blue and orange) and $c_{MT} = 0.8$ mg/ml, $c_A = 1.5$ μM , motors' concentration is kept at 60 nM for 0.4 mg/ml (120 nM for 0.8 mg/ml). Right: black points come from different GUVs, blue curve is the mean. C) Temporal behavior of the microtubule density near the membrane $f(\phi, t)$ (see Section 3.5.4.3) averaged along all membrane showing that the total MT intensity at the equatorial plane along the membrane changes over time, with a correlation time of ≈ 5.6 s. Conditions are $c_{MT} = 0.8$ mg/ml, $c_A = 2$ μM , $c_K = 120$ nM. 140
- 3.20 **Extraction of the membrane-near active forcing $f(\phi, t)$:** A) Starting from the equatorial plane images, we extract the intensity of microtubules f in a small area close to the membrane's position to obtain the active forcing pushing on the membrane. From this we can recover the behavior of MTs over time and space and connect it to membrane deformations. B) The MT intensity is correlated along the membrane, with visible correlation peaks seen at $\Delta\phi \approx \pi/2$ and $\Delta\phi \approx \pi$, indicating that bundles do not act as point forces but have a distinct organization. This is sketched in the picture reporting high intensity of microtubules at a quarter and at a half of the GUV perimeter, as shown by the correlation function. 141
- 3.21 **Spectral behavior of the membrane-near active forcing $f(\phi, t)$:** The fluctuation spectrum of the forcing $f(\phi, t)$ does not follow the same scaling as the membrane but rather an exponential one, coherent with the fact that microtubules move for a given time across the membrane and then disappear. Indeed, the microtubule fluctuations are enhanced at $q < 5$, indicating low-mode distributions of the forcing, which decays as q increases. 142
- 3.22 **Comparison of the spectral behavior of microtubules and membrane:** A) Microtubules fluctuate with the same correlation as the membrane, indicating that membrane deformations are indeed caused by the local pushing due to microtubules, i.e., it is the microtubules organization which fixes the time coherence of membrane fluctuations, whereas the fluctuations of the membrane are also tuned by the membrane mechanics. B) The organization of the microtubules correlates also with the membrane fluctuations. Vesicles showing deformations peaked at a given wavelength also exhibit a microtubules' density (red bars) with the same symmetry. C) Microtubules fix the membrane correlation. As long as microtubules are present, the membrane remains deformed. The picture show a ≈ 10 seconds long deformation driven by the presence of microtubules. 143
- 3.23 **Comparison of the behavior of the AMF in bulk and in GUVs:** A) By analyzing the microtubule intensity of a 3D bulk fluid ($c_{MT} = 0.8$ mg/ml, $c_A = 4$ μM , $c_K = 120$ nM) inside virtual circles with roughly the same size of a GUV ($R_0 \approx 25$) we show the effect of confinement on the AMF. B-C) Both the time and spatial correlation of the bulk AMF is decreased with respect to that of a confined one. Compare with Figures 3.20.B and 3.19.C D-E) Also the spectral behavior of the bulk fluid is different from that of a confined one, with both the q -scaling of the time correlation and of the membrane fluctuation decaying faster. This indicates that confinement enhances the time and space persistence of microtubules. Scale bars are 25 μm . . . 144

3.24	Simulations confirm experimental results: A) We simulated GUVs containing active bundles. B) As activity α of the bundles is increased, the fluctuations' spectrum also is enhanced and tends towards the $\sim 1/q^3$ scaling. B) Similarly, the membrane's fluctuation spectrum becomes detached from the time correlation τ_q in an activity-dependent way. D) The microtubules and the membrane fluctuation times are superimposable. E) The MT fluctuation spectrum is exponential.	146
3.25	Curvature and density of filaments: A) Microtubules accumulate at the membrane where high-curvature deformations are present and have a distinct 3D organization as shown from these snapshots of the same simulated GUV at different planes. B) Bundles curve along the membrane, fixing its curvature and, in return, being affected by it. This is shown here by isolating only a few bundles out of all the present ones. C) As in experiments, simulated bundles accumulate on the membrane D) Membrane and bundles curvature. Bundles deviate strongly from their equilibrium elongated shape due to activity and confinement and especially show a peak at $k \approx 1/R_0$ indicating an effect due to the GUV. E) Bundles accumulate in areas of higher curvature. Compare with Figure 3.19	147
4.1	Gelsolin affects the actin filaments' length Different gelsolin to actin ratio lead to different mean filaments length, as computed from TIRF images. A histogram for an actin:gelsolin ratio of 1:100 is shown, together with linear fit to compute different expected lengths based on the ratio.	154
4.2	cDICE setup A) Size and shape of the cDICE chamber, both 3D-printer and made out of Petri dishes, and capillary. Ruler for reference. The syringe and tubing is used to flow the mix inside the capillary. The hole to extract GUVs is also visible. B) the chamber is put on a rotating motor and the solutions are added sequentially inside with a pipette. C) Finally, the capillary is inserted in the decane solution and pressure is applied to form GUVs.	159
4.3	FRAP experiments on EggPC SLBs Example of a FRAP experiment, showing recovery of the fluorescent signal, and curves fitted as explained in 4.5 to extract the diffusion coefficient (in units of $\mu m^2/s$). 14 different curves are shown.	162
4.4	Computation of GUVs' contour: Schematic of the detection approach. Starting from the center of the GUV, we look for peaks of high intensity along the radial direction. This is repeated for different polar angles ϕ (red lines). The intensity values along the direction are histogrammed (right) and the radial position at which the intensity is maximum (blue line) is isolated (yellow dots). The radial position corresponding to the peak of the histogram is obtained with a parabolic fit close to the maximum intensity value.	168
4.5	Computation of configurations from Cytosim simulations A) Histogram of relative speed for each configuration. Motors are marked as M and crosslinkers as XL , arrows in the legend indicate the filament's plus end. As expected, configurations have a peak in relative speed at $0 \mu m/s$ and $\pm v_0$. B) Histogram of relative distances between different configurations. All data at $N = 2750$, $r_x = 75$, $r_m = 36$, $V = 2750 \mu m^3$	175

Appendix A

The Monge representation and the Helfrich-Canham energy in Fourier form

A.1 The Monge representation

First, we need to describe the surface of a membrane (this part is based on Boal 2012). To do that, we imagine a planar membrane on the xy plane and define a position vector such that at each point on the xy -plane we get as third coordinate a value $h(x, y)$ giving us the height of the membrane in that point, i.e.

$$\mathbf{r} = (x, y, h(x, y)) \quad (\text{A.1})$$

Of course we supposed the membrane deformations are small such that $h(x, y)$ is single valued. This representation will help us to find the properties of the membrane in terms of the position on the plane and is equivalent to the description of a curve in terms of a coordinate s .

We can express the tangent vectors, defining a tangent plane

$$\begin{aligned} \mathbf{t}_x &= \partial_x \mathbf{r} = (1, 0, \partial_x h) := (1, 0, h_x) \\ \mathbf{t}_y &= \partial_y \mathbf{r} = (0, 1, \partial_y h) := (0, 1, h_y) \end{aligned} \quad (\text{A.2})$$

where the subscript indicates a partial derivative. From them, using a vector product, we can map an area on the plane $dxdy$ to an area da on the membrane. Indeed, by geometrical arguments (as a segment dx corresponds to a segment $|\mathbf{t}_x|dx$

$$da = |\mathbf{t}_x \times \mathbf{t}_y|dxdy = \sqrt{1 + h_x^2 + h_y^2}dxdy := \sqrt{g}dxdy \quad (\text{A.3})$$

where we have defined the metric $g = 1 + h_x^2 + h_y^2$. We can also define a (normalised) vector normal to the surface as

$$\mathbf{n} = \frac{\mathbf{t}_x \times \mathbf{t}_y}{|\mathbf{t}_x \times \mathbf{t}_y|} = \frac{(-h_x, -h_y, 1)}{\sqrt{1 + h_x^2 + h_y^2}} \quad (\text{A.4})$$

From all this, we can find the curvatures we need, namely the mean (c_m) and Gaussian (c_G) curvatures. Results from differential geometry indicate that (some of the following coefficients are defined later on)

$$c_m = \frac{g_{xx}b_{yy} + g_{yy}b_{xx} - 2g_{xy}b_{xy}}{2g} \quad (\text{A.5})$$

and

$$c_G = \frac{b_{xx}b_{yy} - b_{xy}^2}{g} \quad (\text{A.6})$$

where g is the metric defined after Equation A.3, and we have the coefficients¹

$$g_{ij} = (\partial_i \mathbf{r}) \cdot (\partial_j \mathbf{r}) \quad \text{for } i, j = x, y$$

and

$$b_{ij} = -(\partial_i \mathbf{r}) \cdot (\partial_j \mathbf{n}) \quad \text{for } i, j = x, y$$

We can skip directly to the result we are interested in, i.e., the (approximate) form of the mean and Gaussian curvature in terms of the height h i.e.

$$\begin{aligned} c_m &= \frac{h_{xx} + h_{yy}}{2} \\ c_G &= h_{xx}h_{yy} - h_{xy}^2 \end{aligned} \tag{A.7}$$

A.2 The Helfrich-Canham energy in Fourier space

We can now rewrite the Helfrich-Canham energy given by Equation 1.45 in the Monge representation using equations for the curvature and the area in the Monge representation A.7 and A.3 as

$$E_b = \int \sqrt{1 + h_x^2 + h_y^2} dxdy \left(\frac{K_b}{2} (h_{xx} + h_{yy})^2 + \lambda \right) \tag{A.8}$$

by expanding for small $h_x \ll 1$, i.e. for small undulations, as $\sqrt{1 + h_x + h_y} \approx 1 + \frac{1}{2}(h_x^2 + h_y^2) + \dots$ and only maintaining terms up to $\approx h^2$

$$\begin{aligned} E_b &\approx \int (1 + h_x^2 + h_y^2) dxdy \left(\frac{K_b}{2} (h_{xx} + h_{yy})^2 + \lambda \right) \approx \\ &\approx \int \cancel{dxdy} \lambda + \frac{1}{2} \int dxdy (\lambda (h_x^2 + h_y^2) + K_b (h_{xx} + h_{yy})^2) \approx \\ &\approx \frac{1}{2} \int dxdy (\lambda (h_x^2 + h_y^2) + K_b (h_{xx} + h_{yy})^2) \end{aligned} \tag{A.9}$$

where we neglect the constant $\int dxdy \lambda$.

We now substitute the function $h(\mathbf{X})$, where \mathbf{X} is a point on the plane, with its Fourier transform using the identity

$$h(\mathbf{X}) = \frac{A}{4\pi^2} \int d\mathbf{q} h(\mathbf{q}) e^{i\mathbf{q} \cdot \mathbf{X}} \tag{A.10}$$

where A is the total area, $h(\mathbf{q})$ are the continuous Fourier coefficients at the 2D wave-vector $\mathbf{q} = (q_x, q_y)$.

The final result² for the energy in Fourier form is defining $q = |\mathbf{q}|$

$$E_b \approx \frac{A}{8\pi^2} \int d\mathbf{q} (\lambda q^2 + K_b q^4) h(\mathbf{q}) \bar{h}(\mathbf{q}) \tag{A.11}$$

with \bar{h} being the complex conjugate of h . This is Equation 1.46

¹It can be proved that these coefficients g_{ij} form a 2x2 matrix, whose determinant is g

²To see that quickly, one can use the well known properties allowing for the substitutions of the derivatives as $h_x \rightarrow iq_x h(\mathbf{q})$ and $h_{xx} = -q_x^2 h(\mathbf{q})$ and keeping in mind that as we are now using a complex function, magnitudes involve a conjugation of h into \bar{h} .

Appendix B

Motion of filaments propelled by SLB-bound motors

Consider the situation in which N motors are bound to a microtubule, each of them exerting (and receiving) a force \mathbf{F}_M , and thus generating a total force $N\mathbf{F}_M$ on the microtubule.

Because of the force free condition at the micron scale (see Section 1.1.1.2), this force must be exactly balance by the drag force of the microtubule \mathbf{F}_{MT} i.e.,

$$N\mathbf{F}_M + \mathbf{F}_{MT} = 0 \quad (\text{B.1})$$

If the microtubule is moving at speed \mathbf{v}_{MT} then, by Stokes' law,

$$\mathbf{F}_{MT} = \gamma_{MT}\mathbf{v}_{MT} \quad (\text{B.2})$$

where γ_{MT} is the drag coefficient of the microtubule. At the same time, we can write for the motor

$$\mathbf{F}_M = \gamma_M\mathbf{v}_M \quad (\text{B.3})$$

where now \mathbf{v}_M is the velocity of the motor on the substrate and \mathbf{F}_M is the reaction force on the motor, coming from pushing the filament. On a glass substrate, this velocity would be vanishing, as motors can not move (or rather, the drag would be infinite), but in this case they can slip on the membrane.

However, motors are also stepping on the filament (with some speed \mathbf{v}_{step}) in opposite direction while slipping, which means that the speed at which the microtubule moves is the difference of these two contributions, i.e. the slipping and the stepping. This is because part of the working distance of the stepping motors is converted into slip on the membrane rather than into push on the microtubule (Fig. 2.4 shows a schematic of the involved speeds). Thus \mathbf{v}_{MT} is reduced, with respect to \mathbf{v}_{step} by a quantity \mathbf{v}_M , i.e.,

$$|\mathbf{v}_{MT}| = |\mathbf{v}_{step}| - |\mathbf{v}_M| \quad (\text{B.4})$$

We can now combine all the obtained equations B.1, B.2 and B.3 and get

$$0 = N\mathbf{F}_M + \mathbf{F}_{MT} = N\gamma_M\mathbf{v}_M + \gamma_{MT}\mathbf{v}_{MT} \quad (\text{B.5})$$

to obtain an equation for the speed of the microtubule given by

$$\mathbf{v}_{MT} = -N \frac{\gamma_M}{\gamma_{MT}} \mathbf{v}_M \quad (\text{B.6})$$

and we can now use Equation B.4 to substitute \mathbf{v}_M getting

$$|\mathbf{v}_{MT}| = - \left(\frac{1}{1 + \frac{\gamma_{MT}}{N\gamma_M}} \right) |\mathbf{v}_{step}| \quad (\text{B.7})$$

which directly relates the speed of the microtubule to the stepping speed of the motor.

It is already clear from this expression that, unless γ_M is infinite (i.e., the drag force of the substrate is strong) the microtubule will move at only a fraction of the motors' stepping speed.

To connect this model to experimental parameters, we can use the Stokes-Einstein relation to bind γ_M to the diffusion coefficient of the motors as

$$\gamma_M = \frac{k_B T}{D_{M,1D}} \quad (\text{B.8})$$

where $k_B T$ is Boltzmann's constant times the temperature T , and $D_{M,1D}$ is the diffusion coefficient of the motors *along* the microtubule (as the motors only slip parallel to the microtubule) and hence in $1D$. Of course, by the way diffusion works in multiple dimensions, $D_{M,1D} = D_{M,2D}/2 = \alpha D_{SLB}/2$, i.e. we can related the $1D$ diffusion coefficient of a motor to its $2D$ one and this latter can be thought to be directly proportional to that of the SLB, where α is a constant depending on the way motors are bound to the lipid substrate ($\alpha \approx 2$ in [Grover et al. 2016]).

On the other hand, if we approximate a microtubule to a cylindrical rod of length L and radius r at a distance h from a surface, by Stokes law, we can compute the drag force on the microtubule as

$$\gamma_{MT} = \frac{2\pi\eta L}{\ln(2h/r)} \quad (\text{B.9})$$

where η is the fluid viscosity. Hence, we can rewrite Equation B.7 as

$$|\mathbf{v}_{MT}| = - \left(\frac{1}{1 + c \frac{D_{SLB}}{\lambda}} \right) |\mathbf{v}_{step}| \quad (\text{B.10})$$

where we have defined $c = \frac{\alpha\pi\eta}{k_B T \ln(2h/r)}$ as a parameter-dependent constant and $\lambda = N/L$ is the motors' linear density along the microtubule, presumably proportional to the surface density of motors.